1996

Non-linear Analysis Of Liners For Rigid Pipe Rehabilitation

Khaled El-Sawy

NON-LINEAR ANALYSIS OF LINERS FOR RIGID PIPE REHABILITATION

BY

Khaled El-Sawy

Faculty of Engineering Science

Department of Civil Engineering

Submitted in partial fulfilment

of the requirements for the degree of

Doctor of Philosophy

Faculty of Graduate Studies

The University of Western Ontario

London, Ontario

July 1996

ISBN 0-612-15045-3

Canada

ABSTRACT

Most damaged pipelines are structurally safe, but due to hydraulic requirements renovations are required. One solution is to apply an internal polymer liner. The critical external fluid pressure at which the liner may collapse is the target of this research. The Finite Element Method (FEM) is used and a rigorous non-linear interaction analysis allowing for large deformations and material plasticity is developed. Liners are assumed to be either perfectly circular or circular with some initial local or global geometrical imperfections. The typical local imperfection is defined as a wavy intrusion into the liner. The global imperfections take the shape of an ovalization in the damaged host pipe or an eccentric position of the loosely fitted liner relative to the damaged pipeline. A parametric study is undertaken to determine the effect of the geometrical parameters (e.g. liner thickness to radius ratio, imperfection size, ovality and size of gap between the liner and the host pipe). A comparison is made with experimental data available for circular liners, and there is good agreement with the numerical solution.

It is shown that critical external fluid pressure depends heavily on the ratio of liner thickness to radius. Thick liners experience a modest stability increase as a result of host pipe support compared to the significant stability increase for thin liners. Local geometrical imperfections have a very substantial effect on the buckling strength. The imperfection sensitivity is particularly significant for thin liners. Ovalling in the host pipe decreases stability somewhat relative to circular host pipes. Stability of loosely fitted liners degrades seriously if a significant gap exists between the liner and the host pipe, particularly when the liner is thin. Generally, the pressure which causes yield in the liner materials represents the

peak value that the structure can sustain, and inelastic stability can reasonably be estimated using that point of first yield. The current ASTM design practice employs a single stability value for all liners which is not conservative for thick liners. The thesis presents an efficient new design approach based on the parametric study which includes the effect of the liner thickness to radius ratio, liner ovality, and local imperfections.

Keywords: stability, buckling, liner, rigid pipe, imperfection, rehabilitation, trenchless technology.

ACKNOWLEDGEMENTS

I would like to express my love and appreciation to my mother, without whose encouragement this work would never have been possible. I will never forget her prayers for me in a time I really needed these prayers. I am also grateful to my wife Abeer and my son Moustafa for their patience, continuous support and encouragement throughout this study.

I would like to express my sincerest gratitude to Professor Ian Moore for his valuable technical support, guidance, and encouragement throughout this study. I am grateful to him for supporting me financially during my research. I will never forget his enthusiasm and expertise in this research. Conducting this work under his guidance and supervision was a rewarding experience.

Finally, I thank Dr. Ashraf Hefny and all my graduate student colleagues (Chuntao, Richard, Trudy) for their fruitful discussions that helped me greatly in my research.

TABLE OF CONTENTS

LIST OF TABLES

LIST OF FIGURES

Chapter Three

Chapter Four

Chapter Five

Chapter Six

Chapter Seven

Chapter Eight

CHAPTER ONE

Introduction

1.1. General Overview

The deteriorating infrastructure, in North America and worldwide, has been well documented in many journals and magazines. The cost of infrastructure renewal over the next two decades will be substantial (billions of dollars). To address this problem, cost-effective technology is required to obtain maximum benefit from the limited resources available for this purpose. The trenchless rehabilitation of damaged pipelines is developing rapidly as a competitive alternative to conventional methods of pipeline replacement. The advantage stems from its cost savings associated with reduction of disturbance to the surroundings.

The design engineer for such pipeline or sewer rehabilitation usually considers two typical situations. The damaged pipeline is either structurally safe (partially deteriorated) and can carry the soil and surcharge loads for a considerable period of time (the design lifetime of the rehabilitated pipeline), or it is fully deteriorated and unable to support the soil load above it. Both cases are usually considered in the design codes (e.g. ASTM [41]) and it is up to the designer to decide which case to consider. This type of decision usually requires sufficient sampling of the existing pipeline to determine whether the pipeline can carry the soil pressure safely.

Most of the damaged pipelines are structurally safe, but due to hydraulic requirements (e.g. leakage) renovation is required. One solution is to apply an internal polymer liner to the pipeline. In this case, any loads due to the soil surrounding the pipeline are carried by

the rigid pipeline while the liner carries only the pressure from any inside fluid or the ground water pressure which is transmitted through the cracked pipeline (Fig. 1.1a). In the process of liner installation, the liner may be temporarily subjected to another type of pressure, when grout is pumped around the liner to fill any gaps between the liner and the host pipeline. In all these loading cases, the liner should be designed to carry such pressure with an adequate factor of safety. It is well reported in the literature (Aggarwal and Cooper [1], Kyriakedis and Babcock [28] and Lo and Zhang [34]), that the encased liner may collapse at a certain critical pressure.

To plan the strategy for evaluating the critical liner pressure, two issues should be discussed. Firstly, the nature of the pipe lining process being used in industry should be considered. This review of lining technologies will, for example, indicate what liner geometries can be expected. Secondly, the method of analysis to be used and its associated assumptions need to be defined. This requires a review of previous work in this field.

1.2. Liner Installation Techniques

The construction industry is actively looking for ways to reduce the cost of rehabilitation relative to conventional pipe replacement. Many construction techniques have been developed and used to install liners into damaged pipes without the need for soil excavation associated with pipe replacement. All installation techniques depend primarily on the visco-elastic and thermoplastic nature of the polymer material.

If the installation procedure is not carefully controlled, the final liner may end up being loose relative to the damaged host pipeline and an eccentric alignment of the liner with respect to the host pipeline may occur. It is also possible that local imperfections may

develop due to existing obstacles in the damaged host pipeline. This obstacle shape is mirrored in the final installed liner. If the host pipeline shape is not circular (due to any previous deformations during the lifetime of the pipeline), then the installed liner is also non-circular. Generally, the most common geometry is an oval pipeline shape which then leads to an oval liner within it.

Therefore, the liners considered in this thesis are assumed to be either perfectly circular (Fig. 1.1a) or circular with some initial geometrical imperfection (Fig. 1.1b). The imperfections may vary from a localized imperfection to a global one. The local imperfection is defined as a wavy intrusion into the liner (Fig. 1.2a) introduced by the liner installation technique or due to imperfections in the damaged host pipe. The global imperfection takes the shape of an ovalization of both the circular liner and the host pipe (Fig. 1.2c) or an eccentric position of the liner relative to the centre of the damaged host pipe (Fig. 1.2b).

1.3. Previous work for Liner Stability

The buckling of a circular ring subjected to external pressure was studied in the last century by Levy [30]. The buckling pressure, P_{cr}, for a ring of radius, R, cross sectional moment of inertia, I, and modulus of elasticity, E, is defined by

$$P_{cr} = \frac{3EI}{R^3} \tag{1.1}$$

Generally, the elastic solution for the ring case can be easily adopted for the pipe case by simply adjusting the elastic Young's modulus, E, to be $\frac{E}{(1-\nu^2)}$, where ν is Poisson's ratio.

It is well known that when an elastic ring is encased in a rigid cavity, the critical pressure

can increase significantly [11, 29, 46, and 47]. This has led many researchers to study the case of a ring encased in a rigid cavity.

The encased ring (or liner) stability problem appeared in the literature in many different forms according to the engineering application being examined. The most common stability problem types are encased ring (or liner) subjected to thermal expansion [12, 16, 22 and 33] or under pressure loading [11, 29, 46, and 47]. The two types differ significantly in their boundary conditions. For thermal expansion problems, the detached part of the ring (due to buckling) has no longer any contact pressure acting on it. On the other hand, for the pressure case, the detached portion of the encased ring is still subjected to the applied external pressure. It is therefore important to distinguish between these two types in the literature review of the problem. A detailed literature review of the encased ring or liner stability problem is provided in Chapter two.

1.4. Parameters to be Considered and Method of Analysis

To plan the method of analysis for the liner problem, it is important to identify the different parameters which may affect the critical pressure of liners. These parameters include the following:

- the liner thickness to radius ratio,
- the size and the shape of any existing geometrical imperfections in the liner or the rigid host pipe,
- the distribution of the applied pressure (uniform or hydrostatic), and
- the non-linear material parameters

The Finite Element Method (FEM) has been used successfully to analyse many problems in various fields. The power of the Finite Element Method stems from its ability to deal with difficult geometries and complicated material behaviour. Therefore, the Finite Element Method is used in this thesis to analyse the liner problem. Many key issues should be considered in the Finite Element Analysis. These are summarized in the following topics:

- geometrical non-linearities (large deformations),
- interaction between the liner and the rigid cavity,
- type of the incremental/iterative solution algorithms, and
- material non-linearities.

As large liner deformations are expected, the FEM analysis should allow for geometrical non-linearity (in a small strain scheme). Therefore, the Updated Lagrangian approach is used.

The modelling of the interaction between the liner and the rigid cavity strongly influences the behaviour of the encased liner. A new interaction method is developed to rigorously model the frictional interface between the liner and the rigid host pipe.

The traditional solution algorithms (e.g. Newton-Raphson and Modified Newton-Raphson iterative numerical techniques shown in Fig. 1.3a) fail to predict the post-peak behaviour and may even lead to solution instability before the pressure reaches its critical value. The Arc Length Control Method represents a suitable alternative in this case where neither incremental loads nor incremental displacements are prescribed. Instead, a constraint equation is used, which may be visualized for a single degree of freedom as an arc of certain radius which intersects the load deflection curve in a point (Fig. 1.3b).

The behaviour of polymer materials is significantly time-dependent and ultimately the Finite Element Analysis should accurately model the rheology of the material. The work in the present study is directed towards an evaluation of liner buckling using elastic or elasto-plastic approximations for polymer behaviour. Subsequent work should include the use of more sophisticated non-linear time dependent material models.

1.5. Organization of the Thesis

This thesis consists of nine inter-related chapters. Chapter one is an introduction to define the problem and the organization of the thesis. Chapter two is a literature review to identify the state of the art techniques in the field of liner stability. The Finite Element Method coupled with a rigorous interaction scheme is used to solve the liner stability problem and chapters three and four provide details of the numerical formulation. In chapter three, the formulation of the Finite Element Method applied to a multi-layered structural element is discussed. The incremental algorithm used to analyse large deformation problems is presented. Details of the Arc Length Control method and elasto-plastic material model are also included in chapter three. Chapter four discusses the development of the rigorous interaction technique and its application to solve interaction problems featuring frictional interfaces.

In Chapter five the problem of an encased circular liner is considered. A comprehensive parametric study is presented. The perfect circular liner is considered first and the Finite Element results are compared against the available analytical solutions and experimental data. The effect of pressure distribution (i.e. uniform or hydrostatic) is studied. The circular liner with a local wavy imperfection is considered later in the chapter. The effect of

thickness to radius ratio and size of local imperfection on the critical pressure is examined.

Chapter six deals with the problem of an encased circular liner with either an ovalization or eccentricity imperfection. Both the oval liner case and the oval liner with a wavy imperfection case are considered. A parametric study to analyse the effect of the different parameters on the critical pressure, bending moment, and thrust in the oval liner is presented. For the liner with eccentricity imperfection, the effect of the size of the gap between the liner and the host pipe on the critical pressure is established.

Chapter seven investigates the effect of material non-linearity on the critical pressure of circular liners. A simplified bi-linear elasto-plastic material model is used to investigate the effect. While the study of material non-linearity is neither complete nor exact (because of the complicated time-dependent behaviour of the polymer materials), it clearly demonstrates the impact of material yield.

Based on the results of chapters five to seven, a design method is developed in chapter eight. The results are organized in several charts suitable for design purposes. Finally, conclusions drawn from the study are discussed in chapter nine.

In all chapters, references are cited by author and reference number written between square brackets [ ], and are detailed in alphabetical order at the end of the dissertation. Equations are numbered sequentially within each chapter, with all symbols defined where first introduced. Figures appear in order at the end of each chapter.

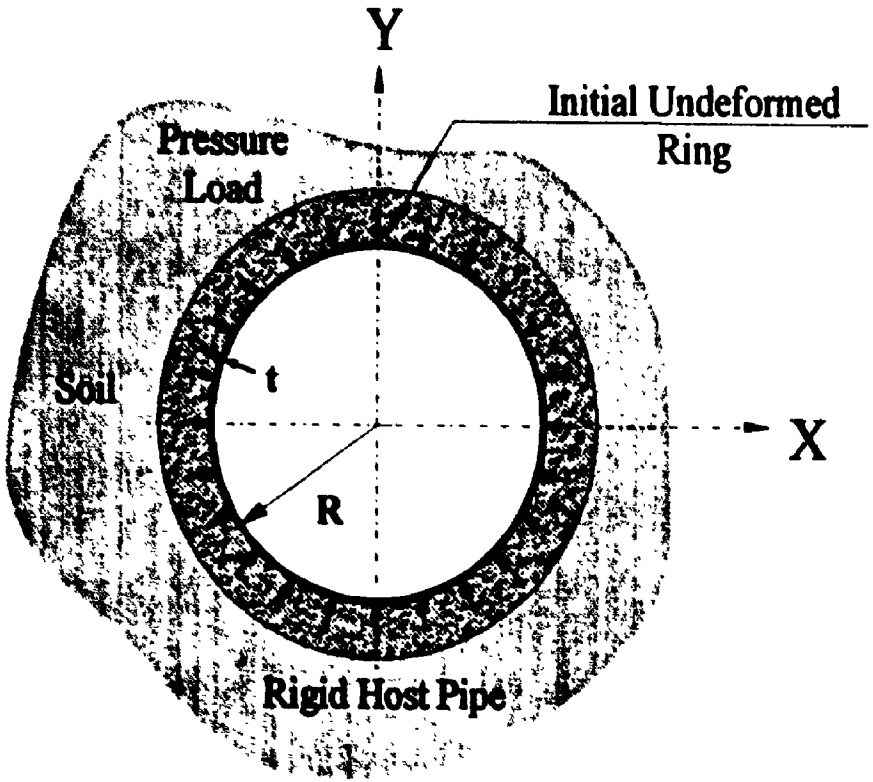

Figure 1.1a. Perfect Liner

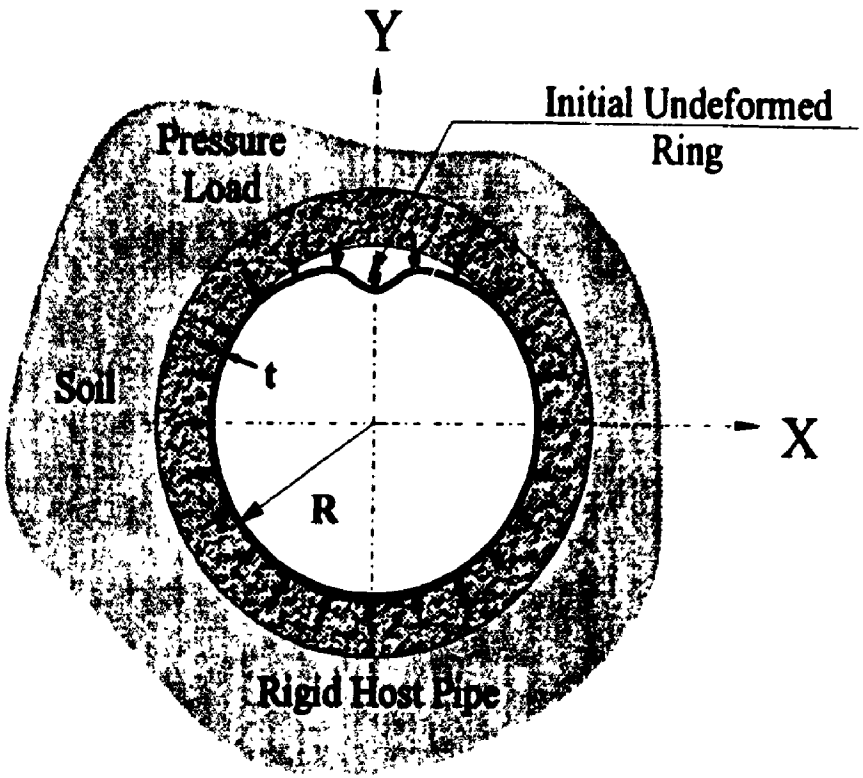

Figure 1.1b. Imperfect Liner

Figure 1.1. Definition of The Problem

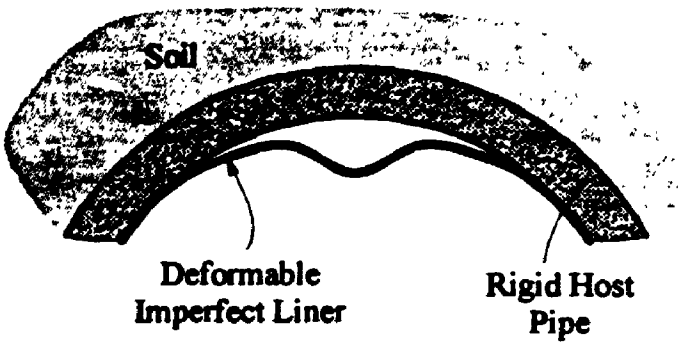

Figure 1.2a. Local Imperfection

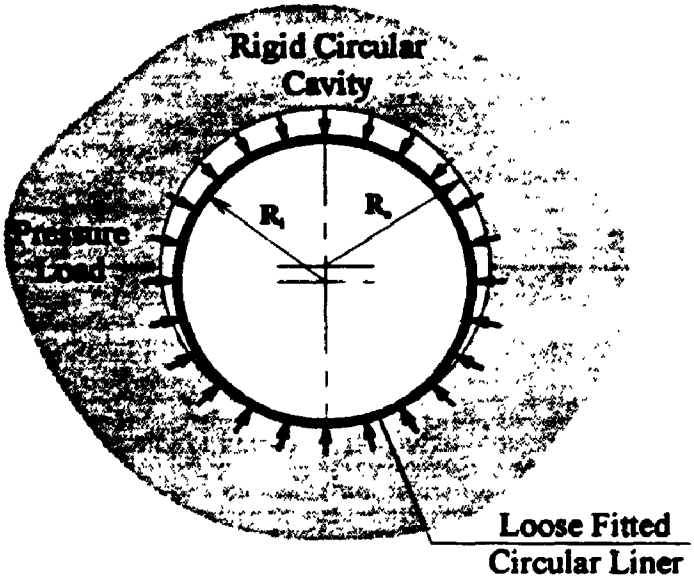

Figure 1.2b. Global Loose Fitting Imperfection

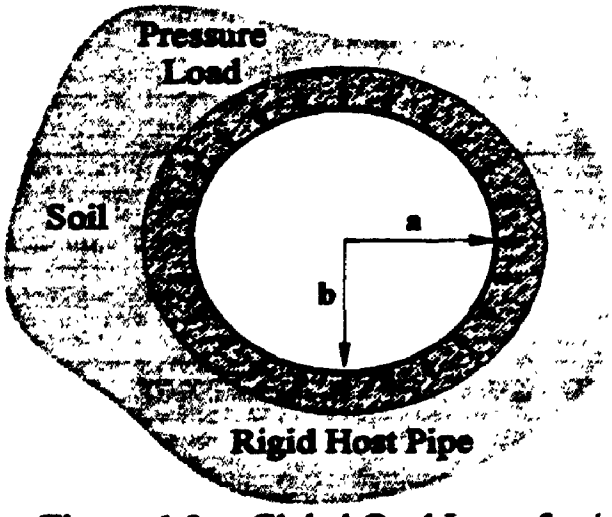

Figure 1.2c. Global Oval Imperfection

Figure 1.2. Definition of The Imperfection Geometry

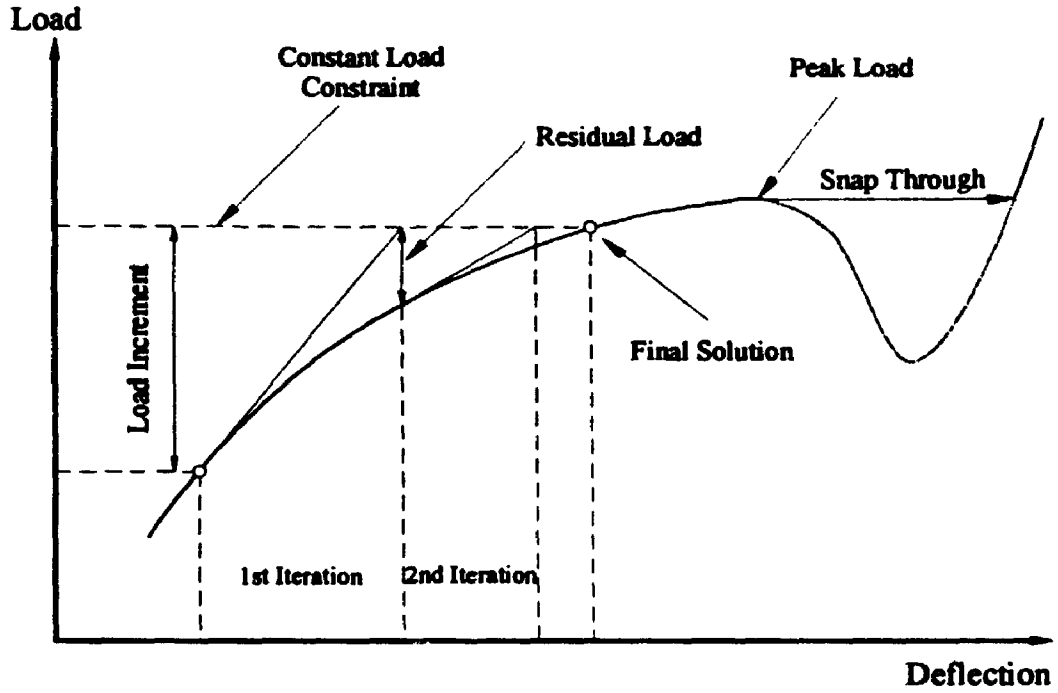

Figure 1.3a. Newton-Raphson Method

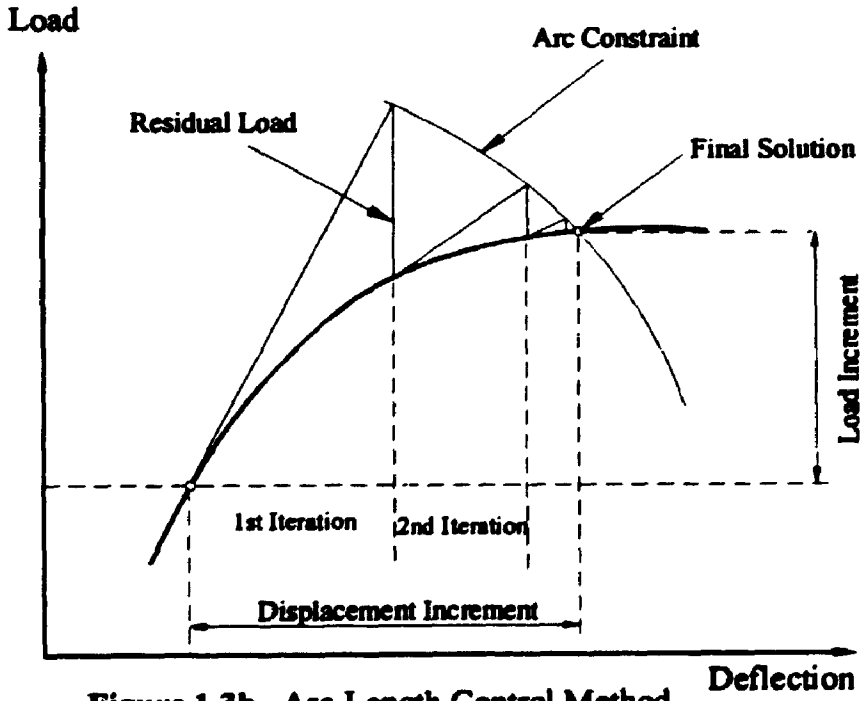

Figure 1.3b. Arc-Length Control Method

Figure 1.3. Newton-Raphson and Arc Length Control Methods

CHAPTER TWO

Literature Review

2.1. Introduction

In this chapter the general behaviour of encased liners is discussed and the significance of geometrical imperfections is considered. Past literature devoted to the topic of liner stability is reviewed. Conclusions are drawn concerning the adequacy of current design practice, and areas of research and development are listed.

2.2. General Overview

The behaviour of the liner encased in a rigid host pipe is complex to analyse. To study the liner behaviour under external pressure, it is important to investigate the influence of different parameters on that behaviour. Parameters such as the shape of the liner, the liner thickness to radius ratio, the shape and size of any imperfections, the pressure distribution, and any material non-linearity, should be considered.

Because of the rigidity of the host pipe, any soil loads are carried by the host pipe while the liner carries only the pressure from the ground water, the grouting pressure during installation, and the internal fluid pressure. Generally failure of liners is either due to material yielding or elastic instability (buckling). The yielding of the liner results from local stresses generated by the combination of thrust and bending moment, while elastic instability is associated with hoop compressions generated in the liner due to the applied loads.

In order to ensure that the liner performance is satisfactory, the liner should be designed and installed so as to guard against each of the possible failure modes. The design methods

have evolved over a period of time, and there has been a progressive development in the understanding of these performance limits.

The concept of comparing the buckling pressures for unsupported and encased liners has been employed by both researchers and developers of design codes. The idea has been to determine a quantity called "enhancement factor", K, which includes all known and unknown parameters to define the critical pressure for the encased liner as

$$K = \frac{P_{cr} \text{ for Encased Liner}}{P_{cr} \text{ for Encased Liner}} \tag{2.1}$$

where P_{cr} is the buckling pressure of the liner.

Each previous study targeting the estimation of critical pressure for encased liners had its own simplifying assumptions. Sometimes these assumptions and their implications have a significant effect on the value of the critical pressure. It is therefore important to identify the different parameters which may influence the critical pressure of liners and to determine the value of the existing theories for predicting that pressure.

To plan a strategy for evaluating the critical liner pressure, two issues should be discussed. The first issue is the type of imperfection which should be considered. This requires the review of the available pipe lining technologies since they contribute significantly to the formation of these imperfections. The second issue is the method of analysis and its associated assumptions. The following two sections review the different liner installation techniques and their associated advantages and disadvantages, and the available literature dealing with the analysis of a liner encased in a rigid cavity.

2.3. Review of the Available Pipe Lining Technology

Many construction techniques had been developed and used to install a liner into the damaged pipe without the need for soil excavation associated with pipe replacement. The construction industry is continually looking for ways to reduce the cost of rehabilitation relative to conventional pipe replacement. Most of the techniques used for the lining process (called trenchless techniques) can be categorized into three major types; the *reduction* and/or *expansion* type; the *folded poly pipe* type, and the *cured-in-place pipe* (CIPP) type. Many versions of the first technology are available nowadays. A good review of the available versions is found in Svetlik [43]. For more details the reader may refer to Hannan [20] and the ASTM specifications [41]. All installation techniques depend primarily on the visco-elastic and thermoplastic nature of the polymer material.

Liner Expansion

A custom diameter liner of relatively thin wall is chosen to provide a 3% to 8% annular clearance between the liner outer diameter (OD) and the damaged pipe inner diameter (ID). As pressure is applied to the interior of the liner, it strains within its ductile limit to contact the damaged pipe wall. For a specific time, the pressure is used to maintain the liner in place (i.e. constant strain conditions) while the polymer material begins to stress-relieve visco-elastically. The pressure required to keep the liner in place drops significantly with time. After the removal of the pressure, the liner accepts the larger diameter of the damaged pipe as its own new diameter with very limited strain recovery. If the stress-relief time of the liner is not sufficient, the liner will contract back significantly and become loose relative to the damaged pipe being lined, causing an initial alignment imperfection.

At ambient temperature, the pressure needed to initiate the liner molding to fit the damaged pipe is usually greater than 700 kPa (100 psi). The usage of hot water or low pressure steam to accelerate the process works effectively but adds to the installation cost. Finally, this technique is only suitable for pressurized pipelines. Other techniques should be used for gravity or low pressure pipelines.

Rolldown Reduction of Liners

The basic idea in this technique is the reduction of the liner outer diameter (OD) followed by the insertion of the liner into the damaged pipeline. Two pairs of dual rollers are used to apply external loads to the liner to reduce its OD. The liner is reduced in OD as it passes across the roller pairs. The reduction in the liner OD can be categorized into three types of deformations; immediately recoverable after load removal (elastic deformations), permanent (plastic deformations), and near term recoverable (i.e. visco-elastic deformations which need time to recover). The liner has to be squeezed significantly to allow for enough visco-elastic OD reduction to permit sufficient time for the installation before visco-elastic recovery. The liner thickness, rolling configuration and roller pressure should be carefully controlled otherwise the liner may either end up loose relative to the damaged pipe, or it may lock-up in the host pipe halfway through the process of lining the pipeline segment.

Hot Swage Reduction of Liners

Hot swaging of the liner facilitates reduction in the OD of the liner. The liner is introduced into a pre-heated chamber and is left for a specific residency time. The time is affected by the liner thickness and the initial liner temperature. In this heating process, the

strength of the liner and the coefficient of elasticity reduces. Hence, the force needed to push the liner into the swaging die, the pull force needed to keep the liner straight, and the tension on the line to minimize elastic and visco-elastic recovery, reduce significantly. Once installed, the hot swaged liner will dramatically enlarge in diameter and axially foreshorten somewhat.

Visco-Elastic Reduction of Liners

The key idea in this technique is to reduce the OD of the liner by passing the liner through gradually undersized sets of rollers and then apply a set of proprietary tools to hold this reduction of size for a specific duration. This duration should be long enough to allow for stress relaxation in the material of the polymer liner. The effect of this process is to decrease the recoverable elastic deformations relative to the time-dependent recoverable visco-elastic deformations. The time-dependent deformations should be large enough to let the liner installation process finish before the liner becomes locked into the host pipe. Depending upon the liner size, size reductions of 9% to 19% of the liner OD have been used with an immediate elastic recoverable portion of about 4% to 6%.

Folded Poly-Pipe

In this technique, the liner is manufactured in a folded shape with the required dimensions. The spool of folded liner is positioned near the insertion manhole and is placed in a heating chamber. The liner is preheated to about 200°C in a heating chamber and then is pulled through the damaged pipeline with a cable attached to a power winch. The liner is inflated by hot air to take the shape of the damaged host pipeline. The existence of any

obstruction in the damaged pipeline may cause the liner to wrinkle. Therefore, undesirable obstructions should be removed before the installation process. This may need point repair excavations which reduce the cost-effectiveness of the method.

Cured in Place Pipe (CIPP)

The fundamental product is a felt liner (sometimes called soft liner), sized to the length and diameter of the existing pipeline, and is impregnated with a thermoset resin system to provide structural capabilities after curing in the host pipeline. All of the techniques available today utilize existing manhole access for insertion. This soft liner aspect is what permits the liner to bend and manoeuvre through the manhole frame, channel and existing pipeline conditions to achieve its final position. The same flexible characteristics that permit insertion of the liner from manholes also allows for formation of deficiencies in the final liner due to imperfections in the host pipeline. A belly, sag, or offset in the pipeline is mirrored in the renovated pipe. Missing parts of the pipeline will appear as a bulge in the liner. This would suggest that the pipeline segments which have these undesirable conditions should be excavated and repaired prior to lining; hence reducing the cost-effectiveness of this type of lining.

2.4. Choice of the Appropriate Imperfection

The previous description of the available liner installation technologies suggests that:

- if the installation procedure is not carefully controlled, the final liner may end up being loose relative to the damaged host pipeline and an eccentric alignment of the liner with respect to the host pipeline may occur,

- it is also possible that local imperfections may develop due to any existing obstacle in the damaged host pipeline. This obstacle shape is mirrored in the final installed liner, and
- if the host pipeline shape is not circular (due to any previous deformations during the lifetime of the pipeline), the best guess is an oval pipeline shape which would produce an oval liner.

Therefore the liners considered in this thesis are assumed to be either perfectly circular (Fig. 2.1a) or circular with some initial geometrical imperfection (Fig. 2.1b). The imperfections may vary from a localized imperfection to a global one. The local imperfection is defined as a wavy intrusion into the liner (Fig. 2.2a) introduced by the liner installation technique or due to imperfections in the damaged host pipe. The global imperfection takes the shape of an ovalization to the circular liner (Fig. 2.2c) or a eccentric position relative to the damaged pipe (Fig. 2.2b).

2.5. Literature Survey

Before discussing the method of analysis used in the thesis, it is important to review the previous work done by other researchers to study encased liner (or ring) stability. This provides useful information about the different analyses and their associated assumptions.

The buckling pressure of a circular ring subjected to a pressure was studied in the last century by Levy [30]. The buckling pressure, P_{cr}, for a ring of radius, R, cross sectional moment of inertia, I, and modulus of elasticity, E, is defined by

$$P_{cr} = \frac{3EI}{R^3} \qquad (2.2)$$

Generally the solution for the ring case can be adopted for the pipe case by simply adjusting the elastic Young's modulus, E, to be $\frac{E}{(1-\nu^2)}$, where ν is Poisson's ratio. Many researchers have studied the case of a ring encased in a rigid cavity. This stability problem appeared in the literature in different forms according to the engineering application being examined. Faulty design occurs if an unsuitable solution is used for a certain application. It is therefore important to survey the literature to differentiate between each of the available solutions, and then to assign each of them to a specific problem.

2.5.1. Thermal Expansion of a Circular Ring Encased in a Smooth Rigid Circular Cavity

In this problem (Fig. 2.3) the circular ring is subjected to thermal expansion which mobilizes a hoop thrust around the ring circumference. Buckling occurs when the hoop thrust reaches a critical value (the buckling thrust). This phenomenon is well known and is generally called thermal buckling. The same buckling mechanism occurs if the circular rigid cavity contracts or shrinks radially towards the ring (this is known as the shrink buckling phenomenon). This problem is discussed by Lo *et al* [33].

The initial and final shapes of the buckled ring are specified, making the solution an upper bound to the actual solution. They solved the large-deflection equilibrium equations for the curved beam and gave a solution for the critical thrust in an implicit form in terms of elliptic functions. A numerical trial-and-error method is required to calculate the critical thrust from this solution.

Chicurel [12], examined the same problem and developed a solution based on the assumption that the buckled portion of the ring subtends a small portion of the circumference

of the pipe. He found the approximate buckling thrust, N_{cr}, to be

$$N_{cr} = 2.67 E A \left(\frac{I}{A R^2} \right)^{\frac{3}{5}} \tag{2.3}$$

where E denotes Young's modulus, R is the average radius of the circular ring, and A and I are the ring cross sectional area and moment of inertia respectively. This solution is more conservative than the solution proposed by Lo *et al*; it almost represents a 33% reduction in the critical thrust.

El-Bayoumy [16] solved the shrink buckling problem by employing the energy method and an approximation of shallow arch theory. He reduced the boundary value problem to a solution of purely algebraic equations. His results indicated that the ring will not buckle unless an external disturbance is present. This disturbance may take the form of a very small geometrical or material imperfection in the pipe or the rigid cavity. El-Bayoumy in his paper, did not define the critical buckling thrust, but defined the critical value for the wall contraction, D. Although El-Bayoumy's results did not have an analytical form, his results have been examined by the author. The critical contraction, D, can be approximated by

$$\frac{D}{R} = 2.64 \left(\frac{I}{A R^2} \right)^{\frac{3}{5}} \tag{2.4}$$

This can be rewritten to define the approximate critical thrust as

$$N_{cr} = EA \left(\frac{D}{R} \right) = 2.64 E A \left(\frac{I}{A R^2} \right)^{\frac{3}{5}} \tag{2.5}$$

which is in good agreement with the solution obtained by Chicurel [12].

While the solutions of Chicurel and El-Bayoumy are in good agreement, they differ from Lo *et al* solution by almost 33%. This raises the question of the validity of the small

deformati ı or shallow arch assumption used in both the Chicurel and El-Bayoumy studies.

2.5.2. Thermal Expansion of a Circular Ring Encased in an Imperfect Smooth Circular Rigid Cavity

This problem is similar to the previous one except that the circular rigid cavity has a geometrical imperfection. Two types of imperfection have been considered in the literature. The first imperfection type is an obstacle on the rigid cavity touching the ring at a single point (Fig. 2.4a), while the second is a "*wavy out-of-roundness*" imperfection extending on a small portion of the circumference of the rigid cavity (Fig. 2.4b). The case of a point obstacle is considered by Hsu *et al* [22]. They provided a set of curves to define the critical thrust as a function of the height of the point obstacle and the thickness to radius ratio of the ring.

The other case of the wavy imperfection is studied by Bucciarelli and Pian [8]. They used the shallow-beam approximation to solve the problem. Three sub-types of wavy imperfections are considered and the stability for each imperfection is estimated. The results are shown in a set of curves; among them are curves describing the variation of the buckling load versus the imperfection geometry (i.e. wave length and depth).

2.5.3. Buckling of a Circular Ring Encased in a Smooth Rigid Cavity and Subjected to a Unidirectional Distributed Load

This problem, shown in Fig. 2.5, is different in nature from the thermal expansion problem. The applied load is not radially symmetric and a non-linear load-deflection behaviour can be traced. Pian and Bucciarelli [38], have considered this problem and

developed both approximate and exact solutions. The two solutions compared well when the length of the detached portion of the ring was very small compared to the ring circumference, which was the assumption used to develop the approximate solution. The approximate solution was based on the shallow shell assumption for the detached portion of the ring. The exact solution was semi-analytical and required a solution by an iterative trial-and-error procedure.

Almost at the same time, Zagustin and Herrmann [48] considered this problem and simplified it using the assumption that the detached portion of the ring was very small compared to the ring circumference. They derived the following closed form solution for the critical vertical distributed load P_{cr}

$$P_{cr} = 1.985\,E\left(\frac{t}{R}\right)^{\frac{11}{5}} \tag{2.6}$$

which compares well with the exact solution of Pian and Bucciarelli's [38].

2.5.4. Buckling of a Circular Ring Encased in a Smooth Rigid Cavity and Subjected to a Uniform Pressure

The classical problem of buckling of an encased circular ring under uniform pressure (Fig. 2.6a) has been examined by many researchers. Cheney [11] used small deflection, linear theory and included membrane deformations in his analysis (he considered an extensional ring). He further assumed that the walls of the rigid cavity move inward as the ring deforms. He assumed that the cavity resists outward movement but not inward movement. The principle of minimum potential energy was used to derive the equations of equilibrium governing the buckling of the circular ring. For a circular ring with radius, R,

diameter, D, Young's modulus, E, cross sectional area, A, and moment of inertia, I, Cheney's solution can be written as

$$P_{cr} = \frac{(k^2 - 1)\, EI}{R^3} \tag{2.7}$$

$$k = \frac{\pi}{2}\left(\frac{R}{\rho}\right)^{\frac{2}{5}} \tag{2.8}$$

where ρ is the ring cross section radius of gyration ($\rho = \sqrt{\frac{I}{A}}$).

For the case of an encased plain liner (the long pipe case in contrast to the ring) with Poisson's ratio, ν, and thickness, t, and a diameter to thickness ratio bigger than 30 (i.e. $D/t > 30$), Eqns. 2.7, 2.8 can be written as

$$P_{cr} = 2.55\, \frac{E}{1 - \nu^2}\left(\frac{t}{D}\right)^{\frac{11}{5}} \tag{2.9}$$

Later Glock [18] analysed the same stability problem but, unlike Cheney, Glock's solution does not require the walls of the cavity to move inward with the ring while it deforms. A non-linear deformation theory and the principle of minimum potential energy were used to develop Glock's solution. Glock's solution is based on a pre-assumption of the deformed shape of the detached part of the ring and can be written as

$$P_{cr} = 0.969\, \frac{EI}{R^3}\left(\frac{AR^2}{I}\right)^{\frac{2}{5}} \tag{2.10}$$

For the case of an encased plain liner, Eqn. 2.10 can be rewritten as

$$P_{cr} = 1.0025\, \frac{E}{1 - \nu^2}\left(\frac{t}{D}\right)^{\frac{11}{5}} \tag{2.11}$$

2.5.5. Buckling of an Imperfect Circular Ring Encased in a Smooth Rigid or Flexible Cavity and Subjected to Uniform Pressure

The same imperfection used before by Bucciarelli and Pian [8] for the rigid cavity is considered again but for the ring itself (Fig. 2.6a). Yamamoto and Matsubara [46, 47] studied the buckling pressure for the pipe case (in contrast to the ring case). They have used the Finite Element Method to show that the critical buckling load can be more than three times that of the unrestrained pipe (Levy's solution). Kyriakides and Babcock [27], provided experimental evidence which indicated that long confined imperfect pipes under external pressure can develop a buckle which propagates. The buckling process is initiated by a substantial initial imperfection at one location in the pipe and, driven by pressure, the buckle can propagate and destroy the whole pipe structure. A theoretical study of this problem was reported by Kyriakides and Youn [29]. The imperfection parameters are its amplitude Δ_o and its arc length, $2S_o$ (Fig. 2.6b). They solved the large deformation equilibrium equations and obtained a semi-analytical solution for the case of inextensional ring. They concluded that the buckling pressure is a function of the wavy imperfection amplitude, Δ_o. A more general case was considered later by Li and Kyriakides [31], where the imperfect inner ring is encased in a flexible smooth concentric circular ring. The pressure is applied externally and also in the cavity formed by the imperfection. They concluded that the mode of collapse and the limiting load were dependent on the geometric characteristics of the two rings and the initial imperfection.

2.5.6. Buckling of a Circular Ring Encased in a Smooth Rigid Cavity and Subjected to a Radial Point Load

Bottega [7] has considered the problem of an encased circular ring subjected to a radial point load (Fig. 2.7). The problem was addressed as a moving intermediate boundary problem using the calculus of variations. A closed-form analytical solution was obtained and the results of parametric studies employing the solution were presented. The results, presented in the form of load-deflection plots, revealed unstable "snap-through" behaviour of the ring for critical values of the applied load.

2.5.7. Thermal Expansion of an Elliptical Ring Encased in a Smooth Rigid Cavity

Soong and Choi [40], have studied the effect of the ovality of a ring encased in a rigid cavity (Fig. 2.8a) on the stability of that ring when subjected to a thermal expansion. Three buckling cases are considered; the no-friction one buckle case (buckle is symmetric about the short axis), the no-friction two buckle case, and the no-slip buckle case. In all the cases, the buckling is assumed to occur at the flatter part of the ring. They have solved the large deformation equilibrium equations of the ring. The solution was semi-analytical and a set of differential equations are derived and solved numerically. The problem was more difficult than the case of a circular ring due to the changing radius of curvature for the part of the ring sliding on the walls of the rigid cavity. A parametric study was conducted and the results were presented showing that the critical thrust in the ring decreased with the increase of the ellipticity. Their results are a series of curves defining the thrust at the crown (point of maximum radius of curvature) versus the critical thrust for different thickness to radius ratios, where the radius used is the radius of a circle whose circumference is equal to the

ellipse circumference. They found that for the elliptical rings the ellipticity reduced the critical thrust because buckling occurred at the flatter part of the ring. Another finding is that neglecting the bending moments, generated due to the change in the radius of curvature of the attached part of the ring due to its slippage on the rigid elliptical cavity walls, has an insignificant effect on the buckling thrust.

Li and Guice [32] studied the reduction factor of the hoop thrust at buckling of an elliptical ring compared to the circular ring of a radius, R_o, equal to the average of both the ellipse radii, a, and, b, (i.e., $R_o=(a+b)/2$) where a is the long radius (Fig. 2.9). The ring is assumed to be subjected to a thermal expansion. They approximated the buckled portion of the ellipse as an axially compressed beam with a given initial shape (the shape is defined by Chicurel [12]). They obtained an approximate closed form solution for the ovality reduction factor α given by

$$\alpha = \frac{1}{\left(1+\frac{q}{100}\right)^{\frac{8}{5}}\left(1-\frac{q}{100}\right)^{\frac{1}{5}}} \qquad (2.12)$$

where q is percentage ovality and is defined by $\frac{(R_o-b)}{R_o}\times 100$ or $\frac{(a-R_o)}{R_o}\times 100$.

Li and Guice assumed that the influence of ellipticity on the thermal expansion solution was identical to ovality effects for the case of ring under external pressure (Fig. 2.8b). However, the external pressure problem is a different case with different boundary conditions. In the external pressure case, after a portion the ring separates from the confining rigid cavity, it is still subjected to the pressure load. In contrast, pressure is released following separation in the case of thermal buckling.

2.5.8. Buckling of a Loosely Fitted Circular Liner Under Pressure

Lo and Zhang [34] studied the effect of the loose fitting imperfection (Fig. 2.10) on the critical liner pressure. In that study an approximate solution for the critical buckling pressure was obtained based on the analogy between the buckling of the detached part of the liner and the buckling of shallow arches. No consideration is given to the circumferential deformations occurring in the liner. The symmetrical one buckle case and asymmetrical two buckle case were both studied and a range for the expected critical pressures was calculated. A comparison had been made between the expected range of the critical pressures and the experimental results. The comparison showed that this simple solution may be an appropriate one.

2.5.9. Experimental Work of Aggarwal and Cooper

Aggarwal and Cooper [1] reported a series of test results. These results are very useful because they include a relatively large number of samples (49 specimens), a relatively large range of standard dimension ratios (D/t ranges from 29.9 to 90.2), and a variety of material properties; Young's modulus varies from 9.6×10^5 kPa to 25.7×10^5 kPa (139,370 psi to 373,105 psi). The experimental results are discussed and shown in chapter five in Table 5.1.

In their report, Aggarwal and Cooper [1], described the test procedure for installing the "Insituform" lining (Fig. 2.11). The test started with insertion of the liner into the steel host pipe. Then rubber O-rings were placed and flanges were tightened to seal the outside surface of the lining. The valve at the top of the steel pipe was opened and water was pumped into the bottom until all the air in the gap between the liner and the host steel pipe was displaced. The upper valve was then closed and the pressure was applied and recorded until failure.

The pressure was increased in increments of approximately 1/10th of the expected failure pressure, until failure. No record of the total time to failure is reported. Most linings failed structurally, but some leaked at weak spots and results could not be used. The gap between the liner and the host steel pipe is reported, but no mention of how it was measured or calculated is shown.

Test specimens of approximately 15 mm wide were cut from portions of the lining which had been subjected to pressure testing. The specimens were tested in flexure on a 96 mm span to calculate the Young's modulus of the liner material. The Young's modulus is then used to calculate the buckling pressure of the unsupported liner (Levy's solution [30]) to estimate the enhancement factor, K.

Many important factors which influence the interpretation of the results are summarized in the following

- the size of the gap between the liner and the host steel pipe,
- the boundary conditions of the liner due to clamping at its ends,
- liner length to diameter ratios,
- the value of the calculated short term Young's modulus compared to the actual value for the test, and
- type of structural failure (i.e. localized due to material defects or global due to buckling)

These factors are discussed in more detail in chapters five and six. The main conclusion of this experimental work is that an enhancement factor $K \geq 7$ is obtained for most of the specimens and; therefore, $K=7$ is recommended for design. This value of the enhancement factor is recommended later by the ASTM in its design specifications.

2.5.10. ASTM Design Specifications

Currently the engineering practice reported in various ASTM standards [41], involves the calculation of the critical pressure of the circular and elliptical (oval) liners through application of two factors to the critical pressure of the free liner. The first factor is an enhancement factor to account for the increase in the liner stability due to encasement. The second factor is a reduction factor which is applied to the value of the critical pressure for the encased perfect circular liner (i.e. after applying the enhancement factor).

The following equation is shown in ASTM specifications F1216-93 [41]

$$P = \frac{2K E_L}{(1 - \nu^2)} \frac{1}{(DR - 1)^3} \frac{\alpha}{FS} \tag{2.13}$$

where

P critical external pressure,

DR outside diameter to thickness ratio $(D_o+t)/t$ of the liner, and $D_o = 2 R_o$ is the liner centerline diameter,

α ovality reduction factor defined by

$$\alpha = \left[\frac{1 - \frac{q}{100}}{\left(1 + \frac{q}{100}\right)^2} \right]^3 \tag{2.14}$$

q percentage ovality of the elliptical liner of radius R_o equal to $(a+b)/2$, where $2a$ and $2b$ are the length of the elliptical liner axes. The percentage ovality is q defined by

$$q = 100 \times \left(\frac{R_o - b}{R_o} \right) = 100 \times \left(\frac{a - R_o}{R_o} \right) \tag{2.15}$$

FS Factor of safety (FS=2),

E_L Long-term Young's modulus of the liner,

K enhancement factor due to encasement, and

ν Poisson's ratio for the liner material.

The ASTM recommends a value K=7 for all liners. This matches the value recommended by Aggarwal and Cooper [1] based on experimental work (this is discussed in detail in chapters five and six). This value of the enhancement factor K is recommended for all liners (i.e. perfect or imperfect, thin or thick, ... etc) although the experimental work accomplished by Aggarwal and Cooper did not include the effect of any local geometrical imperfections. The ASTM restricts the size of local imperfections through the restriction of the size of any obstacles in the damaged host pipeline. The size of any obstacle should not exceed the lesser of 16% of the pipeline inner diameter or 25 mm, otherwise a point repair excavation is performed on the damaged pipeline.

The reduction factor α is derived assuming similarity between the behaviours of the unsupported pipe and the encased pipe relative to their perfect circular counterparts. Hence,

$$\alpha = \frac{P_{cr} \textit{ for Elliptical Unsupported Pipe under Pressure Load}}{P_{cr} \textit{ for Circular Unsupported Pipe under Pressure Load}} = \frac{P_{cr} \textit{ for Elliptical Encased Pipe under Pressure Load}}{P_{cr} \textit{ for Circular Encased Pipe under Pressure Load}} \tag{2.16}$$

The following equations for the moment, M, and normal force, N, per unit length of the liner are used in the ASTM specifications to account for ovality in the liner

$$N = \left(1 + \frac{q}{100} \right) P R_o \tag{2.17}$$

$$M = \frac{q}{100}\left(1 + \frac{q}{100}\right) P R_o^2 \qquad (2.18)$$

These equations are defined for the free oval liner and are assumed to be applicable for the encased oval liner where ovality is defined by q (Eqn. 2.15). The appropriateness of the similarity between the free and encased oval liners has been criticised and discussed by McAlpine [35]. He pointed out that the wrong mathematical model is used to develop the thrusts and bending moments in the liner.

2.6. Conclusions of the Literature Survey

Analytical and numerical modelling of the collapse behaviour of constrained circular rings and pipes has been carried out by various researchers, but because of the non-linear nature of the problem, the results of these studies vary according to the assumptions used. The following sections discuss the different assumptions used.

2.6.1. Inextensional Liner Assumption

One of the major assumptions, used by many authors (e.g. [29]) to simplify the analytical solution, is that the pipe is inextensional (i.e., thickness to radius ratio approaches zero for plain liners). This assumption, while reasonable for problems where thickness to radius ratio is very small, is unreasonable for most of the practical polymer liners. It may lead to poor solutions for liners with a relatively large thickness to radius ratio.

2.6.2. The Shallow Arch Assumption

The approximation of the liner behaviour using the shallow arch model is also questionable. This strategy has been used by many researchers [16, 8, 38, 48, and 34]. The assumption took two forms; either the liner is analysed using the shallow arch equilibrium equations or the buckling of the detached part of the liner is approximated by the buckling of a shallow arch with pinned or fixed end conditions. The two assumptions are completely different. The first is used when liner deformations are small and the detached part of the liner extends for a small angle [8, 16, 38, and 48] which is a good approximation under these circumstances. The second [34] uses the solution reported by Timoshenko and Gere [44] for the buckling of an arch with pinned or fixed ends. This approximation violates the boundary conditions of the problem, since the ends of this arch are flexible (due to the flexibility of the attached part of the liner) and the location of these ends is load dependent.

It is clear that the first assumption may be valid for some encased ring cases, but its applicability to the liner problem should be investigated. The second assumption, although greatly simplifying the analysis, should not be used.

2.6.3. Imperfections Shape and Size

Another aspect of the liner problem is the existence of any material or geometrical imperfections. Material imperfections are very hard to measure and this issue has received little attention. On the other hand, many studies had been conducted to evaluate the effect of the geometrical imperfections [8, 29, 31, 12, and 32]. The types of imperfection used in these studies can be categorized as either global or local imperfections.

The global imperfections are related to the whole arrangement of the pipe and the rigid

cavity. The global imperfections reported in literature are either due to ovality in the liner or eccentric alignment of the liner with respect to the host pipe due to lack of fit.

The local imperfections are due to local deviation from the original pipe or rigid cavity shapes. The local imperfections have taken the form of a section assumed to be detached from the cavity while the rest of the pipe was assumed to be in perfect contact with the rigid cavity confining it.

The previous research showed that both types of imperfection are important and should be considered. It is essential to assess their effect on the liner stability.

2.6.4. Distribution of the Pressure

A uniform pressure distribution is assumed in all the previous work dealing with liners under external pressure; but a hydrostatic distribution, where pressure varies with depth, has never been considered. This issue may be important for liners with low pressure head capacity where the nonuniform portion of the pressure (i.e. the portion of pressure above or below the average value) is significant with respect to the uniform part (i.e. the average value). The effect due to this nonuniform pressure needs more investigation.

2.6.5. Material Non-linearity

The polymer material behaviour is strongly time dependent. Although the problem of a liner under external pressure is an old one, no previous research considering material non-linearity appears to be available.

For fluid pressure sustained over a long period, the "long term" material response controls the pipe deformations (and therefore the non-linear buckling process). The Young's

modulus for the polymer material, E, is often modelled as time-dependent $E(t)$, where t is time. It can be defined at any time t in terms of the time-dependent stress, $\sigma(t)$, and strain, $\varepsilon(t)$, under uniaxial loading by

$$E(t) = \frac{\sigma(t)}{\varepsilon(t)} \tag{2.19}$$

It is clear that for problems involving sustained stress, $E(t)$ decreases as time increases. The modelling of such material behaviour is dependent on finding and using appropriate material constitutive relationships.

2.7. General Conclusions from the Literature Review

The general conclusion of these studies is summarized as follows:

- The assumption of an inextensional liner needs to be investigated for the liner problem.
- The small deformation (shallow arch assumption) may be valid for some cases but may be inappropriate for others; it requires investigation.
- Material imperfections are difficult to assess and are left for a future study.
- The buckling resistance of the pipe is strongly influenced by the shape and size of any initial imperfections. The influence of such imperfections should be assessed.
- The effect of the distribution of the external pressure on the critical liner pressure needs also to be investigated.
- The effect of the global imperfections (i.e. oval or eccentric liners) on the liner stability is important and requires more investigation.
- The rheology of the polymer material is an important factor, but in the absence of a good understanding of the elastic case, the elastic solution should be investigated first and then

followed by an appropriate rheological analysis of the problem. The elasto-plastic assumption seems to be a good start to give some insight into the non-linear behaviour of the liners.

2.8. Method Of Analysis and Assumptions

The geometry of the circular liner problem is so simple and ideal that developing an analytical solution may be the best choice. However, even for this simple geometry, there are some other difficulties due to the following factors:

- the significantly changing geometry of the problem as the external pressure increases,
- the possible liner bonding, slipping, re-bonding, and separation from the rigid host pipeline during the loading process, and
- the materially non-linear behaviour.

Analytical and semi-analytical methods used before to solve this problem have sacrificed the accuracy of the solution by using some simplifying assumptions. An example of such simplifications is in Kyriakides and Youn [29] where the assumption of inextensional elastic liner is used. Although this assumption may be valid for the case those authors studied (the case of encased thin steel rings), it is inappropriate for the case of relatively thick polymer liners.

For more complicated geometries featuring geometrical or material imperfections, the Finite Element Method emerges as a powerful solution technique. The Finite Element Method has been used successfully to analyse many problems in various fields. The power of the Finite Element Method stems from its ability to deal with difficult geometries and complicated material behaviour. Therefore, the Finite Element Method is used in this thesis

to analyse the liner problem. The important issues related to the FEM are summarized in the following:

- The liner is modelled using an isoparametric multi-layer curved structural element which is a degenerated version of its two dimensional counterpart. This element is very popular and has an advantageous definition of the element cross section through layers. This allows for tracing the spread of plasticity (induced by curvatures) through the cross section.
- The non-linear behaviour of the liner interface has to be considered in the analysis. A rigorous interaction technique is developed which extends the previous work of Katona [24] for the case of small deformations to include the case of large deformations and non-matching interface nodes. The rigorous solution for the interaction problem is straightforward and does not sacrifice the simplicity of the FEM approach. In this study, the interface is assumed to be a frictional adhesive one with a conventional *Coulomb* failure criterion. The technique examines the interaction of two bodies, namely the *Slave* and *Master* bodies. It simulates frictional slip, separation, bonding and re-bonding of the slave body with respect to the master allowing for large deformations and non-matching nodes at the interface. The proposed solution is iterative where two levels of iterations are used. The first iteration is used to satisfy equilibrium and to deal with the geometrical non-linearity, while the second is used to satisfy the interaction conditions at the interface.
- As the liner problem deals with the evaluation of the critical pressure, a snap-through behaviour for the load-deflection of the liner is expected where sudden instability occurs once the critical pressure (peak load) is reached (Fig. 2.12a). The traditional incremental

solution algorithms (e.g. Newton-Raphson and modified Newton-Raphson shown in Fig. 2.12a) fail to predict the post-peak behaviour, and the solutions can diverge when the pressure approaches its critical value. The Arc Length Control Method represents a suitable alternative for this case where neither incremental loads nor incremental displacements are prescribed, but a constraint equation is used instead. The constraint equation may be visualized for a single degree of freedom as an arc of certain radius which intersects the load deflection curve at a point which represents the solution for that increment (Fig. 2.12b). There are many available methods depending on the shape of the constraint equation used. The Crisfield method [13] is relatively simple and is used in the thesis. This method facilitates the evaluation of the liner peak load and post-peak load-deflection behaviour

- As large liner deformations are expected, the FEM analysis should allow for large geometrical non-linearity (in a small strain scheme). Therefore, the incremental Updated Lagrangian method is the best choice to model such geometrical non-linearities, because the modified geometry is required for the interaction technique to check penetration of the liner nodes into the rigid cavity to decide the mode of interaction (details are given later in chapter four which deals with development of the rigorous interaction technique).
- The behaviour of polymer materials is significantly time-dependent and the correct FE analysis should accurately model the rheology of the material. This is consigned to a second stage in the research project, which should follow development of the linear elastic solutions. The work in this study is mainly concerned with the first stage of the project (i.e. the development of an elastic solution). Elasto-plastic material behaviour is also briefly considered, through the use of a bi-linear elasto-plastic uniaxial stress-strain

relationship, to explore the effect of plasticity on the critical liner pressure. Extra work is required to model the time-dependent behaviour of the polymer liner material and evaluate its effect on the variation of the critical pressure with time.

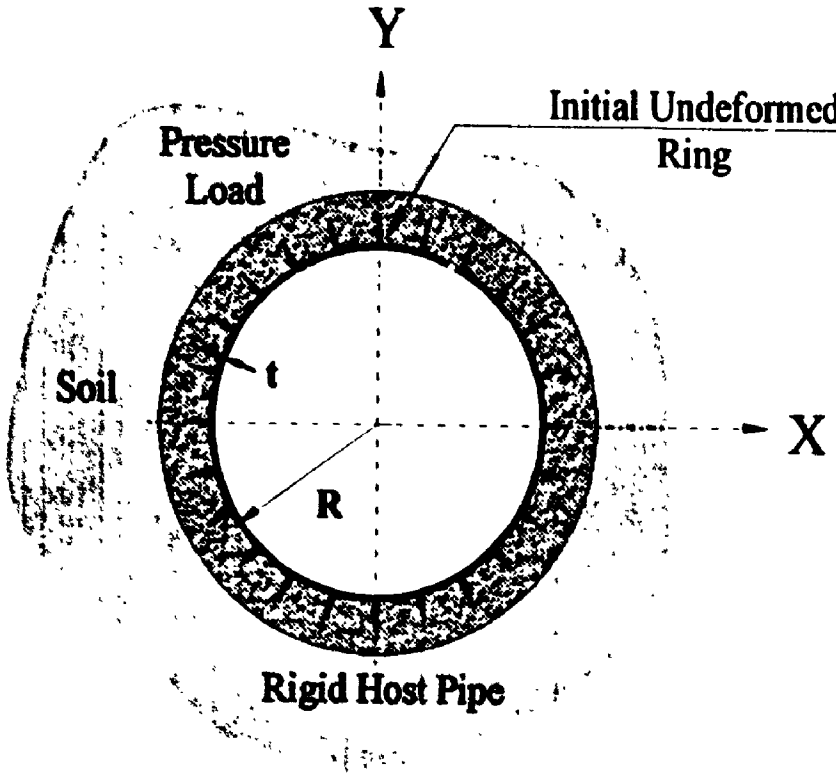

Figure 2.1a. Perfect Liner

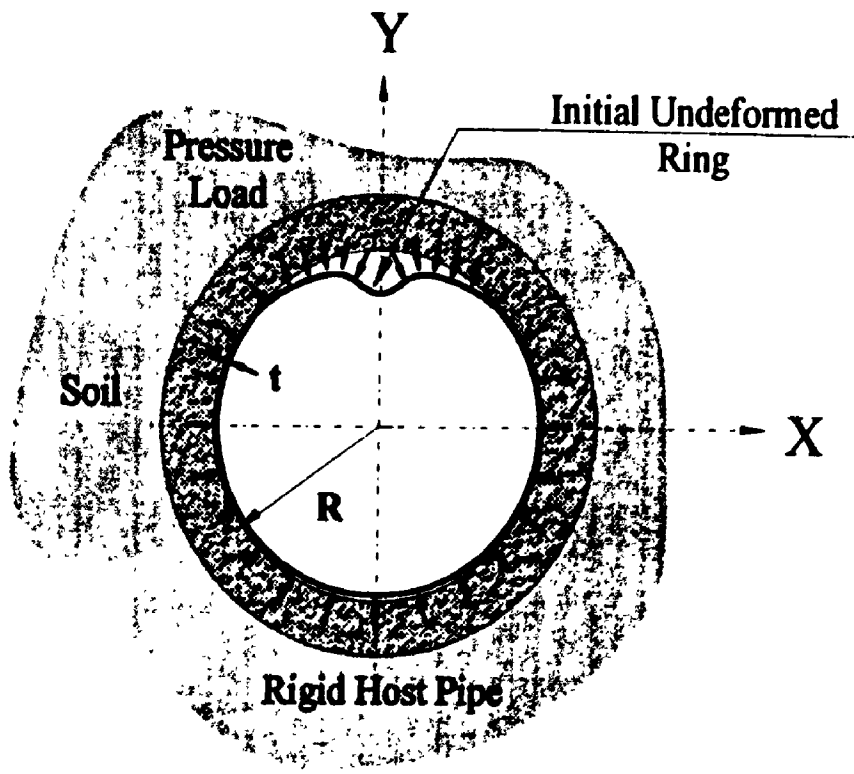

Figure 2.1b. Imperfect Liner

Figure 2.1. Definition of The Liner Buckling Problem

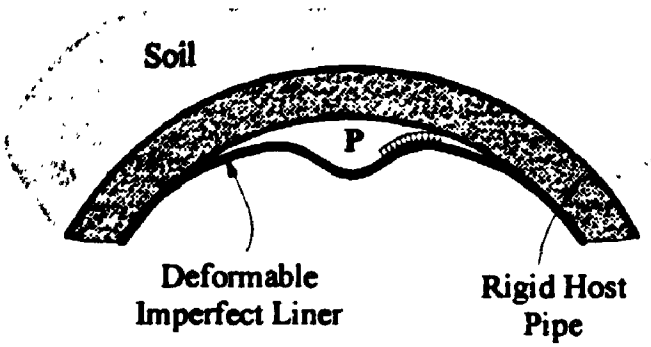

Figure 2.2a. Local Imperfection

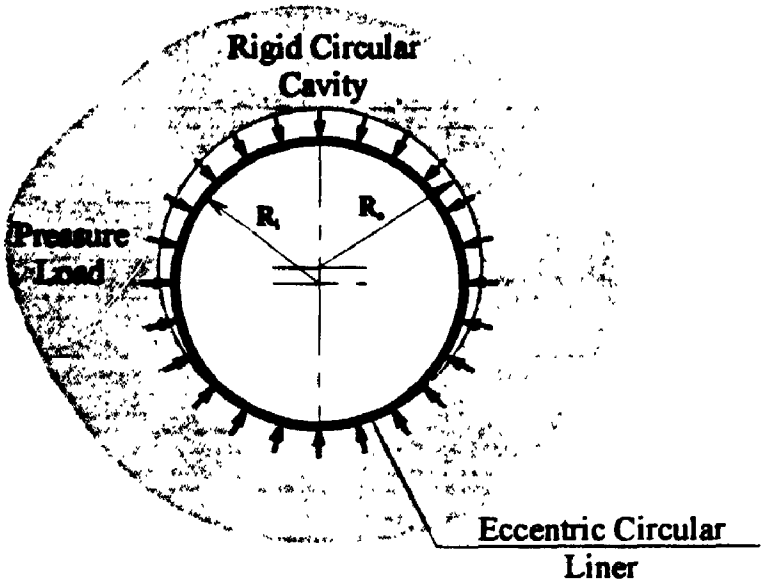

Figure 2.2b. Global Eccentric Imperfection

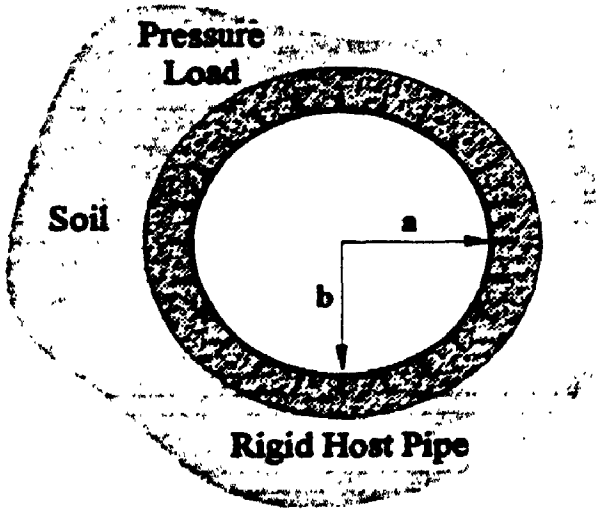

Figure 2.2c. Global Oval Imperfection

Figure 2.2. Definition of The Imperfection Geometry

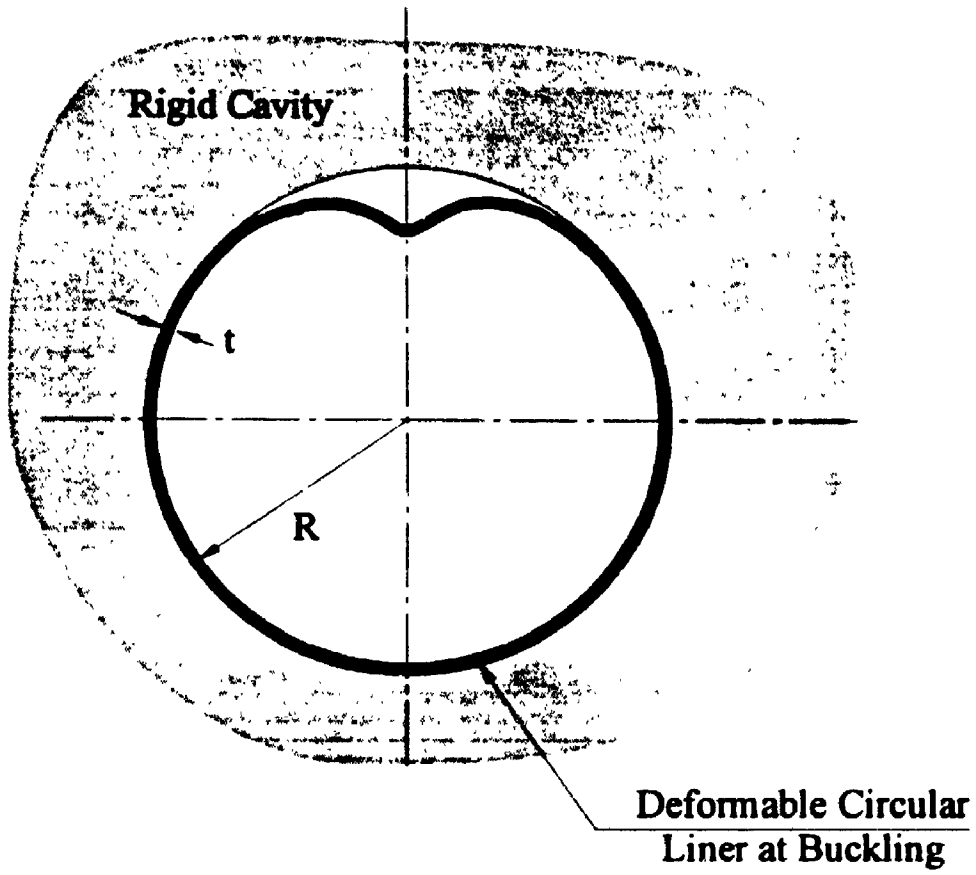

Figure 2.3. Buckling Due to Thermal Expansion

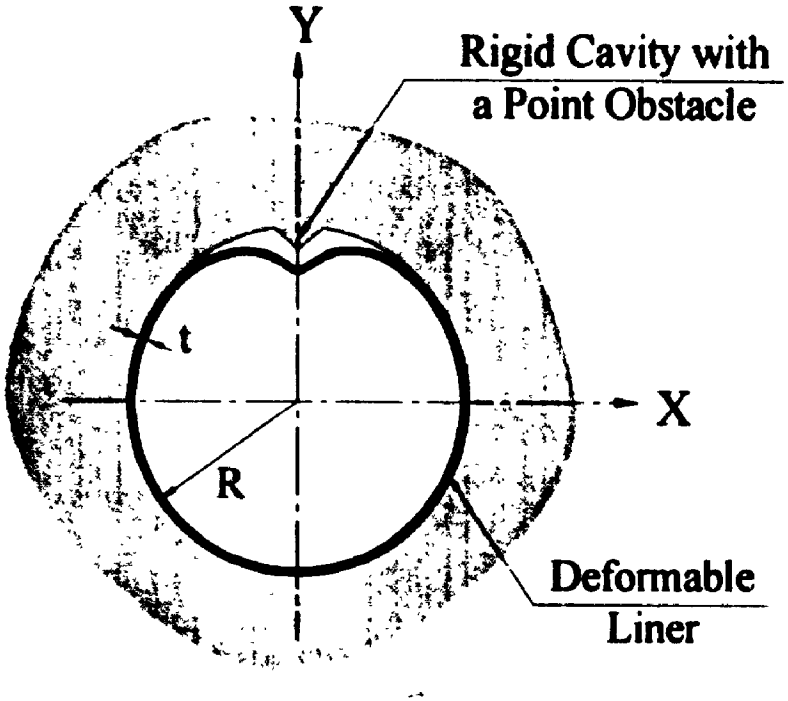

Figure 2.4a. Buckling Due to a Point Obstacle in the Rigid Cavity

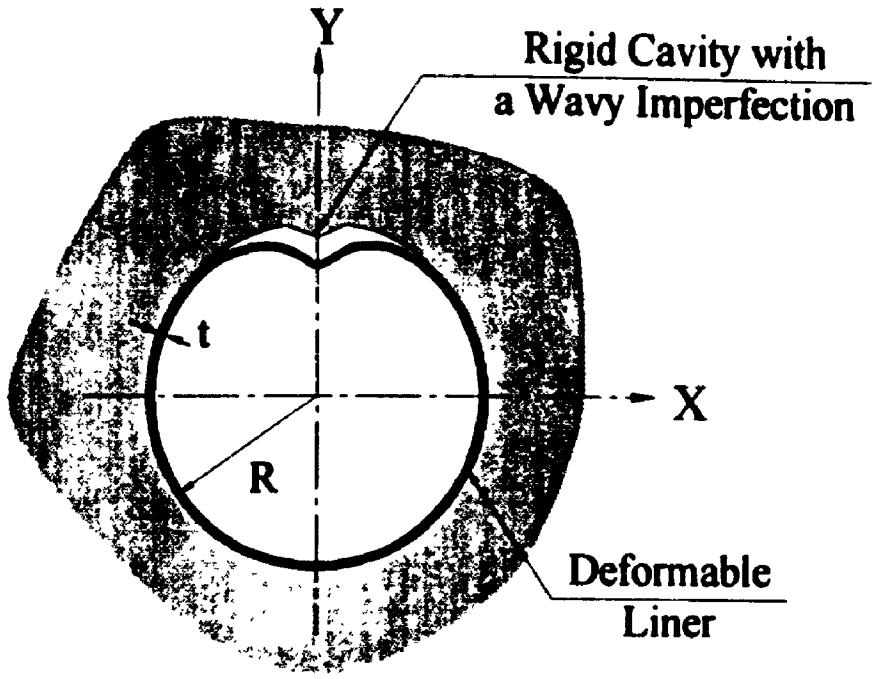

Figure 2.4b. Buckling Due to a Wavy Imperfection in the Rigid Cavity

Figure 2.4. Buckling Due to Thermal Expansion in an Imperfect Rigid Host Pipe

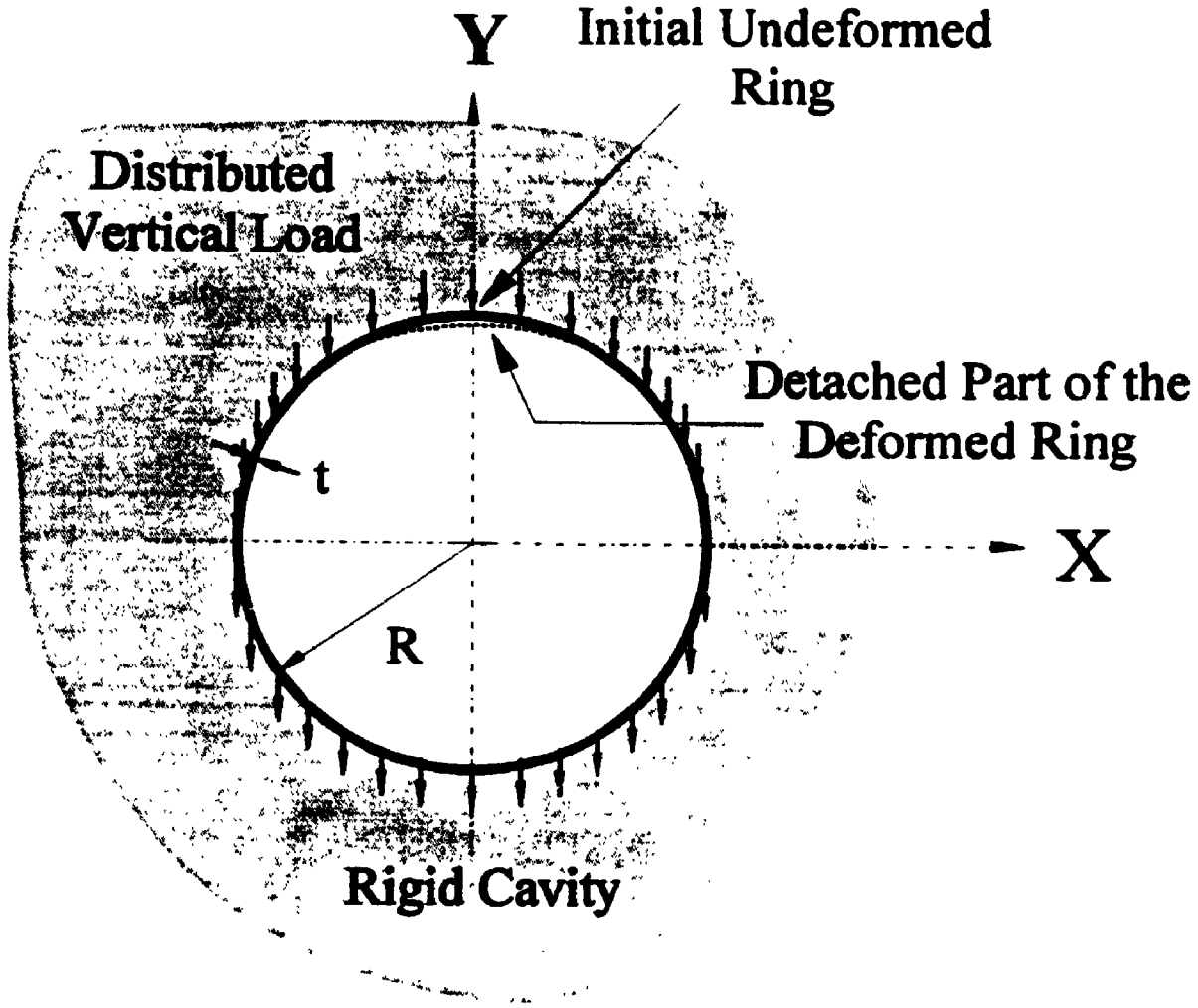

Figure 2.5. Buckling of an Encased Ring Due to Distributed Load

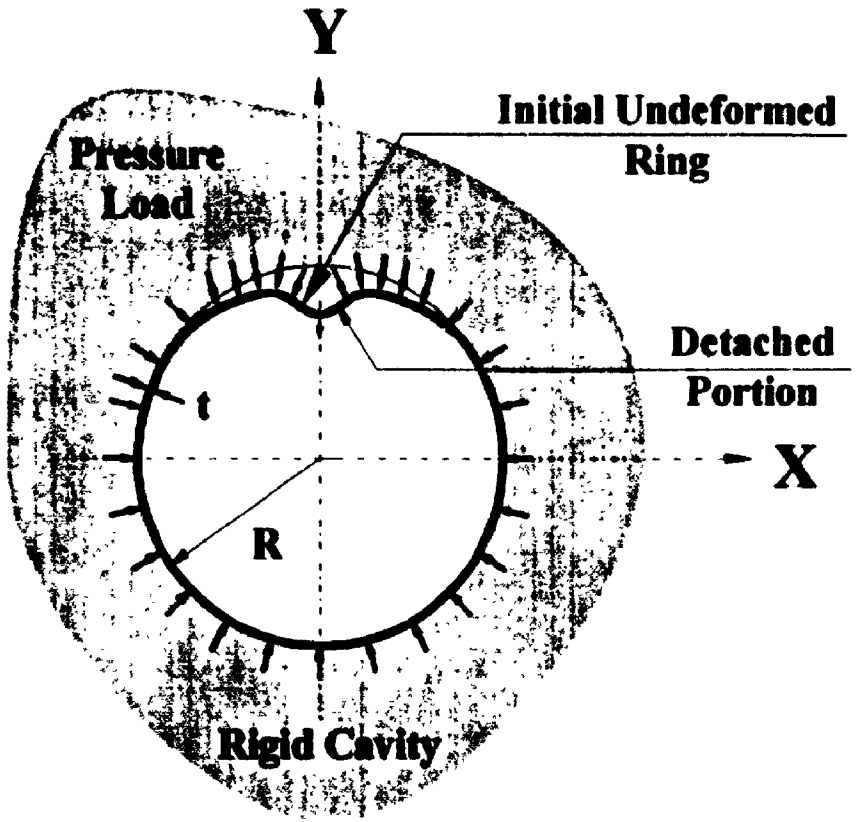

Figure 2.6a. An Imperfect Circular Ring Encased in a Smooth Rigid Cavity

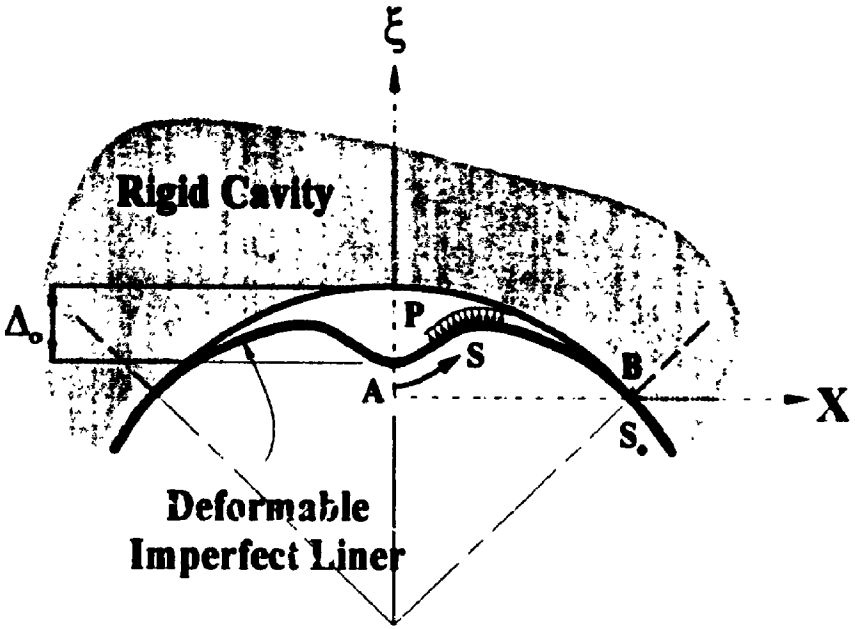

Figure 2.6b. Imperfection Geometry

Figure 2.6. Buckling of an Imperfect Circular Ring Encased in a Smooth Rigid Cavity and Subjected to a Uniform Pressure

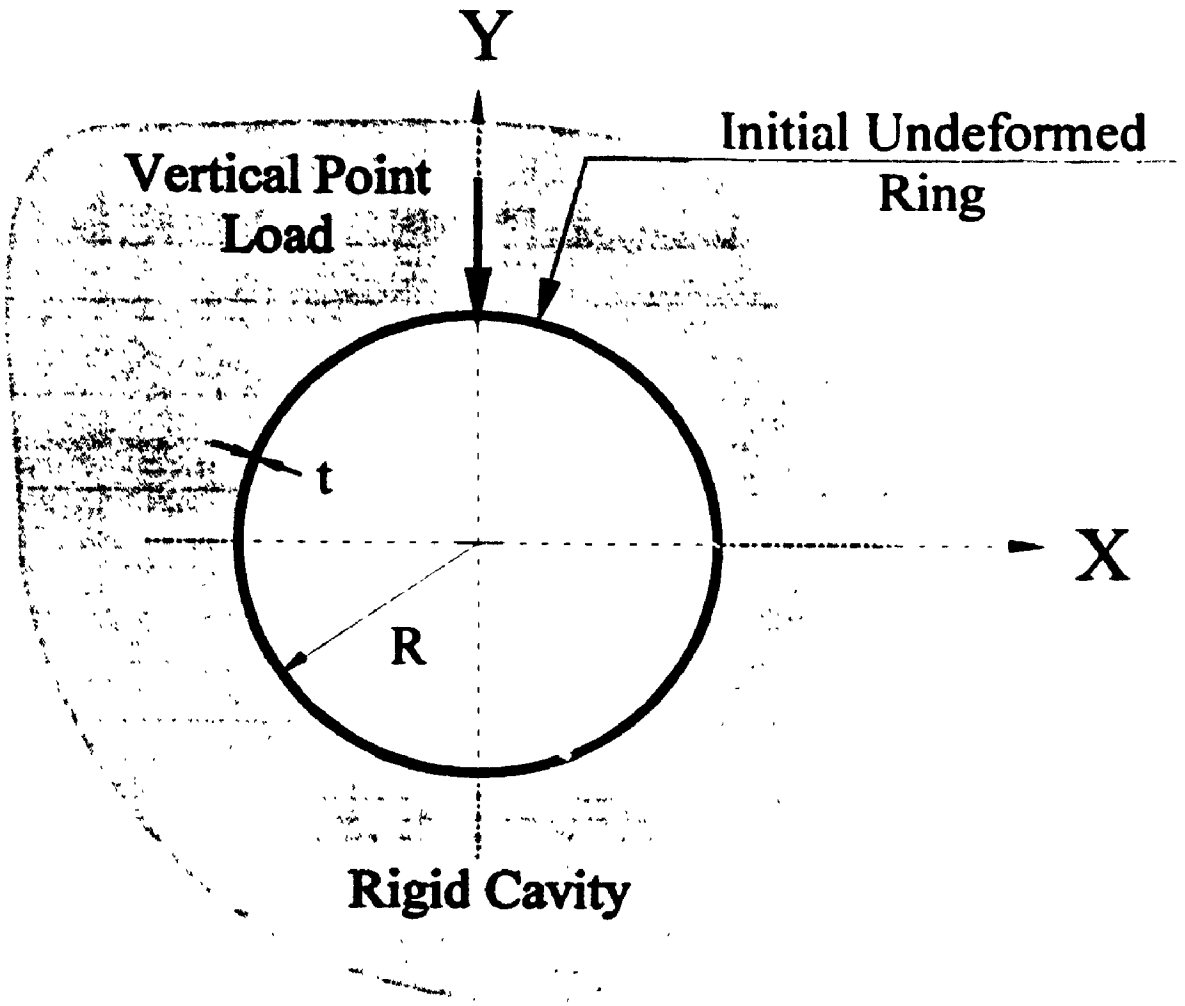

Figure 2.7. Buckling of a Circular Ring Due to a Point Load

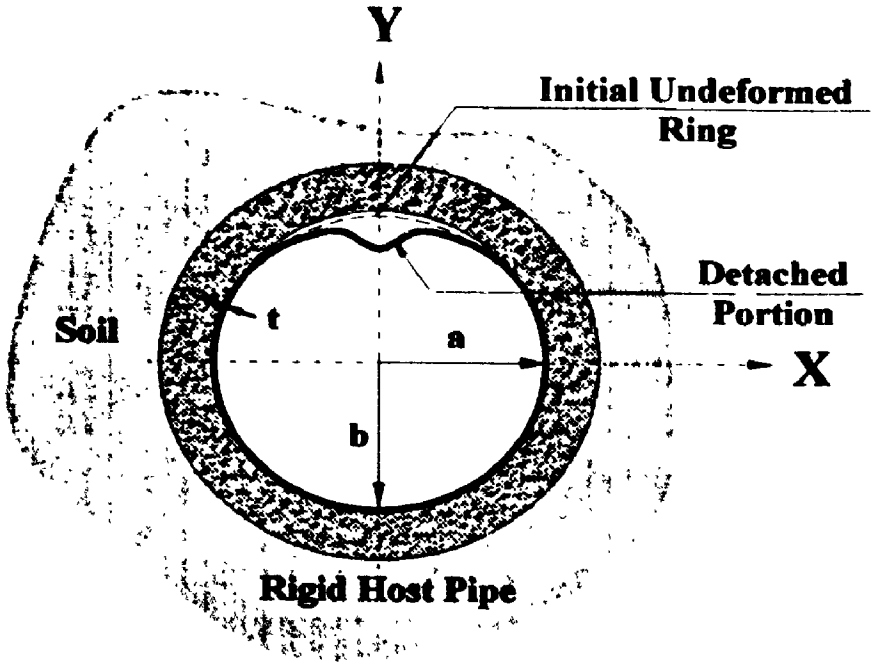

Figure 2.8a. Buckling Due to Thermal Expansion

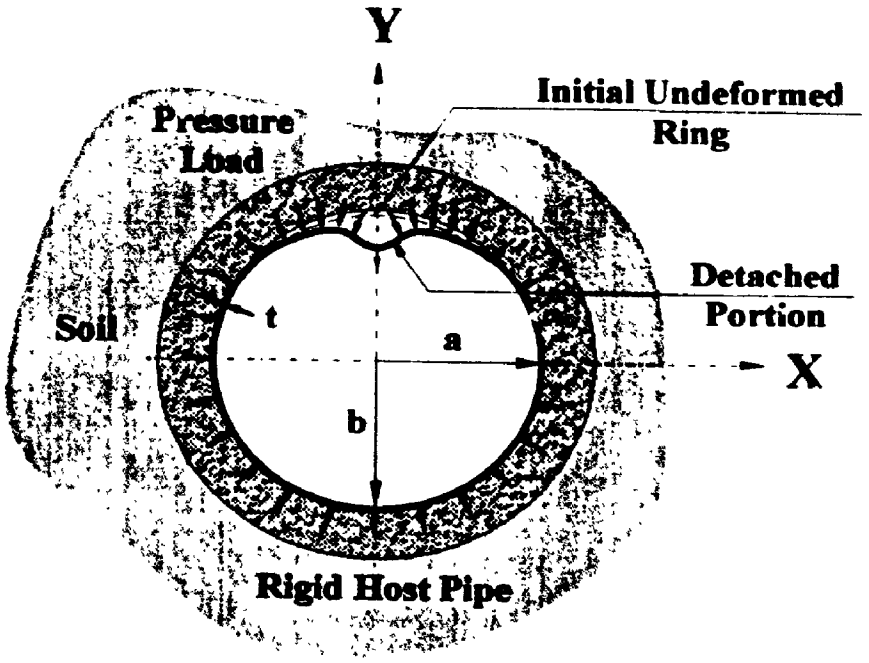

Figure 2.8b. Buckling Due to Pressure Load

Figure 2.8. Definition of Two Different Buckling Problems

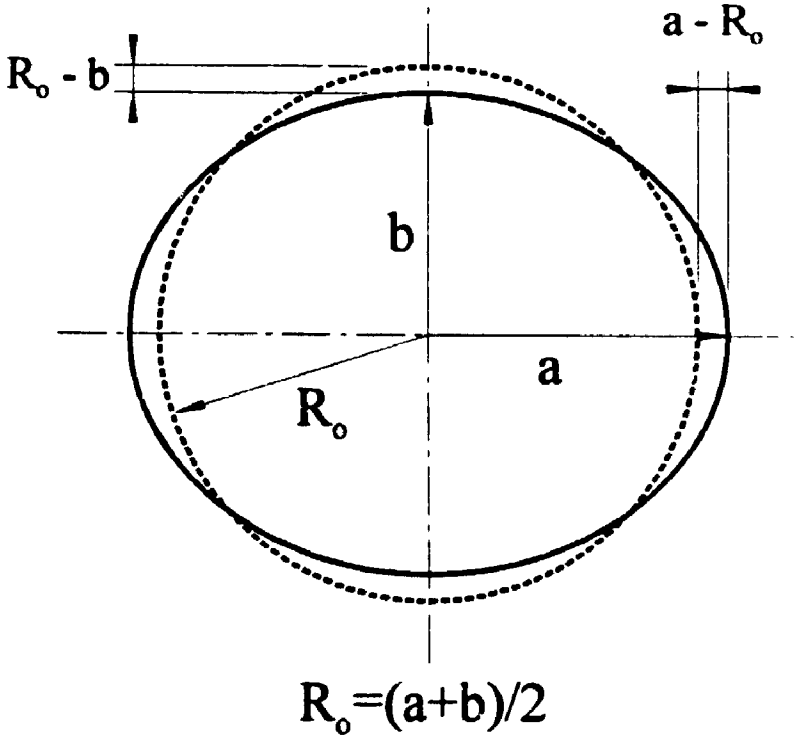

Figure 2.9. Definition of Ovality Geometrical Parameters

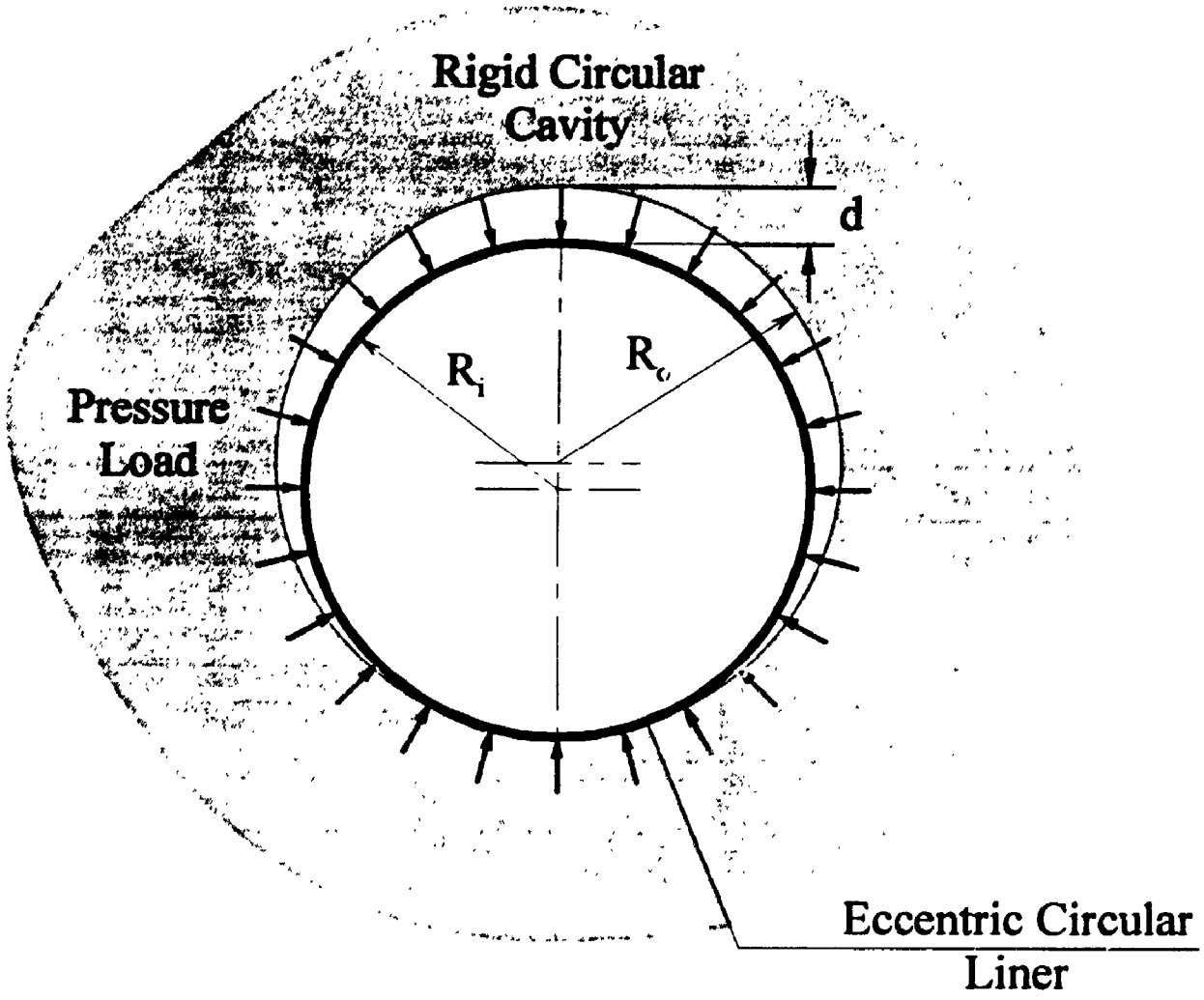

Figure 2.10. Problem Definition of a Loosely fitted Circular Liner

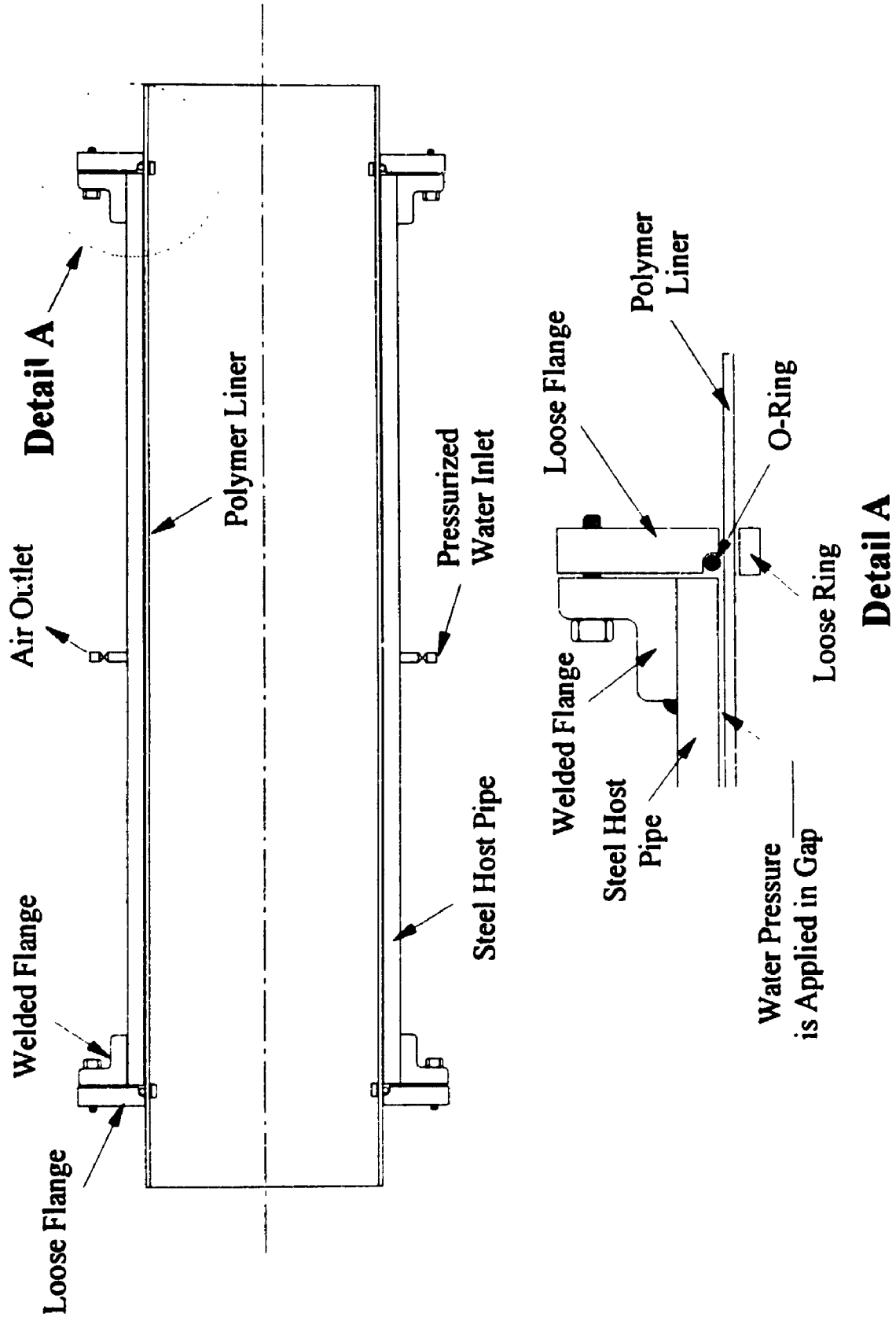

Figure 2.11. Aggarwal and Cooper Experiment Setup

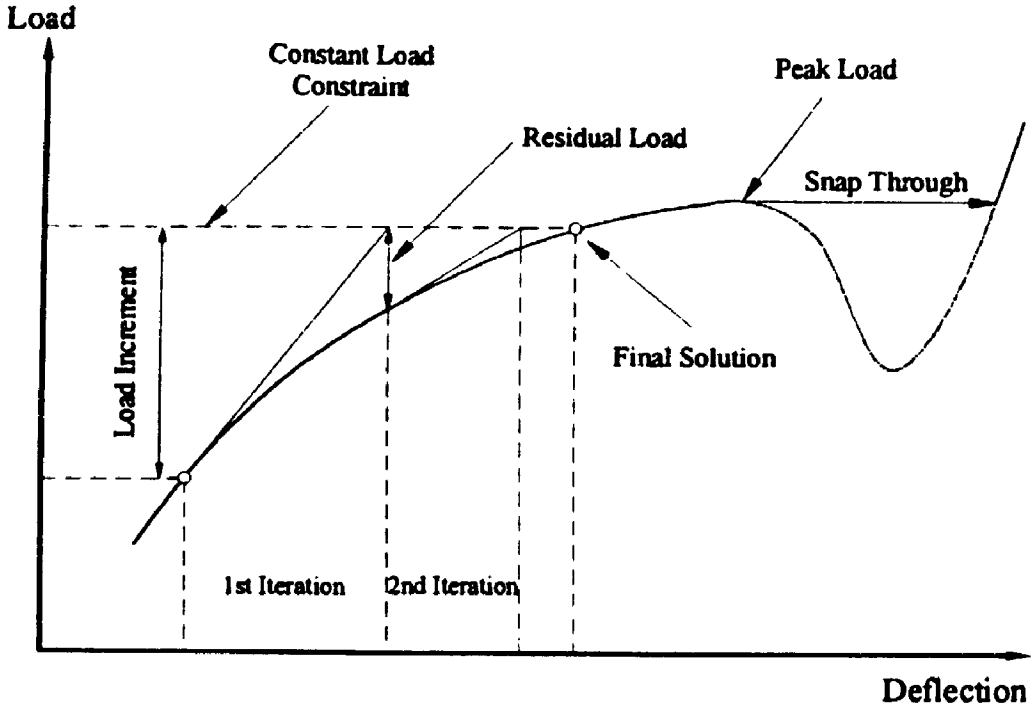

Figure 2.12a. Newton-Raphson Method

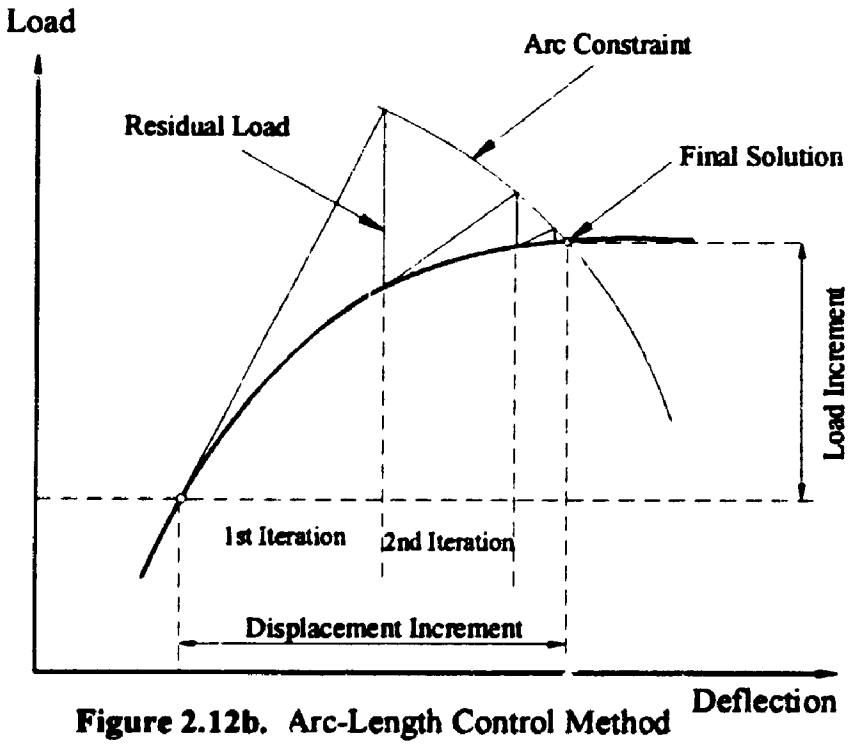

Figure 2.12b. Arc-Length Control Method

Figure 2.12. Newton-Raphson and Arc Length Control Methods

CHAPTER THREE

Geometrically Non-linear Elasto-Plastic Analysis with Tracing of Post-Peak Behaviour

3.1. Introduction

An essential part of the Finite Element Method analysis is the choice of the appropriate analysis method and the best element type for a particular problem. This choice is rarely obvious, and this is the reason why research is still continuing in this area. The purpose of this chapter is to describe and examine different aspects of the geometrically non-linear elasto-plastic analysis applied in the rest of the thesis. It also provides a detailed derivation of the structural element matrices (e.g. stiffness matrix).

For problems exhibiting a peak load with snap through buckling, the Arc Length Control Method is discussed. Although the element discussed in this chapter is not new, many finite element techniques are combined together to enable the element to analyse many different types of problems, including those with material and geometrical non-linearities, irregular curved element shapes and irregular element cross sections.

For small strains associated with large displacements and rotations, two different approaches have generally been pursued in incremental non-linear Finite Element Analyses. In the first, static and kinematic variables are referred to an updated configuration in each load step. This procedure is generally called *Eulerian, moving coordinate* or *Updated Lagrangian* (UL); the last name is used in this study. In the second approach, which is generally called the Total Lagrangian formulation (TL), all static and kinematic variables are referred to the initial undeformed configuration. Both procedures are used by many researchers. For a good review of both methods, the reader may refer to Bathe *et al* [6] and

Bathe [3] It is important to recognize that when using any of these formulations the same answer should be obtained if all the variables are correctly transformed from one frame of reference to another. This chapter provides details of the non-linear structural element for both Total Lagrangian and Updated Lagrangian analyses. The Arc Length Control Method is described and the performance of the element is also reported through comparison of solutions to various test problems with other available results.

3.2. The Structural Element Geometry and Displacement Definitions

The structural element considered here is derived (or degenerated) from its two dimensional (2D) counterpart as it will be shown later (sometimes the element is called the degenerated structural element). As in all thin structural elements, it is assumed that plane sections remain plane after deformation. This assumption reduces the number of degrees of freedom describing the two dimensional element. For example, a 2D element with 2×4 nodes is described by X and Y coordinates defined at each node. The element can be defined by four nodes only; each having X, Y and slope coordinates. Each two facing nodes degenerate into a single node with an extra slope coordinate to describe the geometry in the element cross section. Figure 3.1 shows the two systems of coordinates used to define the element geometry; the global system (X, Y) and the natural system (ξ, η). It also shows the 2D element versus the degenerated structural element, in both global and natural coordinates. The global coordinates of a point, with natural coordinates (ξ, η), on the m-noded degenerated element can be defined by

$$\begin{Bmatrix} X \\ Y \end{Bmatrix} = \begin{bmatrix} N_1 & 0 & N_2 & 0 & \dots & N_m & 0 \\ 0 & N_1 & 0 & N_2 & \dots & 0 & N_m \end{bmatrix} \begin{Bmatrix} X_1 \\ Y_1 \\ X_2 \\ Y_2 \\ \vdots \\ X_m \\ Y_m \end{Bmatrix} + \frac{\eta t}{2} \begin{bmatrix} N_1 & 0 & N_2 & 0 & \dots & N_m & 0 \\ 0 & N_1 & 0 & N_2 & \dots & 0 & N_m \end{bmatrix} \begin{Bmatrix} \cos(\phi_1) \\ \sin(\phi_1) \\ \cos(\phi_2) \\ \sin(\phi_2) \\ \\ \cos(\phi_m) \\ \sin(\phi_m) \end{Bmatrix} \qquad \textbf{(3.1)}$$

where

m is the number of element nodes,

ξ, η are the natural coordinates of a point inside the element, where η=1 at the external fibre and η=-1 at the internal fibre (Fig. 3.1)

X, Y are the coordinates at a point with natural coordinates (ξ, η),

N_i is the shape function at a point with natural coordinates (ξ, η),

X_i, Y_i are the coordinates of the i*th* node,

t is the element cross section depth,

ϕ_i is the angle between the X-axis and the normal to the element surface at the i*th* node.

$\sum_{i=1}^{m} N_i X_i$ is the X-coordinate of the point of natural coordinates (ξ, η=0),

$\sum_{i=1}^{m} N_i Y_i$ is the Y-coordinate of the point of natural coordinates (ξ, η=0),

$\sum_{i=1}^{m} \frac{\eta t}{2} N_i \cos(\phi_i)$ is cos(ϕ) at the point of natural coordinates (ξ, η=0), and

$\sum_{i=1}^{m} \frac{\eta t}{2} N_i \sin(\phi_i)$ is sin(ϕ) at the point of natural coordinates (ξ, η=0),

The shape functions defined by N_i at the i*th* node are as follows:

Three Noded Element

$$N_1 = \frac{1}{2}(\xi^2 + \xi)$$
$$N_2 = (1 - \xi^2) \qquad \textbf{(3.2)}$$
$$N_3 = \frac{1}{2}(\xi^2 - \xi)$$

Four Noded Element

$$
\begin{aligned}
N_1 &= \frac{1}{16}\left(9\xi^3 + 9\xi^2 - \xi - 1\right) \\
N_2 &= \frac{9}{16}\left(-3\xi^3 - \xi^2 + 3\xi + 1\right) \\
N_3 &= \frac{9}{16}\left(3\xi^3 - \xi^2 - 3\xi + 1\right) \\
N_4 &= \frac{1}{16}\left(-9\xi^3 + 9\xi^2 + \xi - 1\right)
\end{aligned}
\tag{3.3}
$$

Five Noded Element

$$
\begin{aligned}
N_1 &= \frac{2}{3}\xi\left(\xi^2 - \frac{1}{4}\right)(\xi + 1) \\
N_2 &= -\frac{8}{3}\xi\left(\xi^2 - 1\right)\left(\xi + \frac{1}{2}\right) \\
N_3 &= 4\left(\xi^2 - 1\right)\left(\xi^2 - \frac{1}{4}\right) \\
N_4 &= -\frac{8}{3}\xi\left(\xi^2 - 1\right)\left(\xi - \frac{1}{2}\right) \\
N_5 &= \frac{2}{3}\xi\left(\xi^2 - \frac{1}{4}\right)(\xi - 1)
\end{aligned}
\tag{3.4}
$$

The displacement field for the 2D element is described by two translational degrees of freedom in the X and Y directions. To describe the displacement field for the degenerated element, an extra rotational degree of freedom at each node has to be introduced to describe the displacement variation in the element cross section. Figure 3.2 shows a plane section before and after deformation. Using an isoparametric definition for the displacement field, the displacements u and v in the X and Y directions at any point with natural coordinates (ξ, η) on the degenerated element can be described by

$$\begin{Bmatrix} u \\ v \end{Bmatrix} = \begin{bmatrix} N_1 & 0 & N_2 & 0 & \dots & N_m & 0 \\ 0 & N_1 & 0 & N_2 & \dots & 0 & N_m \end{bmatrix} \begin{Bmatrix} u_1 \\ v_1 \\ u_2 \\ v_2 \\ \vdots \\ u_m \\ v_m \end{Bmatrix} + \frac{\eta t}{2} \begin{bmatrix} N_1 & 0 & N_2 & 0 & \dots & N_m & 0 \\ 0 & N_1 & 0 & N_2 & \dots & 0 & N_m \end{bmatrix} \begin{Bmatrix} \cos(\phi_1 + \alpha_1) - \cos\phi_1 \\ \sin(\phi_1 + \alpha_1) - \sin\phi_1 \\ \cos(\phi_1 + \alpha_2) - \cos\phi_2 \\ \sin(\phi_2 + \alpha_2) - \sin\phi_2 \\ \vdots \\ \cos(\phi_m + \alpha_m) - \cos\phi_m \\ \sin(\phi_m + \alpha_m) - \sin\phi_m \end{Bmatrix} \quad (3.5)$$

where

u_i, v_i are the displacements of the ith node,

$\sum_{i=1}^{m} N_i u_i$ is the horizontal displacement of the point of natural coordinates (ξ, η=0),

$\sum_{i=1}^{m} N_i v_i$ is the vertical displacement of the point of natural coordinates (ξ, η=0),

$\sum_{i=1}^{m} N_i \cos(\phi_i+\alpha_i)$ is $\cos(\phi+\alpha)$ at the point of natural coordinates (ξ, η=0), and

$\sum_{i=1}^{m} N_i \sin(\phi_i+\alpha_i)$ is $\sin(\phi+\alpha)$ at the point of natural coordinates (ξ, η=0).

3.2.1. Jacobian of transformation Between Natural and Global Coordinate Systems

As in all Finite Element formulations, the formulation starts in the natural coordinates and then is transformed into the global ones. This needs the definition of the Jacobian matrix. The Jacobian matrix defines the relation between the partial derivatives of any quantity with respect to natural coordinates relative to the partial derivatives with respect to the global coordinates. Considering the shape functions, the Jacobian matrix, [J], is defined as follows

$$\begin{Bmatrix} \frac{\partial N_i}{\partial \xi} \\ \frac{\partial N_i}{\partial \eta} \end{Bmatrix} = \begin{bmatrix} \frac{\partial x}{\partial \xi} & \frac{\partial y}{\partial \xi} \\ \frac{\partial x}{\partial \eta} & \frac{\partial y}{\partial \eta} \end{bmatrix} \begin{Bmatrix} \frac{\partial N_i}{\partial x} \\ \frac{\partial N_i}{\partial y} \end{Bmatrix} = [J] \begin{Bmatrix} \frac{\partial N_i}{\partial x} \\ \frac{\partial N_i}{\partial y} \end{Bmatrix} \quad (3.6)$$

The inverse of the Jacobian matrix $[J]^{-1}$ defines the following relation

$$\begin{Bmatrix} \frac{\partial N_i}{\partial x} \\ \frac{\partial N_i}{\partial y} \end{Bmatrix} = [J]^{-1} \begin{Bmatrix} \frac{\partial N_i}{\partial \xi} \\ \frac{\partial N_i}{\partial \eta} \end{Bmatrix} = \begin{bmatrix} A_{11} & A_{12} \\ A_{21} & A_{22} \end{bmatrix} \begin{Bmatrix} \frac{\partial N_i}{\partial \xi} \\ \frac{\partial N_i}{\partial \eta} \end{Bmatrix} \tag{3.7}$$

3.3. Analysis Type, Frame of Reference and the Strain Definition

To deal with problems exhibiting large deformations and finite rotations (geometrical non-linearity), two well known types of analysis are used, namely the Total and the Updated Lagrangian types. Total Lagrangian analysis uses the initial undeformed shape as the frame of reference. Every quantity should be expressed in that frame of reference (e.g. deformations, strains and stresses). This definition of the deformations measured from the initial geometry seems a good choice, but for the stresses and strains this definition results in quantities which have to be transformed to the deformed shape frame of reference in order to be interpreted. On the other hand, Updated Lagrangian analysis uses the current deformed shape, at any given load level, as the frame of reference. That facilitates the interpretation of the strains and stresses because no transformations are needed, but requires regular transformations once the geometry changes. The following sections discuss the different types of analyses and the corresponding definition of strains and stresses.

3.4. The Total Lagrangian Analysis

3.4.1. Constitutive Equations

The material behaviour is defined using constitutive equations which describe the relations between stresses and strains. The incremental stress-strain relationship can be written as

$$d\{\sigma\} = [D]\, d\{\varepsilon\} \tag{3.8}$$

where $\{\sigma\}$ and $\{\varepsilon\}$ are the stress and strain vectors respectively and the operator, d, is used to express the changes in stresses and strains associated with a small load increment. In the above definition, the strains, $\{\varepsilon\}$, are the *Green's* strains (or *Green-Lagrange's* strains) and the stresses, $\{\sigma\}$, are the *Second Piola-Kirchhoff* stresses. These stresses and strains are defined in the initial undeformed body and the only way to interpret their meaning is to transform them into the current deformed shape. When transformed, the strains and stresses become the usual small deformation strains and stresses (*Almansi* strains and *Cauchy* stresses). These stresses and strains are discussed in more detail in the section dealing with the Updated Lagrangian formulation.

Often, it is difficult to accurately simulate the actual material behaviour. Usually some simplifications are applied to make the material model as simple as possible while not sacrificing the accurate modelling of the important aspects of the actual material response. This study approximates the material response as either elastic or elasto-plastic following yield defined using the Von-Mises yield criterion.

3.4.2. Elastic Constitutive Equations

To define the stresses and strains, the local coordinate system (X', Y') is used as shown in Fig. 3.2. The axis X' is tangent to the η=0 line while the Y' axis is the outward normal to the surface. According to the beam theory assumptions, the stress, $\sigma_{y'}$, and the strain, $\varepsilon_{y'}$, defined in the local coordinate system, are zero. The incremental stress-strain relationship in the local axes can be written as

$$d\{\sigma'\} = [D']\ d\{\varepsilon'\}\ ; \quad \begin{matrix} \{\sigma'\}^T = [\sigma_{x'}\ \ \sigma_{y'}\ \ \sigma_{x'y'}\ \ \sigma_z] \\ \{\varepsilon'\}^T = [\varepsilon_{x'}\ \ \varepsilon_{y'}\ \ \varepsilon_{x'y'}\ \ \varepsilon_z] \end{matrix} \tag{3.9}$$

where the matrix $[D']$ for the elastic material under plane stress conditions is defined by

$$[D'] = [D'_e] = \begin{bmatrix} E & 0 & 0 & 0 \\ 0 & 0 & 0 & 0 \\ 0 & 0 & G & 0 \\ 0 & 0 & 0 & 0 \end{bmatrix}; \quad \begin{matrix} \{\sigma'\}^T = [\sigma_{x'}\ \ 0\ \ \sigma_{x'y'}\ \ 0] \\ \{\varepsilon'\}^T = [\varepsilon_{x'}\ \ \varepsilon_{y'}\ \ \varepsilon_{x'y'}\ \ \varepsilon_z] \end{matrix} \tag{3.10}$$

For plane strain conditions the matrix $[D']$ is defined by

$$[D'] = [D'_e] = \begin{bmatrix} \frac{E}{1-\nu^2} & 0 & 0 & \frac{\nu E}{1-\nu^2} \\ 0 & 0 & 0 & 0 \\ 0 & 0 & G & 0 \\ \frac{\nu E}{1-\nu^2} & 0 & 0 & \frac{E}{1-\nu^2} \end{bmatrix}; \quad \begin{matrix} \{\sigma'\}^T = [\sigma_{x'}\ \ 0\ \ \sigma_{x'y'}\ \ \sigma_z] \\ \{\varepsilon'\}^T = [\varepsilon_{x'}\ \ \varepsilon_{y'}\ \ \varepsilon_{x'y'}\ \ 0] \end{matrix} \tag{3.11}$$

where E and G are the material Young's and shear moduli respectively, and ν is the Poisson's ratio. The shear modulus G is related to Young's modulus E through Poisson's ratio ν and is defined by

$$G = \frac{E}{2(1+\nu)} \tag{3.12}$$

It is appropriate to mention that the work done by the stress in the Z direction is zero in both cases of plane stress and plane strain. As usual, the fourth column and the fourth row in the $[D']$ matrix are cancelled for the Finite Element calculations of the stiffness matrix and the $[D']$ matrix becomes a 3×3 matrix as shown

$$[D'] = \begin{bmatrix} \frac{E}{1-\nu^2} & 0 & 0 \\ 0 & 0 & 0 \\ 0 & 0 & G \end{bmatrix}; \quad \text{(Plane Strain)}$$

$$[D'] = \begin{bmatrix} E & 0 & 0 \\ 0 & 0 & 0 \\ 0 & 0 & G \end{bmatrix}; \quad \text{(Plane Stress)} \qquad (3.13)$$

For the calculation of the stress σ_z in the Z direction the 4×4 $[D']$ matrix, defined in Eqns. 3.10 and 3.11, is used.

The local stress-strain matrix $[D']$ is transformed into matrix $[D]$ in the global coordinates using the following relation

$$[D] = [T]\,[D']\,[T]^T \qquad (3.14)$$

where

$$[T] = \begin{bmatrix} C^2 & S^2 & CS \\ S^2 & C^2 & -CS \\ -2CS & 2CS & C^2 - S^2 \end{bmatrix} \qquad (3.15)$$

The matrix $[T]$ is called the transformation matrix in which C=cos(ϕ), S=sin(ϕ), and the angle ϕ is the angle between the outward normal to the element surface (the local Y' axis) and the global X axis.

3.4.3. Compatibility Equations

The Green-Lagrange strains used in the Total Lagrangian analysis are defined by

$$\{\varepsilon\} = \begin{Bmatrix} \varepsilon_x \\ \varepsilon_y \\ \gamma_{xy} \end{Bmatrix} = \begin{Bmatrix} \dfrac{\partial u}{\partial x} \\ \dfrac{\partial v}{\partial y} \\ \dfrac{\partial u}{\partial y} + \dfrac{\partial v}{\partial x} \end{Bmatrix} + \begin{Bmatrix} \dfrac{1}{2}\left(\dfrac{\partial u}{\partial x}\right)^2 + \dfrac{1}{2}\left(\dfrac{\partial v}{\partial x}\right)^2 \\ \dfrac{1}{2}\left(\dfrac{\partial u}{\partial y}\right)^2 + \dfrac{1}{2}\left(\dfrac{\partial v}{\partial y}\right)^2 \\ \dfrac{\partial u}{\partial x}\dfrac{\partial u}{\partial y} + \dfrac{\partial v}{\partial x}\dfrac{\partial v}{\partial y} \end{Bmatrix} \tag{3.16}$$

where the first term in the right hand side represents the linear part of the strains and the second term represents the non-linear part. In small deformation analyses, the second term is considered second order and is neglected. Equation 3.16 can be rewritten as

$$\{\varepsilon\} = \left(\begin{bmatrix} 1 & 0 & 0 & 0 \\ 0 & 0 & 0 & 1 \\ 0 & 1 & 1 & 0 \end{bmatrix} + \frac{1}{2} \begin{bmatrix} \dfrac{\partial u}{\partial x} & \dfrac{\partial v}{\partial x} & 0 & 0 \\ 0 & 0 & \dfrac{\partial u}{\partial y} & \dfrac{\partial v}{\partial y} \\ \dfrac{\partial u}{\partial y} & \dfrac{\partial v}{\partial y} & \dfrac{\partial u}{\partial x} & \dfrac{\partial v}{\partial x} \end{bmatrix} \right) \begin{Bmatrix} \dfrac{\partial u}{\partial x} \\ \dfrac{\partial v}{\partial x} \\ \dfrac{\partial u}{\partial y} \\ \dfrac{\partial v}{\partial y} \end{Bmatrix} \tag{3.17}$$

$$\{\varepsilon\} = \left([H] + \frac{1}{2}[A_\theta] \right) \{\theta\} \tag{3.18}$$

According to Eqns. 3.17 and 3.18, the variation in strain vector $d\{\varepsilon\}$ can be defined by

$$d\{\varepsilon\} = \left([H] + [A_\theta] \right) d\{\theta\} \tag{3.19}$$

The matrices $\{\theta\}$, $[A_\theta]$ and $d\{\theta\}$ for the degenerated element are defined by

$$\{\theta\} = \begin{Bmatrix} \theta_1 \\ \theta_2 \\ \theta_3 \\ \theta_4 \end{Bmatrix} = \begin{Bmatrix} \frac{\partial u}{\partial x} \\ \frac{\partial v}{\partial x} \\ \frac{\partial u}{\partial y} \\ \frac{\partial v}{\partial y} \end{Bmatrix} = \begin{Bmatrix} A_{11}\frac{\partial u}{\partial \xi} + A_{12}\frac{\partial u}{\partial \eta} \\ A_{11}\frac{\partial v}{\partial \xi} + A_{12}\frac{\partial v}{\partial \eta} \\ A_{21}\frac{\partial u}{\partial \xi} + A_{22}\frac{\partial u}{\partial \eta} \\ A_{21}\frac{\partial v}{\partial \xi} + A_{22}\frac{\partial v}{\partial \eta} \end{Bmatrix} \tag{3.20}$$

or

$$\{\theta\} = \begin{Bmatrix} \theta_1 \\ \theta_2 \\ \theta_3 \\ \theta_4 \end{Bmatrix} = \sum_{i=1}^{m} \begin{Bmatrix} A_{11}\frac{\partial N_i}{\partial \xi}\left[u_i + \frac{t\eta}{2}\left[\cos(\phi_i+\alpha)-\cos\phi_i\right]\right] + A_{12}\frac{tN_i}{2}\left[\cos(\phi_i+\alpha)-\cos\phi_i\right] \\ A_{11}\frac{\partial N_i}{\partial \xi}\left[v_i + \frac{t\eta}{2}\left[\sin(\phi_i+\alpha)-\sin\phi_i\right]\right] + A_{12}\frac{tN_i}{2}\left[\sin(\phi_i+\alpha)-\sin\phi_i\right] \\ A_{21}\frac{\partial N_i}{\partial \xi}\left[u_i + \frac{t\eta}{2}\left[\cos(\phi_i+\alpha)-\cos\phi_i\right]\right] + A_{22}\frac{tN_i}{2}\left[\cos(\phi_i+\alpha)-\cos\phi_i\right] \\ A_{21}\frac{\partial N_i}{\partial \xi}\left[v_i + \frac{t\eta}{2}\left[\sin(\phi_i+\alpha)-\sin\phi_i\right]\right] + A_{22}\frac{tN_i}{2}\left[\sin(\phi_i+\alpha)-\sin\phi_i\right] \end{Bmatrix} \tag{3.21}$$

$$\left[A_\theta\right] = \begin{bmatrix} \theta_1 & \theta_2 & 0 & 0 \\ 0 & 0 & \theta_3 & \theta_4 \\ \theta_3 & \theta_4 & \theta_1 & \theta_2 \end{bmatrix} \tag{3.22}$$

$$d\{\theta\} = \sum_{i=1}^{m} \begin{Bmatrix} A_{11}\frac{\partial N_i}{\partial \xi} & 0 & -\left[A_{11}\frac{\partial N_i}{\partial \xi}\frac{t\eta}{2} + A_{12}\frac{tN_i}{2}\right]\sin(\phi_i+\alpha_i) \\ 0 & A_{11}\frac{\partial N_i}{\partial \xi} & +\left[A_{11}\frac{\partial N_i}{\partial \xi}\frac{t\eta}{2} + A_{12}\frac{tN_i}{2}\right]\cos(\phi_i+\alpha_i) \\ A_{21}\frac{\partial N_i}{\partial \xi} & 0 & -\left[A_{21}\frac{\partial N_i}{\partial \xi}\frac{t\eta}{2} + A_{22}\frac{tN_i}{2}\right]\sin(\phi_i+\alpha_i) \\ 0 & A_{21}\frac{\partial N_i}{\partial \xi} & +\left[A_{21}\frac{\partial N_i}{\partial \xi}\frac{t\eta}{2} + A_{22}\frac{tN_i}{2}\right]\cos(\phi_i+\alpha_i) \end{Bmatrix} \begin{Bmatrix} du_i \\ dv_i \\ d\alpha_i \end{Bmatrix} \tag{3.23}$$

or

$$d\{\theta\} = \sum_{i=1}^{m} [G] \, d\{\delta_i\} \tag{3.24}$$

where A_{11}, A_{12}, A_{21} and A_{22} are the elements of $[J]^{-1}$ (inverse matrix of the Jacobian) at (ξ,η), and $[G_i]$ is defined at the ith node of the element. Equations 3.17 to 3.24 would enable the variation in the strain $d\{\varepsilon\}$ to be related to the variation in the displacements $d\{\delta\}$.

$$d\{\varepsilon\}_{3\times 1} = \left([H]_{3\times 4} + [A_\theta]_{3\times 4}\right) \left[[G_1]_{4\times 3} \; [G_2]_{4\times 3} \; \cdots \; [G_m]_{4\times 3}\right] d\{\delta\}_{3m\times 1} \tag{3.25}$$

or

$$d\{\varepsilon\}_{3\times 1} = \left[[B_1]_{3\times 3} \; [B_2]_{3\times 3} \; \cdots \; [B_m]_{3\times 3}\right] d\{\delta\}_{3m\times 1} = [B]_{3\times 3m} \; d\{\delta\}_{3m\times 1} \tag{3.26}$$

where

$$d\{\delta\}_{3m\times 1} = \left\{du_1 \; dv_1 \; d\alpha_1 \mid du_2 \; dv_2 \; d\alpha_2 \mid \cdots \; du_m \; dv_m \; d\alpha_m\right\}^T \tag{3.27}$$

$$[B_i]_{3\times 3} = \left([H]_{3\times 4} + [A_\theta]_{3\times 4}\right) [G_i]_{4\times 3} \tag{3.28}$$

and

$$[B]_{3\times 3m} = \left([H]_{3\times 4} + [A_\theta]_{3\times 4}\right) [G]_{4\times 3m} \tag{3.29}$$

It is also useful to develop the expression for the variation of $[B]$ at this stage as it will be used later in the development of the element stiffness matrix. In Eqn. 3.29, the matrix $[H]$ is constant and matrices $[A_\theta]$ and $[G]$ are functions of the deformations $\{\delta\}$. The variation of $[B]$ is expressed by

$$\begin{aligned} d[B] &= [H] \, d[G] + [A_\theta] \, d[G] + d[A_\theta] \, [G] \\ d[B]^T &= d[G]^T \, [H]^T + d[G]^T \, [A_\theta]^T + [G]^T \, d[A_\theta]^T \end{aligned} \tag{3.30}$$

3.4.4. Equations of Equilibrium

The basic equations of static equilibrium of a body can be written as

$$\{\psi\} = \{R\} - \int_{V_o} [B]^T \{\sigma\}\, dV = \{R\} - \{P\} = 0 \qquad (3.31)$$

where $\{R\}$ is the applied forces vector, and $\int_{V_o} [B]^T \{\sigma\} dV$ represents the equivalent forces due to the internal stresses in the body. The quantity $\{\Psi\}$ is defined as the vector of residuals which should be minimized to zero. This can be visualized as out of balance forces required to bring the displaced body into equilibrium. The vector of residuals, $\{\Psi\}$, is a function of the nodal displacement $\{\delta\}$ of the body as well as the quantity $\int_{V_o} [B]^T \{\sigma\} dV$. It is inconvenient to directly solve Eqn. 3.31 because both the matrix $[B]$ and $\{\sigma\}$ are complicated functions of $\{\delta\}$. The best choice is to derive an incremental equation of equilibrium from Eqn. 3.31 and set up an iterative procedure to solve it. The incremental equation of motion is written as

$$d\{\psi\} = d\{R\} - \int_{V_o} d[B]^T \{\sigma\}\, dV - \int_{V_o} [B]^T d\{\sigma\}\, dV = 0 \qquad (3.32)$$

and a Newton-Raphson iterative technique is used to solve it. The load is applied in increments at which several equilibrium iterations are used to ensure that the residuals, $d\{\Psi\}$, do not exceed a certain small tolerance. In each iteration a better estimate of the stresses and displacements is obtained, thus increasing the accuracy of the numerical solution.

3.4.5. Element Stiffness Matrix for Total Lagrangian Analysis

From Eqns. 3.9 and 3.26, the term $\int_{V_o} [B]^T d\{\sigma\} dV$ in Eqn. 3.32 can be expressed as

$$\int_{V_o} [B]^T d\{\sigma\}\, dV = \int_{V_o} [B]^T [D]\, d\{\varepsilon\}\, dV = \left(\int_{V_o} [B]^T [D] [B]\, dV \right) d\{\delta\} = [K_o]\, d\{\delta\} \qquad (3.33)$$

where $[K_o]$ is the linear and non-linear contribution to the total stiffness matrix, $[K]$.

From Eqn. 3.30 the term $\int_{V_o} d[B]^T \{\sigma\}\, dV$ can be written as

$$\int_{V_o} d[B]^T \{\sigma\}\, dV = \int_{V_o} [G]^T\, d[A_\theta]^T \{\sigma\}\, dV + \int_{V_o} d[G]^T [H]^T \{\sigma\}\, dV + \int_{V_o} d[G]^T [A_\theta]^T \{\sigma\}\, dV \quad \textbf{(3.34)}$$

or

$$\int_{V_o} d[B]^T \{\sigma\}\, dV_o = [K_{\sigma 1}]\, d\{\delta\} + [K_{\sigma 2}]\, d\{\delta\} + [K_{\sigma 3}]\, d\{\delta\} \quad \textbf{(3.35)}$$

where the matrices $[K_{\sigma 1}]$, $[K_{\sigma 2}]$, and $[K_{\sigma 3}]$ are the contribution of the stresses existing in the element to the total stiffness matrix $[K]$ and they are called *initial stress matrices*. Therefore, the total element stiffness matrix is defined by

$$[K] = [K_o] + [K_{\sigma 1}] + [K_{\sigma 2}] + [K_{\sigma 3}] \quad \textbf{(3.36)}$$

and the derivation of the different stress matrices is detailed in the following paragraphs.

The variation in matrix $[A_\theta]$ (i.e. $d[A_\theta]$) can be expressed by

$$d[A_\theta] = \begin{bmatrix} d\theta_1 & d\theta_2 & 0 & 0 \\ 0 & 0 & d\theta_3 & d\theta_4 \\ d\theta_3 & d\theta_4 & d\theta_1 & d\theta_2 \end{bmatrix} \quad \textbf{(3.37)}$$

Also, the quantity $d[A_\theta]^T \{\sigma\}$ can be written as

$$d[A_\theta]^T \{\sigma\} = \begin{bmatrix} d\theta_1 & 0 & d\theta_3 \\ d\theta_2 & 0 & d\theta_4 \\ 0 & d\theta_3 & d\theta_1 \\ 0 & d\theta_4 & d\theta_2 \end{bmatrix} \begin{Bmatrix} \sigma_x \\ \sigma_y \\ \sigma_{xy} \end{Bmatrix} = \begin{bmatrix} \sigma_x & 0 & \sigma_{xy} & 0 \\ 0 & \sigma_x & 0 & \sigma_{xy} \\ \sigma_{xy} & 0 & \sigma_y & 0 \\ 0 & \sigma_{xy} & 0 & \sigma_y \end{bmatrix} \begin{Bmatrix} d\theta_1 \\ d\theta_2 \\ d\theta_3 \\ d\theta_4 \end{Bmatrix} \quad \textbf{(3.38)}$$

or

$$d[A_\theta]^T \{\sigma\} = \begin{bmatrix} \sigma_x & 0 & \sigma_{xy} & 0 \\ 0 & \sigma_x & 0 & \sigma_{xy} \\ \sigma_{xy} & 0 & \sigma_y & 0 \\ 0 & \sigma_{xy} & 0 & \sigma_y \end{bmatrix} \begin{Bmatrix} d\theta_1 \\ d\theta_2 \\ d\theta_3 \\ d\theta_4 \end{Bmatrix} = [S] \{d\theta\} = [S][G]\, d[\delta] \tag{3.39}$$

This would define the matrix $[K_{\sigma 1}]$ as

$$[K_{\sigma 1}]\{\delta\} = \int_{V_o} [G]^T d[A_\theta]^T \{\sigma\} dV = \int_{V_o} [G]^T [S][G]\, dV \quad \{\delta\}$$

$$[K_{\sigma 1}] = \int_{V_o} [G]^T [S][G]\, dV \tag{3.40}$$

To derive the other initial stress stiffness matrices $[K_{\sigma 2}]$ and $[K_{\sigma 3}]$, the variation in matrix $[G_i]$ is calculated first. Neglecting second order terms and using Eqns. 3.23 and 3.24, the variation in matrix $[G_i]$ is expressed by

$$d[G_i]_{4\times 1} = \begin{bmatrix} 0 & 0 & -\left[A_{11}\frac{\partial N_i}{\partial \xi}\frac{t\eta}{2} + A_{12}\frac{tN_i}{2}\right]\cos(\phi_i + \alpha_i) \\ 0 & 0 & -\left[A_{11}\frac{\partial N_i}{\partial \xi}\frac{t\eta}{2} + A_{12}\frac{tN_i}{2}\right]\sin(\phi_i + \alpha_i) \\ 0 & 0 & -\left[A_{21}\frac{\partial N_i}{\partial \xi}\frac{t\eta}{2} + A_{22}\frac{tN_i}{2}\right]\cos(\phi_i + \alpha_i) \\ 0 & 0 & -\left[A_{21}\frac{\partial N_i}{\partial \xi}\frac{t\eta}{2} + A_{22}\frac{tN_i}{2}\right]\sin(\phi_i + \alpha_i) \end{bmatrix} \begin{Bmatrix} du_i \\ dv_i \\ d\alpha_i \end{Bmatrix} \tag{3.41}$$

Consequently, the variation in matrix $[G]$ is defined by

$$d[G]_{4\times m} = \left[d[G_1]_{4\times 1}\ d[G_2]_{4\times 1} \cdots \cdots d[G_m]_{4\times 1} \right] \tag{3.42}$$

This defines the following equation which implicitly defines the stiffness matrices, $[K_{\sigma 2}]$

$$[K_{\sigma 2}]\{\delta\} = \int_{V_o} d[G]^T [H]^T \{\sigma\} dV = \int_{V_o} d[G]^T \begin{Bmatrix} \sigma_x \\ \sigma_{xy} \\ \sigma_{xy} \\ \sigma_y \end{Bmatrix} dV \tag{3.43}$$

The matrix $[K_{\sigma 2}]$ takes the form of

$$[K_{\sigma 2}] = \begin{bmatrix} [K_{\sigma 2}^1] & 0 & \cdots & 0 \\ 0 & [K_{\sigma 2}^2] & \cdots & 0 \\ \vdots & \vdots & \ddots & \vdots \\ 0 & 0 & \cdots & [K_{\sigma 2}^m] \end{bmatrix} \quad \text{where} \quad [K_{\sigma 2}^i] = \begin{bmatrix} 0 & 0 & 0 \\ 0 & 0 & 0 \\ 0 & 0 & K_{\sigma 2}^{ii} \end{bmatrix}$$

and

$$K_{\sigma 2}^{ii} = -\int_{V_o} \begin{Bmatrix} \left[A_{11}\frac{\partial N_i}{\partial \xi}\frac{t\eta}{2} + A_{12}\frac{tN_i}{2}\right]\cos(\phi_i + \alpha_i) \\ \left[A_{11}\frac{\partial N_i}{\partial \xi}\frac{t\eta}{2} + A_{12}\frac{tN_i}{2}\right]\sin(\phi_i + \alpha_i) \\ \left[A_{21}\frac{\partial N_i}{\partial \xi}\frac{t\eta}{2} + A_{22}\frac{tN_i}{2}\right]\cos(\phi_i + \alpha_i) \\ \left[A_{21}\frac{\partial N_i}{\partial \xi}\frac{t\eta}{2} + A_{22}\frac{tN_i}{2}\right]\sin(\phi_i + \alpha_i) \end{Bmatrix}^T \begin{Bmatrix} \sigma_x \\ \sigma_{xy} \\ \sigma_{xy} \\ \sigma_y \end{Bmatrix} dV \tag{3.45}$$

Similarly, the equation defining the stiffness matrix, $[K_{\sigma 3}]$, is expressed by

$$[K_{\sigma 3}]\{\delta\} = \int_{V_o} d[G]^T [A_\theta]^T \{\sigma\} dV = \int_{V_o} d[G]^T \begin{Bmatrix} \theta_1\sigma_x + \theta_3\sigma_{xy} \\ \theta_2\sigma_x + \theta_4\sigma_{xy} \\ \theta_3\sigma_y + \theta_1\sigma_{xy} \\ \theta_4\sigma_y + \theta_2\sigma_{xy} \end{Bmatrix} dV \tag{3.46}$$

The matrix $[K_{\sigma 3}]$ takes the form of

$$[K_{\sigma 3}] = \begin{bmatrix} [K_{\sigma 3}^{1}] & 0 & \dots & 0 \\ 0 & [K_{\sigma 3}^{2}] & \dots & 0 \\ \vdots & \vdots & \ddots & \vdots \\ 0 & 0 & \dots & [K_{\sigma 3}^{m}] \end{bmatrix} \quad \text{where} \quad [K_{\sigma 3}^{i}] = \begin{bmatrix} 0 & 0 & 0 \\ 0 & 0 & 0 \\ 0 & 0 & K_{\sigma 3}^{ii} \end{bmatrix} \tag{3.47}$$

and

$$K_{\sigma 3}^{ii} = -\int_{V_e} \begin{Bmatrix} \left[A_{11}\frac{\partial N_i}{\partial \xi}\frac{t\eta}{2} + A_{12}\frac{tN_i}{2}\right]\cos(\phi_i + \alpha_i) \\ \left[A_{11}\frac{\partial N_i}{\partial \xi}\frac{t\eta}{2} + A_{12}\frac{tN_i}{2}\right]\sin(\phi_i + \alpha_i) \\ \left[A_{21}\frac{\partial N_i}{\partial \xi}\frac{t\eta}{2} + A_{22}\frac{tN_i}{2}\right]\cos(\phi_i + \alpha_i) \\ \left[A_{21}\frac{\partial N_i}{\partial \xi}\frac{t\eta}{2} + A_{22}\frac{tN_i}{2}\right]\sin(\phi_i + \alpha_i) \end{Bmatrix}^T \begin{Bmatrix} \theta_1 \sigma_x + \theta_3 \sigma_{xy} \\ \theta_2 \sigma_x + \theta_4 \sigma_{xy} \\ \theta_3 \sigma_y + \theta_1 \sigma_{xy} \\ \theta_4 \sigma_y + \theta_2 \sigma_{xy} \end{Bmatrix} dV \tag{3.48}$$

3.4.6. Integration Along the Element and Across the Layers

The numerical integration for any quantity $g(x, y)$ is achieved by expressing the integrand in the natural system of coordinates (i.e. use $f(\xi,\eta)=g(x, y)$) and then using the Gauss-Legrende quadrature technique. This can be illustrated in the following relation.

$$\int_{V_e} g(x, y)\, dV = \int_{-1}^{1}\int_{-1}^{1} f(\xi, \eta)\, d\, |J|\, d\xi\, d\eta = \sum_{i=1}^{n}\sum_{j=1}^{p} f(\xi_i, \eta_j)\, d\, w_i\, w_j \tag{3.49}$$

where (n, p) are the number of integration points in the (ξ, η) directions respectively, $|J|$ is the determinant of the Jacobian matrix of transformation, d is the constant section width, and (w_i, w_j) are the quadrature weights. If the element has a varying width, a number of layers would be introduced and sub-integration would be applied in each layer. Assuming that the element consists of l layers, the integration in Eqn. 3.49 can be written as

$$\int_{V_o} g(x, y)\, dV = \frac{1}{l}\sum_{k=1}^{l}\int_{-1}^{1}\int_{-1}^{1} f\left(\xi, \frac{1}{l}(\beta + l - 2k + 1)\right) d_l\, d\xi\, d\beta$$
$$= \frac{1}{l}\sum_{k=1}^{l}\sum_{i=1}^{n}\sum_{j=1}^{p} f\left(\xi_i, \frac{1}{l}(\beta_j + l - 2k + 1)\right) d_l\, w_i\, w_j \qquad (3.50)$$

where d_l is the lth layer width, (ξ_i, β_j) are the usual natural coordinates for (n×p) Gauss integration points and (w_i, w_j) are their corresponding weights. Moreover, when the material properties of the layers are different, different material stress-strain matrices are used in each layer.

A study by Kerja and Cywiński [25] showed that the degenerated element considered here is generally too stiff with full numerical integration, due to locking behaviour, and usually a reduced integration scheme is used. The number of Gauss integration points used per layer for a 3-noded element in the (ξ, η) directions are (2×2), while (3×2) points and (4×2) points are used for a 4-noded and 5-noded elements respectively.

3.5. Element Formulations for the Updated Lagrangian Analysis

The same derivation for the Total Lagrangian formulations applies for the updated Lagrangian case, except that the static and kinematic variables are referred to the current deformed shape. This would require the updating of the nodal coordinates as the body deforms and would allow for 2nd order terms to be neglected in the definition of the strains. The strains are expressed as

$$\{\varepsilon\} = \begin{Bmatrix} \varepsilon_x \\ \varepsilon_y \\ \varepsilon_{xy} \end{Bmatrix} = \begin{Bmatrix} \dfrac{\partial u}{\partial x} \\ \dfrac{\partial v}{\partial y} \\ \dfrac{\partial u}{\partial y} + \dfrac{\partial v}{\partial x} \end{Bmatrix} \qquad (3.51)$$

This would simplify the formulations because of the following

$$[A_0] = [0] \; ; \qquad d[A_0] = [0] \; ; \qquad [B] = [H]\,[G] \tag{3.52}$$

$$\int_{V_t} d[B]^T \{\tau\}\, dV = \int_{V_t} d[G]^T\,[H]^T\,\{\tau\}\, dV = [K_{\tau 2}]\, d\{\delta\} \; ; \qquad [K_{\tau 1}] = [K_{\tau 3}] = [0] \tag{3.53}$$

where V_t is the current volume at time t. The time, t, here is a virtual quantity to simulate the load level at the current configuration. The stress vector, $\{\tau\}$, represents the Cauchy stress vector at time t. The subscript τ is used instead of σ to show that the stiffness matrix is dependent on the Cauchy stresses instead of the 2nd Piola-Kirchhoff stresses.

3.6. Transformation of 2nd Piola-Kirchhoff Stresses to Cauchy Stresses

The stresses that appear in the Total Lagrangian formulations are defined as 2nd Piola-Kirchhoff stresses. These stresses have to be transformed into Cauchy stresses to facilitate interpretation of the stress results. If the solution is found by considering only the stress resultants (i.e. integrating the stresses over the volume to get shear, thrust and bending moments) there would be no need for this kind of transformation as long as the integration of the stresses is achieved over the initial undeformed volume, V_o.

For the Updated Lagrangian formulation, the transformation is inevitable because of the continuous updating of the geometry after each increment or iteration. The main steps of the Updated Lagrangian procedure are summarized as follows:

- The procedure starts with the current deformed geometry and the known solution for the internal stresses (Cauchy stresses $\{\tau_t\}$) at time t.
- The load increment is applied and the incremental deformations, $d\{\delta\}$, are calculated. The incremental strains, $d\{\varepsilon\}$, and incremental 2nd Piola-Kirchhoff stresses, $d\{\sigma\}$, due

to these incremental deformations are calculated. At this stage the total Cauchy stress vector, $\{\tau_{t+\Delta t}\}$, at the new deformed shape can not be directly calculated. This is because the previous stress vector, $\{\tau_t\}$, is of the Cauchy type while the stress increment ,$d\{\sigma\}$, is of the 2nd Piola-Kirchhoff type.

- A transformation is applied to the incremental 2nd Piola-Kirchhoff stress vector, $d\{\sigma\}$, to get the equivalent incremental Cauchy stress vector, $d\{\tau\}$.
- Total Cauchy stress vector at the new deformed shape, $\{\tau_{t+\Delta t}\}$, is calculated by

$$\{\tau_{t+\Delta t}\} = \{\tau_t\} + d\{\tau\} \tag{3.54}$$

The transformation of the 2nd Piola-Kirchhoff stresses, $\{\sigma\}$, defined at time t_2 and referred to configuration at time t_1, to Cauchy stresses $\{\tau\}$, at time t_2, is achieved using the following relations

$$\begin{bmatrix} \tau_x & \tau_{xy} \\ \tau_{xy} & \tau_y \end{bmatrix} = \frac{1}{|X_{t_2}^{t_1}|} \left[X_{t_2}^{t_1}\right] \begin{bmatrix} \sigma_x & \sigma_{xy} \\ \sigma_{xy} & \sigma_y \end{bmatrix} \left[X_{t_2}^{t_1}\right]^T \tag{3.55}$$

where matrix $\left[X_{t_2}^{t_1}\right]$ is the stress transformation matrix and is defined by

$$\left[X_{t_2}^{t_1}\right] = \begin{bmatrix} \dfrac{\partial X_{t_2}}{\partial X_{t_1}} & \dfrac{\partial X_{t_2}}{\partial Y_{t_1}} \\ \dfrac{\partial Y_{t_2}}{\partial X_{t_1}} & \dfrac{\partial Y_{t_2}}{\partial Y_{t_1}} \end{bmatrix} \tag{3.56}$$

The matrix $\left[X_{t_2}^{t_1}\right]$ can be defined for the degenerated element for (t_2=t and t_1=0)as follows

$$\left[X_t^0\right] = \begin{bmatrix} \sum_{i=1}^{m} \frac{\partial N_i}{\partial x}(x_i+u_i) & \sum_{i=1}^{m} \frac{\partial N_i}{\partial y}(x_i+u_i) \\ \sum_{i=1}^{m} \frac{\partial N_i}{\partial x}(y_i+v_i) & \sum_{i=1}^{m} \frac{\partial N_i}{\partial y}(y_i+v_i) \end{bmatrix} = \begin{bmatrix} \sum_{i=1}^{m} A_{11} \frac{\partial N_i}{\partial \xi}(x_i+u_i) & \sum_{i=1}^{m} A_{21} \frac{\partial N_i}{\partial \xi}(x_i+u_i) \\ \sum_{i=1}^{m} A_{11} \frac{\partial N_i}{\partial \xi}(y_i+v_i) & \sum_{i=1}^{m} A_{21} \frac{\partial N_i}{\partial \xi}(y_i+v_i) \end{bmatrix} \tag{3.57}$$

where (u_i, v_i) are the nodal deformations measured from the initial configuration (t_1=0) at the ith node and (x_i, y_i) are the nodal coordinates at time (t_1=0)

3.7. Transformation of the Material Constitutive Relations

In the TL formulation, the material matrix, [D], relates the 2nd Piola-Kirchhoff stresses to the Green-Lagrange strains, while for the UL formulation, matrix [D] relates the Cauchy stresses to the small Almansi strains. To use the same definition of the material constitutive relations when using the two different formulations, TL and UL, a transformation for the material matrix, [D], is required. Before applying the transformation, there now appears a question as to whether the generalized Hooke's law applies to the TL or the UL formulation. The answer for this question is that when the *strains are small* (but displacements and rotations are large; the assumption used in this study) the transformation applied for the matrix [D] is merely due to material rotation. Therefore, since the material is assumed *elastic and isotropic*, the transformation does not change the compone..ts of the stress-strain matrix [D] and the use of either formulation to characterize the material response is equivalent.

3.8. Material Plasticity Model

The stress-strain relationship presented so far is for the elastic material. The actual material behaviour can be more complicated and history dependent than merely simple elasticity. This section discuss the general plasticity concepts and finally applies them to the elasto-plastic model used in this study. The material discussed herein is assumed to follow an elasto-plastic behaviour with work hardening where a limiting yield stress, Y, is

recognized after which work hardening occurs. Two main issues need to be discussed to define the plasticity, namely the yield criterion and the flow rule. These are discussed in the following sections.

3.8.1. Yield Function and Stress-Strain Relationship

It is quite generally postulated, as an experimental fact, that the yielding can only occur if the stresses, $\{\sigma\}$, satisfy the general yield criterion defined by

$$F(\sigma, k) = 0 \tag{3.58}$$

where k is a hardening parameter. This equation can be viewed as defining three regions, an elastic region where the function $F(\sigma,k)$ is less than zero, an elasto-plastic region where $F(\sigma,k)$ equals zero and another region where $F(\sigma,k)$ is greater than zero (in which no material could ever exist). The instantaneous location of the yield surface defined by $F(\sigma,k)=0$ is dependent on the hardening parameter, k.

3.8.2. Flow Rule

The flow rule defines the plastic strain increments, $d\{\varepsilon_p\}$, at yielding. It was first suggested by Von Mises in 1928 that the plastic strain increments are related to the yield surface. At that time, the validity of this assumption was criticised by many workers in that field, but at the present time the assumption appears generally accepted for many materials. The plastic strains are assumed to be

$$d\{\varepsilon_p\} = d\mu \left\{\frac{\partial F}{\partial \sigma}\right\} \tag{3.59}$$

where the multiplier, $d\mu$, has to be defined. This rule is known as the *normality principle*,

because it assumes that the incremental strains are perpendicular to the yield surface. This defines what is called the *associated flow rule* because both the yield surface and the incremental plastic strains are associated to the same function, $F(\sigma,k)$. To generalize the concept, another function, $Q(\sigma,k)$, called the *plastic potential* is used to define the incremental plastic strains

$$d\{\varepsilon_p\} = d\mu \left\{\frac{\partial Q}{\partial \sigma}\right\} \tag{3.60}$$

This general case is called the *non-associated flow rule*. This defines the associated flow as a subset of the general case when $Q(\sigma,k)$ is equal to $F(\sigma,k)$.

3.8.3. Incremental Stress-Strain Relationship

The main assumption used to develop the incremental stress-strain relationship is that the total strain increment, $d\{\varepsilon\}$, is divisible into an elastic strain increment, $d\{\varepsilon_e\}$, and a plastic strain increment, $d\{\varepsilon_p\}$. This can be written as

$$d\{\varepsilon\} = d\{\varepsilon_e\} \qquad F(\sigma, k) \le 0 \quad \text{Elastic Case} \tag{3.61}$$

or

$$d\{\varepsilon\} = d\{\varepsilon_e\} + d\{\varepsilon_p\} \qquad F(\sigma, k) = 0 \quad \text{Elasto-Plastic Case} \tag{3.62}$$

where plastic strains increments exist only at yielding and the elastic strain increments are related to the elastic stress increment by a symmetric matrix of constants, $[D_e]$.

$$d\{\varepsilon_e\} = [D_e]^{-1}\, d\{\sigma\} \tag{3.63}$$

The state of stresses after adding the stress increment is not known beforehand and has to be acquired by an "assume and satisfy" procedure. The details of this procedure are discussed later in this chapter.

Differentiating the function, $F(\sigma,k)$, the following equations may be written

$$dF = \frac{\partial F}{\partial \sigma_x} d\sigma_x + \frac{\partial F}{\partial \sigma_y} d\sigma_y + \frac{\partial F}{\partial \sigma_z} d\sigma_z + \frac{\partial F}{\partial \sigma_{xy}} d\sigma_{xy} + \frac{\partial F}{\partial \sigma_{xz}} d\sigma_{xz} + \frac{\partial F}{\partial \sigma_{yz}} d\sigma_{yz} + \frac{\partial F}{\partial k} dk \qquad (3.64)$$

or

$$\left\{\frac{\partial F}{\partial \sigma}\right\}^T d\{\sigma\} - A\, d\mu = 0 \qquad \text{where} \qquad A = -\frac{\partial F}{\partial k}\frac{dk}{d\mu} \qquad (3.65)$$

Then, to relate the strain increments to the stress increments, Eqns. 3.60, 3.62, 3.63 and 3.65 are combined and the result is written as

$$\begin{Bmatrix} d\{\varepsilon\} \\ 0 \end{Bmatrix} = \begin{bmatrix} [D_e]^{-1} & \left\{\frac{\partial Q}{\partial \sigma}\right\} \\ \left\{\frac{\partial F}{\partial \sigma}\right\}^T & -A \end{bmatrix} \begin{Bmatrix} d\{\sigma\} \\ d\mu \end{Bmatrix} \qquad (3.66)$$

From the previous equation, the unknown factor, $d\mu$, can be eliminated and the relation between the incremental stresses and total incremental strains (i.e. the total of the elastic and plastic incremental strains) is written as

$$d\{\sigma\} = [D_{ep}]\, d\{\varepsilon\} \qquad (3.67)$$

where

$$[D_{ep}] = [D_e] - [D_e]\left\{\frac{\partial Q}{\partial \sigma}\right\}\left\{\frac{\partial F}{\partial \sigma}\right\}^T [D_e]\left[A + \left\{\frac{\partial F}{\partial \sigma}\right\}^T [D_e]\left\{\frac{\partial Q}{\partial \sigma}\right\}\right]^{-1} \qquad (3.68)$$

following the substitution of

$$d\mu = \frac{\left\{\frac{\partial F}{\partial \sigma}\right\}^T [D_e]\, d\{\varepsilon\}}{A + \left\{\frac{\partial F}{\partial \sigma}\right\}^T [D_e]\left\{\frac{\partial F}{\partial \sigma}\right\}} \qquad (3.69)$$

For elasto-plastic behaviour, the matrix $[D_{ep}]$ replaces the elasticity matrix, $[D_e]$. It is

important to mention that the elasto-plastic matrix is only symmetric for the case of associated plasticity and it is dependent on the total stresses (not the incremental ones).

3.8.4. Elasto-Plastic Relations Applied to Von Mises Yield Criterion

Von Mises assumed that the yield surface is defined by

$$F(\sigma, k) = \bar{\sigma} - Y(k) = 0 \tag{3.70}$$

in which k is the hardening parameter, Y is the instantaneous uniaxial yield stress (a function of k) and $\bar{\sigma}$ is the Von Mises equivalent stress. In the plane stress and plane strain cases, $\bar{\sigma}$ is given by

$$\bar{\sigma} = \sqrt{\sigma_x^2 + \sigma_y^2 + \sigma_z^2 - \sigma_x \sigma_y - \sigma_x \sigma_z - \sigma_y \sigma_z + 3\sigma_{xy}^2} \tag{3.71}$$

Using the Von Mises definition for the yield function, the derivatives of the function F with respect to the stress components can be written as

$$\left\{\frac{\partial F}{\partial \sigma}\right\} = \frac{3}{2\bar{\sigma}} \begin{Bmatrix} \sigma_x - \sigma_m \\ \sigma_y - \sigma_m \\ \sigma_z - \sigma_m \\ 2\sigma_{xy} \\ 2\sigma_{yz} \\ 2\sigma_{zx} \end{Bmatrix} \tag{3.72}$$

where σ_m is the mean stress

$$\sigma_m = \frac{\sigma_x + \sigma_y + \sigma_z}{3} \tag{3.73}$$

To define the constant, A, used for the definition of the elasto-plastic matrix, $[D_{ep}]$, the uniaxial stress-strain relationship is used. Figure 3.3a shows the variation of the uniaxial

equivalent stress, $\bar{\sigma}$, versus the uniaxial equivalent strain, ε_u, where the slope to the curve in the elastic range is initially E (Young's modulus) and later defined by E_t (tangential Young's modulus). The figure shows the general relationship and the different loading and unloading paths. Initially the loaded material behaves elastically until the yield point is reached after which plasticity occurs and the loading path follows a new elasto-plastic path. Unloading in the elastic range results in no final plastic strain, but a permanent strain develops when unloading after stresses exceeded the yield stress. The strain in the elasto-plastic range can be split into an elastic part and a plastic part. Figure 3.3b shows $(\bar{\sigma}\text{-}Y_0)$ versus the uniaxial plastic strain, ε_{up}, where the slope of the curve is defined by the hardening parameter, H. The relation between H, the initial Young's modulus, E, and the tangential Young's modulus, E_t, can be written as

$$H = \frac{E E_t}{E - E_t} \tag{3.74}$$

The equivalent plastic strain increment, $d\bar{\varepsilon}_p$, is defined by

$$d\bar{\varepsilon}_p = \frac{2}{3}\sqrt{d\varepsilon_x^2 + d\varepsilon_y^2 + d\varepsilon_z^2 - d\varepsilon_x d\varepsilon_y - d\varepsilon_x d\varepsilon_z - d\varepsilon_y d\varepsilon_z + \frac{3}{4}d\varepsilon_{xy}^2} \tag{3.75}$$

and the instantaneous yield stress, $Y(k)$, is defined by

$$Y(k) = Y_0 + \int H \, d\bar{\varepsilon}_p \tag{3.76}$$

where Y_0 is the initial yield stress. If simple work hardening is assumed, then

$$dk = \sigma_x d\varepsilon_{px} + \sigma_y d\varepsilon_{py} + \ldots = \{\sigma\}^T d\{\varepsilon_p\} \tag{3.77}$$

Now, using the flow rule to substitute for the plastic strain increment,

$$dk = d\mu \, \{\sigma\}^T \left\{\frac{\partial Q}{\partial \sigma}\right\} \quad \text{or} \quad \frac{dk}{d\mu} = \{\sigma\}^T \left\{\frac{\partial Q}{\partial \sigma}\right\} \tag{3.78}$$

Substituting the previous definition of $\frac{dk}{d\mu}$ into the definition of parameter, A, in Eqn. 3.65, A can be written as

$$A = \frac{\partial F}{\partial k} \{\sigma\}^T \left\{\frac{\partial Q}{\partial k}\right\} \tag{3.79}$$

To relate the parameter, A, to the hardening parameter, H, the uniaxial case with an associated flow rule is considered. For this case,

$$dk = Y(k)\, d\varepsilon_{up} \qquad \text{and} \qquad \frac{\partial F}{\partial k} = -\frac{\partial Y(k)}{\partial k} = -\frac{\partial Y(k)}{\partial \varepsilon_{up}} \frac{1}{Y(k)} = -\frac{H}{Y(k)} \tag{3.80}$$

At yield for the uniaxial case,

$$\sigma = -Y(k)\,, \qquad \frac{\partial Q}{\partial \sigma} = \frac{\partial F}{\partial \sigma} = 1\,, \qquad \sigma \frac{\partial Q}{\partial \sigma} = -Y(k) \tag{3.81}$$

From the previous equations, the parameter, A, is defined as

$$A = \frac{\partial F}{\partial k} \{\sigma\}^T \left\{\frac{\partial Q}{\partial k}\right\} = \frac{-H}{Y(k)} [-Y(k)] = H \tag{3.82}$$

The hardening parameter H (called the *plasticity modulus)* reestablishes the well known Prandtl-Reuss stress-strain relations.

In this study, the relationship between uniaxial equivalent stress and uniaxial equivalent strain is assumed bi-linear (Figs. 3.3c and 3.3d) with a slope value equals E initially and a constant value, E_t, after reaching the first yield. Also, an associated flow rule with simple work hardening is assumed. For the bi-linear stress-strain relationship the hardening parameter, H, is constant and the definition of the elasto-plastic stress-strain matrix is

$$[D_{ep}] = [D_e] - [D_e] \left\{\frac{\partial F}{\partial \sigma}\right\} \left\{\frac{\partial F}{\partial \sigma}\right\}^T [D_e] \left[H + \left\{\frac{\partial F}{\partial \sigma}\right\}^T [D_e] \left\{\frac{\partial F}{\partial \sigma}\right\}\right]^{-1} \tag{3.83}$$

Also, the parameter, $d\mu$, represents the equivalent uniaxial plastic strain increment for the general state of stress and can be defined by

$$d\mu = d\bar{\varepsilon}_{up} = \frac{\left\{\frac{\partial F}{\partial \sigma}\right\}^T [D_e]\, d\{\varepsilon\}}{H + \left\{\frac{\partial F}{\partial \sigma}\right\}^T [D_e] \left\{\frac{\partial F}{\partial \sigma}\right\}} \tag{3.84}$$

3.9. Algorithm for the Determination of the State of Stress

The determination of the strain increment from the known displacement increment involves only kinematics, but the determination of the state of stress is more difficult and an iterative algorithm is required. This is because the new state of stress is not known beforehand. The main task of the algorithm is to integrate $[D_{ep}]\, d\{\varepsilon\}$ to calculate the stress increment. The algorithm should deal with different issues concerning this integration which are summarized in the following points.

- It is essential to identify the elastic and plastic portions of the strain increment when transiting from the elastic state into yielding and then plastic flow in the same strain increment. There exists a positive number α between zero and unity at which first yield occurs. The previous elastic stress state is referred to by the subscript 0 while the stress on the yield surface is referred to by subscript 1.

$$\begin{aligned} \sigma_{x1} &= \sigma_{x0} + \alpha\, d\sigma_x \\ \sigma_{y1} &= \sigma_{y0} + \alpha\, d\sigma_y \\ \sigma_{z1} &= \sigma_{z0} + \alpha\, d\sigma_z \\ \sigma_{xy1} &= \sigma_{xy0} + \alpha\, d\sigma_{xy} \end{aligned} \tag{3.85}$$

This defines the Von Mises equivalent stress as the yield stress, Y,

$$Y^2 = \sigma_{x1}^2 + \sigma_{y1}^2 + \sigma_{z1}^2 - \sigma_{x1}\sigma_{y1} - \sigma_{y1}\sigma_{z1} - \sigma_{z1}\sigma_{x1} + 3\,\sigma_{xy1}^2 \tag{3.86}$$

Combining Eqns. 3.85, 3.86 and rearranging leads to a quadratic equation

$$A\alpha^2 + B\alpha + C = 0 \tag{3.87}$$

in which A, B and C are defined by

$$\begin{aligned} A &= d\sigma_x^2 + d\sigma_y^2 + d\sigma_z^2 - d\sigma_x d\sigma_y - d\sigma_y d\sigma_z - d\sigma_z d\sigma_x + 3d\sigma_{xy}^2 \\ B &= d\sigma_x\left(2\sigma_{x0} - \sigma_{y0} - \sigma_{z0}\right) + d\sigma_y\left(2\sigma_{y0} - \sigma_{z0} - \sigma_{x0}\right) + \\ &\qquad d\sigma_z\left(2\sigma_{z0} - \sigma_{x0} - \sigma_{y0}\right) + 6\sigma_{xy0}\, d\sigma_{xy} \\ C &= \sigma_{x0}^2 + \sigma_{y0}^2 + \sigma_{z0}^2 - 3\sigma_{x0}\sigma_{y0} - 3\sigma_{y0}\sigma_{z0} - 3d\sigma_{z0}\sigma_{x0} + 3\sigma_{xy}^2 - Y^2 \end{aligned} \tag{3.88}$$

The root of Eqn. 3.87 is calculated ignoring the negative value for α. Thus, for an increment of strain, $d\{\varepsilon\}$, only the $\alpha\, d\{\varepsilon\}$ term is considered elastic and the rest is dealt with using the elasto-plastic constitutive relations.

- At the end of each increment (or iteration if an incremental iterative technique is used), if the stress increment brings the total stress state outside the yield surface an additional correction to the stresses is essential to bring back the stresses to the yield surface. Following the work by Nayak and Zienkiewicz [36], the stress correction, $d\{\sigma_c\}$, is given by

$$d\{\sigma_c\} = -\frac{\left\{\dfrac{\partial F}{\partial \sigma}\right\}(\bar{\sigma} - Y)}{\left\{\dfrac{\partial F}{\partial \sigma}\right\}^T \left\{\dfrac{\partial F}{\partial \sigma}\right\}} \tag{3.89}$$

- The calculation of the stress increment associated with a given strain increment involves the integration of $[D_{ep}]\, d\{\varepsilon\}$, where $[D_{ep}]$ is non-linear and a suitable integration technique is required for accurate calculations. The sub-incremental method proposed by Huffington [23] is used where the strain increment is subdivided into smaller sub-increments. At each sub-increment, the stress sub-increment is calculated using the

second order Runge-Kutta integration method. The sub-incremental technique gives a good approximation for the stress state, which has the advantage of larger load increments for a given accuracy. The number of sub-increments used is determined by limiting the sub-increment equivalent strain to 0.0002 (Bushnell [9]).

- In the incremental analysis with equilibrium iterations, one of the major problems is the fictitious numerical unloading in different iterations during the same load increment. This may lead to serious errors and path dependent behaviour of the structure if numerical unloading is assumed to be irreversible. To avoid this difficulty several different approaches had been adopted by researchers. Bushnell [9] used a strategy where geometrical non-linearities and material non-linearities are separated and are dealt with using two different types of iterations. For each load increment, a set of Newton-Raphson iterations are performed (called displacement iterations). In each displacement iteration the material properties are kept constant, until displacements converge. The accumulated strains are then used to iterate to calculate the stress increments and update the material properties (called material iterations). The process continues by moving from displacement iteration to material iteration until any further updating of the material properties has very little effect on the structure displacements. This procedure obtains convergence but at considerable cost in computing time.

  Another approach is used by Harding *et al* [21] and Frieze *et al* [17], where they update the material properties only at the end of the load increment and consequently requires very small load steps resulting in a slow and costly analysis.

  A more efficient strategy is used by Nyssen [37], where he assumed incremental

reversibility of the plastic behaviour. He assumed that "*A point which deforms plastically during one increment is assumed to unload plastically until the plastic work done becomes again equal to its value at the beginning of the considered increment*". Figure 3.5 illustrates the assumption, where the last converged state, in the previous increment, is represented by point 1. A load increment is applied and the point deforms plastically to reach point 2. If any unloading happens during the current increment, the point deforms plastically until it reaches the last converged state (point 1) and then unloads elastically (point 3).

The advantages of this approach compared to others is discussed by Nyssen [37]. Thus at the beginning of each iteration the accumulated plastic strain is set to zero, and is updated in each sub-increment. Elastic unloading only occurs when the accumulated plastic strain becomes negative.

Figures 3.4a and 3.4b show the details of the algorithm. The main steps are summarized as follows:

1 Calculate the total strain increment, $d\{\varepsilon\}$, from the displacement increment, $d\{\delta\}$

2 If the previous state of stress is elastic

2*a* Assume that the new state of stress is elastic and the calculate the elastic stress increment, $d\{\sigma\}$

2*b* Check the yield criterion using the current stresses (i.e. $\{\sigma\} + d\{\sigma\}$)

- if the state of stress is still elastic
  - Update stresses and return.
- If the state of stress becomes plastic

- Calculate the pure elastic portion of the strain (i.e the elastic ratio α)
- Get the elasto-plastic portion of the strain, $(1-\alpha)\, d\{\varepsilon\}$
- Calculate the elastic stress increment then update the total stresses and start the sub-incrementing procedure (step 4)

3 If the previous state is plastic, then the strains are assumed to be completely elasto-plastic.

4 Calculate the equivalent plastic strain

5 Calculate the number of sub-increments, N_{sub}

6 Initialize the accumulated equivalent plastic strain in the increment to zero (i.e. $D\bar{\varepsilon}_{pn} = 0$)

7 Loop for $n = 1$ to N_{sub} sub-increments

7a Calculate the nth elasto-plastic sub-increment strains, $d\{\varepsilon_{pn}\}$

7b Calculate the equivalent plastic strain in the sub-increment, $d\bar{\varepsilon}_p$

7c Update the accumulated equivalent plastic strain

7d If the increment accumulated plastic strain is positive (i.e. $D\bar{\varepsilon}_{pn} > 0$), assume plastic loading

- Update the instantaneous yield stress
- Use the classical second order Runge-Kutta integration method to calculate the stress sub-increment and then go to step *7i*.

7e If the increment accumulated plastic strain is negative (i.e. $D\bar{\varepsilon}_{pn} < 0$), assume unloading with incremental reversibility of the plastic strains

7f Calculate the plastic portion of the sub-incremental strains

7g Subtract the plastic portion of strain from the total sub-incremental strains to get the

elastic portion

7h Calculate the elastic stress sub-increment

7i Calculate the Von Mises equivalent stress after adding the stress sub-increment

7j Check the yield criterion

7k If the stresses are outside the yield surface, correct the stresses back to the yield surface and go to step *7i*

7l Update the total stresses by adding the stress sub-increment

7m if the number of sub-increments, n, is not equal N_{sub} go to step *7a*

7n Set the total stress equal to the sub-incremental total stress.

3.10. Incremental Iterative Procedures

The equation of static equilibrium and its incremental form are defined by

$$\{\psi\} = \lambda\{R\} - \int_{V_o} [B]^T \{\sigma\}\, dV = \lambda\{R\} - \{P\} = 0 \tag{3.90}$$

$$d\{\psi\} = d\lambda\,\{R\} - \int_{V_o} d[B]^T \{\sigma\}\, dV - \int_{V_o} [B]^T d\{\sigma\}\, dV = 0$$

$$d\{\psi\} = d\lambda\,\{R\} - [K_T]\, d\{\delta\} = 0 \tag{3.91}$$

where $\{R\}$ is the nominal proportional load vector, and λ is the load multiplier.

These equations are difficult to solve directly and therefore some form of iterative technique is required. Two main incremental iterative procedures are used within the thesis; the Newton-Raphson procedure and the Arc-Length Control procedure. Both methods use the repeated solution of a system of linear equations in the form of $[K]\, d\{\delta\} = d\lambda\ \{R\}$ to reach the final solution. The final solution consists of a series of applied load vectors, $\{R\}$, and

the corresponding displacement vectors, $\{\delta\}$, at the nodal points of the body. To solve for each pair of vectors, a set of additional constraint equations are needed to reduce the number of unknowns. The constraint used in the Newton-Raphson method is a constant load increment, $d\{R\}$, (or a predefined load vector, $\lambda\{R\}$). This can be visualized as applying a load increment and calculating the corresponding displacement increment. For the Arc Length Control Method, different constraint equations can be applied. The first constraint equation was introduced by Riks [39] and Wempner [45]. For a single degree of freedom, it took the shape of an arc constraint (instead of the horizontal line in the Newton-Raphson method). This equation constrains both the load and the displacement increments to a certain relation. This was later modified by Crisfield [13] to constrain only the norm of the incremental displacement vector to a constant value (called the *arc-length*). Both procedures and their advantages and disadvantages are discussed in the following sections.

3.10.1. The Newton-Raphson Incremental/Iterative procedure

The Newton-Raphson procedure is often used for the solution of non-linear problems. In this iterative procedure, the equilibrium equation is linearized and the following iterative equation is used

$$\{\psi\}_{i+1} = \{\psi\}_i + \left[\frac{\partial \psi}{\partial \delta}\right]_i d\{\delta\}_i = \{\psi\}_i - [K_T]_i\, d\{\delta\}_i = 0 \qquad (3.92)$$

where i is the iteration counter and $[K_T]_i$ is the stiffness matrix corresponding to the displacements at iteration, i (called tangential stiffness matrix). The process is illustrated in Fig. 3.6a where the load is applied in increments (i.e. the constraint equation is $d\{R\}$=constant), the subscript n stands for the increment counter and the total incremental

displacement at the end of iteration, i, is defined by

$$\Delta\{\delta\}_i = \sum_{k=1}^{i} d\{\delta\}_k \tag{3.93}$$

The iterative procedure continues until the residual forces $\{\psi\}$, are negligible.

The Newton-Raphson procedure, despite its rapid quadratic convergence, can be expensive and inconvenient. This is due to the fact that the tangent stiffness matrix has to be calculated and factorized at each iteration. Even in some non-associative elasto-plasticity cases the matrix becomes non-symmetric and a non-symmetric solver is required.

One of the ways to avoid this problem is to formulate the tangent stiffness matrix only at the first iteration (the Modified Newton-Raphson Method) or the first two iterations and then keep it constant over the rest of the iterations. This would save computing time, but will slow down the convergence rate and more iterations may be required. Another draw back of both the Newton-Raphson method and its modified version is that they fail once a behaviour exhibiting a peak load is encountered. Thus the peak load is underestimated because a numerical, rather than structural, instability occurs. At this time, it is essential to resort to another technique. The Arc-Length Control Method emerges as a convenient alternative for these cases.

3.10.2. Arc-Length Control Procedure

In the Arc-Length Control Method, the load increment is not chosen arbitrarily, like in the Newton-Raphson method, but adjusted at each iteration under the arc-length constraint equation. The Arc-Length Control Method has many versions depending on the constraint equation used. In this section details are given of the Crisfield method [13]. For the

interested reader, a survey on most of the available methods can be found in Carrera [10]. Figure 3.6b shows the details of the iterations applied in an arc-length increment. The load is assumed to be proportional and the load vector is defined by $\lambda\{R\}$ where $\{R\}$ is the nominal load vector and λ is a load multiplier. The residual load vector at the start of the ith iteration is defined by $\{\psi\}_i$ which is calculated using

$$\{\psi\}_i = \lambda_i \{R\} - \{P\}_i = \lambda_i \{R\} - \int_V [B]_i^T \{\sigma\}_i \, dV \tag{3.94}$$

The displacement vector, $d\{\delta_r\}_i$ due to the residual force vector at the ith iteration is defined by

$$d\{\delta_r\}_i = [K]_i^T \{\psi\}_i \tag{3.95}$$

The procedure starts with the choice of an arc length, l, which is used to constrain the norm of the accumulated incremental displacement to a movement of that length in the load-deformation space. The constraint equation takes this form

$$\Delta\{\delta\}_i^T \Delta\{\delta\}_i = l^2 \tag{3.96}$$

where $\Delta\{\delta\}_i$ is the accumulated incremental displacement at the end of the ith iteration. This accumulated displacement is defined by

$$\Delta\{\delta\}_i = \sum_{k=1}^{i} d\{\delta\}_k \tag{3.97}$$

where $d\{\delta\}_i$ represents the ith iterative displacement vector. From Fig. 3.6c the following definition of the accumulated displacement vector can be drawn

$$\Delta\{\delta\}_i = \Delta\{\delta\}_{i-1} + d\{\delta\}_i = \Delta\{\delta\}_{i-1} + d\lambda_i \{\delta_c\}_i + \{\delta_r\}_i \tag{3.98}$$

where the characteristic displacement $\{\delta_c\}_i$ is defined by

$$\{\delta_c\}_i = [K_T]_i^{-1} \{R\} \tag{3.99}$$

Substituting the equation for the cumulative displacement into the constraint equation results in the quadratic equation

$$A(d\lambda_i)^2 + Bd\lambda_i + C = 0 \tag{3.100}$$

in which

$$\begin{aligned} A &= \{\delta_c\}_i^T \{\delta_c\}_i \\ B &= 2\ [\Delta\{\delta\}_{i-1} + \{\delta_r\}_i]^T\ \{\delta_c\}_i \\ C &= [\Delta\{\delta\}_{i-1} + \{\delta_r\}_i]^T\ [\Delta\{\delta\}_{i-1} + \{\delta_r\}_i] - l^2 \end{aligned} \tag{3.101}$$

The solution of this quadratic equation results in two roots (i.e. two values for $d\lambda_i$). The appropriate root maintains a positive projection of the current accumulated incremental displacement vector on the previous one within the ith iteration, namely $\Delta\{\delta\}_i$ and $\Delta\{\delta\}_{i-1}$. This condition prevents doubling back on the load-deformation curve and can be written as

$$\theta = \Delta\{\delta\}_{i-1}^T \Delta\{\delta\}_i = +(ve) \tag{3.102}$$

where $\Delta\{\delta\}_i$ is calculated using

$$\begin{aligned} d\{\delta\}_i &= d\lambda_i \{\delta_c\}_i + \{\delta_r\}_i \\ \Delta\{\delta\}_i &= \Delta\{\delta\}_{i-1} + d\{\delta\}_i \end{aligned} \tag{3.103}$$

However, if both roots maintains two positive projections, then the one closer to the linear solution $-\left(\frac{C}{B}\right)$ should be chosen. Once the root, $d\lambda_i$, is chosen, the iterative displacement and the accumulated incremental displacement vectors are calculated according to Eqn. 3.103. For the case of the first iteration at the mth loading increment

$$\Delta\{\delta\}_0 = 0\ ; \quad \{\delta_r\}_1 = 0 \tag{3.104}$$

and the solution for the quadratic equation becomes

$$d\lambda_i = \pm \frac{l}{\sqrt{\{\delta_c\}_i^T \{\delta_c\}_i}} \tag{3.105}$$

where the choice for the sign follows the sign of stiffness matrix determinant, $|K_T|$, or the sign of $\{R\}^T \{\delta_c\}_1$.

A correction to the chosen arc-length may be applied in each increment to promote convergence in the same desired number of iterations per increment. The arc-length may be written as

$$l_n = l_{n-1} \left(\frac{J_d}{J_{n-1}} \right)^{\frac{1}{m}} \tag{3.106}$$

where J_d is the desired optimum number of iterations, l_n is the arc-length for the nth increment, J_{n-1} is the number of iterations required in the $(n-1)$th increment to achieve convergence, and m is an arbitrary chosen constant (usually 2).

The Arc-Length Control Method has been used by many researchers to study geometrical non-linearities. However, when the method is applied to both geometrical and material non-linearities, some problems may arise. These problems are due to the unloading which occurs when the iterative technique is used. This is overcome by assuming incremental reversibility of the plastic deformations (discussed before). With this assumption, negative displacement changes due to iterations do not cause the whole structure to unload fictitiously leading to numerical divergence.

3.11. Numerical Results

In order to verify the behaviour of the present formulation, extensive comparisons between available solutions and the present predictions are given.

3.11.1. Cantilever Beam Under Tip Moment

The problem of an elastic cantilever subjected to an end moment is considered. Both TL and UL formulations are used. The solution is checked against the available numerical and analytical solutions of the problem.

Using a set of consistent units, the cantilever is modelled using five 5-noded structural elements with Young's modulus $E=3\times10^7$, and Poisson's ratio $\nu=0$. It has a length $L=12.0$, cross section (1×1) and is subjected to an end moment $M=\lambda\left(\frac{\pi EI}{L}\right)$. Figure 3.7 shows the model used.

For the TL formulation, an incremental Newton-Raphson technique with equilibrium iterations is used. Different moment increment sizes are used to study the convergence of the numerical solution. The parameters used correspond to $d\lambda=0.05$, 0.10, 0.20, and 0.4. Figure 3.8 shows that good convergence is accomplished when the total moment $M=2\left(\frac{\pi EI}{L}\right)$ is applied in ten equal increments (i.e. $d\lambda=0.2$). The solution shows good agreement with the results of Bathe and Bolourchi [4] (Fig. 3.8). In that work, 45 equal moment increments are used to achieve $\lambda=0.9$. It is also important to mention that in [4] no equilibrium iterations were performed because the moment increment was so small that a linear approximation was sufficient. The emphasis is that for this non-linear element, the load increments do not have to be small because the equilibrium iterations make the proper corrections. This is contrary to the linearized formulations used in [4] which diverge if the solution deviates for the actual non-linear solution. Figure 3.7 shows the cantilever geometry and the deformed shapes at different load levels.

The same problem of the cantilever subjected to an end moment is solved using the UL formulation. The convergence study shows poor convergence relative to the TL case. For

an increment size of ($d\lambda$=0.2) the solution diverges after five increments, while for ($d\lambda$=0 1) it converges but with insufficient accuracy. Enough accuracy is obtained when using ($d\lambda$=0.05). A comparison between the solution for different load increment sizes is shown in Fig. 3.9. Another comparison between the UL and TL solutions is obtained (Fig. 3.10). There is a noticeable difference when the strains become relatively large (λ>0.9). This may be attributed to the difference in the definition of the stress-strain relationship applied to each formulation at large strains.

The UL solution is also compared with the analytical closed form solution

$$\delta_x = \frac{EI}{M}\left[1 - \cos\left(\frac{ML}{EI}\right)\right] = \frac{L}{\pi\lambda}\left[1 - \cos(\lambda\pi)\right] \tag{3.107}$$

$$\delta_y = L - \frac{EI}{M}\sin\left(\frac{ML}{EI}\right) = L\left[1 - \frac{\sin(\lambda\pi)}{\pi\lambda}\right] \tag{3.108}$$

Figure 3.10 shows that the UL solution compares well with the analytical closed form solution. This is because the analytical solution is defining the stress-strain relationship as the relation between the incremental Cauchy stresses and the incremental Almansi strains.

3.11.2. Cantilever Beam Under Uniformly Follower Distributed Load

The problem of a cantilever subjected to a follower external pressure P is considered. Figure 3.11 shows a cantilever of length, L, and cross sectional moment of inertia, I, modelled using five 5-noded structural elements. The cantilever material has Young's modulus, E, and Poisson's ratio, ν. The cantilever cross section dimensions are chosen such that the depth of the cross section is 1/100th of the cantilever length (i.e. the thin structure assumption should be appropriate). The Updated Lagrangian formulation is used to study

the problem. The pressure $P=\lambda\left(\frac{EI}{L^3}\right)$ is applied in increments ($d\lambda$=1.0) and equilibrium iterations are used. Since the geometry of the cantilever is changing with load, the error introduced due to the usage of the equivalent nodal load vector (due to the pressure) defined by the previous iteration geometry is automatically incorporated into the residual force vector in the new equilibrium iteration. Other techniques modify the stiffness matrix due to the effect of this load, which produces a non-symmetric stiffness matrix. This technique is not used herein because of the extra time required to solve a non-symmetric system of linear equations.

Figure 3.12 shows the results of both the FEM analysis and those of Argyris and Symeonidis [2] for the horizontal and vertical displacements at the cantilever tip. Good agreement is clearly obtained between the two solutions. The deformed shapes at different load levels (λ=5, 10, and 15) are shown in Fig. 3.11.

3.11.3. A Ring Subjected to Two Point Loads

This section considers the problem of a circular ring of radius, R, and cross sectional moment of inertia, I, subjected to two equal and opposite point loads as in Fig. 3.13a. The ring material has Young's modulus, E, and Poisson's ratio, ν. The ring is modelled using six 3-noded structural line elements. Because of symmetry, only one quadrant of the ring is modelled. Different ring thickness to radius ratios (t/R=0.02, 0.10, 0.20, and 0.30) are used to study the effect of the t/R ratio on the results. For comparison purposes another model using 8-noded *geometrically non-linear* 2D elements is used. For t/R=0.02, and 0.10, fifty 8-noded elements are used (Fig. 3.13b), while for t/R=0.20, and 0.30, one hundred 8-noded elements are used arranged as in Fig. 3.13c. Figures 3.14 and 3.15 show the vertical

displacement, u_y, at the ring crown and the horizontal displacement, u_x, at the ring spring line versus the load, P, for both the 2D elements and the structural line elements. The figures show that for the vertical displacements both solutions are in good agreement, but for the horizontal displacements the agreement exists only at a maximum ratio of t/R=0.10. This difference is due to "plane cross section remains plane after deformation" approximation used in the structural element formulation which is poor for thick rings This would suggest the usage of a maximum t/R ratio of 0 10 for the ring problems and similar pipe problems. It is important to note that the large strain formulation used for the 2D elements produces a non-symmetric stiffness matrix which adds more expense to the solution. The deformed shapes of the ring quadrant at different load levels for the different models are shown in Fig. 3.13. Figure 3.16 shows the deformed shape of the structural element model at P=0.0, 1.5, and 2.5.

3.11.4. A Deep Clamped-Hinged Arch Subjected to a Vertical Point Load

The problem of a deep clamped-hinged arch subjected to a vertical point load is considered in this section. The circular arch of radius, R=100m, and thickness, t=1.0m, extends for an angle, ϕ=215° (Fig. 3.17). The arch has Young's modulus, E, and cross sectional moment of inertia, I, where EI=10^6 kN.m^2. Five 5-noded elements are used to model the arch. A trial solution with the Newton-Raphson incremental technique failed at $EI/(PR^2)$=9.0. The solution was repeated using the Arc-Length Control method. The arch shows a snap-through behaviour at $EI/(PR^2)$=9.1 and the behaviour is traced even after the limit load. Figure 3.18 shows the load deflection behaviour at the arch crown. The vertical and horizontal displacements at the arch crown, u_x and u_y respectively, are plotted against

the normalized load $EI/(PR^2)$. The FEM results are checked against the analytical solution by Da Deppo and Schmidt [14]. Good agreement with the analytical solution is evident. This would suggest that the Arc-Length Control Method behaves well with the geometrically non-linear structural element. Figure 3.17 shows the deformed shapes at different load levels.

3.11.5. Collapse Analysis of an Elasto-Plastic Ring Under External Pressure

This section deals with the buckling and post-buckling analysis of an elasto-plastic ring in the large deformation regime. The circular ring has an initial imperfection defined by

$$R_\theta = R\left(1 + \frac{w_o}{R}\cos(2\theta)\right) \tag{3.109}$$

where R=100m is the original circular ring radius, w_o/R=0.008 is the imperfection size as defined in Fig. 3.19a, and R_θ is the radius at any angle, θ, measured anticlockwise from the horizontal X-axis.

The ring is modelled using six 5-noded structural elements with initial Young's modulus, E=10^7 kN/m^2, and Poisson's ratio, ν=0. Different ring thickness to radius ratios are used to examine the convergence of the solution; t/R=0.00055991, 0.0055991, and 0.055991. The normalized vertical displacement, u_y/R, at the ring crown is shown versus the normalized pressure, $\frac{4P}{E}\left(\frac{R}{t}\right)^3$, for the three different t/R ratios (Fig. 3.20). The deformation increases rapidly when the load reaches the value defined by the elastic buckling load , $\frac{4P}{E}\left(\frac{R}{t}\right)^3 = 1.0$. There is no noticeable difference in the results, and t/R=0.055991 is used for the rest of the calculations.

To study the effect of plasticity on the pre-buckling and post-buckling behaviours, an

initial yield stress, Y_o=42000 kN/m^2, and a bi-linear uniaxial stress-strain relation are used. Different E/E_t ratios are considered to study the effect of the strain hardening on the post-buckling behaviour. Two layers are used to describe the element cross section to fully trace the development of the plasticity across it. One layer may be used, but an overestimation of the buckling load may occur depending on the load increment. The Newton-Raphson method is used for the cases E/E_t=1.0, 1.2, while the Arc-Length Control method is used of the other values of E/E_t. Figure 3.21 shows the different normalized load-deflection results for E/E_t=1.0, 1.2, 1.5, 5.0, and 50.0. The results compare well with the semi-analytical solution of Kyriakides and Babcock [27]. It is clear that the behaviour for E/E_t<1.2 is stable, while for (E/E_t>1.2), a snap through buckling may occur. Figure 3.22 shows the deformed shape at different load levels for E/E_t=1.0, 50.0.

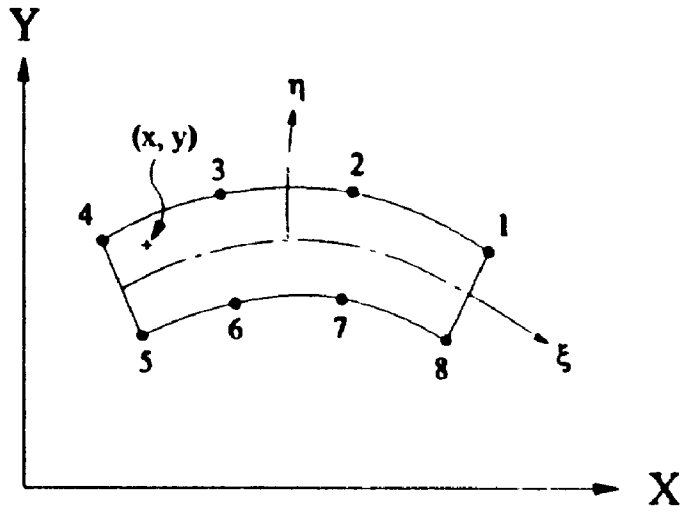

2D Continuum Element

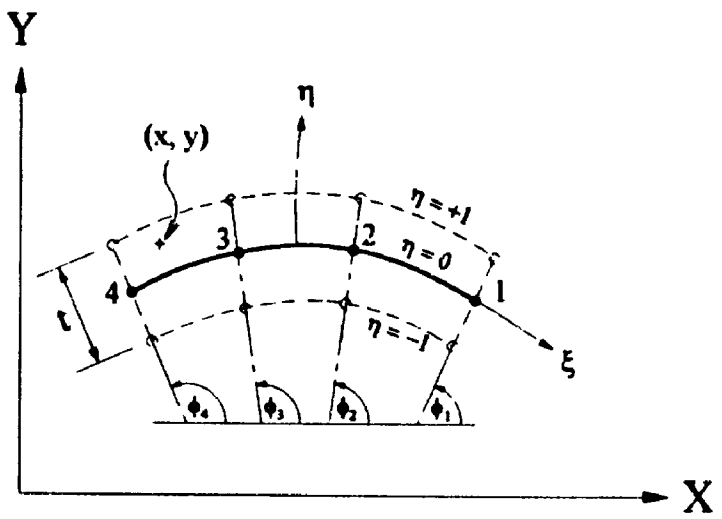

Definition of the Degenerated Structural Element

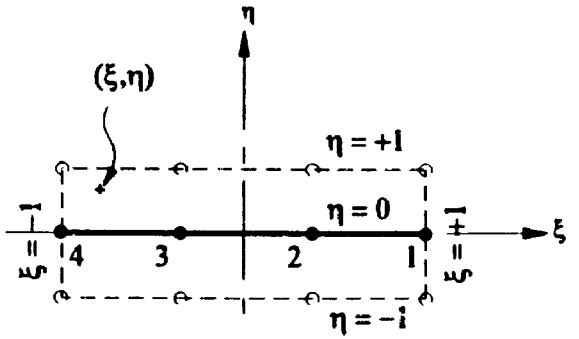

The Degenerated Structural Element in Natural Coordinate System

Figure 3.1. 2D Element and the Degenerated Structural Element in Global Coordinate System (X and Y) and Natural Coordinate System (ξ and η)

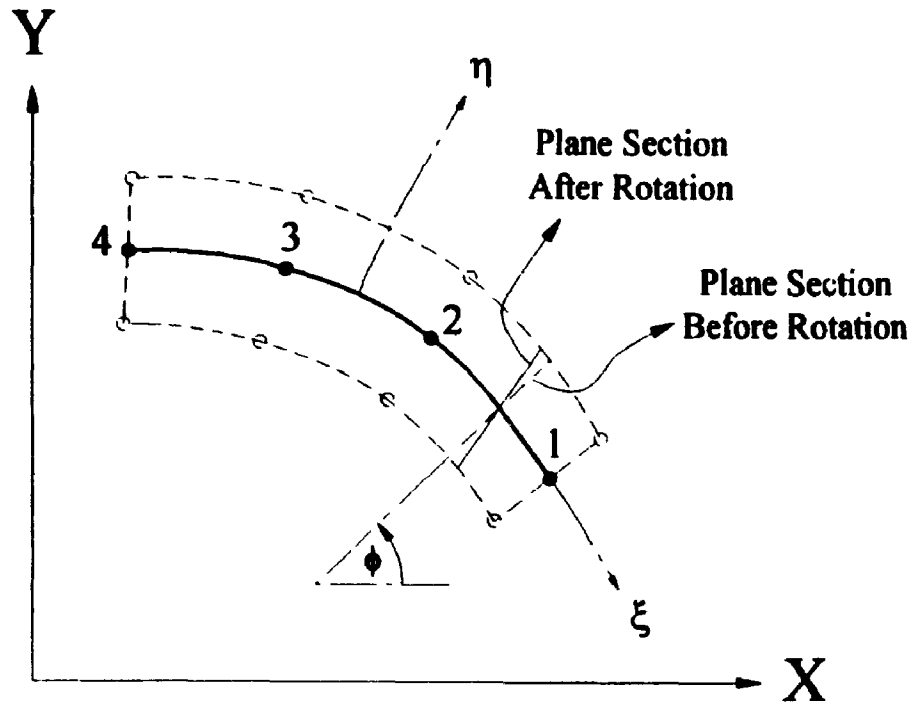

Definition of Element Rotation

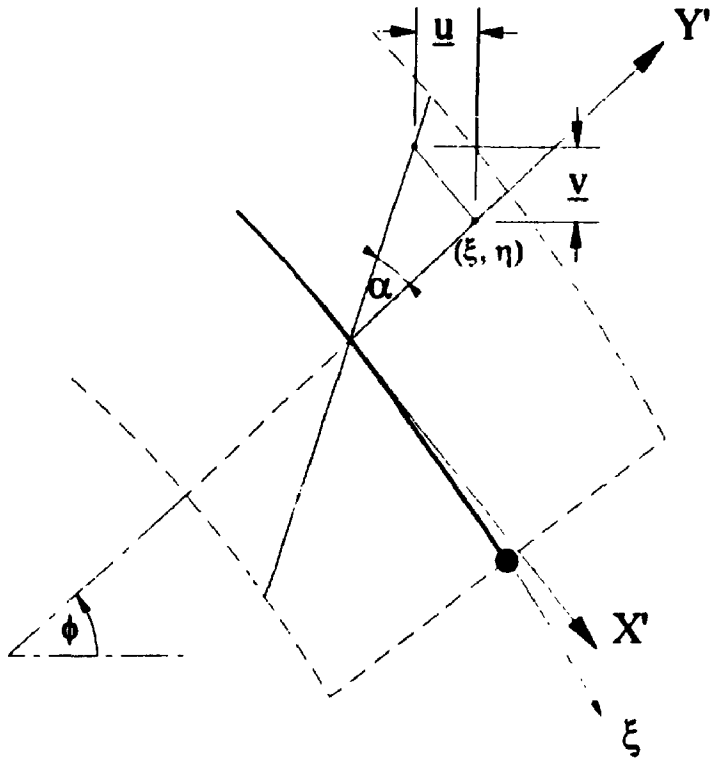

$$u(\xi,\eta) = u(\xi,0) + \underline{u} = u(\xi,0) + \frac{\eta t}{2}\left[\cos(\phi+\alpha) - \cos\phi\right]$$

$$v(\xi,\eta) = v(\xi,0) + \underline{v} = v(\xi,0) + \frac{\eta t}{2}\left[\sin(\phi+\alpha) - \sin\phi\right]$$

Figure 3.2. Displacement Field for the Degenerated Element

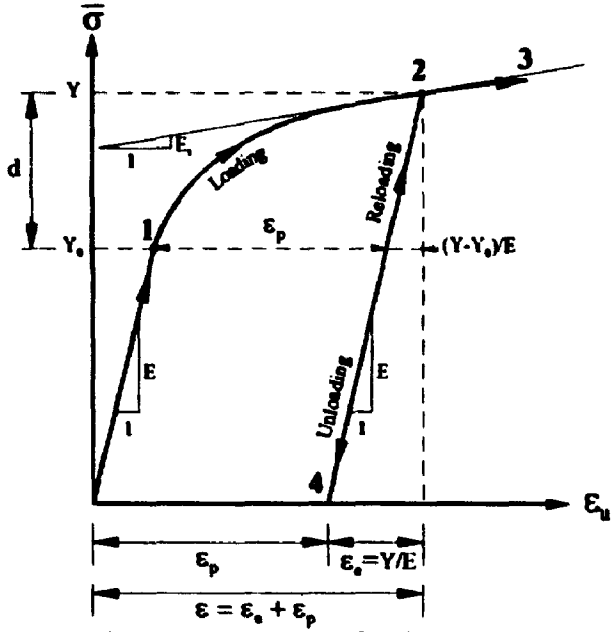

Figure 3.3a. Uniaxial Stress-Strain Relationship

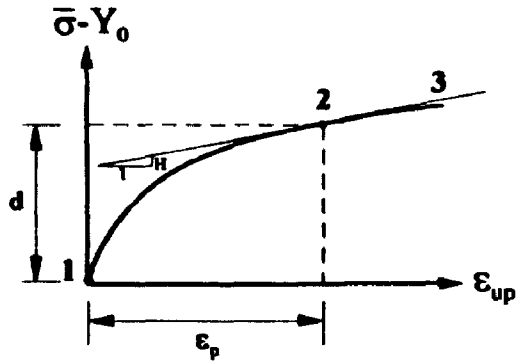

Figure 3.3b. Plastic Uniaxial Strain versus Increase in Yield Stress

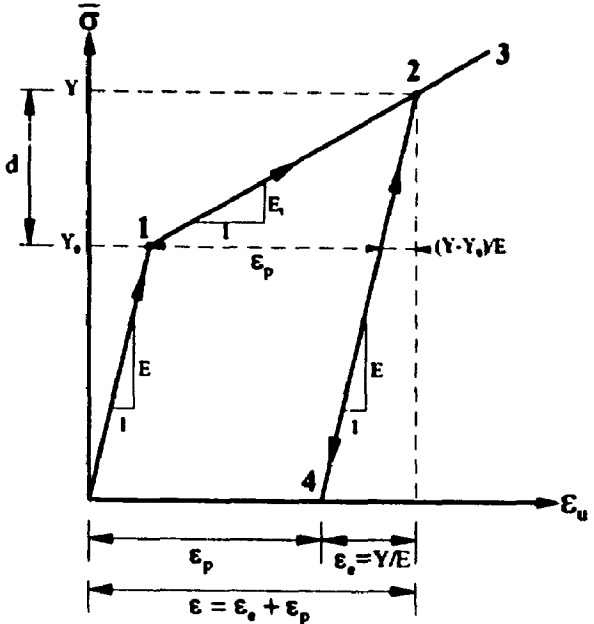

Figure 3.3c. Bi-Linear Uniaxial Stress-Strain Relationship

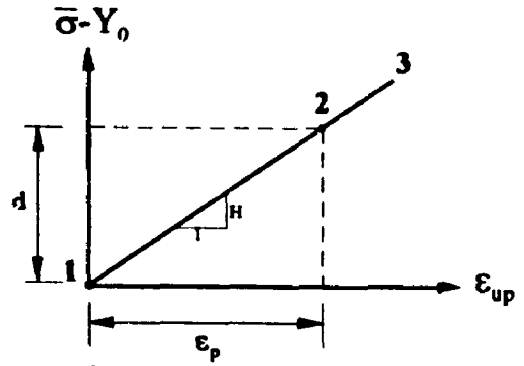

Figure 3.3d. Bi-Linear Plastic Uniaxial Strain versus Increase in Yield Stress

Figure 3.3. Uniaxial Stress-Strain Relationships

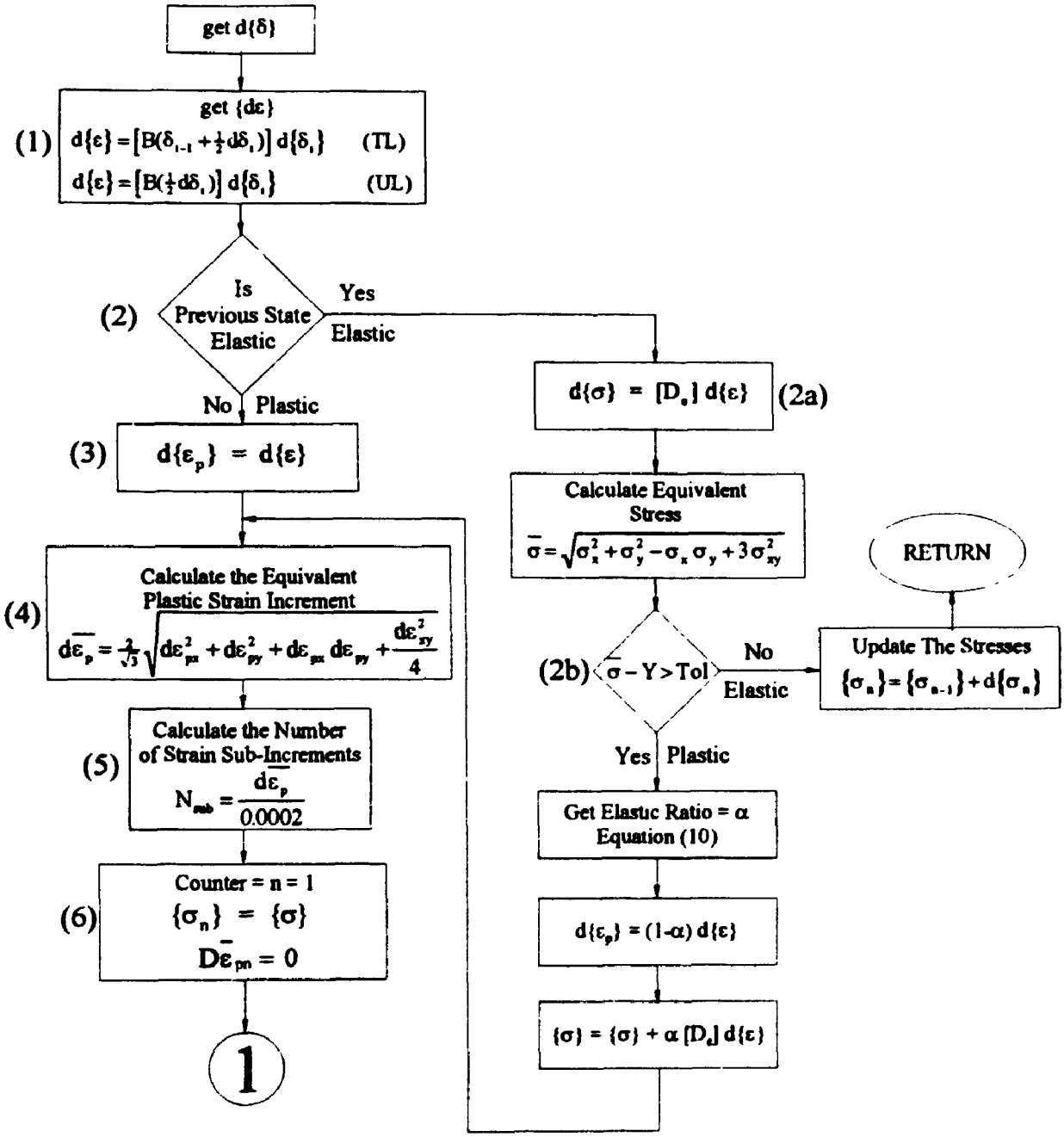

Figure 3.4a. Flow Chart for the Calculation of Stress Increment (Part a)

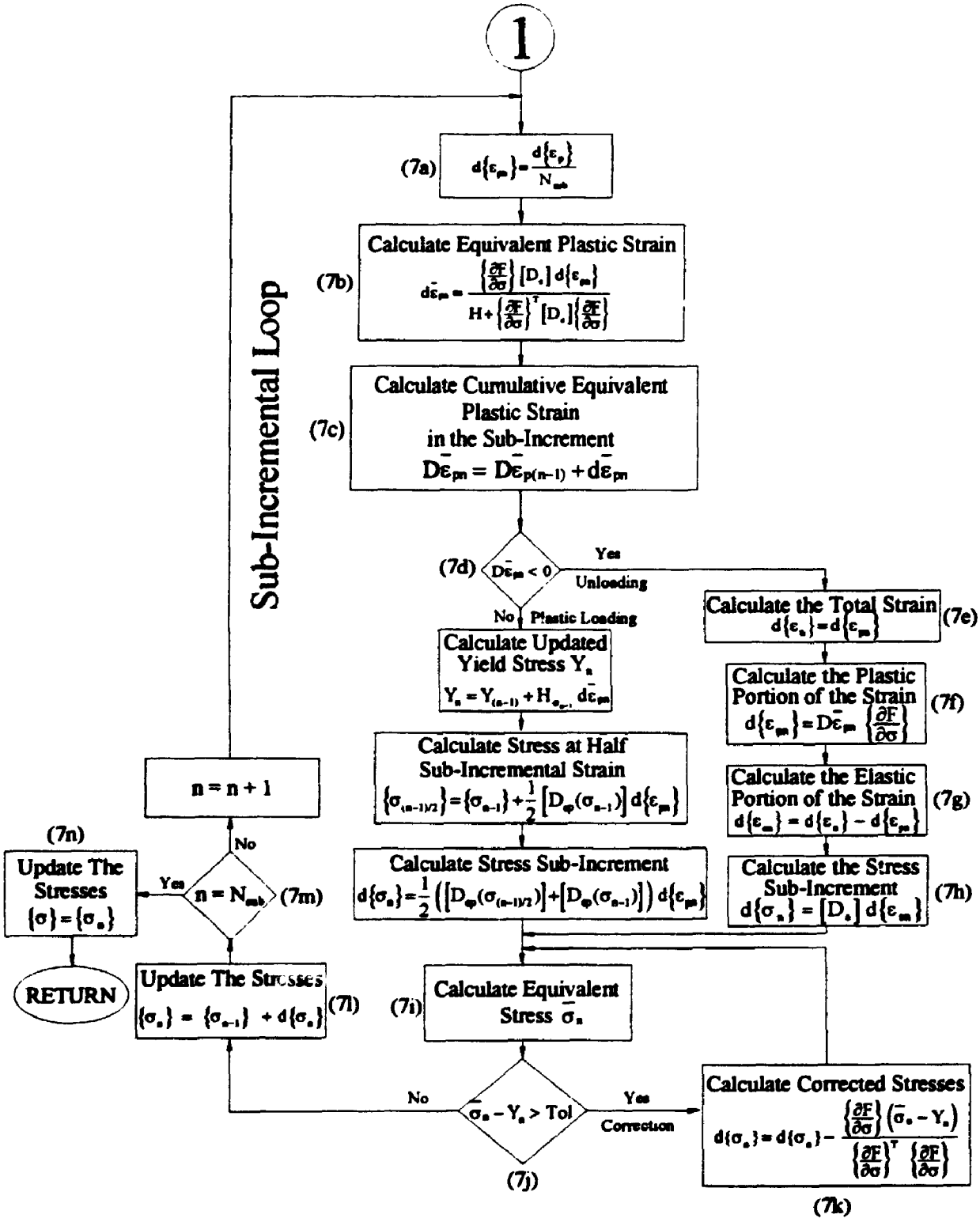

Figure 3.4b. Flow Chart for the Calculation of Stress Increment (Part b)

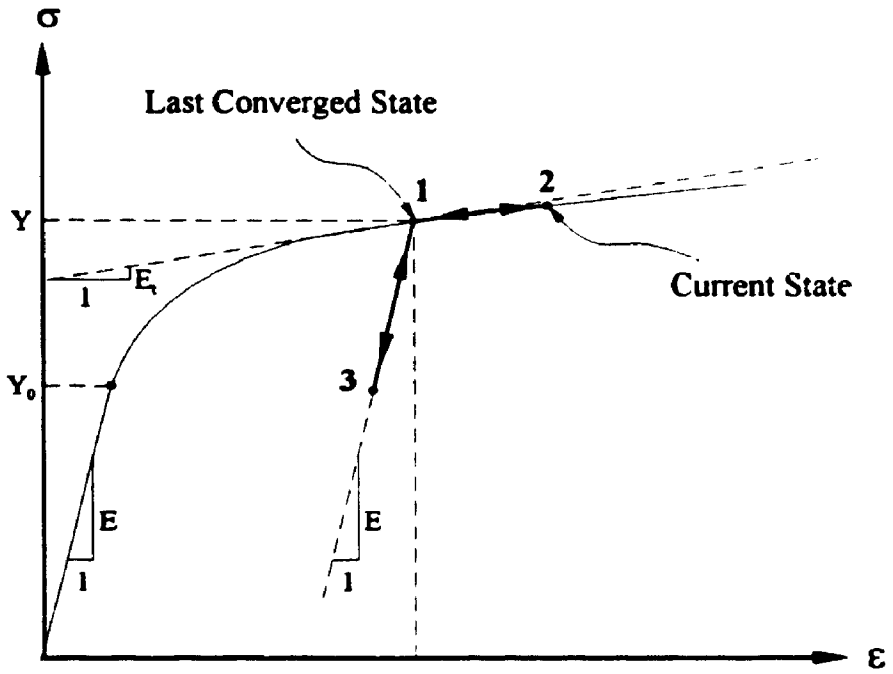

Figure 3.5. Stress-Strain Curve and Incremental Plastic Strain Reversibility Assumption

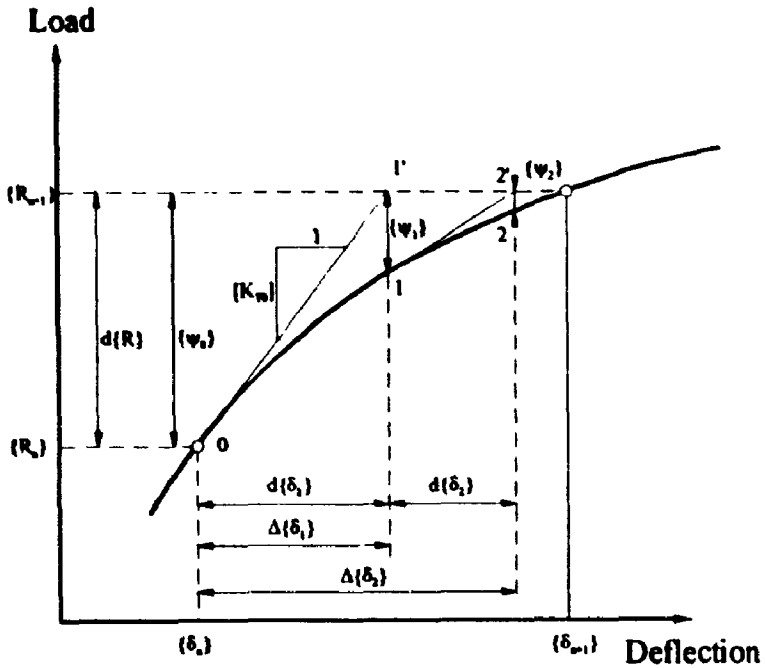

Figure 3.6a. Newton-Raphson Method

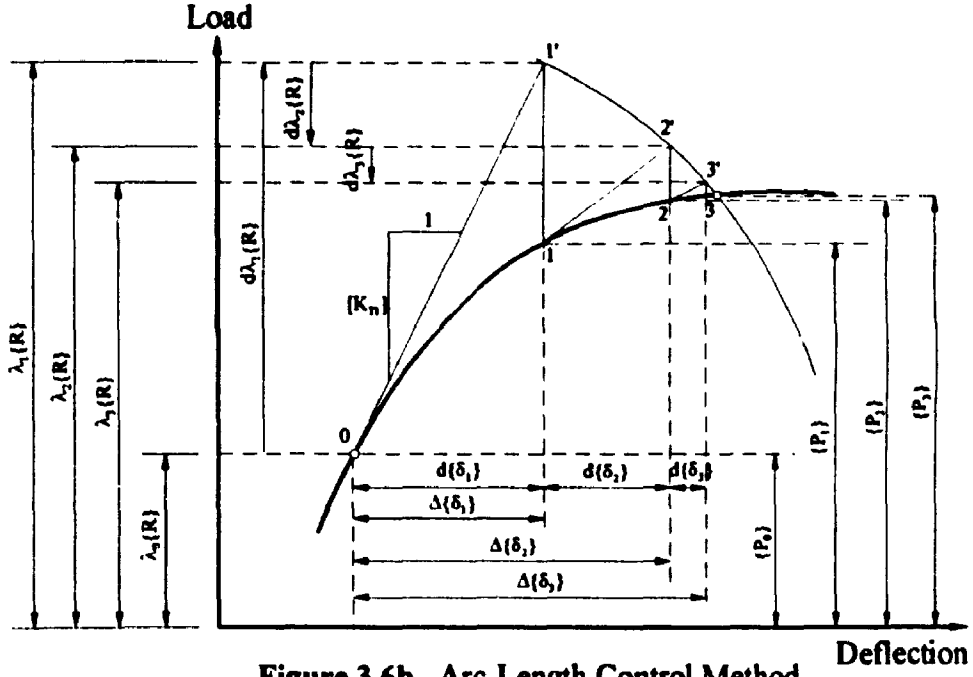

Figure 3.6b. Arc-Length Control Method

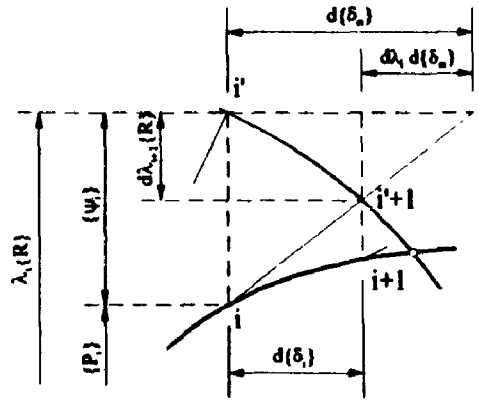

Figure 3.6c. Details of Arc-Length Control Method

Figure 3.6. Details of the Newton Raphson and the Arc-Length Control Methods

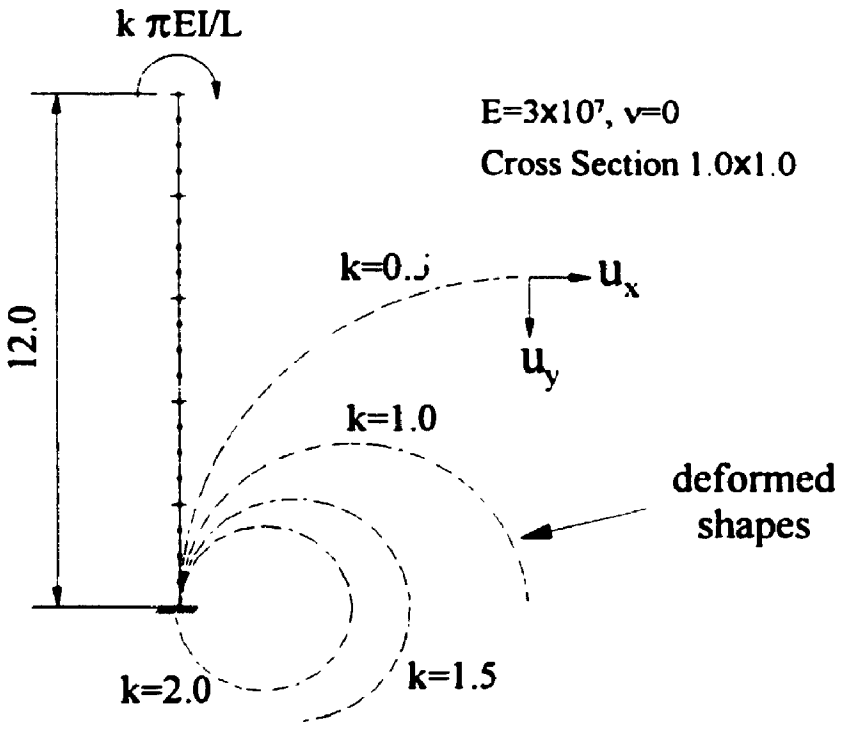

Figure 3.7. Cantilever Subjected to an End Moment

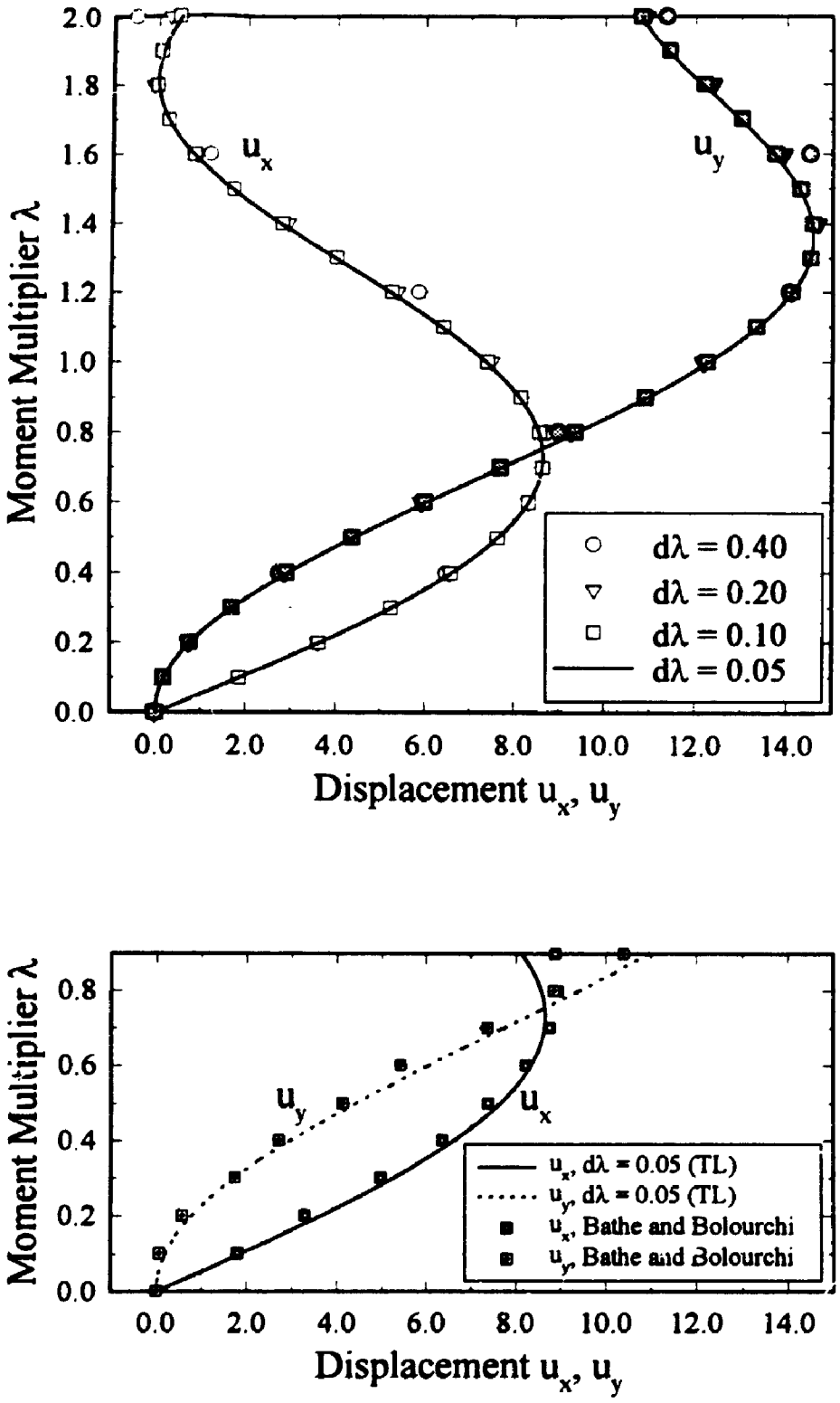

Figure 5.8. Total Lagrangian Analysis Results For a Cantilever Subjected to an End Moment

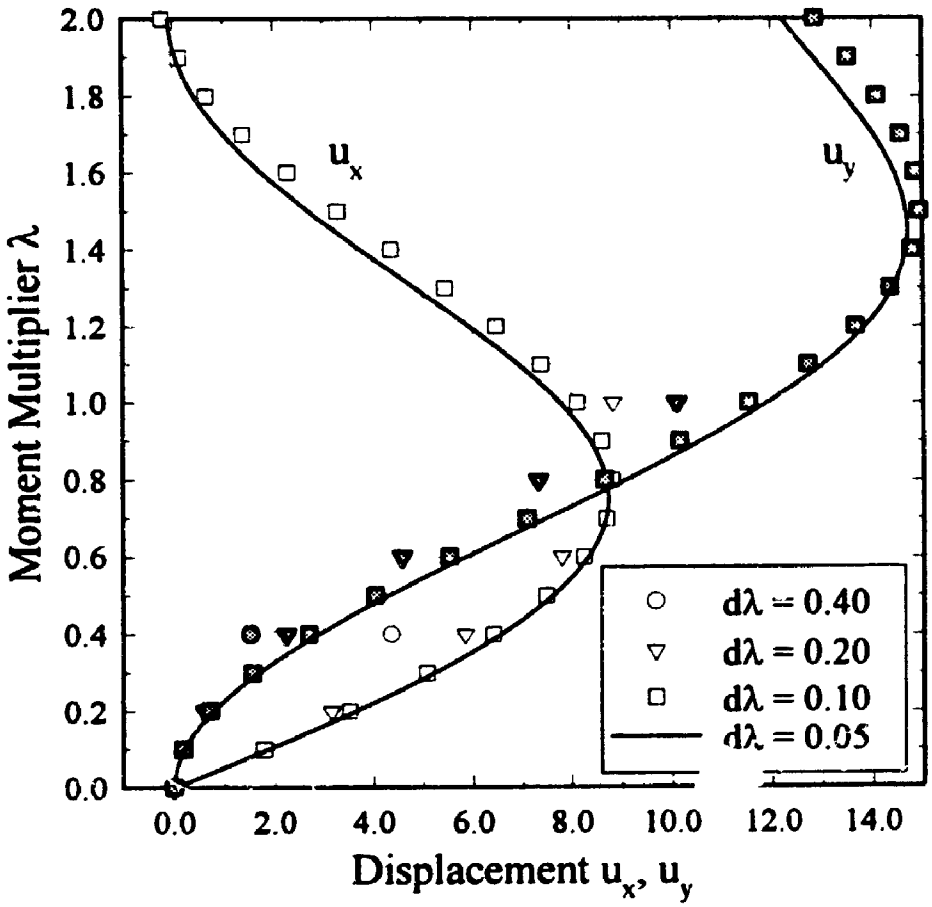

Figure 3.9. Updated Lagrangian Analysis Results For a Cantilever Subjected to an End Moment

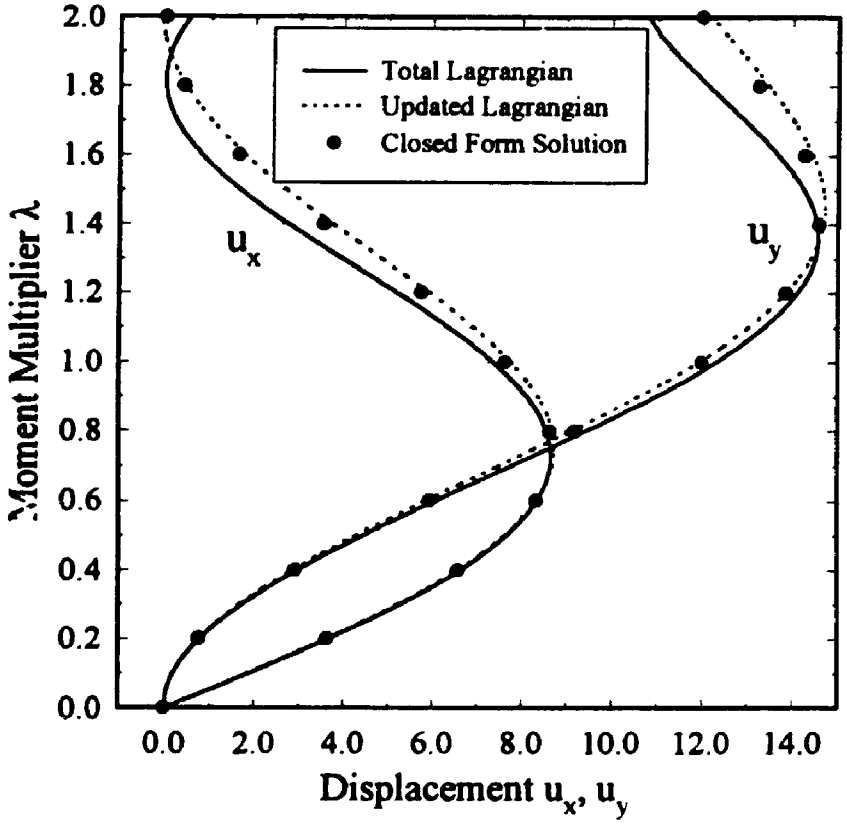

Figure 3.10. Total Lagrangian Analysis Results vs. Updated Lagrangian Analysis For a Cantilever Subjected to an End Moment

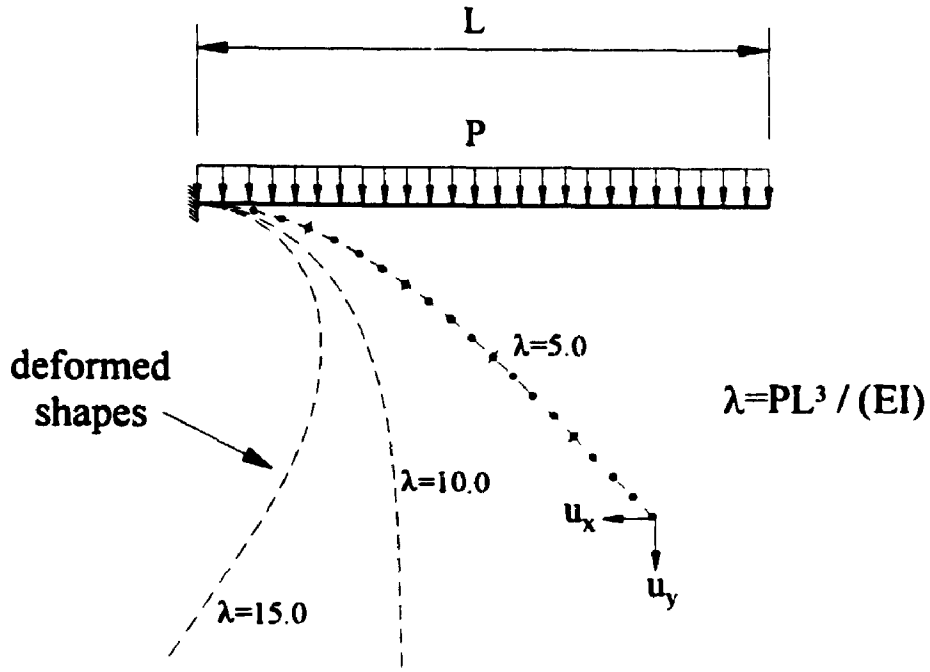

Figure 3.11. Cantilever Subjected to a Uniform Follower Traction

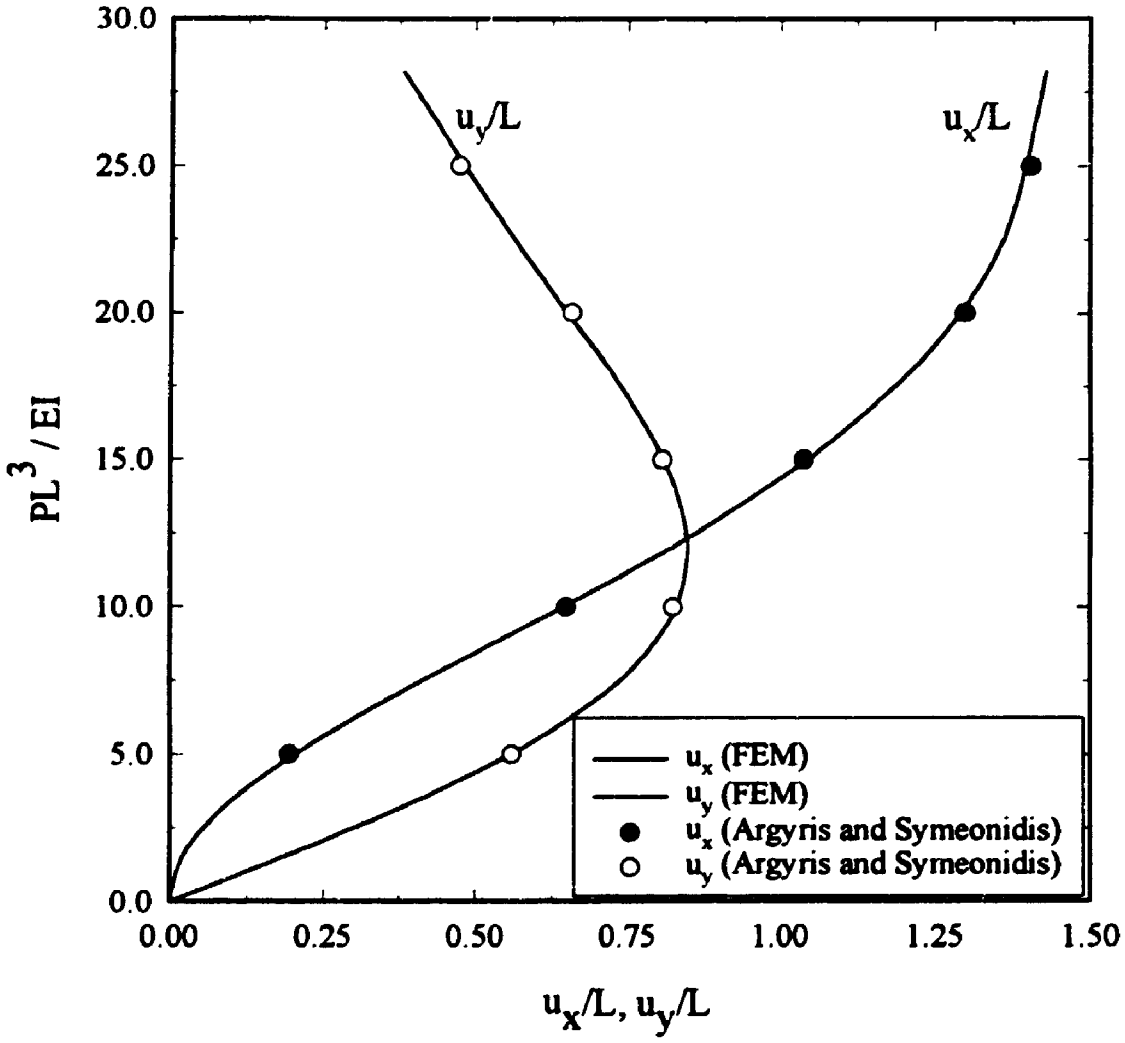

Figure 3.12. Displacement of a Cantilever Tip Subjected to a Uniform Follower Traction

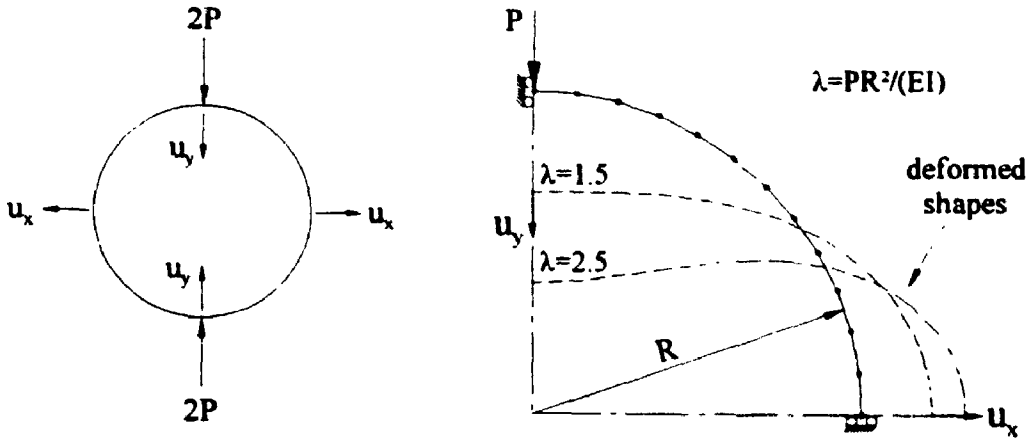

Figure 3.13a. Ring Subjected to Two End Loads
Modelled by six *3*-noded Curved Line Elements

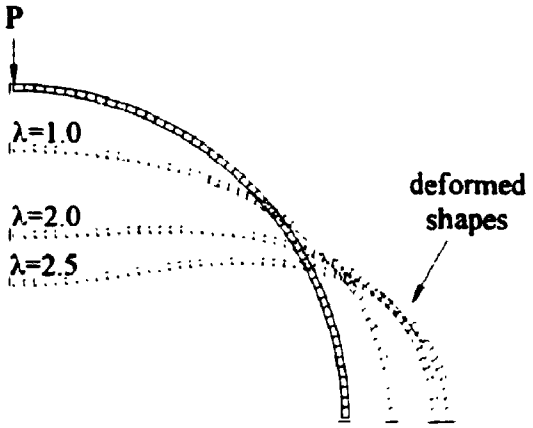

Figure 3.13b. Ring Subjected to Two End Loads
Modelled by Fifty *8*-noded Rectangular Elements

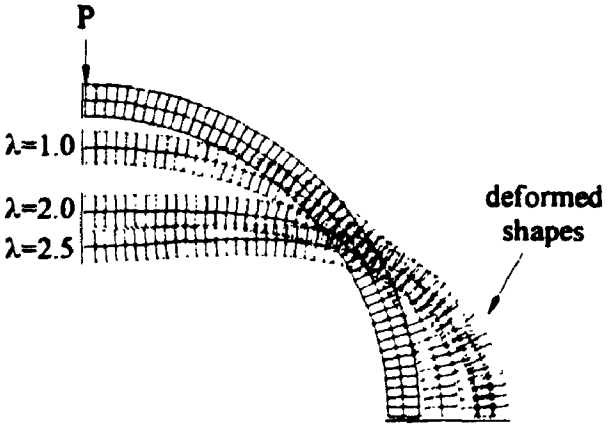

Figure 3.13c. Ring Subjected to Two End Loads
Modelled by One Hundred *8*-noded Rectangular Elements

Figure 3.13. Deformation of a Ring Subjected to Two End Loads

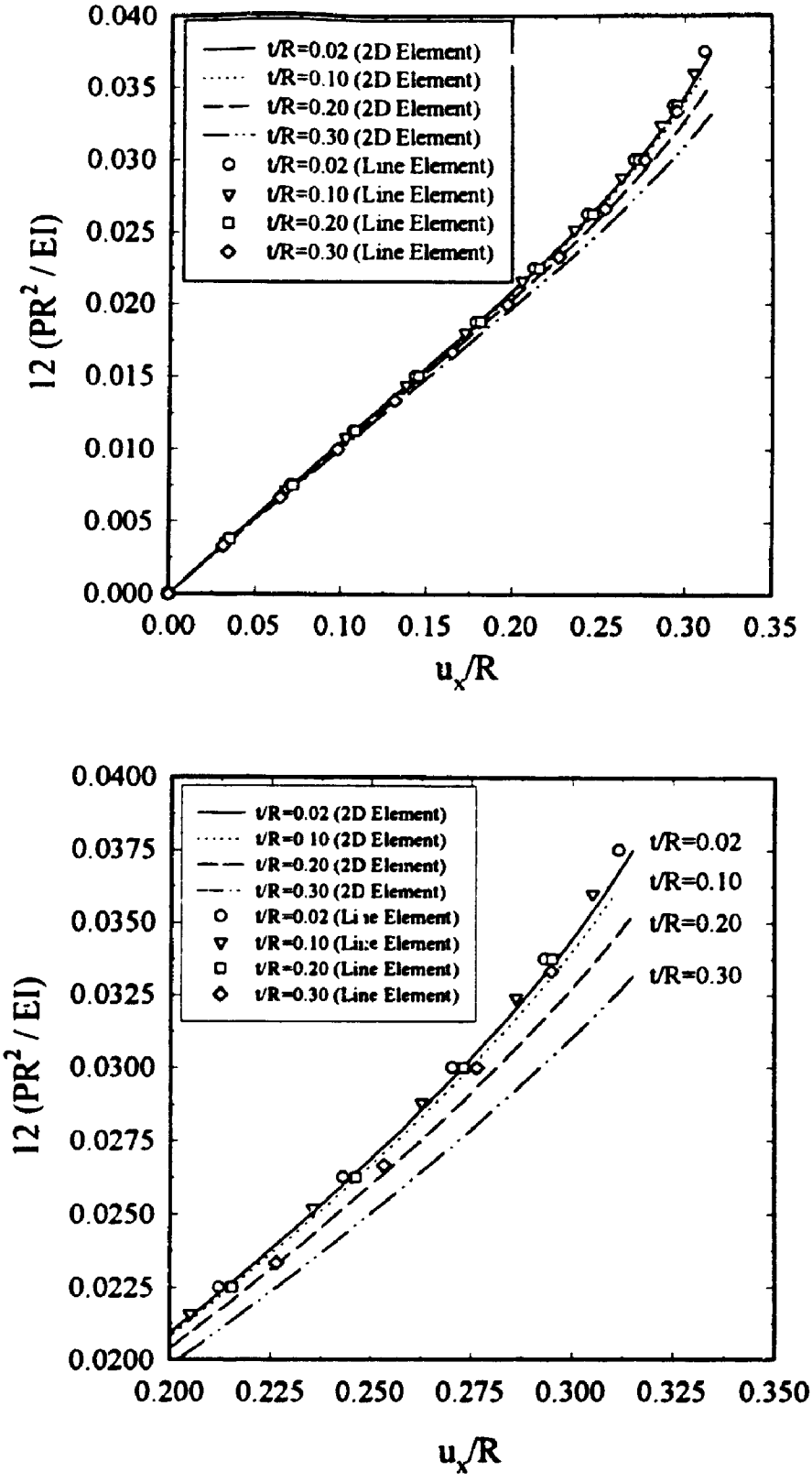

Figure 3.14. Horizontal Displacement for the Ring Problem Using 2-D Elements and Line Curved Elements

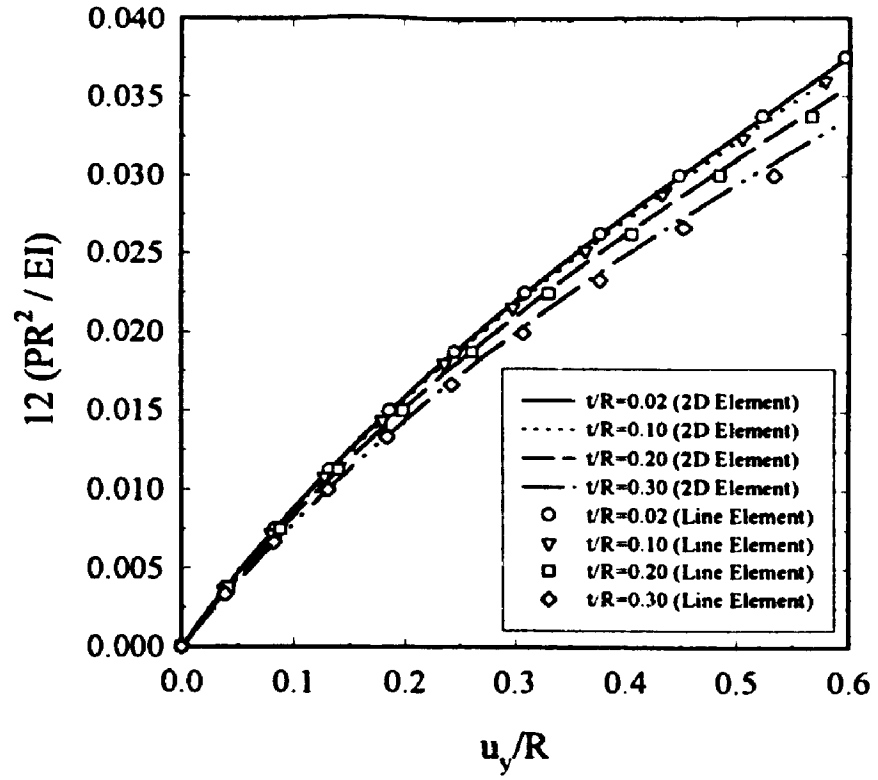

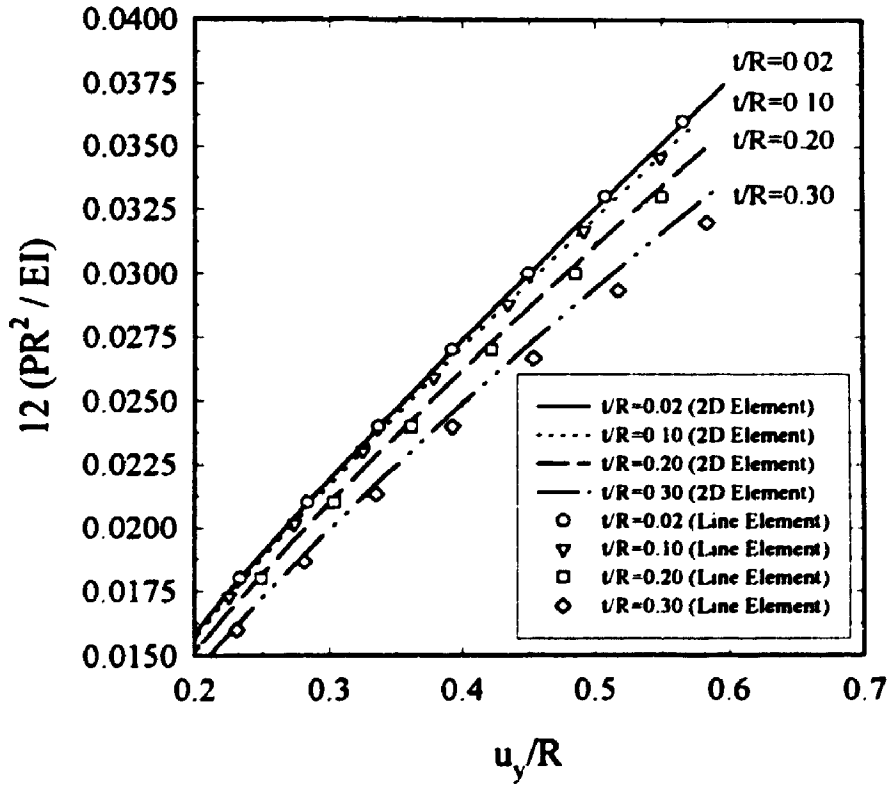

Figure 3.15. Vertical Displacement for the Ring Problem Using 2-D Elements and Line Curved Elements

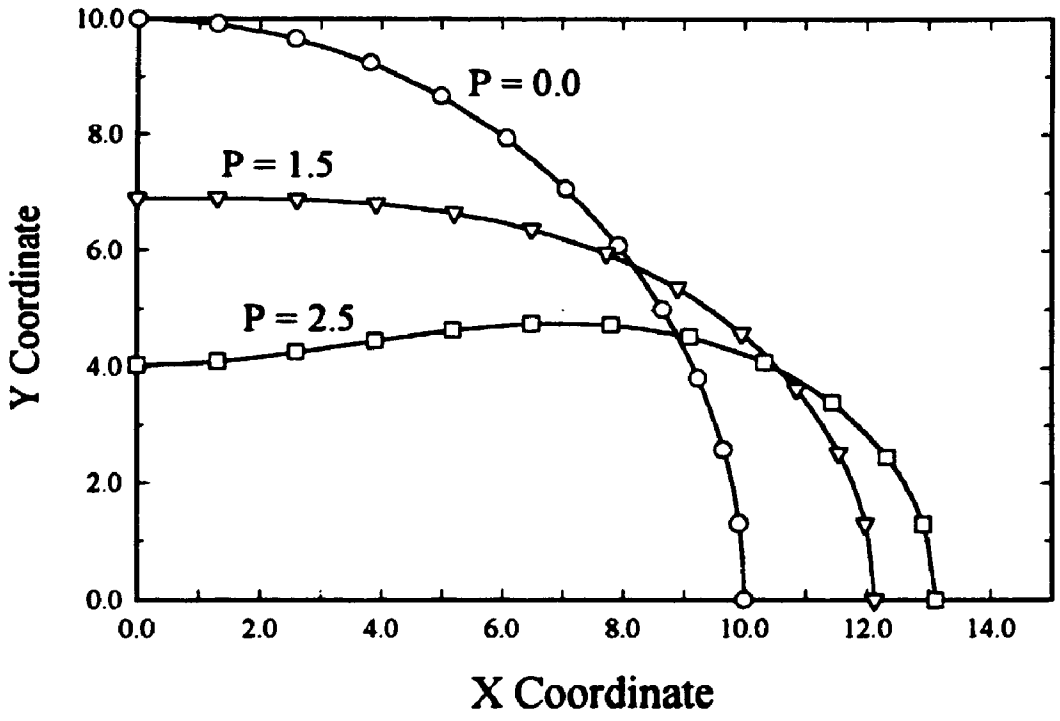

Figure 3.16. Deformed Shape of the Ring Quadrant Under Different Loads (t/R=0.02)

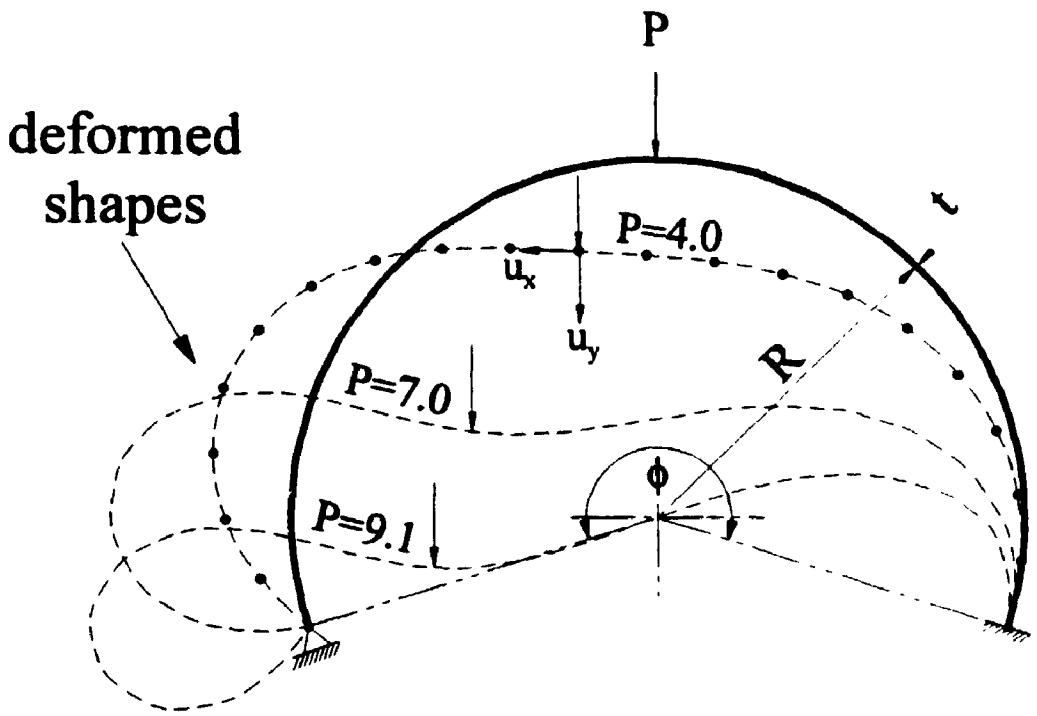

Figure 3.17. Clamped-Hinged Arch Subjected to a Point Load
R=100.0, ϕ=215°, t=1.0, EI=10^6

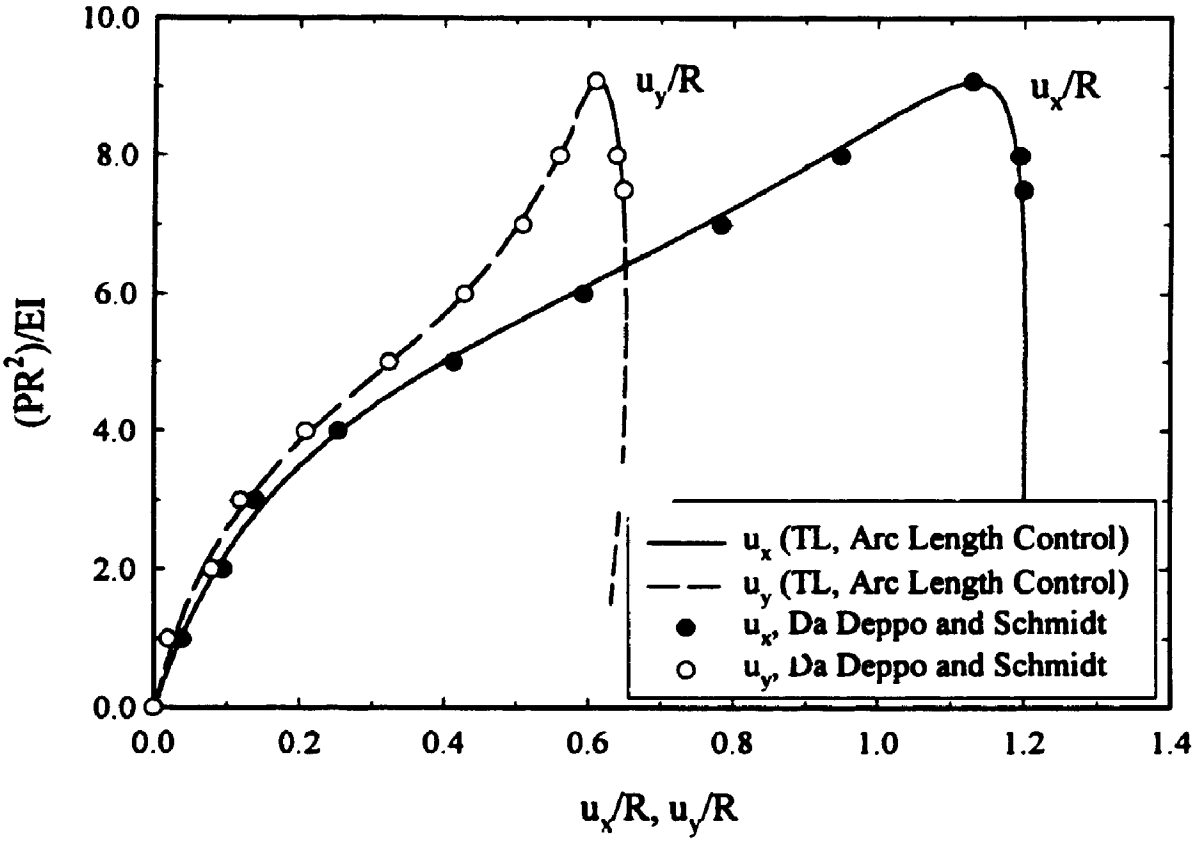

Figure 3.18. Response of a Clamped-Hinged Arch Subjected to a Point Load

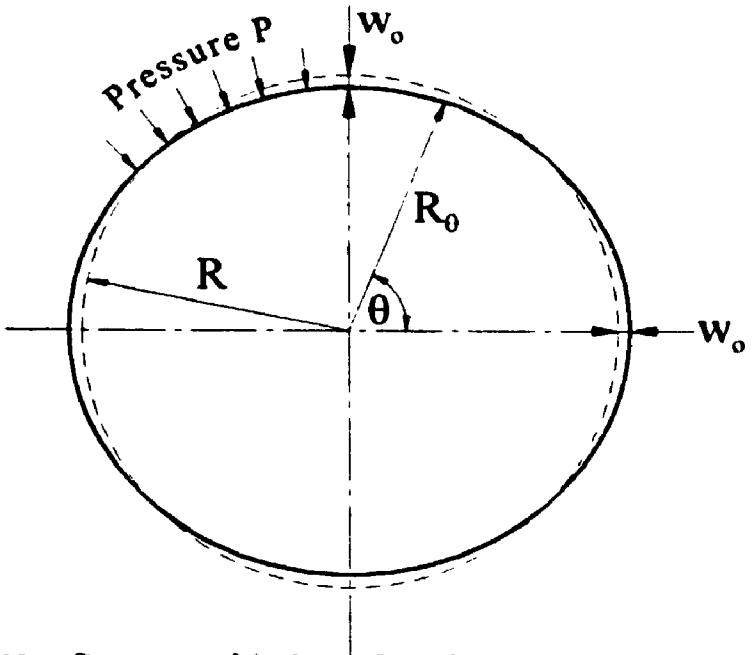

Figure 3.19a. Geometry of the Imperfect Ring Subjected to a Pressure Load

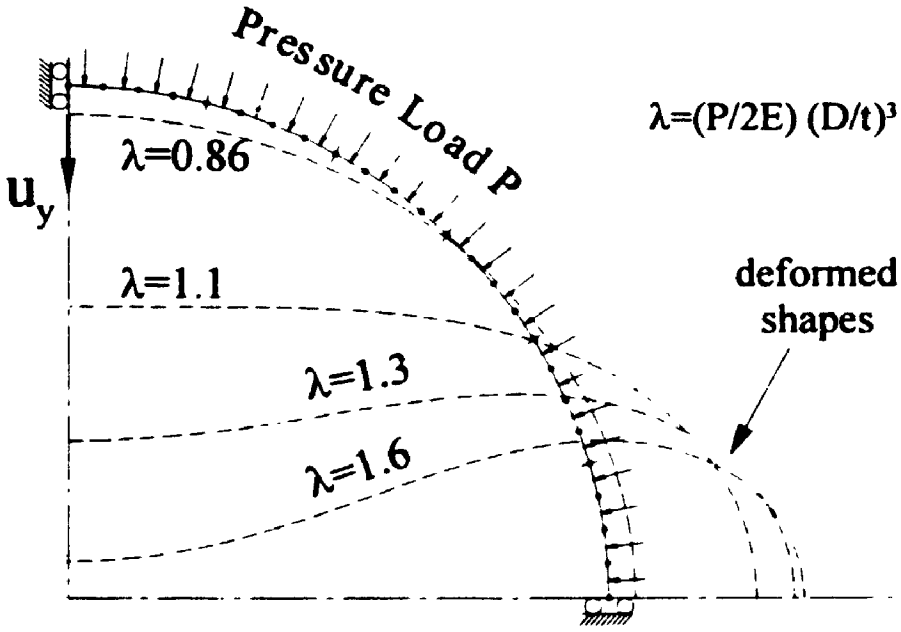

Figure 3.19b. Deformed Shape for an Imperfect Ring Subjected to a Pressure Load ($E/E_t=1$)

Figure 3.19. Geometry and Deformed Shape for an Imperfect Ring Subjected to a Pressure Load ($E/E_t=1$)

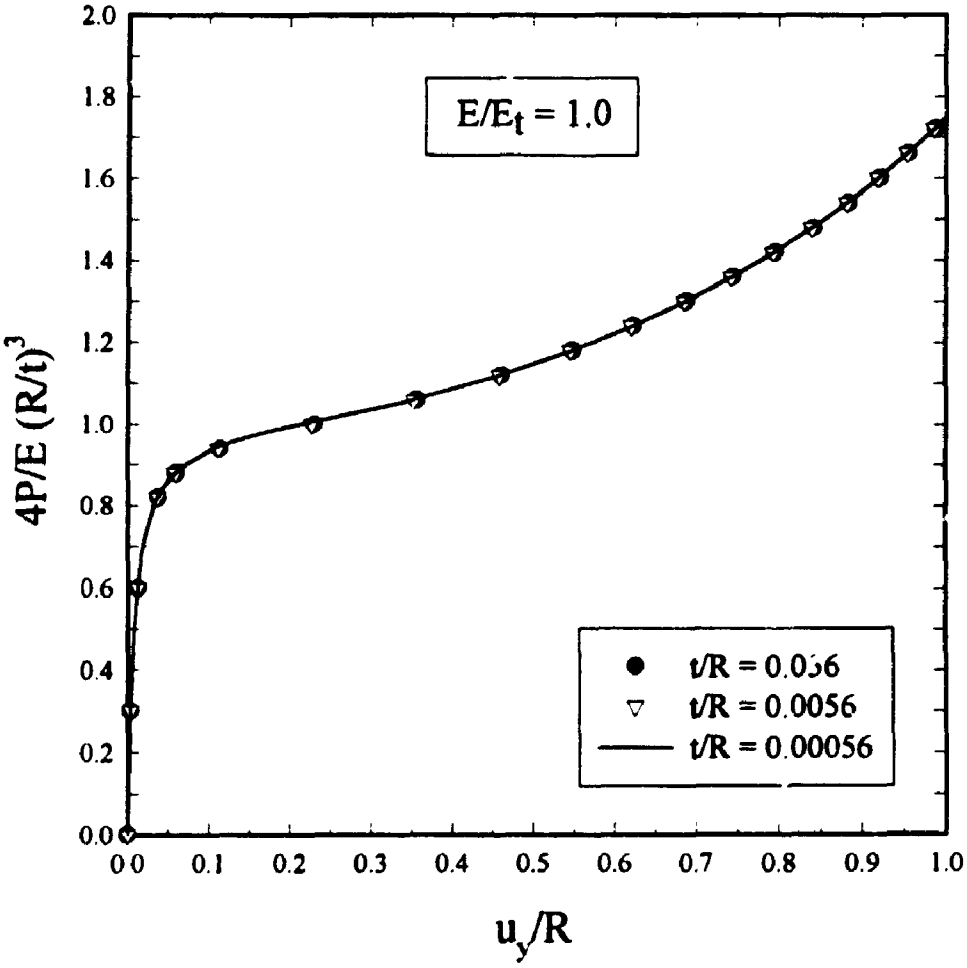

Figure 3.20. Response of a Ring Under Pressure for Different (t/R) Ratios

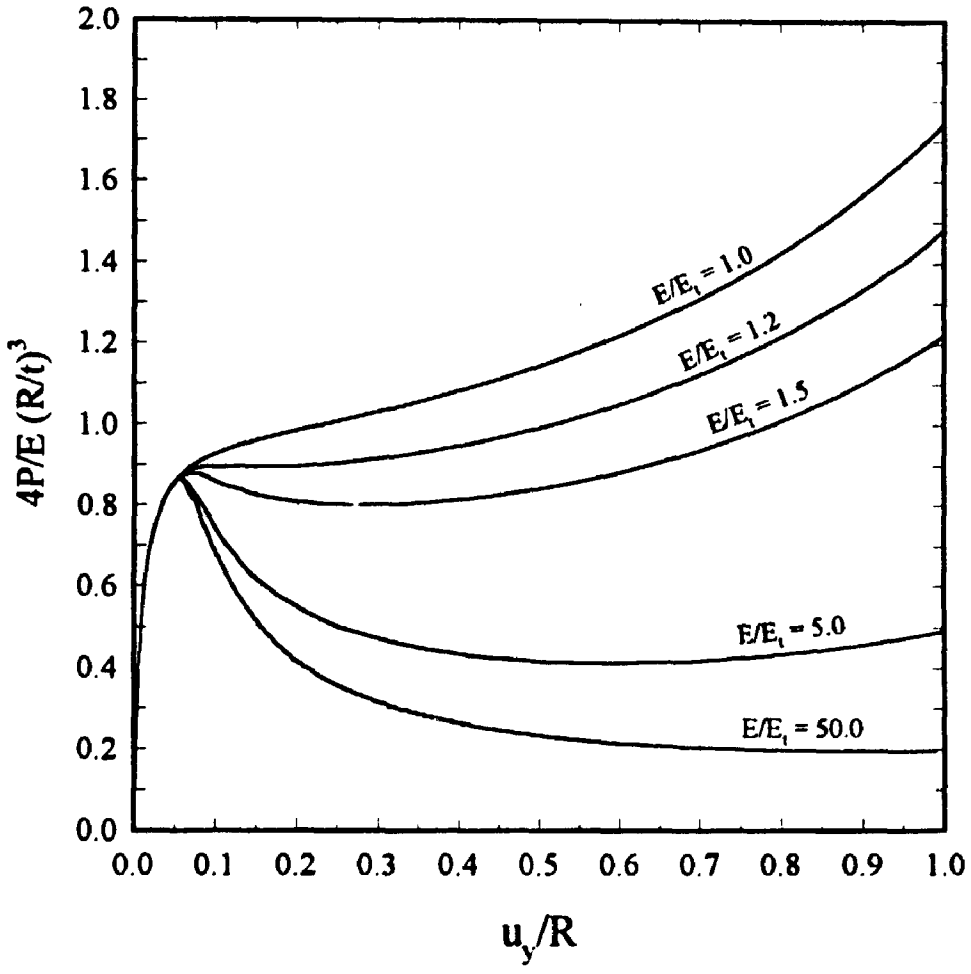

Figure 3.21. Variation of Post-Buckling Behaviour with Strain Hardening ratio E/E_t

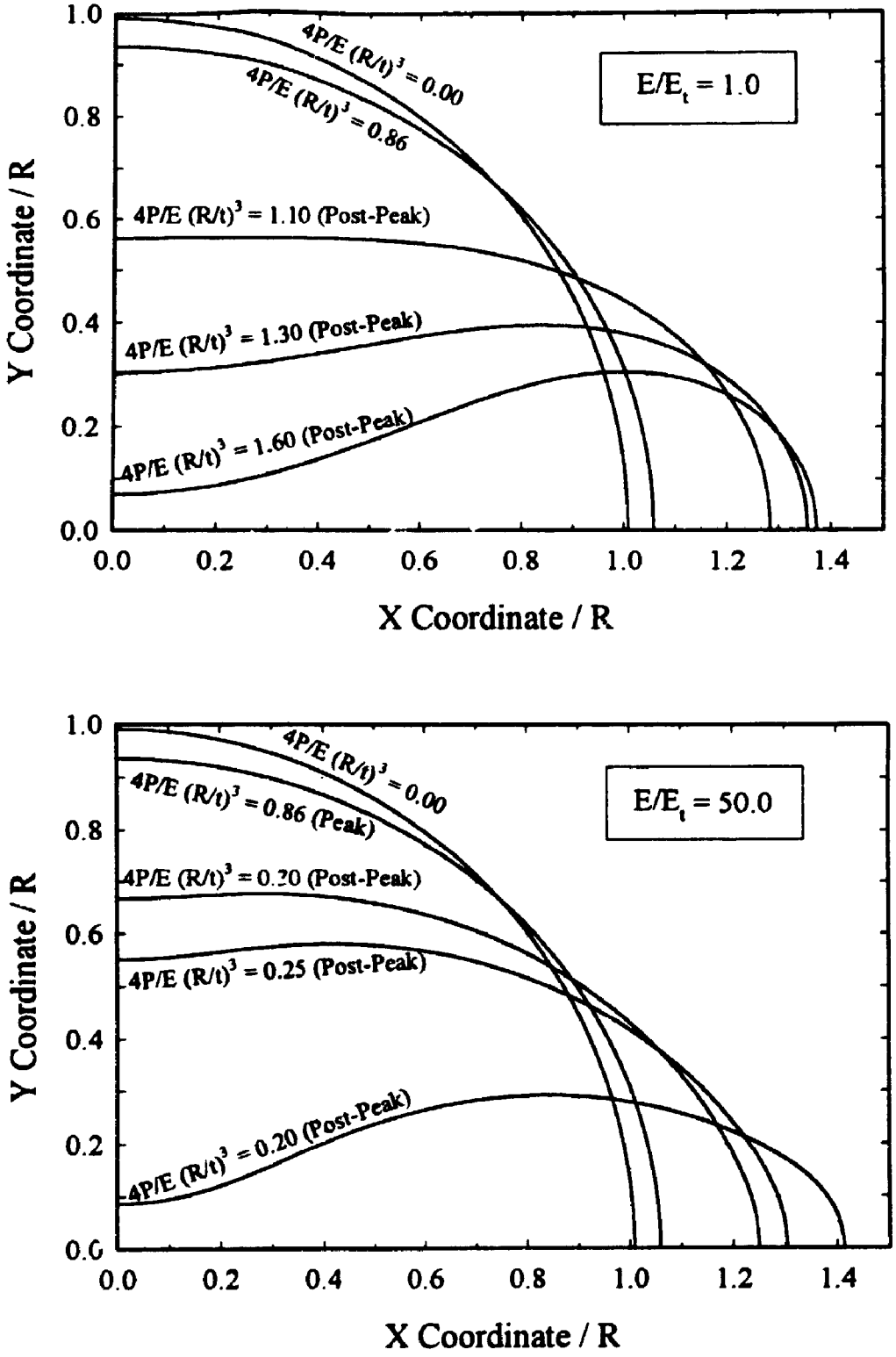

Figure 3.22. Deformed Shape of the Imperfect Ring at Different Load Levels (E/E_t=1.0, 50.0)

CHAPTER FOUR

A Rigorous Two-level Iterative Finite Element Technique for Non-linear Interaction Problems

4.1. Introduction

Various problems arising in applied mechanics involve interaction between two bodies having separation, bonding, re-bonding and slip at the interface. Simple finite element models assume one of the two extremes, *bonded interface* or *smooth interface*. Alternatively, the two interacting bodies are modelled individually and surface contact kinematic conditions are enforced by prescribing displacement constraints to prevent each body from penetrating the other. Surface contact also involves contact force conditions. Typically these conditions are a *no tension* limit condition for interface normal forces and a *frictional* limit condition for interface tangential forces.

Lagrange multiplier methods and penalty function methods are the two most commonly used approaches to enforce finite element surface contact and displacement constraints. Lagrange multiplier methods are alternatively referred to as mixed or hybrid variational method by some researchers, and penalty methods are commonly referred to as contact, gap, spring, or joint element methods.

Each of the two methods has advantages and drawbacks. The penalty approach results in solutions which only approximately satisfy the contact conditions. The accuracy of the approximate solution depends mainly on the penalty parameter which may be thought of as a spring connecting any two interacting nodal points. The correct choice of this parameter is the essence of the algorithm. It is also required for this method that the interacting bodies should have matching interface nodes and deformations should be small. In spite of this

drawback, the penalty function approach is popular because of its simplicity and the unchanged structure of the solved equations (i.e. no additional unknowns are introduced).

On the other hand, the Lagrange multiplier approach satisfies the interface constraints exactly by adding additional equations and unknowns into the system of equations to be solved. Although the solution does not suffer the approximation faced in the penalty approach, the introduction of new unknowns adds to the cost of solving the interaction problem. Moreover, the associated system of equations may have zero diagonal entries. The Lagrange multiplier method is preferred to the penalty function approach because of its applicability for large deformations and non-matching interface nodes.

The aim of this chapter is to describe the rigorous formulation used for solving the liner interaction problem subjected to large deformations. The rigorous solution for these problems is straightforward and does not sacrifice the simplicity of the FEM approach. In this study the deformations are assumed to be large enough to change the geometry of the problem and the interface is assumed to be a frictional adhesive one with a *Coulomb* failure criterion. The technique examines the interaction of two bodies, namely the *Slave* and *Master* bodies. It simulates frictional slip, separation, bonding and re-bonding of the slave body with respect to the master body allowing for large deformations and non-matching nodes at the interface. The proposed solution uses two levels of iterations. The first iteration is used to satisfy equilibrium and to deal with the geometrical non-linearity, while the second is used to satisfy the interaction conditions at the interface. The proposed technique is illustrated with a number of test problems of varying complexity. These demonstrate that the approach performs well for problems involving interaction of two bodies under large

deformations.

4.2. Definition of the Problem

The problem of interaction between two bodies subjected to large deformations is a challenging one. Where deformations are small, the assumption of "node to node" interaction (Fig. 4.1a) is valid and the solution is straight forward while in the case of large deformations the *node to surface* interaction (Fig. 4.1b) or *surface to surface* interaction [5] has to be modelled which makes the problem more difficult. In this study, the choice of *node to surface* interaction is made because it is more appropriate and general. Furthermore, interface behaviour, such as separation, bonding, re-bonding, and slippage, must be modelled.

A simple rigorous approach to solve these problems is developed. This work is an extension of Katona's formulation for the case of small deformations [24]. The features of the rigorous approach are its simplicity and compatibility with FEM solution subroutines. It also avoids the calculation of flexibility matrices for the interacting bodies and the associated problem of rigid body movement [26].

The two interacting bodies are named the *master* and the *slave* bodies. Each body is discretized using nodes and isoparametric elements. The master interface is discretized into a series of interface elements. Each interface element is defined by its nodal connectivity. The order of these nodes is chosen to define the correct outward normal to the master interface. The "node to surface" contact is identified by a *slave node*, S, and a *master interface element*. The projection of the slave node, S, on the master interface is defined by point, S^*. The angle between the outward normal to the master interface at point S^* and the

X-axis is denoted θ and its positive direction is anticlockwise. The displacements in the global X-Y directions are denoted u_x and u_y while the displacements in the local normal and tangential directions are denoted u_n and u_t. Figure 4.2 shows an m-noded master interface element, a slave node, S, and the two coordinate systems.

The relationships between the incremental Cartesian displacements, Δu_x and Δu_y, and the incremental normal and tangential displacements, Δu_n and Δu_t, are as follows

$$\begin{Bmatrix} \Delta u_n \\ \Delta u_t \end{Bmatrix} = \begin{bmatrix} C & S \\ -S & C \end{bmatrix} \begin{Bmatrix} \Delta u_x \\ \Delta u_y \end{Bmatrix} \tag{4.1}$$

$$\begin{Bmatrix} \Delta u_x \\ \Delta u_y \end{Bmatrix} = \begin{bmatrix} C & -S \\ S & C \end{bmatrix} \begin{Bmatrix} \Delta u_n \\ \Delta u_t \end{Bmatrix} \tag{4.2}$$

where $S = \sin(\theta)$ and $C = \cos(\theta)$.

Some relations can also be developed between incremental displacements at the slave node projection, S^*, on an m-noded master interface element defined by m nodes and the incremental displacements at these nodes.

$$\begin{Bmatrix} \Delta u_{xS^*} \\ \Delta u_{yS^*} \end{Bmatrix} = \begin{bmatrix} N_1 & 0 & \cdots & \cdots & N_m & 0 \\ 0 & N_1 & \cdots & \cdots & 0 & N_m \end{bmatrix} \begin{Bmatrix} \Delta u_{x1} \\ \Delta u_{y1} \\ \vdots \\ \vdots \\ \Delta u_{xm} \\ \Delta u_{ym} \end{Bmatrix} \tag{4.3}$$

$$\begin{Bmatrix} \Delta u_{nS^*} \\ \Delta u_{tS^*} \end{Bmatrix} = \begin{bmatrix} CN_1 & SN_1 & \cdots & \cdots & CN_m & SN_m \\ -SN_1 & CN_1 & \cdots & \cdots & -SN_m & CN_m \end{bmatrix} \begin{Bmatrix} \Delta u_{x1} \\ \Delta u_{y1} \\ \vdots \\ \vdots \\ \Delta u_{xm} \\ \Delta u_{ym} \end{Bmatrix} \tag{4.4}$$

where N_1 to N_m are the master interface element shape functions defined at point S^*.

4.3. Governing Equations for the Two Interacting Bodies

The stiffness equations for the two interacting bodies are available using conventional techniques and can be written as

$$\left\{ \begin{Bmatrix} 0 \\ \Delta F_{si} \end{Bmatrix} \right\} + \left\{ \begin{Bmatrix} \Delta R_s \\ \Delta R_{si} \end{Bmatrix} \right\} = \begin{bmatrix} K_s & 0 \\ 0 & K_m \end{bmatrix} \left\{ \begin{Bmatrix} \Delta U_s \\ \Delta U_{si} \end{Bmatrix} \right\} \tag{4.5}$$

$$\left\{ \begin{Bmatrix} 0 \\ \Delta F_{mi} \end{Bmatrix} \right\} \qquad \left\{ \begin{Bmatrix} \Delta R_m \\ \Delta R_{mi} \end{Bmatrix} \right\} \qquad \begin{bmatrix} K_s & 0 \\ 0 & K_m \end{bmatrix} \qquad \left\{ \begin{Bmatrix} \Delta U_m \\ \Delta U_{mi} \end{Bmatrix} \right\}$$

where

$\Delta R_m, \Delta U_m$ are the master body incremental applied forces and displacements at non-interfacial nodes

$\Delta R_s, \Delta U_s$ are the slave body incremental applied forces and displacements at non-interfacial nodes

$\Delta R_{mi}, \Delta U_{mi}$ are the master body incremental applied forces and displacements at the interface nodes

$\Delta R_{si}, \Delta U_{si}$ are the slave body incremental applied forces and displacements at the interface nodes

ΔF_{mi} are the master body incremental interaction forces at the interface nodes

ΔF_{si} are the slave body incremental interaction forces at the interface nodes

K_m is the tangent stiffness matrix of the master body

K_s is the tangent stiffness matrix of the slave body

There are unknowns on both sides of the equation. On the left hand side there are the unknown incremental interaction forces, ΔF_{mi} and ΔF_{si}, while all the displacements shown on the right hand side are unknown. To solve this problem, extra constraint equations relating the two bodies' incremental displacements and incremental interaction forces will be developed to augment Eqn. 4.5.

4.4. The Condensation of the Stiffness Matrices to the Interface

As the solution of the interaction problem is iterative, Eqn. 4.5 is condensed firstly to remove the degrees of freedom which are not concerned with the interaction problem and secondly to reduce the computational effort. The condensed stiffness equations can be written as

$$\begin{Bmatrix} \Delta F_{si} \\ \Delta F_{mi} \end{Bmatrix} + \begin{Bmatrix} \Delta P_{si} \\ \Delta P_{mi} \end{Bmatrix} = \begin{bmatrix} K_{si} & 0 \\ 0 & K_{mi} \end{bmatrix} \begin{Bmatrix} \Delta U_{si} \\ \Delta U_{mi} \end{Bmatrix} \tag{4.6}$$

where

ΔP_{mi} are the condensed incremental applied forces at the master body interface nodes

ΔP_{si} are the condensed incremental applied forces at the slave body interface nodes

K_{mt} is the condensed tangent stiffness matrix of the master body

K_{st} is the condensed tangent stiffness matrix of the slave body

All the rotational degrees of freedom are condensed as the interaction problem concerns constraints on the nodal translations.

4.5. Two-level Iteration Technique

Before proceeding, it is useful to discuss the solution technique employed. As in many non-linear Finite Element analyses, the load is applied in small increments (or steps) while iterations are performed to satisfy the equilibrium of the two bodies. In this study, these equilibrium iterations are called the *Major Iterations*. This major iteration deals with any material or geometrical non-linearities.

A second iteration loop is also introduced into the interaction analysis. These iterations are designated the *Minor Iterations*. Within the minor iteration loop a mode of interaction at each slave interface node is assumed, the constraint equations are formulated and a trial solution is obtained. A check for the validity of the assumed modes determines whether another trial is required.

4.6. Application Of The Constraint Equations To The Governing Equations

As in small deformation analysis featuring node to node interaction, the constraint equations either impose displacement compatibility or force equilibrium. The same concept applies for large deformation analysis involving node to surface interaction. Compatibility and equilibrium equations are derived for each slave interface node, S, and the m-noded

master interface element with which it interacts. The displacement compatibility constraint equations at the *i*th minor iteration take the following form.

$$\{f_1\}_{2\times 1} = [[a] \mid [b] \mid [d]]_{2\times(4+2m)} \begin{Bmatrix} \Delta u'_{xS} \\ \Delta u'_{yS} \\ \text{----} \\ \Delta u'_{x_1} \\ \Delta u'_{y_1} \\ \vdots \\ \vdots \\ \Delta u'_{x_m} \\ \Delta u'_{y_m} \\ \text{----} \\ \Delta F'_{nS} \\ \Delta F'_{tS} \end{Bmatrix}_{(4+2m)\times 1} \tag{4.7}$$

To impose force equilibrium, constraint equations are developed for the *i*th minor iteration.

$$-\begin{Bmatrix} \Delta F'_{xS} \\ \Delta F'_{yS} \\ \text{----} \\ \Delta F'_{x_1} \\ \Delta F'_{y_1} \\ \vdots \\ \vdots \\ \Delta F'_{x_m} \\ \Delta F'_{y_m} \end{Bmatrix}_{(2+2m)\times 1} = \begin{bmatrix} [a]^T \\ \text{----} \\ [b]^T \end{bmatrix}_{(2+2m)\times 2} \begin{Bmatrix} \Delta F'_{nS} \\ \Delta F'_{tS} \end{Bmatrix}_{2\times 1} \tag{4.8}$$

where

Δu^{t}_{xS} is the incremental slave node displacement in the X direction

Δu^{t}_{yS} is the incremental slave node displacement in the Y direction

Δu^{t}_{xm} is the incremental displacement of the *m*th node of the master element in the X direction

Δu^{t}_{ym} is the incremental displacement of the *m*th node of the master element in the Y direction

ΔF^{t}_{nS} is the incremental slave node force normal to the master surface

ΔF^{t}_{tS} is the incremental slave node force tangential to the master surface

ΔF^{t}_{xS} is the incremental slave node force in the X direction

ΔF^{t}_{yS} is the incremental slave node force in the Y direction

$\Delta F^{t}_{x\,m}$ is the incremental force in the X direction for the *m*th node of the master element

$\Delta F^{t}_{y\,m}$ is the incremental force in the Y direction for the *m*th node of the master element

a,b,d are constraint matrix sub-matrices

f_1 is a constant vector

Equation 4.7 is calculated for each slave node and added to the governing system of equations (Eqn. 4.6). Each side of Eqn. 4.8 is added to the corresponding side of Eqn. 4.6 to eliminate the unknown incremental interaction forces.

The new system of equations is written as

$$\begin{Bmatrix} \Delta P_{si} \\ \Delta P_{mi} \\ 0 \end{Bmatrix} + \{F\} = \begin{bmatrix} K_{si} & 0 & A^T \\ 0 & K_{mi} & B^T \\ A & B & D \end{bmatrix} \begin{Bmatrix} \Delta U_{si} \\ \Delta U_{mi} \\ \begin{Bmatrix} \Delta F_{ns} \\ \Delta F_{ts} \end{Bmatrix} \end{Bmatrix} \tag{4.9}$$

where

F are additional load vectors

A,B,D are constraint matrices depending on the modes of interaction

ΔF_{ns} are incremental normal interaction forces at the slave interface nodes

ΔF_{ts} are incremental tangential interaction forces at the slave interface nodes

This places all the unknowns into one side of the equation facilitating the solution. For each slave node and its interacting master interface element a constraint matrix [c] and a load vector {f} are defined. The constraint matrix is expressed as

$$[c] = \begin{bmatrix} 0 & 0 & [a]^T \\ 0 & 0 & [b]^T \\ [a] & [b] & [d] \end{bmatrix} \tag{4.10}$$

These constraint matrices and load vectors augment the system of governing equations yielding Eqn. 4.9.

4.7. Constraint Matrices and Load Vector for Different Interaction Modes

A number of different interaction conditions (or modes) are possible for the slave interface nodes. Three different conditions, namely *Free*, *Sliding* and *Fixed* modes, are

examined. For each mode, the constraint matrix [c] and load vector {f} at the slave node are derived.

Free Mode of Interaction

For this mode, the slave node, S, separates from the master interface and the "total" interaction forces diminish to zero. In other words, the applied "incremental" interaction forces at the slave node, S, at the kth major iteration and the ith minor iteration, should cancel out the "total" interaction forces at the previously converged (k-1)th major iteration. This can be expressed as

$$\begin{Bmatrix} \Delta F_{nS}^{\,i} \\ \Delta F_{tS}^{\,i} \end{Bmatrix} = \begin{Bmatrix} -F_{nS}^{k-1} \\ -F_{tS}^{k-1} \end{Bmatrix} \tag{4.11}$$

and

$$\begin{Bmatrix} \Delta F_{xS}^{\,i} \\ \Delta F_{yS}^{\,i} \end{Bmatrix} = \begin{bmatrix} C & -S \\ S & C \end{bmatrix} \begin{Bmatrix} -F_{nS}^{k-1} \\ -F_{tS}^{k-1} \end{Bmatrix} = \begin{Bmatrix} -CF_{nS}^{k-1} + SF_{tS}^{k-1} \\ -SF_{nS}^{k-1} - CF_{tS}^{k-1} \end{Bmatrix} \tag{4.12}$$

where

F_{nS}^{k-1}, F_{tS}^{k-1} are the total normal and tangential interaction forces at slave node S at the previously converged major iteration (i.e. the (k-1)th major iteration)

In Eqns. 4.11 and 4.12 superscript i stands for the ith minor iteration while superscript k-1 stands for the (k-1)th major iteration.

For this mode the slave incremental interaction forces are known *a priori* and they are used to derive the incremental interaction forces for the master interface nodes by the method of virtual work. The incremental forces at the nodes of an m-noded master interface element are the nodal forces equivalent to point loads equal and opposite to the incremental applied loads at the slave node, S, and can be given by

$$\begin{Bmatrix} \Delta F'_{x_1} \\ \Delta F'_{y_1} \\ \vdots \\ \vdots \\ \Delta F'_{x_m} \\ \Delta F'_{y_m} \end{Bmatrix} = \begin{bmatrix} N_1 & 0 \\ 0 & N_1 \\ \vdots & \vdots \\ \vdots & \vdots \\ N_m & 0 \\ 0 & N_m \end{bmatrix} \begin{Bmatrix} \Delta F_{xS}^{k-1} \\ \Delta F_{yS}^{k-1} \end{Bmatrix} = \begin{bmatrix} CN_1 & -SN_1 \\ SN_1 & CN_1 \\ \vdots & \vdots \\ \vdots & \vdots \\ CN_m & -SN_m \\ SN_m & CN_m \end{bmatrix} \begin{Bmatrix} \Delta F_{nS}^{k-1} \\ \Delta F_{tS}^{k-1} \end{Bmatrix} \tag{4.13}$$

The corresponding constraint matrix, $[c]$, and load vector, $\{f\}$, are defined in Table 4.1.

Fixed Mode of Interaction

When the slave node, S, attaches to the master interface, the displacement compatibility equation for node, S, and its projection, S^*, on the master surface element should be imposed on the governing system of equations. At the kth major iteration and ith minor iteration, the compatibility equation can be written as

$$\begin{Bmatrix} g^{k-1} \\ g^{k-1}\left(\dfrac{\Delta u_{tS^*}^{i-1} - \Delta u_{tS}^{i-1}}{\Delta u_{nS^*}^{i-1} - \Delta u_{nS}^{i-1}} \right) \end{Bmatrix} = \begin{Bmatrix} \Delta u_{nS^*}^{i} \\ \Delta u_{tS^*}^{i} \end{Bmatrix} - \begin{Bmatrix} \Delta u_{nS}^{i} \\ \Delta u_{tS}^{i} \end{Bmatrix} \tag{4.14}$$

where

g^{k-1} is the normal gap between the slave node, S, and the master surface element at the $(k-1)$th major iteration

Δu^{i}_{nS} is the incremental displacement at slave node, S, normal to the master interface at the ith minor iteration

Δu^{i}_{tS} is the incremental displacement at slave node, S, tangent to the master interface at the ith minor iteration

$\Delta u^{i}_{nS^*}$ is the incremental displacement at point S^* normal to the master interface at the ith minor iteration

$\Delta u^{i}_{tS^*}$ is the incremental displacement at point S^* tangent to the master interface at the ith minor iteration

For the tangential displacements it is assumed that the slave node S and its projection S^* are moving in the same direction as calculated in the previous minor iteration.

The terms in the right hand side of Eqn. 4.14 can be written as

$$\begin{Bmatrix} \Delta u^{i}_{nS^*} \\ \Delta u^{i}_{tS^*} \end{Bmatrix} = \begin{bmatrix} CN_1 & SN_1 & \dots & \dots & CN_m & SN_m \\ -SN_1 & CN_1 & \dots & \dots & -SN_m & CN_m \end{bmatrix} \begin{Bmatrix} \Delta u^{i}_{x1} \\ \Delta u^{i}_{y1} \\ \vdots \\ \vdots \\ \Delta u^{i}_{xm} \\ \Delta u^{i}_{ym} \end{Bmatrix} \tag{4.15}$$

$$\begin{Bmatrix} \Delta u^{i}_{nS} \\ \Delta u^{i}_{tS} \end{Bmatrix} = \begin{Bmatrix} C\Delta u^{i}_{xS} + S\Delta u^{i}_{yS} \\ -S\Delta u^{i}_{xS} + C\Delta u^{i}_{yS} \end{Bmatrix} \tag{4.16}$$

Now the equilibrium equations for the interface forces have to be imposed as well. Using the concept of virtual work, the incremental forces at the master interface element nodes can be related to the slave node incremental interaction forces. This relation is written as

$$-\begin{Bmatrix} \Delta F'_{x_1} \\ \Delta F'_{y_1} \\ \vdots \\ \Delta F'_{x_m} \\ \Delta F'_{y_m} \end{Bmatrix} = \begin{bmatrix} N_1 & 0 \\ 0 & N_1 \\ \vdots & \vdots \\ N_m & 0 \\ 0 & N_m \end{bmatrix} \begin{Bmatrix} \Delta F'_{xS} \\ \Delta F'_{yS} \end{Bmatrix} = \begin{bmatrix} CN_1 & -SN_1 \\ SN_1 & CN_1 \\ \vdots & \vdots \\ CN_m & -SN_m \\ SN_m & CN_m \end{bmatrix} \begin{Bmatrix} \Delta F'_{nS} \\ \Delta F'_{tS} \end{Bmatrix} \tag{4.17}$$

Equation 4.17 directly defines the matrix $[b]^T$ in Eqn. 4.8, while matrix $[a]^T$ transforms terms from the normal and tangential system of coordinates to the Cartesian one. The constraint matrix $[c]$ and load vector $\{f\}$ for the "fixed" mode of interaction are defined in Table 4.2.

Sliding Interaction Mode

When the slave node S slides along the master interface, compatibility is prescribed for the displacements normal to the master interface. The compatibility equation can be written as

$$\Delta u'_{nS} - \Delta u'_{nS} = g^{k-1} \tag{4.18}$$

or

$$\begin{bmatrix} CN_1 & SN_1 & \cdots & \cdots & CN_5 & SN_5 \end{bmatrix} \begin{Bmatrix} \Delta u'_{x1} \\ \Delta u'_{y1} \\ \vdots \\ \Delta u'_{x5} \\ \Delta u'_{y5} \end{Bmatrix} - \left(C\,\Delta u'_{xS} + S\,\Delta u'_{yS} \right) = g^{k-1} \tag{4.19}$$

Another condition required for slip is that the total tangential force at the slave node should be equal to the maximum frictional force available. The maximum frictional force is initially unknown, and so has to be estimated according to the previously converged major iteration,

and then has to be modified (or updated) throughout the minor iterations. At the *i*th minor iteration the maximum frictional force is defined by

$$T'_{max} = \left(| F_{nS}^{k-1} + \Delta F'_{nS} |\ \tan(\phi) + c \right)\ \ \mathrm{sgn}\left(F_{tS}^{k-1} + \Delta F'_{tS} \right) \qquad \textbf{(4.20)}$$

and the condition for the sliding state can be expressed as

$$\Delta F'_{tS} = T'_{max} - F_{tS}^{k-1} \qquad \textbf{(4.21)}$$

Like the interaction for the "free" mode, the incremental tangential slave node force is known and will generate a load vector at both the slave node and interacting master interface element nodes. On the other hand, the normal incremental force at the slave node is unknown and a relation between this force and the master slave nodes can be found (as before in the fixed mode). The corresponding constraint matrix and load vector are defined in Table 4.3.

4.8. Formulation of the Residual Force Vector

Two methods are used to calculate the residual load vector $\{\Delta R^k\}$ shown on the left hand side of Eqn. 4.5. In both methods the residual load vector is defined as

$$\{\Delta R^k\} = \{R^k\} - \{F^k\} \qquad \textbf{(4.22)}$$

where

$\{R^k\}$ is the total applied force vector at the *k*th major iteration

$\{F^k\}$ is the nodal force vector which is equivalent (in the virtual work sense) to the current stresses at the *k*th major iteration.

The two methods differ in how the total force vector $\{R^k\}$ is defined at the interfacial nodes. The first method accumulates the incremental interaction forces at the slave nodes throughout the major iterations to get the total forces at the nodes. The total forces at the

master interface nodes are calculated from the total forces at the slave interface nodes using the concept of virtual work.

The second method equates the total interaction forces at the slave interfacial nodes to the equivalent nodal forces due to the current stress state. In other words, the residual forces at the interfacial slave nodes become zero. The total forces at the master interface nodes are calculated as before in the first method.

The two methods are used to study the effect of accumulating the incremental interaction forces (first method). In general, the second method for calculating the residual force vector promoted superior convergence but the final results were, more or less, the same.

4.9. Criteria for Selecting New Modes During Minor Iterations

A comprehensive set of physical criteria to test the validity of an assumed mode is shown in Table 4.4. The table shows a decision matrix used for checking the mode in the previous minor iteration to determine the new most probable mode.

It is worth mentioning that in the third row in Table 4.4 an assumed free mode is correct if the normal gap is greater than zero, otherwise the new mode is assumed fixed. This does not imply a sliding mode can not be reached from a free mode; it simply implies a sliding state must be reached by an iterative path; free to fixed to sliding. For the special case of smooth interface, one can go directly from free to sliding mode without passing by the fixed mode.

4.10. Constraint Equations for Restrained Interface Nodes

The equation for each restrained degree of freedom is deleted from the system leaving only the displacements of the unrestrained degrees of freedom to be determined. However, for restrained slave nodes, while the degree of freedom for one direction is restrained and the corresponding equation is removed, the equations corresponding to the normal and tangential interaction forces at this slave node are not removed from the system of equations. These equations for the interaction forces are required to satisfy force equilibrium at the interface.

4.11. Test Problems

To examine the effectiveness of the proposed method of analysis, several different test problems are examined. The problems have been chosen to check different aspects of the method. In all the analyses, the structural elements used are those described in chapter three. The expected interacting slave nodes are chosen and the expected interacting master surface is discretized by interface elements compatible with the discretization of the master body at the interface. In all the test problems, convergence is achieved through an adequate number of major iterations and one minor iteration is used unless otherwise noted.

4.11.1. A Beam with One Pinned End and the Other Sliding on A Rough Surface

The problem, shown in Fig. 4.3, is chosen for its simplicity and to check the proposed method against the analytical solution which is easily derived. It also demonstrates the ability of the method to detect "fixed" and "sliding" modes, and the applicability of the method when one of the individual interacting bodies is prone to have rotational rigid-body movements. In this case, the initial modes of interaction (sliding or fixed) should be

assumed *a priori*, otherwise a singular system of equations is produced. The beam is modelled using one 5-noded structural element. The beam length L=4 and material properties, EA=100 and EI=100/12, are shown in Fig. 4.3. The free end of the beam is considered a slave node and the rigid surface is modelled using an imaginary 5-noded interface element attached to five restrained nodes. The friction angle ϕ between the beam and the rough surface is 30°. The sliding end of the beam is subjected to a horizontal load P which is increased till a maximum value of $P=0.25$ is reached. This load is then released until P reaches 0.0. Figure 4.3 shows all the data used in the analysis and also the resulting load-displacement relationship for the sliding end of the beam. It is shown that the loaded end of the beam slides in the direction of loading as the applied load increases to the maximum load $P=0.25$. When the load decreases, the loaded end remains fixed to the rough surface until the limiting value of $P=0.067$ is reached, after which it slides in a direction opposite to that of the applied load due to the axial strain energy stored along the beam length. The numerical solution matches the analytical solution.

4.11.2. A Vertical Cantilever Contacting and Separating From Another Horizontal One

This simple problem, shown in Fig. 4.4, demonstrates the ability of the formulation to trace sliding and separation under large deformations. Each cantilever is modelled using a 5-noded structural element. The material properties and the dimensions of both cantilevers are given by EA=100, and EI=100/12. The vertical cantilever surface is considered the master interface while the end of the horizontal cantilever is chosen to be the slave node. The load P is applied in equal increments of $\Delta P=0.05$. Two cases are considered, the rough interface with $\phi=30^{\circ}$, and the smooth one with $\phi=0^{\circ}$. The load-displacement response of

the loaded end of the vertical cantilever is shown. The deformed shapes at load levels $P=2.5$ and $P=-2.5$ for the case of $\phi=0°$ are also shown in the figure.

For the case of $\phi=0°$, the effect of the horizontal cantilever on the behaviour is pronounced at low load levels. Once the slave node slides along the master interface and the horizontal cantilever deforms, its stiffness in the direction normal to the deformed vertical cantilever decreases and its effect on the final deformation is negligible. This is not the case for $\phi=30°$, as full contact between the two cantilevers is maintained without slip and displacements are substantially reduced.

4.11.3. A Long Vertical Cantilever Contacting Another Distant Shorter One

Both the previous problems show bodies initially in contact. The contact is maintained at one node which is easy to trace and visualize. The third problem deals with two bodies initially separate, so that a contact surface is formed after load is applied. The two cantilevers have identical materials and are modelled using 5-noded structural elements. The long cantilever is modelled using 5 structural elements and is chosen to be the master body with its surface defined along the cantilever length. The short cantilever is modelled using 3 structural elements and its nodes are chosen to be the slave nodes. The case of smooth interface $\phi=0°$ is considered.

The problem dimensions, material properties and model discretization are shown in Fig. 4.5. The load-displacement response at the long cantilever loaded end is shown as well as the deformed shapes at load levels $M=3.5$ and $M=5.0$. At load level $M=3.5$, there is only one point of contact between the cantilevers. At the higher load level $M=5.0$, a contact surface develops on which slip occurs.

4.11.4. Problem of A Cantilever Contacting A Rigid Circular Surface

A more complicated problem of a cantilever bending onto a rigid circular surface is considered in Fig. 4.6. The cantilever is considered the slave body and is modelled using five 5-noded structural elements. The smooth rigid circular surface is considered the master surface and is modelled using six 5-noded imaginary interface elements attached to 25 restrained nodes. The material properties of the cantilever and dimensions of the problem are shown in Fig. 4.6. The deformed shape is illustrated at load $P=3.5$ and the load-displacement response at the cantilever loaded end is shown. It is shown that as the applied load increases, the length of the contact surface increases and the free length of the cantilever decreases. This increases the stiffness of the cantilever and consequently decreases the rate of change of displacements.

4.11.5. Problem of A Cantilever Resting Against An Elastic Body

This problem is presented to demonstrate certain capabilities and the limitations of the interaction analysis in more detail. The cantilever is modelled using twelve 3-noded structural elements while the elastic body is modelled using 8-noded isoparametric continuum elements. All the dimensions and material properties (i.e. Young's modulus E and Poisson's ratio ν) are shown in Fig. 4.7. The cantilever is considered the master body with its surface defined along its length, while the elastic body nodes at the cantilever interface are considered the slave nodes. The case of smooth interface is considered. The deflected shapes for three different loading cases are shown in Fig. 4.7.

Trials with different sizes of load increments and different numbers of major and minor iterations are considered. The results are shown in Figs. 4.8, 4.9 and 4.10. Various conclusions can be drawn from the solution of this problem.

1- As in all incremental non-linear analyses, the size of the load increment may affect the accuracy of the results. Figure 4.8 shows that for load increments 0.01 and 0.02, the solution is indistinguishable which implies convergence to the correct numerical solution. Decreased accuracy of the solutions is also clear for the load increments 0.10 and 0.15, although there is a numerical convergence. This is not due to the inappropriate modelling of the interface behaviour, but to the fact that the exact material behaviour is not modelled in the updated Lagrangian formulation which requires small sized load increments.

2- The larger the number of major iterations (equilibrium iterations) the smoother the behaviour becomes. This is due to convergence to the correct interaction modes by minimizing the residual forces (Fig. 4.9). This can be seen from the zig-zag behaviour when using one major iteration compared to using five. Increasing the maximum number of minor iterations from five to ten iterations has no distinguishable effect on the solution. This implies that convergence occurred in less than 5 iterations.

3- Figure 4.10 gives results for alternatively 1, 2 and 5 minor iterations in the case of a relatively large load increment 0.15. For the cases featuring a small number of minor iterations (1 and 2 iterations), no mode convergence is achieved at high load levels ($P>0.95$). When 5 minor iterations are used, the solution accuracy increased compared to the solution at small load increment. This demonstrates the advantage of using

multiple minor iterations which ensures convergence in case of relatively large load increments at which a significant change in the interaction modes may occur. Even in cases of large minor iterations, mode convergence may not be achieved. This behaviour is attributed to the fact that when very small gaps at the interface are present, oscillation between two interaction states (those involving open and closed interface) may occur. The same behaviour is also reported by Katona [24].

The choice of the slave nodes and the master surface needs careful consideration because it may affect the results. Two cases are considered with interchangeable master and slave body definitions. The first case is as before while in the second case the slave nodes are defined along the cantilever length and the master surface is defined along the continuum interface.

Figure 4.11 shows the load-displacement response at the tip of the cantilever for the two different definitions of the master and slave bodies. In the second case, a sudden change in the behaviour is noticed once a new slave node starts to interact with the master surface. To avoid this unrealistic behaviour, this choice of the master and slave bodies should not be used. It is also important to mention that in the second case, the convergence rate is less than the first case. More major iterations are required to try to accommodate the sudden change in the behaviour due to the introduction of a new interacting node.

4.12. Conclusions

A new interaction technique is developed and discussed in this chapter. Some final conclusions may be drawn from this study.

- The method is applicable to a very wide range of applications with interaction involving large deformations.
- The method is applicable when one or both interacting bodies are prone to rigid body movements.
- A study was conducted to examine the effect of various numerical parameters (e.g. increment size and number of major and minor iterations). This study showed that using a small number of minor iterations, in cases where significant mode changes occur or when large increment size is used, may cause the solution to drift from the correct one.
- Sometimes, especially where it is difficult to distinguish between the free and fixed modes, no mode convergence is achieved and the minor iterations oscillate between two interaction states (those featuring open and closed interface). The same behaviour is reported by Katona [24] in the case of small deformations
- In some cases, the choice of the master interface and the interacting slave nodes may affect the solution. Careful consideration should be given to the implications of surface definition to the nodal compatibility.
- The method can also be applied for multi-interacting bodies (although this is not shown here). In that case, the master interface would consist of a number of separate discretized interfaces, from which the correct interface element would be selected for each slave node.

State	Δu^i_{xS}	Δu^i_{yS}	Δu^i_{x1}	Δu^i_{y1}	...	Δu^i_{xm}	Δu^i_{ym}	ΔF^i_{nS}	ΔF^i_{tS}	Load
Free	0	0	0	0	0	0	0	0	0	$-CF_{nS}^{k-1} + SF_{tS}^{k-1}$
	0	0	0	0	0	0	0	0	0	$-SF_{nS}^{k-1} - F_{tS}^{k-1}$
	0	0	0	0	0	0	0	0	0	$N_1\left(CF_{nS}^{k-1} - SF_{tS}^{k-1}\right)$
	0	0	0	0	0	0	0	0	0	$N_1\left(SF_{nS}^{k-1} + CF_{tS}^{k-1}\right)$
	0	0	0	0	0	0	0	:	:	:
	0	0	0	0	0	0	0	0	0	$N_m\left(CF_{nS}^{k-1} - SF_{tS}^{k-1}\right)$
	0	0	0	0	0	0	0	0	0	$N_m\left(SF_{nS}^{k-1} + CF_{tS}^{k-1}\right)$
	0	0	0	0	...	0	0	1	0	$-F_{nS}^{k-1}$
	0	0	0	0	...	0	0	0	1	$-F_{tS}^{k-1}$

Table 4.1. Interface Element Constraint Matrix [*c*] and Load Vector {*f*} for The *Free* Mode of Interaction During the *i*th Minor (Mode Assumption Convergence) Iteration within the *k*th Major Iteration

N_i the *i*th shape function of the master surface line element defined at the point of projection of the slave node on the element

θ angle between the outward normal to the master surface element and the X-axis where *s* and *c* are defined as: $s=\sin(\theta)$ and $c=\cos(\theta)$

T^i_{max} the total maximum shear force between the Slave node and the interacting Master element at the *k*th major iteration and *i*th minor iteration

g^{k-1} the gap between the slave node and the master surface element at the (*k-1*)th major iteration; it is positive if there is no penetration and negative otherwise

F_{nS}^{k-1} the normal component of the total interaction force at the Slave node at the (*k-1*)th major iteration; it is positive if in the same direction as the outward normal to the master surface element

F_{tS}^{k-1} the tangential component of the total interaction force at the Slave node at the (*k-1*)th major iteration.

State	Δu^{i}_{sS}	Δu^{i}_{nS}	Δu^{i}_{n1}	Δu^{i}_{t1}	...	Δu^{i}_{tm}	Δu^{i}_{tm}	ΔF^{i}_{nS}	ΔF^{i}_{sS}	Load
Fixed	0	0	0	0	0	0	0	$-C$	S	0
	0	0	0	0	0	0	0	S	$-C$	0
	0	0	0	0	0	0	0	CN_1	$-SN_1$	0
	0	0	0	0	0	0	0	SN_1	CN_1	0
	0	0	0	0	0	0	0	:	:	0
	0	0	0	0	0	0	0	CN_m	$-SN_m$	0
	0	0	0	0	0	0	0	SN_m	CN_m	0
	$-C$	$-S$	CN_1	SN_1	...	CN_m	SN_m	0	0	g^{k-1}
	S	$-C$	$-SN_1$	CN_1	...	$-SN_m$	CN_m	0	0	$g^{k-1}\left(\frac{\Delta u^{i-1}_{sS^*} - \Delta u^{i-1}_{sS}}{\Delta u^{i-1}_{nS^*} - \Delta u^{i-1}_{nS}}\right)$

Table 5.2. Interface Element Constraint Matrix [*c*] and Load Vector {*f*} for The *Fixed* Mode of Interaction During the *i*th Minor (Mode Assumption Convergence) Iteration within the *k*th Major Iteration

N_i the *i*th shape function of the master surface line element defined at the point of projection of the slave node on the element

θ angle between the outward normal to the master surface element and the X-axis where *s* and *c* are defined as: s=sin(θ) and *c*=cos(θ)

T^{i}_{max} the total maximum shear force between the Slave node and the interacting Master element at the *k*th major iteration and *i*th minor iteration

g^{k-1} the gap between the slave node and the master surface element at the (*k-1*)th major iteration; it is positive if there is no penetration and negative otherwise

F^{k-1}_{nS} the normal component of the total interaction force at the Slave node at the (*k-1*)th major iteration; it is positive if in the same direction as the outward normal to the master surface element

F^{k-1}_{sS} the tangential component of the total interaction force at the Slave node at the (*k-1*)th major iteration.

State	Δu^{i}_{nS}	Δu^{i}_{tS}	Δu^{i}_{x1}	Δu^{i}_{y1}	...	$\Delta u^{i}_{x_m}$	$\Delta u^{i}_{y_m}$	ΔF^{i}_{nS}	ΔF^{i}_{tS}	Load
Sliding	0	0	0	0	0	0	0	$-C$	0	$-S\left(T^{i}_{max}-F^{k-1}_{tS}\right)$
	0	0	0	0	0	0	0	$-S$	0	$C\left(T^{i}_{max}-F^{k-1}_{tS}\right)$
	0	0	0	0	0	0	0	CN_1	0	$SN_1\left(T^{i}_{max}-F^{k-1}_{tS}\right)$
	0	0	0	0	0	0	0	SN_1	0	$-CN_1\left(T^{i}_{max}-F^{k-1}_{tS}\right)$
	0	0	0	0	0	0	0	:	:	:
	0	0	0	0	0	0	0	CN_m	0	$SN_m\left(T^{i}_{max}-F^{k-1}_{tS}\right)$
	0	0	0	0	0	0	0	SN_m	0	$-CN_m\left(T^{i}_{max}-F^{k-1}_{tS}\right)$
	$-C$	$-S$	CN_1	SN_1	...	CN_m	SN_m	0	0	g^{k-1}
	0	0	0	0	...	0	0	0	1	$T^{i}_{max}-F^{k-1}_{tS}$

Table 4.3. Interface Element Constraint Matrix [*c*] and Load Vector {*f*} for The *Sliding* Mode of Interaction During the *i*th Minor (Mode Assumption Convergence) Iteration within the *k*th Major Iteration

N_i the *i*th shape function of the master surface line element defined at the point of projection of the slave node on the element

θ angle between the outward normal to the master surface element and the X-axis where *s* and *c* are defined as: s=sin(θ) and *c*=cos(θ)

T^{i}_{max} the total maximum shear fo. . between the Slave node and the interacting Master element at the *k*th major iteration and *i*th minor iteration

g^{k-1} the gap between the slave node and the master surface element at the (*k-1*)th major iteration; it is positive if there is no penetration and negative otherwise

F^{k-1}_{nS} the normal component of the total interaction force at the Slave node at the (*k-1*)th major iteration; it is positive if in the same direction as the outward normal to the master surface element

F^{k-1}_{tS} the tangential component of the total interaction force at the Slave node at the (*k-1*)th major iteration.

Iteration		Current Minor Iteration I for Slave Node s		
		Fixed Mode	Sliding Mode	Free Mode
Previous Minor Iteration (I-1) for Slave Node s	Fixed Mode	$F_{nS}^{I} > 0$ and $\lvert F_{tS}^{I} \rvert < T_{\max}^{I}$	$F_{nS}^{I} > 0$ and $\lvert F_{tS}^{I} \rvert > T_{\max}^{I}$	$F_{nS}^{I} \leq 0$
	Sliding Mode	$F_{nS}^{I} > 0$ and $T_{\max}^{I}\left(\Delta u_{tS}^{I} - \Delta u_{tS}^{I}\right) < 0$	$F_{nS}^{I} > 0$ and $T_{\max}^{I}\left(\Delta u_{tS}^{I} - \Delta u_{tS}^{I}\right) > 0$	$F_{nS}^{I} \leq 0$
	Free Mode	$g < 0$	Not Applicable	$g > 0$

Table 4.4. Decision Matrix for Selecting New Interaction Mode During Minor (Mode Assumption Convergence) Iteration within the kth Major (Equilibrium) Iteration

$T_{\max}^{I}$ the total maximum shear force between the Slave node and the interacting Master element at the kth major iteration and the ith minor iteration

F_{nS}^{I} the normal component of the total interaction force at the Slave node at the kth major iteration and the ith minor iteration; it is positive if in the same direction as the outward normal to the master surface element

F_{tS}^{I} the tangential component of the total interaction force at the Slave node at the kth major iteration and the ith minor iteration

ΔF_{tS}^{I} the tangential component of the incremental interaction force between the Slave node and the interacting Master element at the kth increment and the ith minor iteration

Δu_{tS}^{I} the tangential component of the slave node incremental displacement at the kth major iteration and the ith minor iteration

Δu_{tS}^{I}. the tangential component of the incremental displacement of the point of projection of the slave node on the master surface element at the kth major iteration and the ith minor iteration

g the gap between the slave node and the master interface at the kth major iteration and the ith minor iteration; it is negative if the slave node penetrates into the master surface element

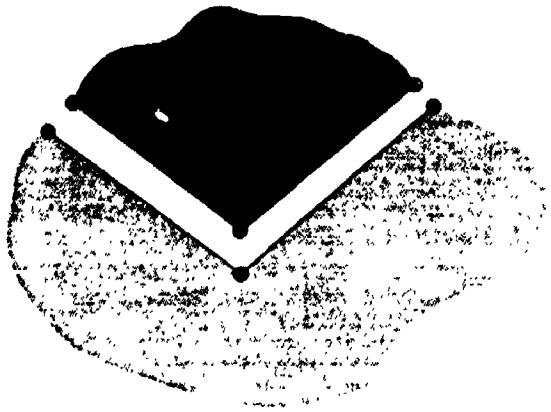

Figure 4.1a Node to Node Interaction

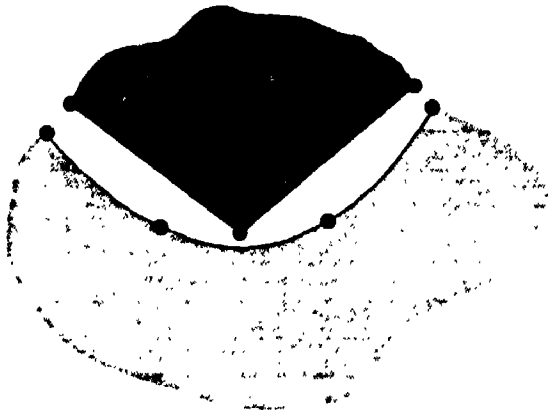

Figure 4.1b Node to Surface Interaction

Figure 4.1. Interaction Types

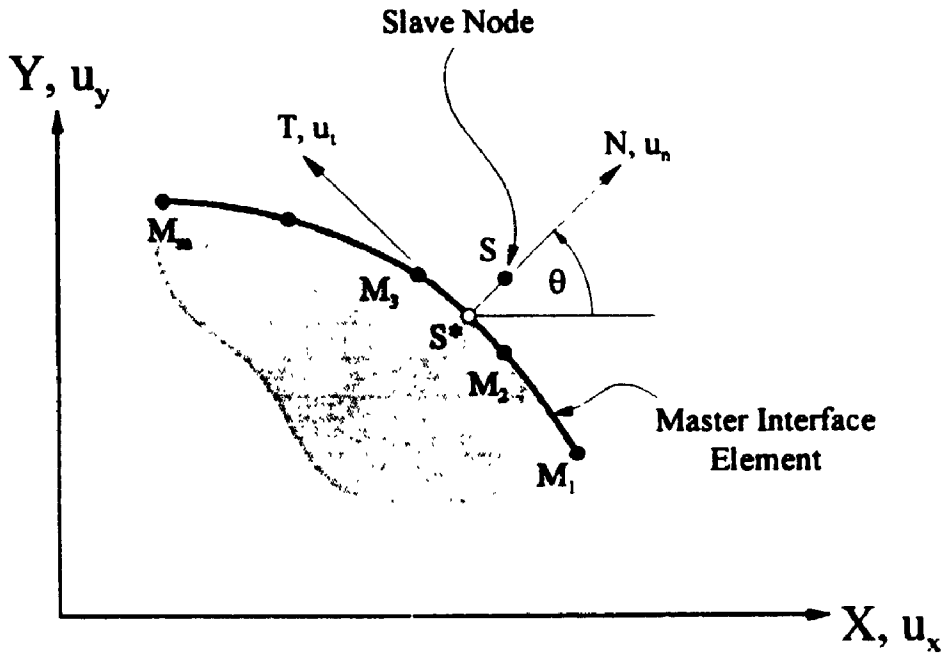

Figure 4.2. System of Coordinates

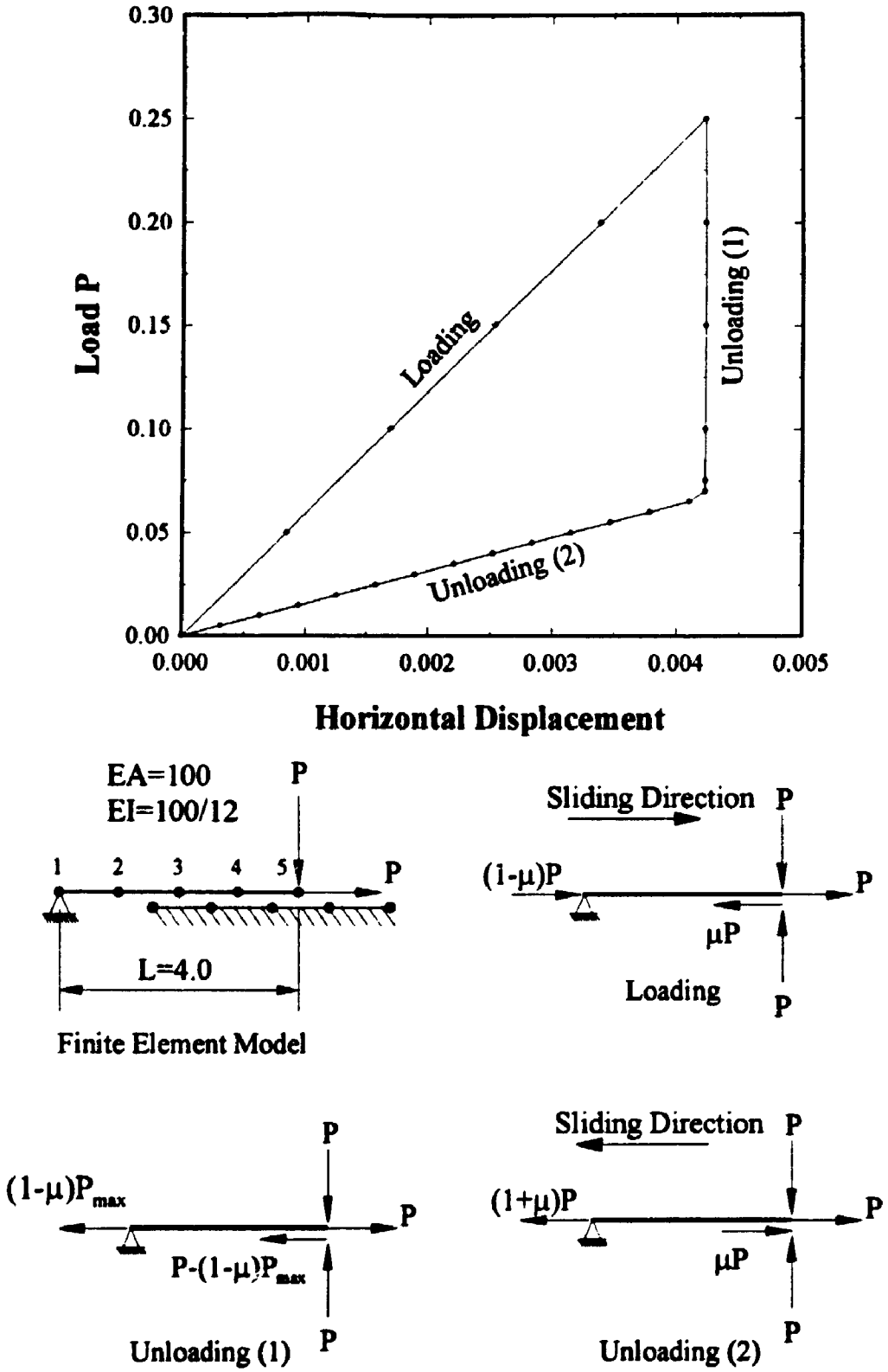

Figure 4.3. Load-Displacement of a Beam with one End Pinned and the Other Sliding on a Rough Surface
(EA=100, EI=100/12, L=4.0, ϕ=30, μ=tan ϕ)

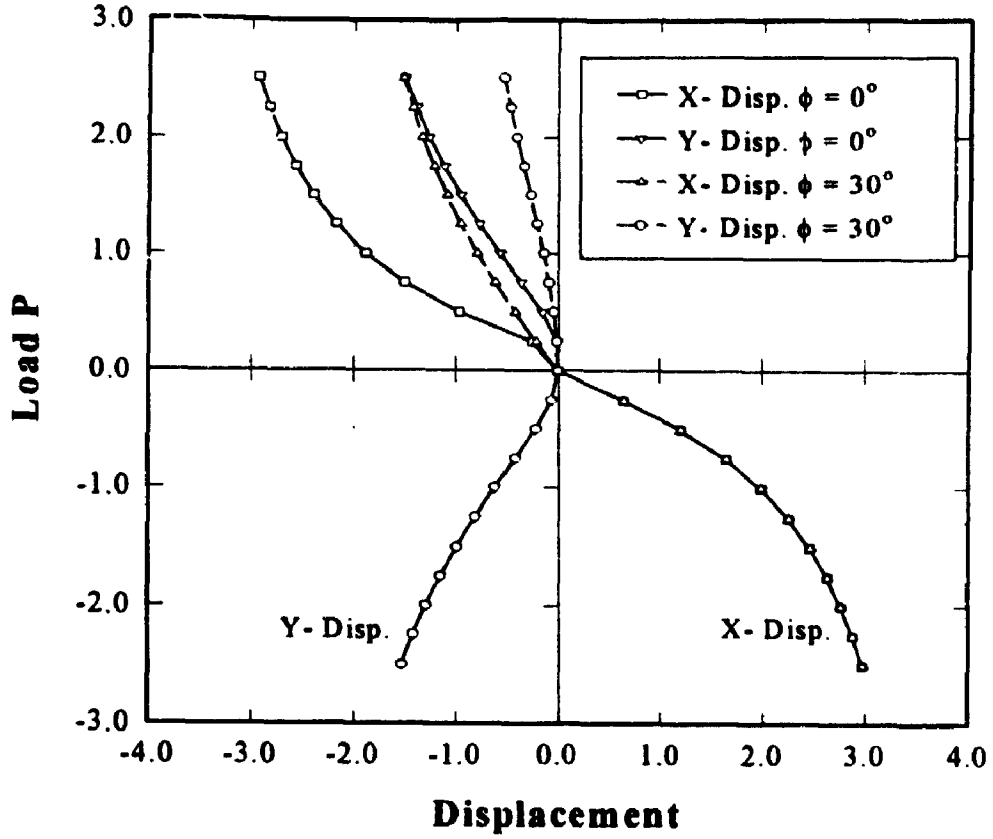

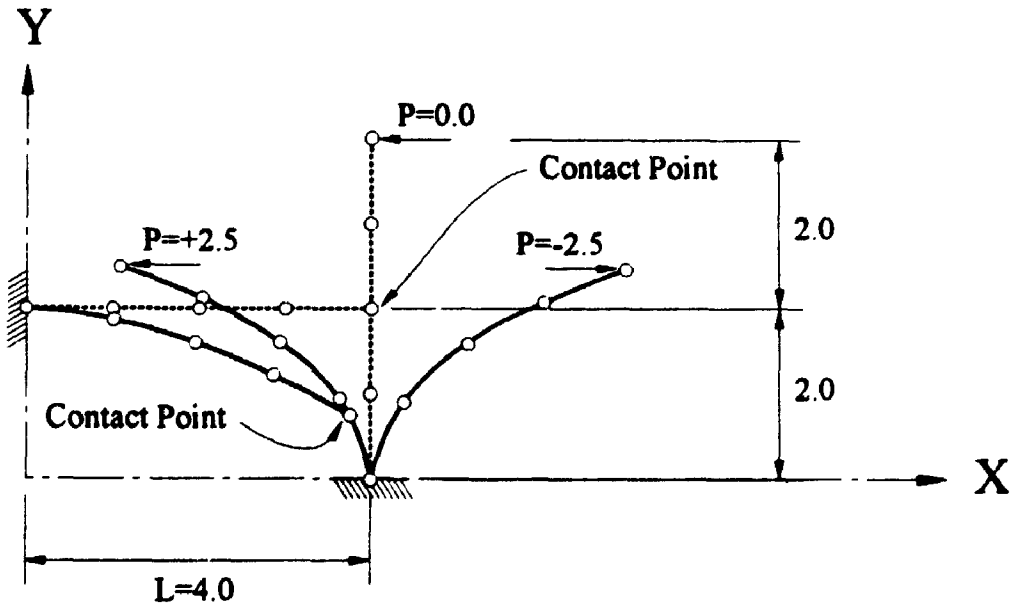

Figure 4.4. Load-Displacement Response for a Vertical Cantilever Contacting and Separating From Another Horizontal One (EA=100, EI=100/12, L=4.0, ΔP=0.05, ϕ=0, 30)

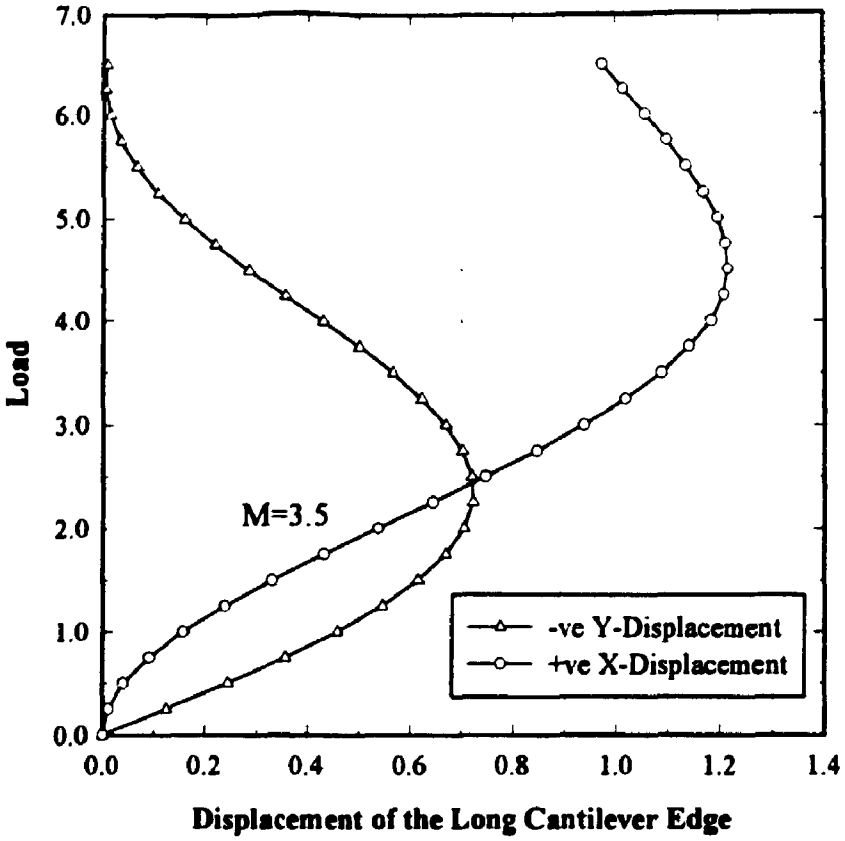

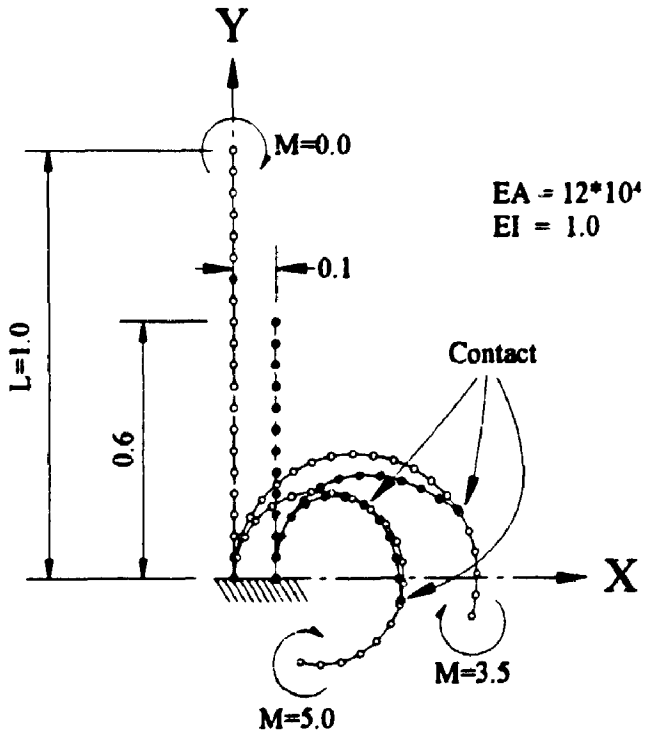

Figure 4.5. Load-Displacement Response of the Loaded End of a Vertical Cantilever Contacting Another Distant Shorter One
(EA=12*10⁴, EI=1.0, L=1.0, ΔM=0.05, ϕ=0.0)

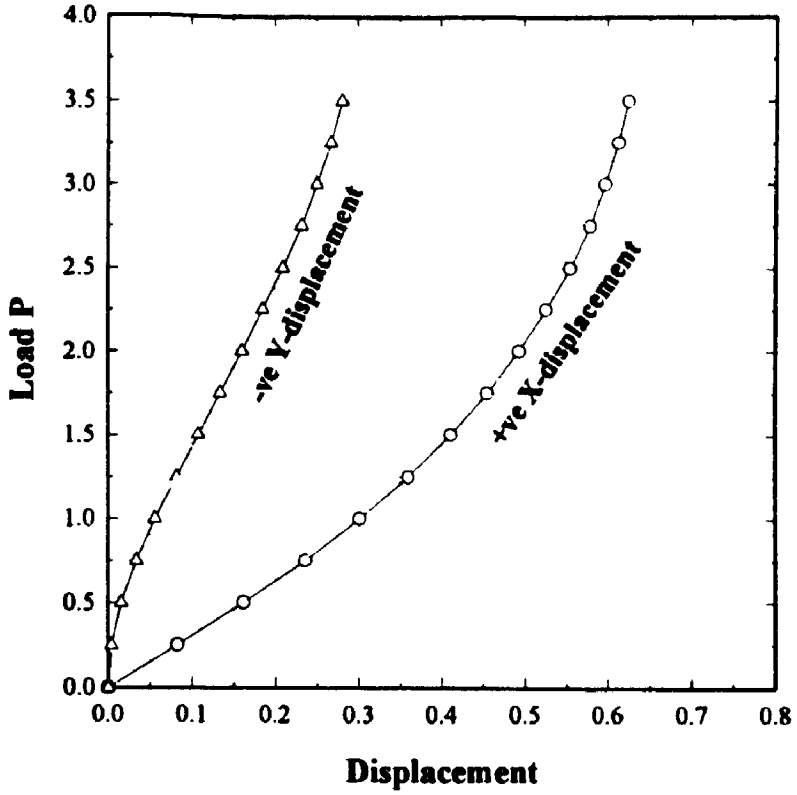

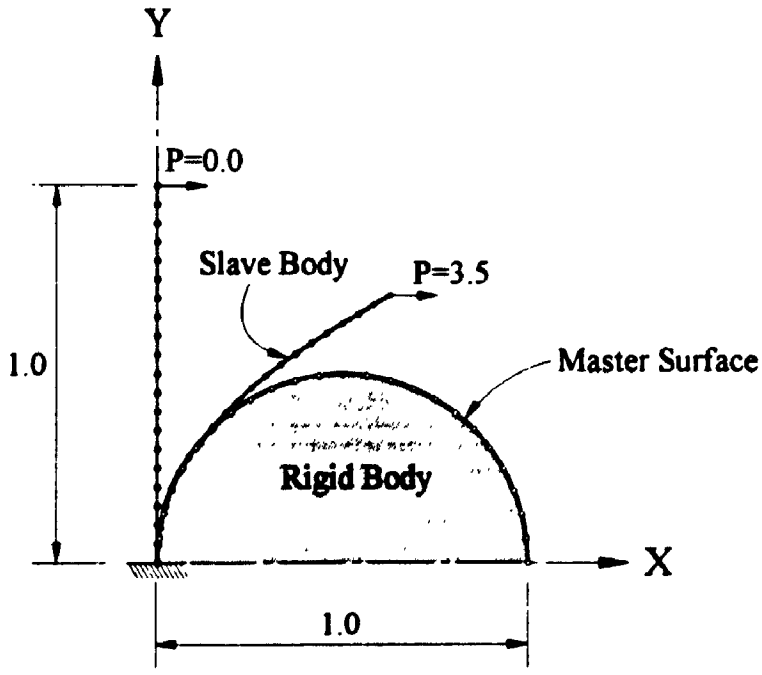

Figure 4.6. Load-Displacement Response of the Loaded End of a Vertical Cantilever Contacting a Rigid Circular Surface
(EA=12*10^6, EI=1.0, L=1.0, ΔP=0.005, ϕ=0.0)

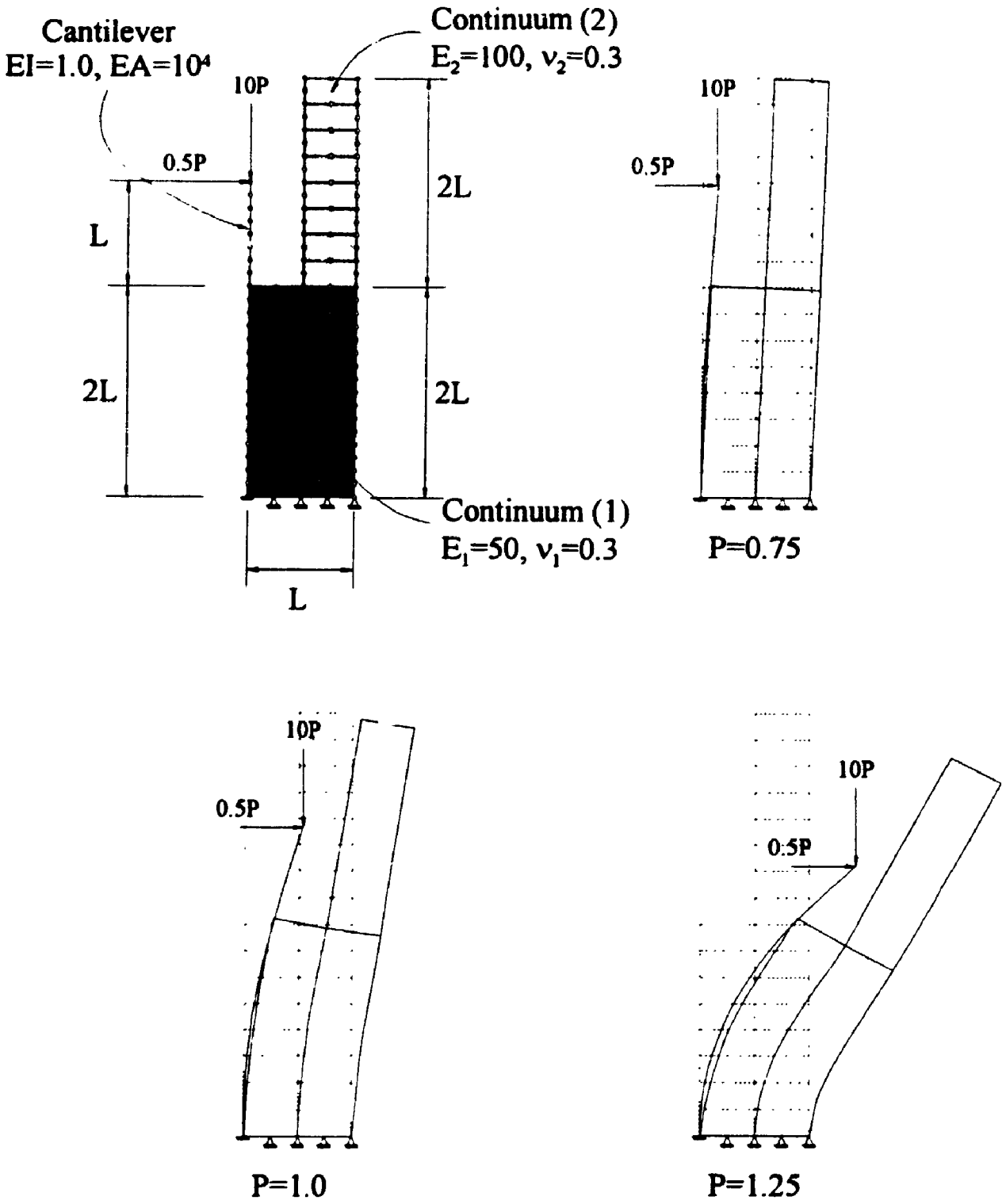

Figure 4.7. A Cantilever Resting on An Elastic Body
($EI=1.0$, $EA=10^4$, $E_1=50.0$, $\nu_1=0.3$, $E_2=100.0$, $\nu_2=0.3$)

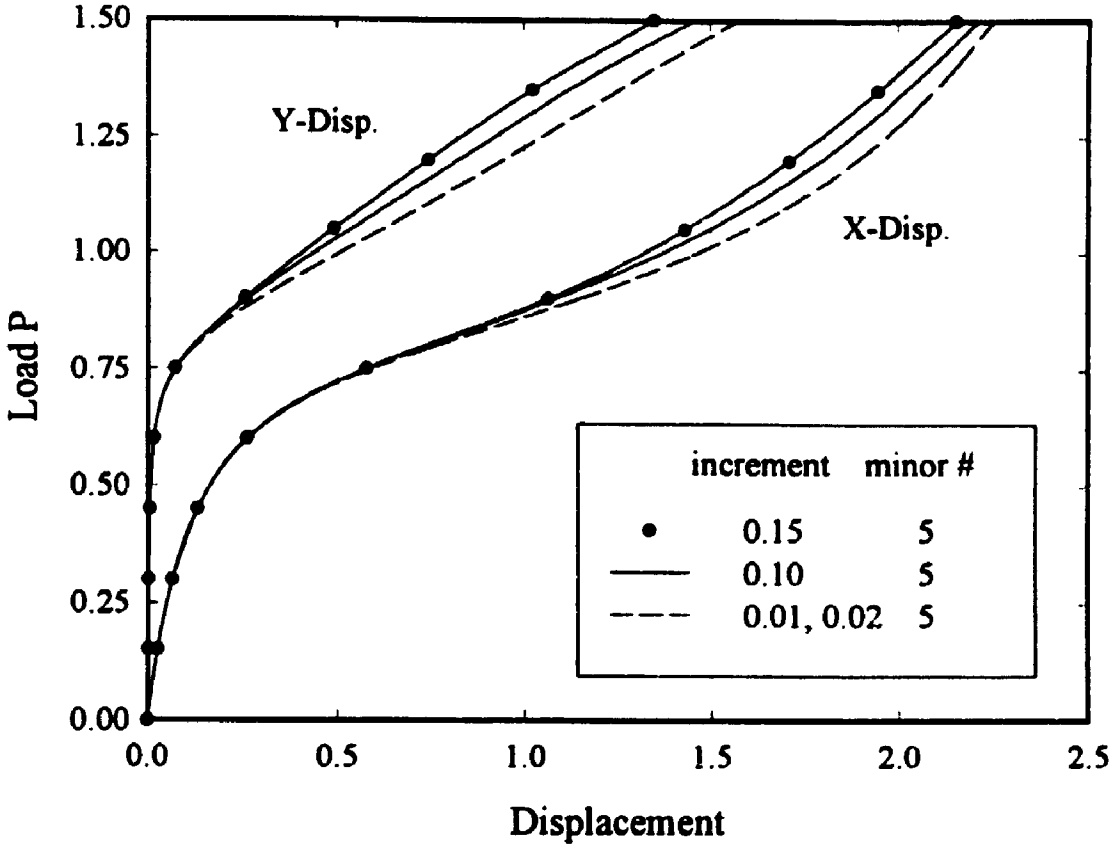

Figure 4.8. Effect of The Load Increment Size

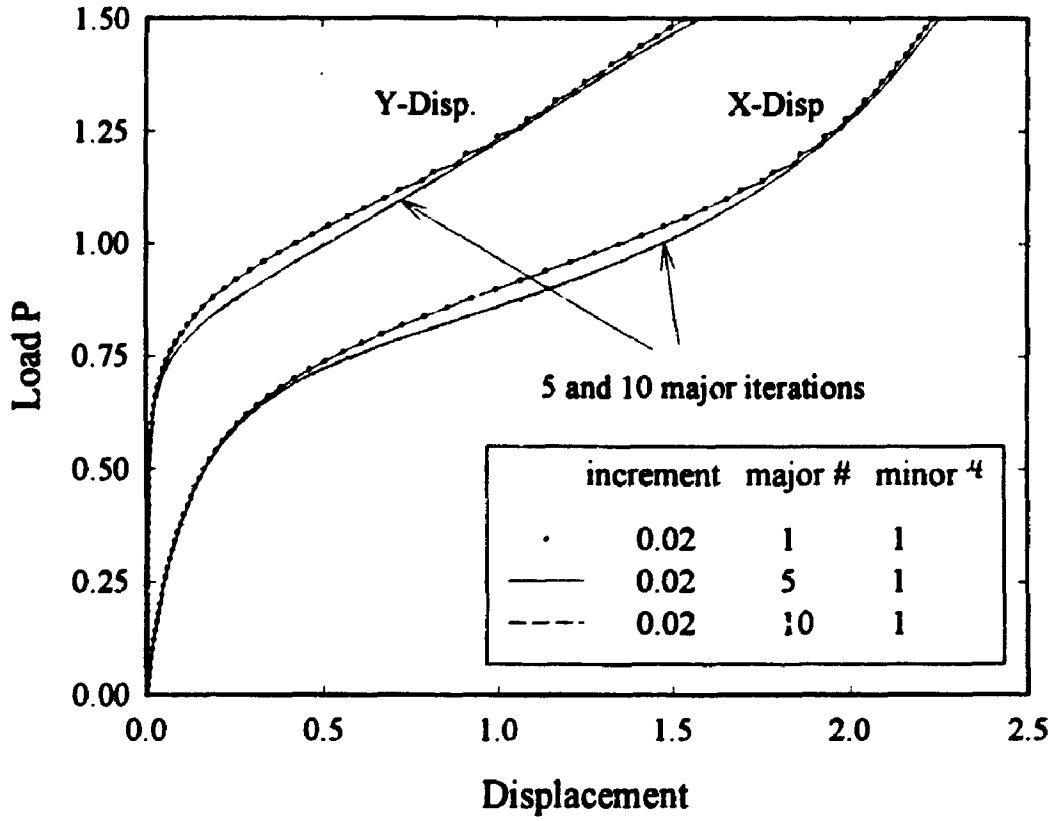

Figure 4.9. Effect of Number of Equilibrium Iterations

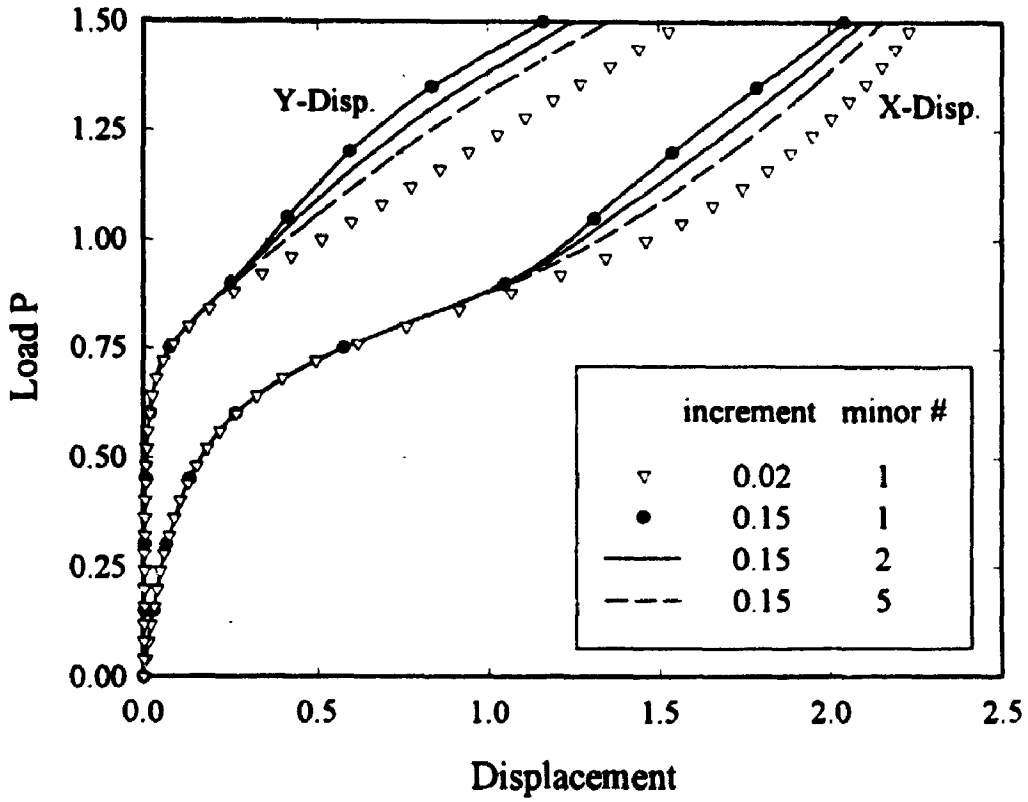

Figure 4.10. Effect of Number of Minor Iterations

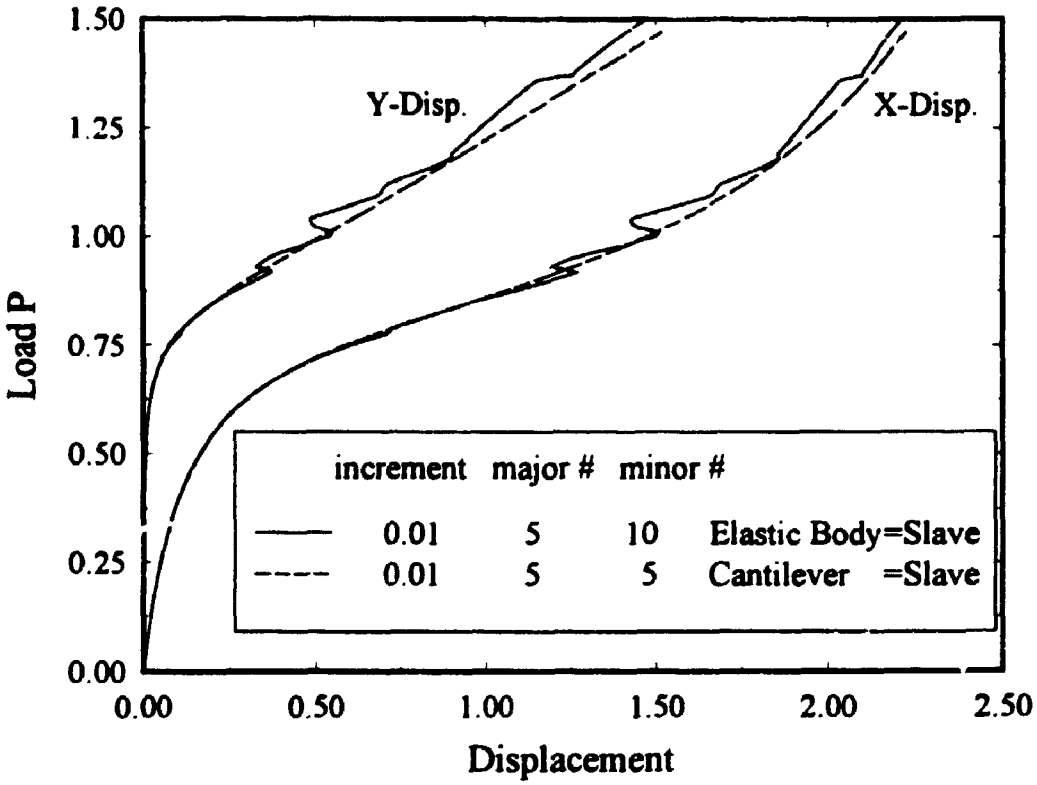

Figure 4.11. Effect of The Change of The Master and Slave Roles

CHAPTER FIVE

Stability Analysis for Perfect and Imperfect Circular Polymer Liners Under the Effect of External Pressure

5.1. Introduction

Various engineering applications require the design of an internal circular liner within a rigid circular structure. Examples include liners used for damaged pipelines and sewer rehabilitation, and concrete tunnels used for transportation of liquid and gases. The purpose of the lining varies; while it provides a smooth surface for fluid flow in pipelines and liquid and gas tunnels, it also prevents concrete from corrosion.

Polymer liners are being used with increasing frequency for the rehabilitation of damaged buried pipelines and sewers as a part of infrastructure renewal in North America and elsewhere. The allure of using these liners is the minimum disruption to the surrounding environment, especially the urban community and traffic. Those same advantages contribute to the cost effectiveness of the lining techniques. This chapter deals with the rehabilitation of damaged circular concrete pipelines using polymer liners. The concrete pipelines are considered rigid and structurally stable, but due to undesirable leakage in the cracked concrete pipeline, a liner is required.

Figure 5.1a shows a typical damaged circular concrete pipe of radius R after being rehabilitated using a polymer liner of thickness t. If the concrete pipe is structurally rigid, the principal loads acting on the liner will be the external ground water pressure, the installation grout pressure, and the fluid pressure inside the liner. It is proven experimentally that the liner buckles at a certain external pressure P_{cr} (critical pressure) [28]. Many studies

targeted the estimation of that critical pressure. The comprehensive literature review performed in chapter two introduced the problem and highlighted its important aspects.

As shown in chapter two, most of the solutions are based on a perfect circular liner. This simplification is inappropriate in most of the cases, because the liner has to take the shape of the damaged concrete pipe and it deviates from the circular shape (i.e. it has imperfections, as shown in Fig. 5.1b). The seriousness of this simplification is discussed in detail in this and the next chapters.

5.2. Outline of the Parametric Study

The parametric study for the critical pressure acting on an encased liner is distributed among this chapter and the next three chapters. This chapter targets the cases of a perfectly circular liner and a circular liner with a small localized imperfection. Chapter six examines the effect of liner ovality and eccentric alignment on the critical pressure. Chapter seven highlights the effect of material non-linearity on the critical liner pressure. Finally chapter eight summarizes the results of all the three chapters and introduces a design method for the calculation of the liner buckling pressure.

5.3. Problem Definition of the Circular Liner with A Localized Imperfection

Figure 5.1 shows the general problem under consideration. A uniform elastic liner is fitted within the damaged rigid pipe. The liner of thickness t and radius R, may be perfectly circular (Fig. 5.1a) or it may feature a local imperfection (Fig. 5.1b) where the liner has separated from the damaged host pipe it is intended to line. The liner material is linear

elastic and has Young's modulus E and Poisson's ratio ν. The liner is loaded on its external boundary with a fluid pressure P.

The problem in its simplest form consists of a perfect circular liner encased in a perfect circular cavity. Even with this simple geometry, difficulties arise stemming from the geometrically non-linear response of the liner. At buckling, one point which is initially in contact with the rigid cavity separates, initiating a gap between the pipe and the rigid cavity. Separation changes the boundary conditions of the problem, and the contact conditions continue to change as load is increased.

In this study, a non-linear Finite Element Method (FEM) is used to assess the stability of a typical polymer liner fitted within a cracked rigid pipe. The details of the FEM are given in the following section.

5.4. Finite Element Model

Many aspects have to be considered in the FE analysis for the critical pressure. They are summarized in the following

- the plane strain assumption versus three dimensional analysis,
- the geometrical non-linearity due to large deformations,
- the uniform and hydrostatic pressure distributions,
- the load deformation behaviour exhibiting a peak load, and
- the non-linear interface model between the liner and the rigid damaged pipe .

It is assumed that the liner and the host pipe are long and that the geometrical, material and loading conditions do not vary along the liner longitudinal axis. It is therefore possible

to reduce the problem to two dimensions (2D) since plane strain conditions will prevail. It is recognized that some real liner configurations involve variations along the liner axis (where localized imperfections exist in the liner longitudinal direction, for example) but such considerations are beyond the scope of this work. Plane strain analysis involves, in most of the cases, higher stresses in the liner for a given external fluid pressure and reductions in stability relative to the three dimensional problem.

To account for the geometrical non-linearity, an updated Lagrangian formulation is adopted. This allows for large deformations in a small strain scheme. It is assumed that the liner deformations will remain symmetric with respect to one of the diameters, and only one half of the liner is considered. The liner is modelled using 5-noded isoparametric structural elements. The plane strain finite elements used are those described in chapter two with thickness t (or more generally with cross-sectional area A and moment of inertia I per unit width).

The applied pressure is modelled using a nonconservative follower type traction load which follows the deformed geometry of the liner. No modification to the stiffness matrix is made due to this nonconservative pressure, but equilibrium iterations are used to satisfy equilibrium at various load increments. Two types of pressure distributions are used in the FEM analysis; uniform and hydrostatic distributions. The uniform pressure does not vary along the liner while the hydrostatic pressure increases linearly with depth. The hydrostatic pressure magnitude depends on the Y-coordinate of the liner nodal points as the liner deforms

The usual Newton-Raphson technique is used in the pre-buckling region. As discussed before in chapter three, this method fails near to the peak load. To identify the peak load and trace the post-buckling behaviour, the Arc Length Control Method is used.

Two bodies are defined; the slave and the master bodies. The liner represents the slave body while the rigid host pipe represents the master body. The rigid master body need not to be modelled, and only the interface is modelled. The rigid smooth interface is defined around the inside of the rigid circular host pipe using fixed (restrained) nodal points. The rigorous interaction technique, discussed in chapter four, is used to model slip and separation at the interface considering large deflections and rotations. The assumptions used in the finite element analysis are

- the plane strain condition is applicable,
- the pipe is extensional,
- the liner material is elastic,
- the deformations are large and the rotations are finite in a small strain scheme,
- the shear deformations are considered, and
- the interface between the liner and the rigid cavity is smooth (which is a conservative assumption).

The following sections describe the analysis of two distinct problems. The first is the case of a circular liner, and the second is the case of a circular liner with a wavy imperfection. The description of the finite element model used is given in each section.

5.5. The Buckling of a Perfect Circular Liner Encased in a Smooth Circular Rigid Host Pipe Under External Pressure

5.5.1. Introduction

The following sections describe the analysis technique and results for the critical pressure of a circular liner encased in a rigid cavity. The critical pressure is shown to be dependent on the thickness to radius ratio. The solution is then checked against the available experimental results and Glock's closed form solution [18].

5.5.2. Geometry

In most buckling problems, there exists a point after which the load-deflection curve may have an infinite number of different possible solutions; this is called the bifurcation point. To overcome this sudden change in the behaviour, a very small imperfection is imposed on the system to obtain the liner critical pressure. Different types of small imperfections are introduced and found to have little impact on the liner stability. The small imperfection used throughout the parametric study for circular liners is ovality imperfection. An oval shape is used instead of the circular one (Fig. 5.2a). The ratio between the ellipse axis length, a and b, is chosen such that any decrease should not change the analysis results. The ratio a/b=1.0005 is found satisfactory. The liner is defined as the slave body using 5-noded curved structural elements. The rigid cavity interface is modelled using 5-noded non-linear interface elements of the same number as the structural elements. Configurations with different numbers of elements are investigated to study the convergence of the numerical FE solution against the number of nodes in the model. Figure 5.2b shows the model used in the analysis, with twelve structural elements. For this problem

t is the liner thickness,

R is the average liner radius (i.e. $(a+b)/2$),

D is the average liner diameter (i.e. $D=2R$)

E is Young's modulus for the liner material, and

ν is Poisson's ratio.

5.5.3. Effect of the Number of Structural Elements on the Convergence

The number of nodes and elements used in any FE model usually affects the numerical accuracy of the results. A convergence study for the effect on the number of nodes and elements used in the FE model is accomplished. Four models with different number of nodes and 5-noded structural elements are used. They correspond to six elements (25 nodes), eight elements (33 nodes), ten elements (41 nodes), and twelve elements (49) nodes. A comparison between the results of the analysis using the four models is shown in Fig. 5.3 for two t/R ratios; t/R=0.01 and t/R=0.05 respectively. The comparison shows the load-deflection of the liner crown. The figure shows that the six elements produce numerically accurate results for thick liners (t/R=0.05), but accuracy decreases as t/R decreases. This is proven by the difference in the results between the six element model and the eight element model for the case of t/R=0.01. This difference between the different t/R ratios may be accounted for by the complicated geometry of the localized deformations in the detached part of the liner which occurs for small t/R ratios. As the t/R ratio increases, the deformations are spread on a longer portion of the liner (the detached part) and the geometry of the deformed shape needs fewer nodes to accurately model its geometry. For the rest of the study, a finite element model of twelve elements (49 nodes) is used.

5.5.4. Effect of Chosen Imperfection on the Critical Pressure

To overcome the bifurcation in the liner response which occurs if the circular shape of the liner is used, a very small imperfection is imposed on the system. Two types of small imperfections are introduced to a finite element model with ten 5-noded structural elements. The first correspond to an ovality introduced to both the liner and the rigid pipe. The ovality is introduced by scaling all the X-coordinates of the liner and the rigid pipe by the ratio a/b where $a/b>1.0$. Three ovality ratios are used, a/b=1.0005, 1.0050, and 1.0300 respectively. The response of the liner crown is shown in Fig. 5.4 for two t/R ratios; t/R=0.01 and 0.05. The difference between the solutions for a/b=1.0005 and a/b=1.0050 is negligible, which supports the use of the ratio a/b=1.0005 for the FE analysis. The normalized critical pressures $\frac{P(1-\nu^2)}{E}$ for the two cases of t/R=0.05 and 0.10 are 8.54×10^{-6} and 307×10^{-4} respectively.

The second type of imperfection used is somewhat crude and it is achieved simply by shifting the Y-coordinates of the crown point downward by an amount Δ. The same two t/R ratios considered for the first imperfection (the ovality imperfection) are considered for the second one. It is not feasible to compare the response of the two imperfections, but instead the critical pressure values are compared. The following results for the critical pressure are obtained

t/R=0.01		t/R=0.05	
Δ/R	P_{cr}	Δ/R	P_{cr}
0.0100	7.04×10^{-6}	0.0100	2.97×10^{-4}
0.0050	7.79×10^{-6}	0.0050	3.03×10^{-4}
0.0010	8.40×10^{-6}	0.0010	3.07×10^{-4}
0.0005	8.48×10^{-6}	0.0005	3.07×10^{-4}

It is clear that the critical pressures compare very well with those that are predicted with the small ovality imperfection. It is also important to notice that the convergence rate of the critical pressure against the imperfection size Δ/R is relatively slower for the case of t/R=0.01 than for the case of t/R=0.05. This implies that the solution is more sensitive to the imperfection size for small values of t/R (i.e. thin liners). For the rest of the circular liner analysis, an ovality imperfection of a/b=1.0005 is used.

5.5.5. Effect of the Liner Thickness to Radius Ratio on the Critical Pressure

A parametric study for the effect of the thickness to radius ratio t/R on the critical pressure is achieved and is shown in Figs. 5.5 and 5.6. In Fig. 5.5, the critical pressure is normalized by $E/(1-\nu^2)$ and is shown against t/R. Another way of interpreting the results involves normalizing the critical pressure by the buckling pressure of the free liner (Levy's solution). This ratio defines an enhancement factor K which is a measure of the effect of encasement on the critical pressure. Figure 5.6 shows the enhancement factor K against the thickness to radius ratio t/R. The discrete points (black circular symbols) define the FEM solution while the solid line defines the least-square method best fit for the FEM results. The best fit equations are defined by

$$P_{cr} = \frac{E}{1-\nu^2}\left(\frac{t}{2R}\right)^{2.19} \tag{5.1}$$

$$K = \frac{1}{2}\left(\frac{2R}{t}\right)^{0.81} \tag{5.2}$$

or more generally as a function of the cross-sectional area A and moment of inertia I of the unit width of the liner

$$P_{cr} = \frac{E}{1-\nu^2}\left(\frac{3I}{AR^2}\right)^{1.095} \tag{5.3}$$

$$K = \frac{1}{2}\left(\frac{AR^2}{3I}\right)^{0.405} \tag{5.4}$$

For consistency, all the following results are presented using t/R ratios instead of $\sqrt{\frac{AR^2}{3I}}$.

It is obvious from the figures that the enhancement factor K increases as t/R decreases. This is mainly due to the smaller circumferential deformations for small values of t/R (i.e. for the cases of higher hoop stiffness) compared to those for the higher values of t/R.

5.5.6. Effect of the Hydrostatic Pressure distribution on the Buckling Pressure

In the previous analysis of the circular liner, the uniform buckling pressure is calculated for different t/R ratios. For that analysis, a very small oval imperfection (a/b=1.0005) is needed to change the critical response from one of bifurcation to a limit load solution. In practice, the applied fluid pressure is not uniform and it will have some variation along the liner circumference. While the uniform pressure does not vary along the liner, the hydrostatic pressure increases linearly with depth. This section studies the effect of the variation in applied fluid pressure on the critical pressure.

For this analysis the model used for the circular liner is again employed but the pressure is assumed to vary hydrostatically (Fig. 5.7). Instead of supporting the bottom of the liner as in the previous solutions (an arbitrary choice that does not influence the solution when pressures are uniform), the top point (crown) is supported to account for the net hydrostatic uplift force and the restoring force exerted by the damaged host pipe on the liner.

The pressure is divided into a triangular and a uniform part. The triangular part is defined by its maximum value at the bottom of the liner γD, where γ is the fluid weight density and D is the liner diameter. To normalize this pressure, the ratio $\omega = \gamma R \frac{(1-\nu^2)}{E}\left(\frac{D}{t}\right)^{2.19}$ is defined.

To study the nonuniform pressure effect on the critical pressure, two t/R ratios are considered; t/R=0.05 and 0.10 with various ω ratios. Figure 5.8 shows the normalized deflection of the bottom point δ/R versus the normalized pressure defined at the bottom point of the liner. The pressure is normalized by the critical pressure for the circular liner, $\frac{E}{(1-\nu^2)}\left(\frac{t}{D}\right)^{2.19}$.

As the buckled region of the liner deforms upward the hydrostatic pressure reduces significantly on most of the buckle length. This reduction in pressure is significant for large values of ω. This may justify the noticeable enhancement in the post-buckling response (Fig. 5.8) when ω varies by two orders of magnitude. Figure 5.8 shows also that the effect of the nonuniform pressure on the critical pressure is negligible compared to the buckling load of the encased liner under uniform pressure equal to the maximum pressure applied at the position of buckling. This would suggest using the maximum pressure applied to the liner for design in contrast to the usage of the average pressure (defined at the centre of the liner). This is a conservative choice, as the imperfection is assumed to be in its worst position (the location of the maximum pressure).

5.5.7. Comparison with Experimental Data

A comparison between the FEM best fit (Eqn. 5.1), and Glock's closed form solution [18] (shown in dashed line) is shown in Figs. 5.5 and 5.6. Glock's closed form solution can be written as

$$P_{cr} = \frac{E}{1-\nu^2}\left(\frac{t}{D}\right)^{2.2} \tag{5.5}$$

$$K = \frac{1}{2}\left(\frac{D}{t}\right)^{0.80} \tag{5.6}$$

The finite element solution (based on a least-square best fit to the results) is close to Glock's solution and the difference between them is in the order of 3%.

Aggarwal and Cooper's test results are very useful because they include a relatively large number of samples (49 specimens). The experimental results are shown in Table 5.1. The details of the experiment has been given in chapter two.

Many important factors which help in the interpretation of the results should be discussed before comparing the experimental results of Aggarwal and Cooper to the finite element results. The factors are summarized in the following

- the size of the gap between the liner and the host steel pipe,
- the boundary conditions of the liner due to clamping of its ends,
- liner length to diameter ratios,
- the value of the calculated short term Young's modulus compared to the actual value for the test, and
- the type of structural failure (i.e. localized due to material defects or global due to buckling)

In this chapter, the first factor of the gap between the liner and the host pipe is ignored, but more discussion of its effect is given in chapter six. The clamping of the liner ends adds additional restraint to the liner ends (other than the restraint from the host pipe). This restraint prevents the liner ends from deforming in both the longitudinal and transverse directions. This increases the liner stability compared to the plane strain case where no restraint is being applied to the long liner other than that from the rigid host pipe. The liner stability also depends on its circumferential deformations as shown before; the less the hoop stiffness the less the liner stability and the enhancement factor K. The clamping of the liner ends prevents the circumferential deformations at the ends and this restraining effect is transmitted to the nearby vicinity. Therefore, it is appropriate to choose the highest possible length to diameter ratio of the liner to minimize this increase in the liner stability. Aggarwal and Cooper did not report the liner length to diameter ratios used in their experiments, but from the pictures provided in their report the ratio is in the range of 3.5 to 4.5, which may not be sufficient to overcome the increase in the stability associated with these ratios. Therefore, it is expected that the experimental results will be higher than the theoretical values.

The elapsed time during each of the liner tests (which may be more than 10 hours) is not reported by Aggarwal and Cooper, and therefore the use of the short term Young's modulus (high values compared to its value after 10 hours) may lead to higher values of the critical pressure of the unsupported liner and consequently lower values of the enhancement factor.

It is reported by Aggarwal and Cooper that localized structural failure was observed. This is, most likely, due to material imperfections or irregular thickness of the liner. This makes

the comparison between the theoretical and experimental values more challenging. This may also explains the scatter of the experimental results.

A comparison between the numerical results and the experimental results of Aggarwal and Cooper's tests (shown in black square symbols) is made in Figs. 5.5 and 5.6. Both the finite element and Glock solutions form a lower bound to almost 90% of the experimental results although it is expected that the theoretical solution should be lower than all the experimental results (because of the end restraints applied to the liner). This is due to the fact that the effect of the gap between the liner and the host pipe is neglected. This factor is discussed in more detail in chapter six. The following conclusions may be drawn from this investigation of perfect circular liners:

- The finite element best fit and Glock's solution are in good agreement with most of the experimental results, (but not all of them as expected) and are reasonable lower bound solutions.
- Lower values of the ratio (t/R) lead to more enhancement relative to the critical pressure for an unsupported pipe. This suggests that the solution of Kyriakides and Youn [29], which is reported earlier and is based on the assumption that the liner is inextensional, is not conservative.
- In the ASTM design code, the recommended value for K is 7, which is the same value recommended by Aggarwal and Cooper [1] for specimens of maximum t/R ratio equal to 0.07. This K value is not conservative for liners with higher t/R ratios (i.e. t/R>.07). Furthermore, it will be shown subsequently that the use of this enhancement factor should be restricted to perfectly circular liners (which are rare in practice). It is important to

study the effect of imperfections on the critical pressure This study is reported in the following sections

5.6. The Problem of an Imperfect Circular Liner in a Smooth Circular Rigid Host Pipe

5.6.1. Introduction

In practice, imperfections in the liner are always present due either to the liner installation technique or to the uneven shape of the rehabilitated pipe. Usually, initial imperfections can initiate buckling in that liner. This significance of imperfections on liner stability is recognized in different codes. For example, the ASTM codes limit the size of the imperfection to the lesser of 16% of the pipeline inner diameter or 25 mm. Many investigators have dealt with the problem of predicting the buckling pressure for the liner, considering the impact of the geometrical imperfections. Bucciarelli and Pian [8], in their study for the buckling of an encased imperfect ring, were the first to introduce a ring imperfection which is symmetric about one of the diameters. They assumed it to be generated such that the imperfect pipe has the same circumferential length as the perfect circular ring.

5.6.2. Mathematical Functions used for the Imperfection

The choice of the shape of the imperfection to be introduced is a difficult task The same imperfection introduced by Bucciarelli and Pian [8] and later used by Kyriakides and Youn [29], is used herein and is termed "function(1)". The imperfection is a single wave of length $2S_o$ and amplitude Δ_o (Fig. 5.9), and its shape is defined by

$$\frac{d^2\xi}{dS^2} = \frac{1}{R}\left\{\beta\left[\cos\left(4.493\frac{S}{S_o}\right) - \cos 4.493\right] 1\right\} \qquad S \le S_o \tag{5.7}$$

together with the boundary conditions

$$\begin{aligned} &\frac{d^2\xi}{dS^2} = \frac{1}{R}[\beta(\,\cdot - \cos(4.494))-1] \neq 0, \quad \frac{d\xi}{dS} = 0 && \text{at } S=0 \\ &\frac{d^2\xi}{dS^2} = -\frac{1}{R}, \quad \frac{d\xi}{dS} = -\frac{S_o}{R} && \text{at } S=S_o \end{aligned} \tag{5.8}$$

where

S is the coordinate along the circumference of the imperfect pipe with its origin at the centre of the imperfection,

R is the radius of the rigid external pipe,

S_o is the S coordinate when the imperfect liner comes in contact with the rigid pipe, and

β is a constant which controls the rate of change of the slope to the imperfect liner at S=0. When using this function, S_o and β are the two parameters that can be varied and Δ_o can be calculated accordingly.

Two other imperfection functions are used, neither of which restricts the initial circumferential length of the imperfect liner. This seems logical for the case of rehabilitation of concrete pipes, as various physical processes can be used to form the inner liner which generate a liner of length exceeding the internal nominal circumference of the rigid host pipe. The two functions used are termed "function(2)" and "function(3)" and are defined respectively as

$$y = A_o + A_1 x^3 + A_2 x^4 + A_3 x^5 \tag{5.9}$$

$$y^2 = \frac{B_o + B_1 x^4}{1 + B_2 x^4 + B_3 x^6} \tag{5.10}$$

where A_0, A_1, A_2, A_3, B_0, B_1, B_2, and B_3 are constants to be calculated from the following boundary conditions

$$\begin{aligned} y(0) &= \Delta_o, \\ \frac{dy}{dx}|_{x=0} &= 0, \\ \frac{d^2y}{dx^2}|_{x=0} &= 0 \end{aligned} \tag{5.11}$$

$$\begin{aligned} y(x_B) \quad &\text{for imperfect liner} = y(x_B) \quad \text{for rigid host pipe}, \\ \frac{dy}{dx}|_{x=x_B} \quad &\text{for imperfect liner} = \frac{dy}{dx}|_{x=x_B} \quad \text{for rigid host pipe}, \\ \frac{d^2y}{dx^2}|_{x=x_B} \quad &\text{for imperfect liner} = \frac{d^2y}{dx^2}|_{x=x_B} \quad \text{for rigid host pipe} \end{aligned} \tag{5.12}$$

The input parameters for these two equations are the coordinates of the two end points A and B (Fig. 5.9). These coordinates can be found (similar to the 1st function) from the imperfection properties Δ_o and S_o. Figure 5.10 shows the different imperfection functions for the case of normalized imperfection amplitude $\delta_o = \frac{\Delta_o}{\pi R}$=(0.0075, 0.01, and 0.03) and normalized imperfection length $s_o = \frac{S_o}{\pi R} = 0.127$

5.6.3. FEM Model Description

The same model used earlier for the analysis of the circular liner is used herein, except that the imperfect part of the liner is modelled using three 5-noded structural elements, while the rest of the liner is modelled using fourteen 5-noded elements. The model used is shown in Fig. 5.11 for a normalized imperfection length $s_o = \frac{S_o}{\pi R} = 0.127$ and a normalized imperfection amplitude $\delta_o = \frac{\Delta_o}{\pi R} = 0.030$.

5.6.4. FE Analysis of Thin Liner

To examine the performance of the FE formulation used in this study, a comparison is made with the semi-analytical solution of Kyriakides and Youn [29]. They were studying the buckling of offshore steel pipelines where the ratio t/R is very small, and this leads to circumferential strains that are negligible relative to the flexural strains. The assumptions made by Kyriakides and Youn [29] in their study were

- the pipe is inextensional (infinite membrane stiffness or liner thickness to radius ratio t/R approaching zero),
- the liner material is elastic,
- the deformations are large and the rotations are finite in a small strain scheme,
- the shear deformations are neglected (which is reasonable for their application),
- the interface between the liner and the rigid cavity is smooth, and
- initial imperfection geometry follows a function used before by Bucciarelli and Pian [8].

For the FE analysis of the imperfect liner, the ratio $AR^2/I=3*10^6$ or $t/R=0.002$ condition is used to approximate the inextensional liner condition. The case of a normalized imperfection length $s_o=\frac{S_o}{\pi R}=0.064$ and a normalized imperfection amplitude $\delta_o=\frac{\Delta_o}{\pi R}=0.0064$ is considered.

First, as a bench mark, the buckling pressure P_{cr} of the free imperfect liner under pressure "P" is calculated. The calculated pressure P_{cr} is close to the well known closed form solution $\frac{3EI}{(1-\nu^2)R^3}$ or in another form $\frac{E}{4(1-\nu^2)}\left(\frac{t}{R}\right)^3$. The deflection of the crown point is drawn versus the normalized pressure and the enhancement factor K (Fig. 5.12). The figure shows that as the pressure increases, the deformation at the crown increases till the peak pressure

is reached. At that pressure, the ring can not carry any further pressure and to sustain equilibrium the pressure should be decreased while the deformation increases. If the pressure is maintained at a level equal to or above the peak pressure, a complete collapse of the liner would occur. This phenomenon is called snap buckling, and as shown in the literature review in chapter two, it is common for all the encased ring or pipe buckling problems. The deflected shape at different load levels is shown in Fig. 5.13.

Figure 5.12 shows also the comparison between the present finite element solution and the results of Kyriakides and Youn [29]. The comparison shows very good agreement between the present finite element results and those of Kyriakides and Youn [29]. It appears that a liner with t/R=0.002 is effectively inextensional, and that shear deformations are indeed small for this thin liner case.

5.6.5. Effect of Membrane Stiffness on the Limit Load

The effect of the ratio of the membrane stiffness of the unit width of the liner (a function of EA) to its flexural stiffness (a function of EI) can change the performance of the liner under the pressure significantly. This effect has been shown for the case of the perfect circular liner in Eqns. 5.1 and 5.2. The same effect is shown in Fig. 5.14 for the case of an imperfect liner with a normalized imperfection length $s_o=\frac{S_o}{\pi R}$=0.064 and a normalized imperfection amplitude $\delta_o=\frac{\Delta_o}{\pi R}$=0.0064. Some conclusions can be draw from this figure:

- The solution in [29] for t/R=0 corresponds to the small thickness to radius ratio t/R=0.002.
- Hoop compression and bending deformations both occur in the liner. Hoop strains ε_θ are approximately given by

$$\varepsilon_\theta = \frac{PR}{Et}(1-\nu^2) = \frac{1}{8}\frac{2P}{P_{cr}}\left(\frac{t}{R}\right)^2 \qquad (5.13)$$

At the peak load, membrane strains are 0.002%, 0.13% and 1.4% for thickness to radius ratios t/R of 0.002, 0.02 and 0.10 respectively.

- As the membrane stiffness decreases, the limit load decreases significantly and the vertical crown displacement at the limit load increases as well (as a result of additional deformations in the circumferential direction of the liner).
- The pre-peak behaviour, for different t/R ratios, is dominated by membrane strains which would also control the peak pressure.
- The post peak behaviour is dominated by flexural strains, and the effect of different t/R ratios diminishes. This is implied by the converging curves for deformations bigger than the peak-load deformation.

It is very clear that neglecting the membrane deformations may lead to poor results that could produce an unsafe liner design.

5.6.6. Effect of Existence of Two Imperfections on the Critical Pressure

Many imperfections may exist in a single liner, which raises a question about the potential of having more than one imperfection and the resulting effect on the critical liner pressure. A study for the case of two liner imperfections is considered. The additional imperfection introduced is a mirror image of the first one (Fig. 5.15). This reduces the effort for the analysis as only one quarter of the problem is considered. Similar results, as reported in the previous section, are shown in Fig. 5.16 and compared to the results of a single imperfection. The effect of the membrane stiffness (or t/R ratio) is also clear. Generally the critical

pressure is higher than the case of a single imperfection which implies that the single imperfection case is more critical for design purposes. This is due to the reduction in the circumferential deformations in the attached part of the liner. The amount of increase in the critical pressure for the case of two imperfections relative to the case of single imperfection, is dependent on t/R ratio. It is shown before that for the case of large hoop stiffness (t/R=0.002), the hoops strains are negligible with respect to the flexural strains and almost no deformations occurred along the attached portion of the liner. This accounts for the similar response and critical pressure for the two imperfection cases. As t/R ratio increases, more strains develop in the circumferential direction and the case of two imperfections shows higher critical pressures.

5.6.7. Effect of the Skew of the Imperfection

The liner imperfection may take any random shape depending on conditions of the damaged host pipe and the installation process. In the previous sections, the imperfection of the circular liner is assumed to be symmetric about one of the diameters. In this section, a skew imperfection (Fig. 5.17) is considered to assess the effect of that skew on the liner behaviour. The same symmetric imperfection used before (function 1) is used with s_o=0.175 and δ_o=0.03. An additional term is added to the imperfection function (function 1) to establish the skew shape of the imperfection. This term is an odd function $y(S)$ and is defined by

$$y(S) = A_0 \; f(S) \tag{5.14}$$

where

$$f(S) = S\,(S^2 - S_1^2)\,(S^2 - S_2^2)\,(S^2 - S_3^2)\,(S^2 - S_4^2), \tag{5.15}$$

S_1, S_2, S_3, and S_4 are defined by

$$S_1 = S_o, \quad S_2 = 0.99 S_o, \quad S_3 = 0.91 S_o, \quad \text{and} \quad S_4 = 0\ 90 S_o\ . \tag{5.16}$$

and the constant A_0 is defined as

$$A_o = 0.1\ \frac{\Delta_o}{f(0.3125\, S_o)} \tag{5.17}$$

The geometry defined using the previous function has an initial slope angle at the crown of about 5°. The whole liner is modelled using thirty four 5-noded structural elements (136 nodes) and thirty four 5-noded interface elements. Two t/R ratios are examined; t/R=0.01 and 0.05. Figure 5.18 shows the liner response at the crown for both cases of symmetric and skew symmetric imperfections. The figure shows that the skew of the imperfection does not affect either the load-deflection of the crown or the critical pressure.

5.6.8. Effect of the Imperfection Geometry; Span S_o and Amplitude Δ_o

It has been reported that the magnitude of the critical pressure of the imperfect liner is highly dependent on the imperfection type and size [29]. Therefore a study has been undertaken to determine the effect of the imperfection parameters S_o and Δ_o on the critical pressure. For "function 1", a limited range of imperfection amplitudes Δ_o is possible for any imperfection length S_o given the requirement that the imperfect liner has circumference equal to the circular host pipe. The three parameters considered in this study are the normalized imperfection length $s_o = \frac{S_o}{\pi R}$, the normalized imperfection amplitude $\delta_o = \frac{\Delta_o}{\pi R}$, and the t/R ratio. Different values of s_o are chosen (s_o=0.064, 0.080, 0.095, 0.111 and 0.127) and the corresponding values for the possible imperfection amplitudes δ_o are calculated to satisfy the differential equation describing the imperfection shape (function "1"). The results for this

study are presented in two ways. The first approach uses the concept of an enhancement factor K (defined before for the circular liner case); the second approach uses the concept of a reduction factor α for the critical pressure of the encased liner due to the existence of a local imperfection.

The change in the normalized critical pressure and the enhancement factor K are shown versus the initial imperfection amplitude at the liner crown in Fig. 5.19 for t/R=0.002 and different imperfection lengths. These results imply the following:

- For any given imperfection length S_o, the critical pressure P_{cr} decreases with increases in the imperfection amplitude Δ_o.
- The effect of the imperfection amplitude Δ_o on the critical pressure P_{cr} is more important than the imperfection length S_o.
- The bigger the amplitude of the imperfection, the lower the critical pressure.
- For practical cases of thin liners with large imperfection amplitudes, the enhancement factor K=3.5 to 4.0 seems appropriate.
- A common lower bound can be drawn for all the imperfection lengths. This envelope may be a good design limit for liner selection.
- The enhancement factor K=145 for the case of no imperfection, obtained from Eqn. 5.2, is an upper bound solution for the imperfect liner.

The critical pressure reduction factor for a perfect encased liner is shown versus the initial imperfection amplitude at the liner crown in Fig. 5.20 for t/R=0.002 and different imperfection lengths. This figure gives a measure for the amount of reduction induced by the imperfection. From this figure, it is concluded that:

- The critical pressure, for small values of t/R, drops rapidly with the existence of a very small imperfection. This is very clear given the drop from unit value (for the perfect liner) to less than 0.1 for a small normalized imperfection amplitude of 0.0025. The sensitivity of the critical pressure to changes in the imperfection amplitude decreases as the imperfection amplitude becomes bigger.
- The sensitivity of liner buckling to these local imperfections imposes difficulties when defining a standard method for testing liners, and for those seeking to interpret experimental results.

To show the effect of the t/R ratio on the results, the same analysis reported for t/R=.002 is repeated for t/R=0.02, 0.05, and 0.10 respectively using the previous imperfection parameters. Figures 5.21 and 5.22 show the envelopes for the enhancement factor K versus the normalized imperfection amplitude for t/R=0.05, and 0.10. Figure 5.23 shows all the envelopes for the different t/R ratios. The following conclusions may be drawn:

- The relative thickness to radius ratio t/R significantly affects the critical pressure, and needs to be considered in the design of liners.
- the greater the t/R ratio, the lower the critical pressure, due to the additional liner deformations permitted in the circumferential direction
- The critical pressure decreases with increases in the imperfection amplitude for all t/R ratios.
- For imperfection amplitude Δ_o/R equal to or greater than 0.1, the enhancement factor K=3.5 seems to be the appropriate minimum value for all values of t/R.

5.6.9. Effect of the Choice of the Imperfection Shape

A comparison between the three imperfection functions (defined previously) is accomplished to study the sensitivity of the solution to the imperfection shape. Figures 5.24 and 5.25 show results of the parametric study obtained for functions "2" and "3" for the case of t/R=0.002 using the same imperfection spans s_o used before for studying imperfection function "1". The difference of limit pressure between the three different cases is in the order of 15%, but the envelopes are almost the same.

5.7. Summary and Conclusions

A finite element analysis to assess the critical pressure acting on an encased liner is described. The FE formulation allows for large deformations in a small strain scheme as well as the non-linear interface behaviour. Two pressure distributions are considered; uniform and hydrostatic distributions.

Two distinct liner cases are considered; perfect and imperfect circular liners. A comprehensive parametric study is accomplished for each case. For perfect liners, the effect of the thickness to radius ratio t/R is identified. The finite element results are compared with available analytical and experimental data. For imperfect liners, the influence of both t/R and imperfection size on the critical pressure are discussed. The following main conclusions may be drawn:

- While the assumption of inextensional liner t/R=0 is acceptable for some applications, it is not the case for a polymer liner subjected to pressure. For example, at the peak load, the hoop strains are 0.002%, 0.13%, and 1.4% for liner thickness to radius r. - t/R of

0.002, 0.02, and 0.1 respectively. This implies that the t/R ratio should be included in the assessment of the critical liner pressure.

- The results of the finite element analysis, for the perfect circle, compares well with Glock's analytical solution [18] and represents a lower bound for almost 90% of the available experimental results.
- It is common to have small geometrical imperfections in a liner. The assessment of the size of these imperfections (i.e. Δ_o) is very important because imperfections reduce the critical pressure significantly.
- The three imperfections examined in this study had critical pressure which varied about 15%. In spite of this variation, the envelope for critical pressure for all the examined cases, is almost the same for the three imperfections.
- The case of a single imperfection is more critical than the case of having two diametrically opposed imperfections. This is due to the reduction in the circumferential deformations in the attached part of the liner. The larger the t/R ratio, the greater the increase in the critical pressure for the case of two symmetric imperfections relative to the case of single imperfection.
- The hydrostatic fluid pressure distribution produces almost the same critical pressure as for the case of uniform pressure distribution.
- The skewness of the imperfection has a minor effect on the critical liner pressure and can be neglected.

Resin	Mean Outer Diameter (mm)	Liner Thickness (mm)	Gap %	Test P_{cr} (psi)	Young's Modulus (N/mm^2)	Yield Stress (N/mm^2)
Epoxy 250/99 P&S	250.20	5.15	1.80	77 00	2370.00	16.10
"	251.20	5.45	1.40	112.00	2200.00	27.60
"	252.70	2.80	0.80	13.90	1910.00	25.70
"	251.60	4.50	1.30	53.80	2270.00	19.80
"	251.60	7.40	1.30	141.00	2380.00	19.40
"	252.80	4.60	0.80	72.00	2250.00	23.90
"	251.40	7.00	1.30	200.00	2130.00	33.20
Poly 405 NUTTAL	252.50	5.80	0.90	46.40	1370.00	20.80
4148/12 Epoxy	244.40	5.20	4.10	58.00	1760.00	36.60
"	248.60	5.45	2.40	54.00	2150.00	38.40
305 GY Epoxy	248.60	4.25	2.40	18.20	1220.00	27.70
"	253.70	4.75	0.40	49.00	1040.00	31.10
"	241.30	5.05	5.30	28.00	2370.00	40.10
Poly 405	252.80	5.30	0.80	94.00	1770.00	28.50
"	252.20	5.05	1.00	64.00	960.00	32.70
"	2· 80	5.05	2.00	92.00	1610.00	27.70
"	248.90	5.75	2.30	92.00	2530.00	21.30
"	249.60	5.42	2.00	81.00	1960.00	31.70
"	250.10	5.68	1.80	91.00	1910.00	26.00
"	250.30	5.62	1.80	97.00	1730.00	28.20
"	247.50	5.55	2.90	94.00	2570.00	34.20
"	247.10	4.95	3.00	62.00	2080.00	35.90
"	247.25	5.12	3.00	68.00	1830.00	34.20
"	247.18	5.08	3.00	67.00	1980.00	31.20
"	247.80	4.90	2.70	96.00	1980.00	29.50
"	248.40	5.20	2.50	72.00	2020.00	31.50
"	247.00	5.15	3.10	89.00	1960.00	32.10
"	249.20	5.60	2.20	88.00	1840.00	33.50
"	246.90	4.10	3.10	51.00	1340.00	35.60
"	247.10	4.85	3.00	61.00	1440.00	36.00

Table 5.1. Experimental Results of Aggarwal and Cooper [1]

Resin	Mean Outer Diameter (mm)	Liner Thickness (mm)	Gap %	Test P_{cr} (psi)	Young's Modulus (N/mm^2)	Yield Stress (N/mm^2)
Poly 405	247.05	4.16	3.00	62.00	1790.00	38.70
"	235.60	4.02	7.50	35.00	1430.00	37.80
"	248.60	4.10	2.40	35.00	1280.00	34.10
Derakane	252.25	6.82	1.00	115.00	1421.00	40.40
"	253.05	6.93	0.70	140.00	1779.00	47.70
"	250.95	6.20	1.50	75.00	1344.00	35.60
"	250.80	6.00	1.60	73.00	1454.00	35.20
"	248.80	3.30	2.40	34.00	1400.00	33.70
"	249.10	3.27	2.20	37.00	1355.00	34.20
Synres	248.05	2.98	2.60	18.00	1220.00	35.70
"	249.00	3.20	2.30	21.00	1649.00	45.00
4168.00	250.20	6.48	1.80	138.00	2141.00	33.10
"	250.85	8.40	1.60	210.00	2097.00	41.40
"	249.05	3.50	2.30	35.00	2443.00	43.10
"	250.85	8.10	1.60	220.00	1787.00	59.10
Synres	250.10	7.60	1.80	180.00	2059.00	53.50
"	249.50	5.60	2.10	78.00	1667.00	41.20
"	252.30	6.98	1.00	132.00	1710.00	45.20
"	249.60	6.90	2.00	99.00	1110.00	43.60

(continued) **Table 5.1.** Experimental Results of Aggarwal and Cooper [1]

Notes:

- Short term Young's modulus E is calculated from the results of a bending test for a specimen of length 105 mm and width 15 mm. The applied force F and the deflection Δ of the specimen are plotted and the value F/Δ is calculated. Young's modulus is calculated using the relation $E = \frac{L^3}{4}\frac{F}{\Delta}\frac{1}{bh^3}$, where L is the specimen span (L=96 mm), and b and h are the cross section width and height respectively.
- No record of the method used to measure the gap between the liner and the host rigid steel pipe.
- The inner diameter of the host steel pipe is 254.8 mm.
- Localized structural failures in the liner are reported by Aggarwal and Cooper.

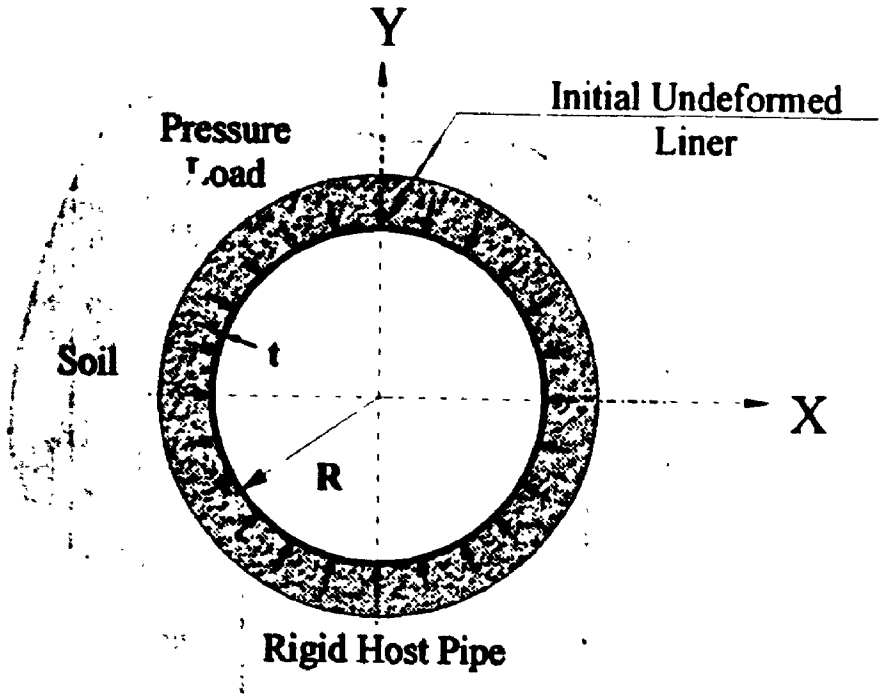

Figure 5.1a Perfect Liner

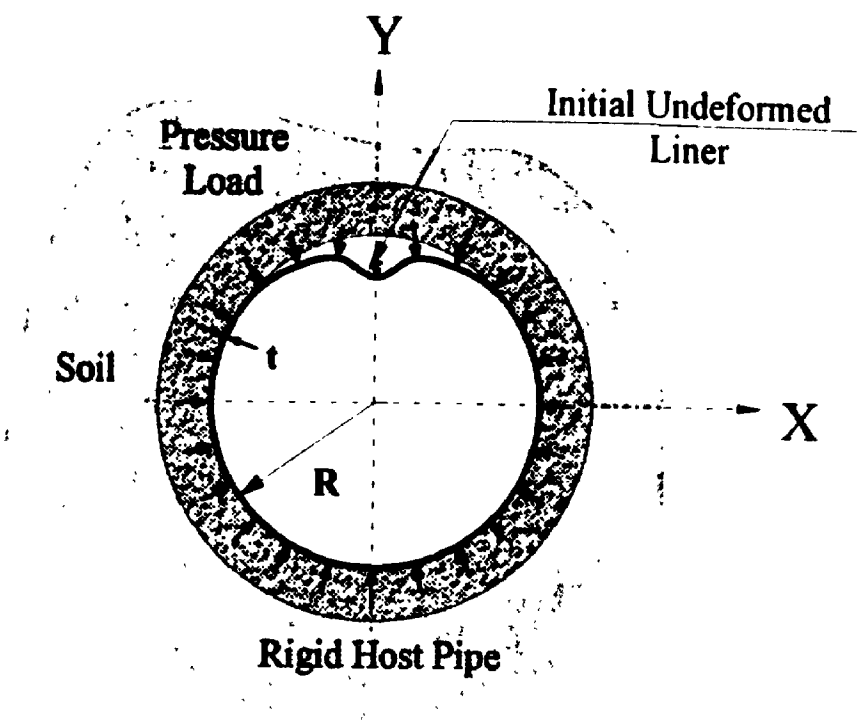

Figure 5.1b Imperfect Liner

Figure 5.1. Definition of The Liner Buckling Problem

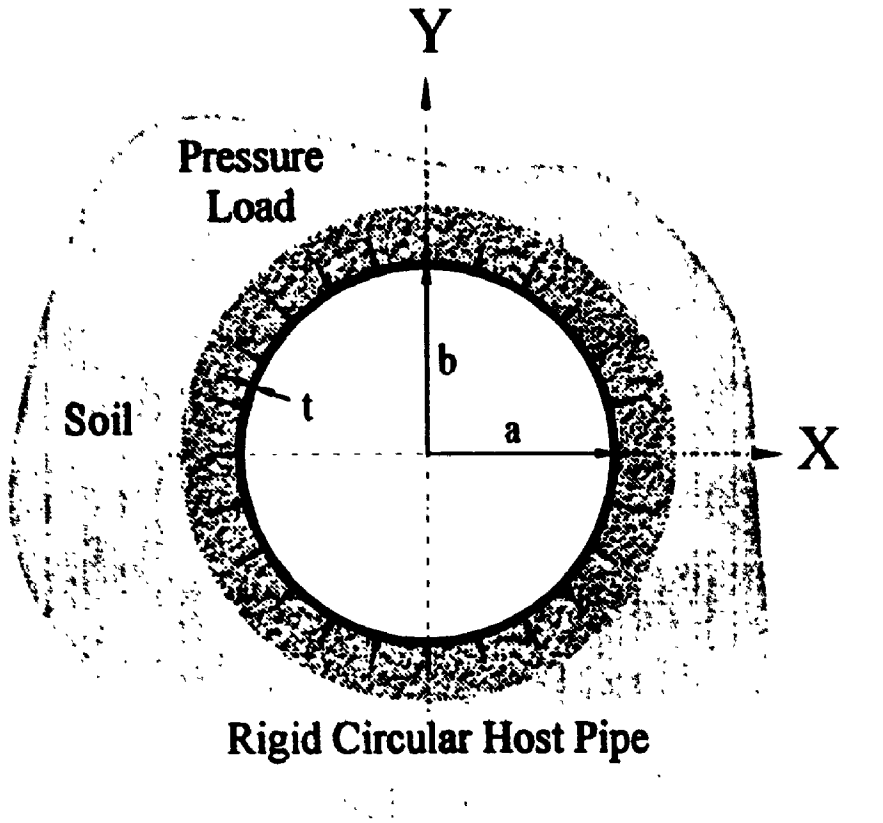

Figure 5.2a. Definition of The Problem

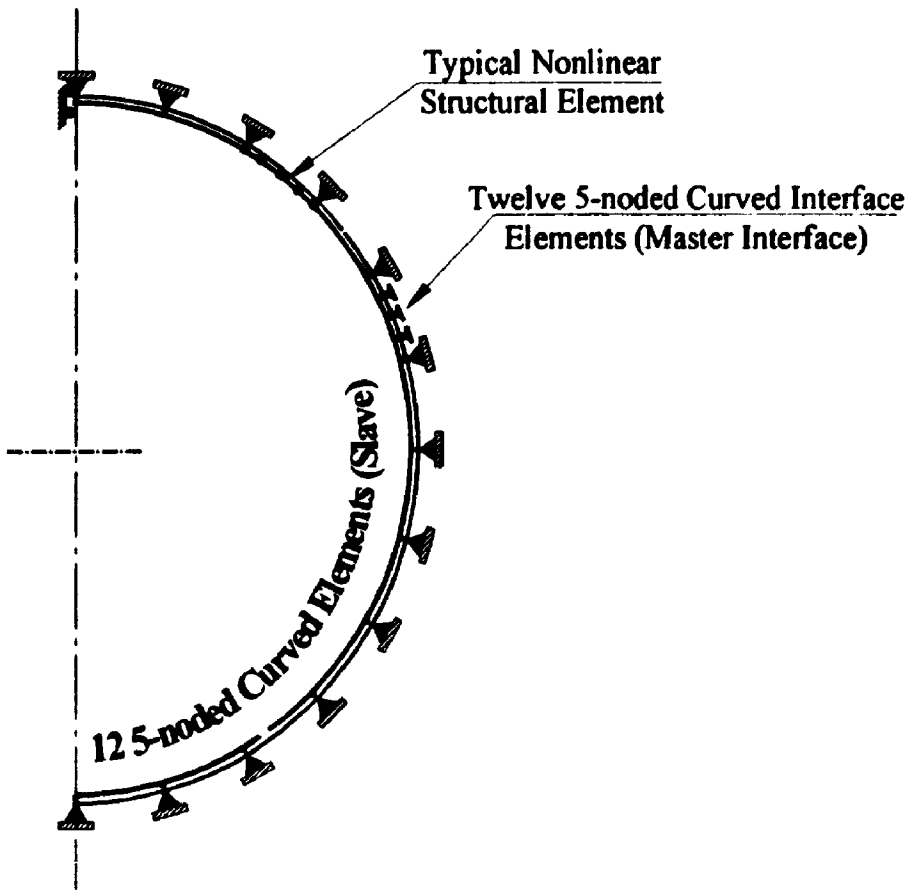

Figure 5.2b. FEM Model

Figure 5.2. Circular Liner Encased in a Rigid Pipe (a/b=1.0005, R=(a+b)/2)

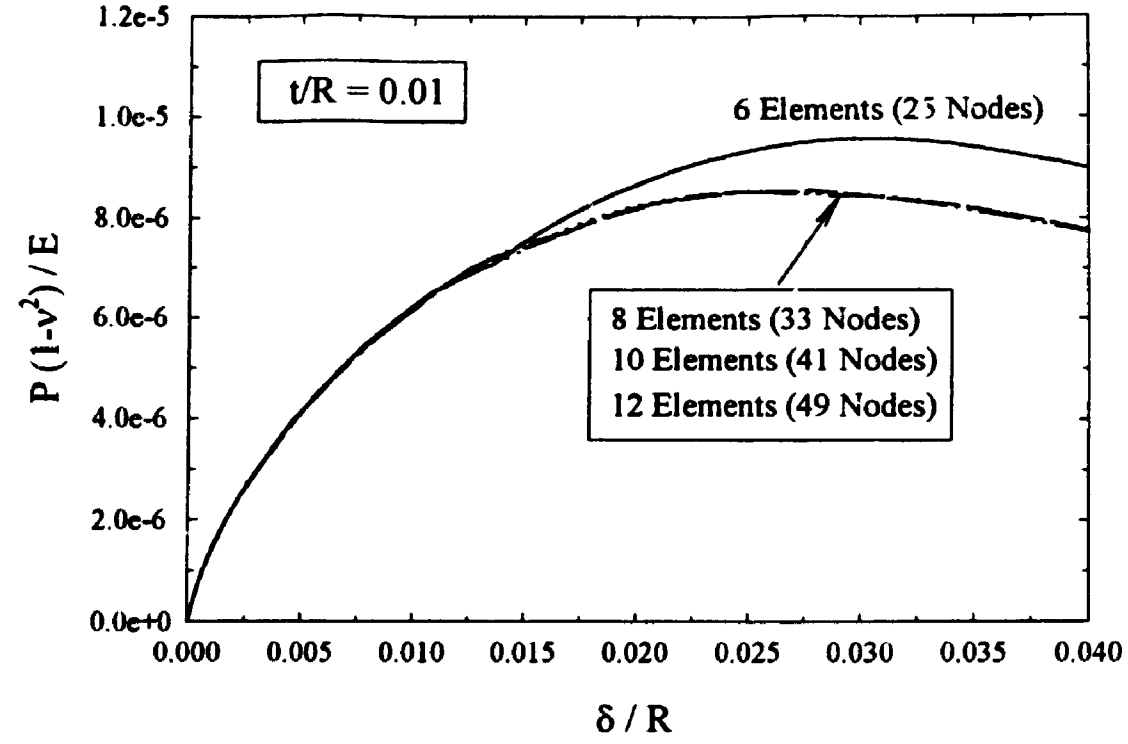

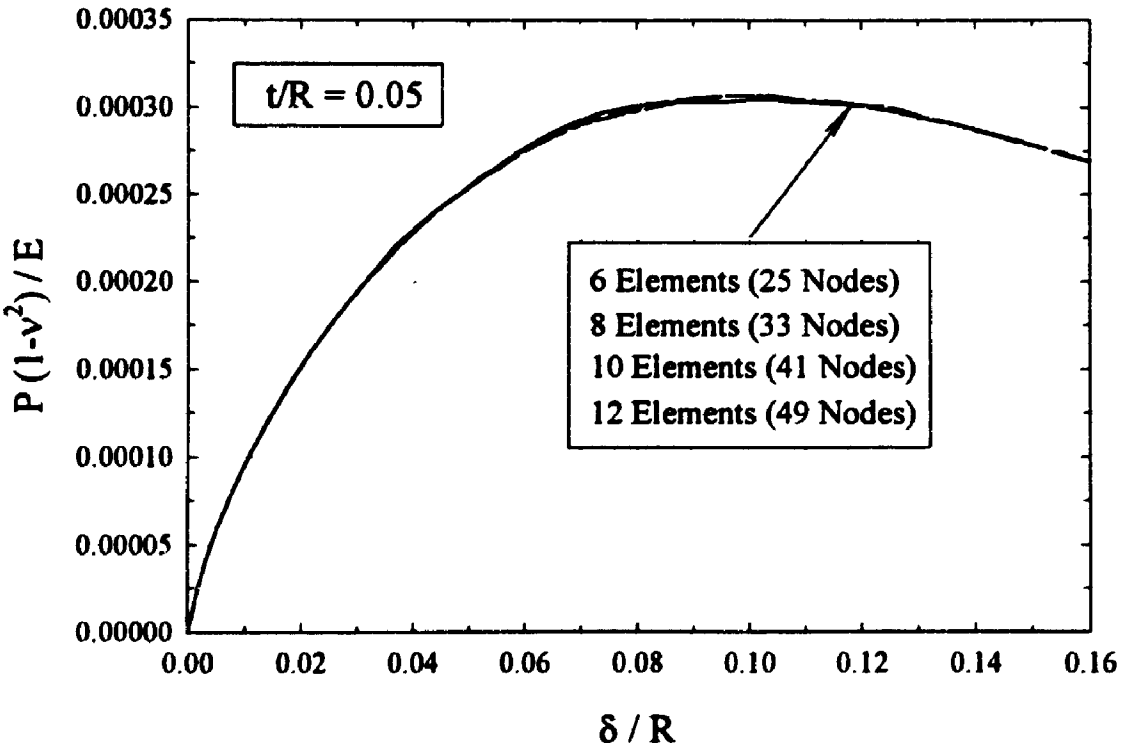

Figure 5.3. Convergence Study for Effect of the Number of Elements Used in the Analysis of Circular Liners

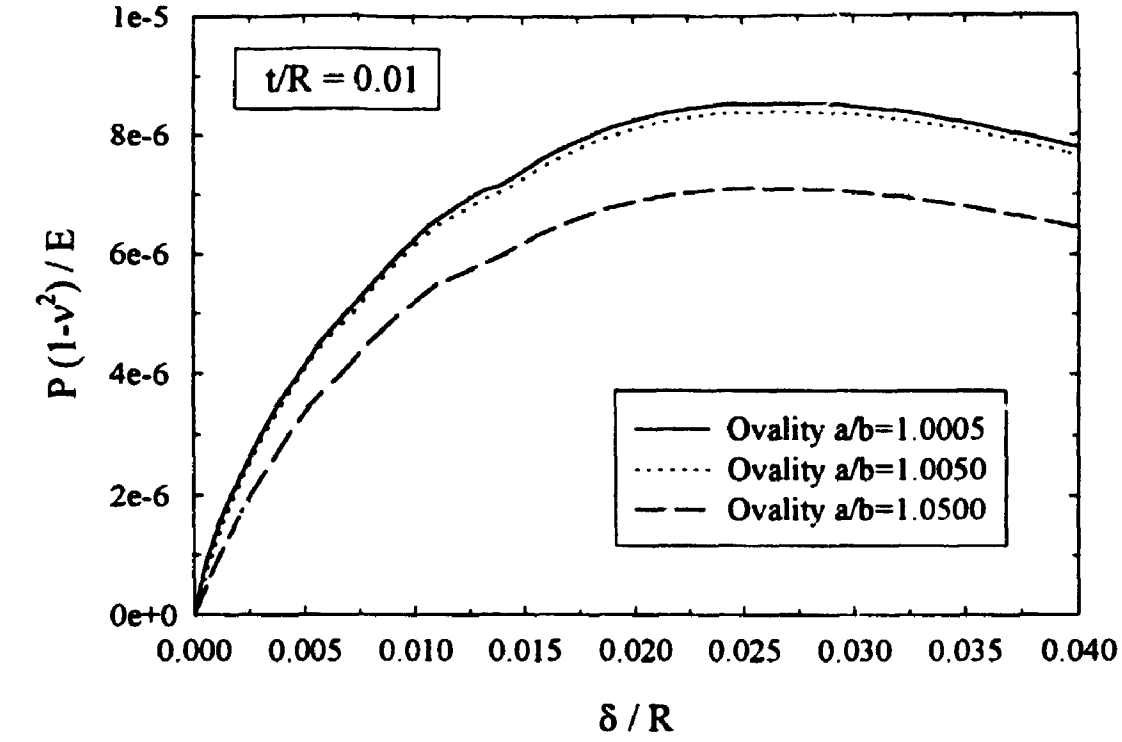

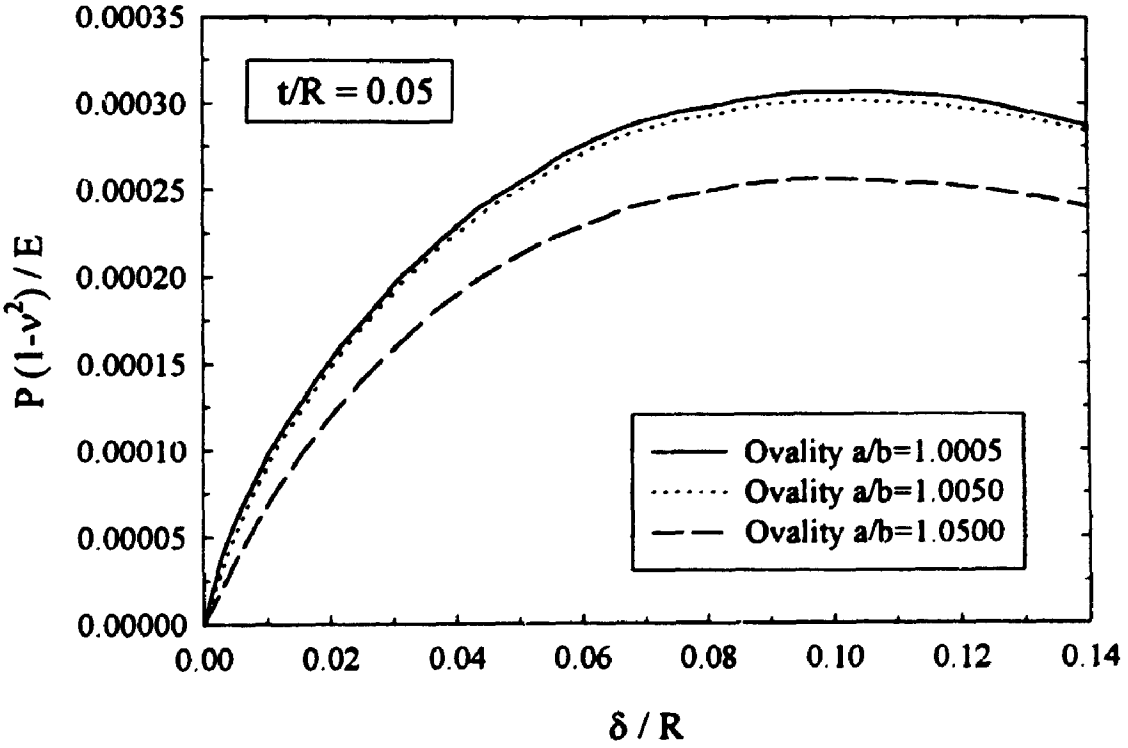

Figure 5.4. Convergence Study for the Effect of the Ovality Ratio a/b Used in the Analysis of Circular Liners

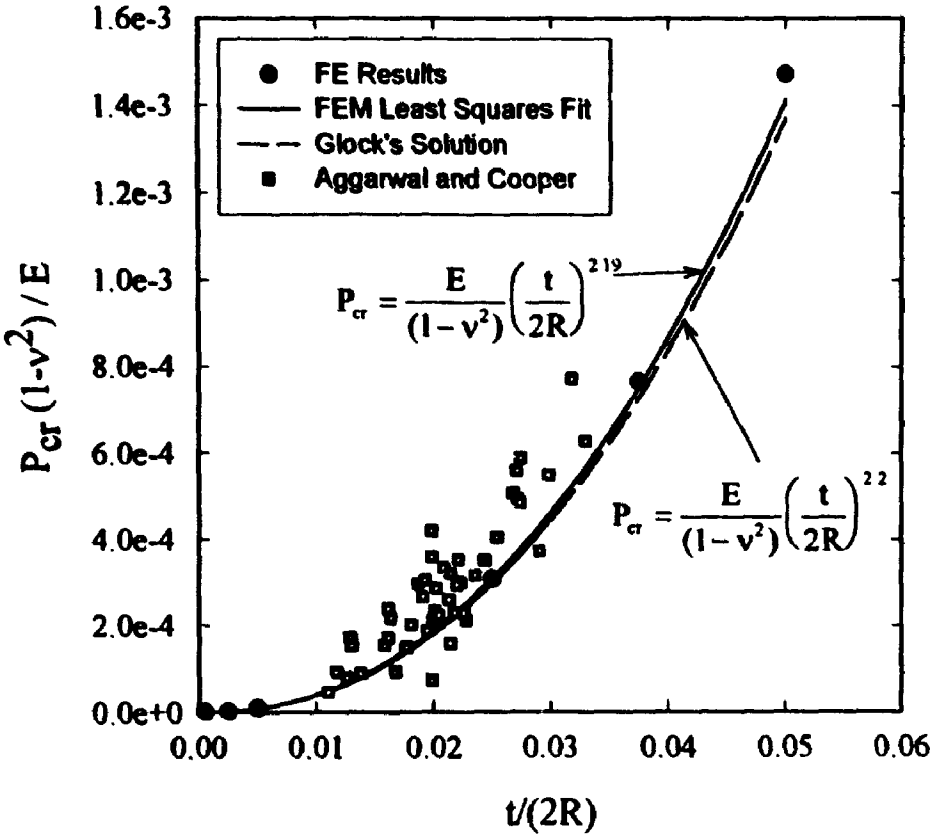

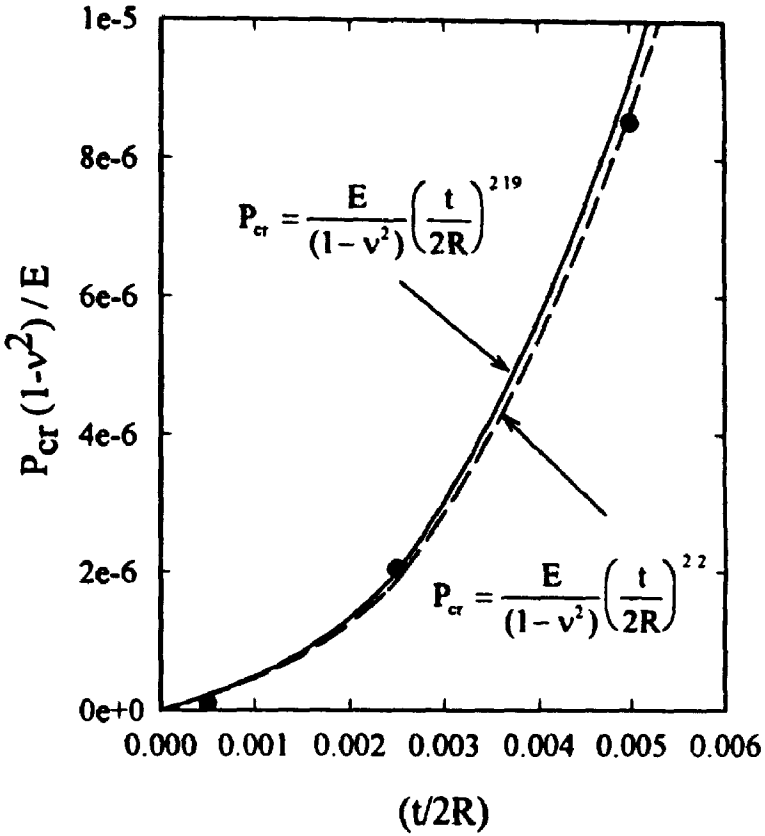

Figure 5.5. Critical Pressure of a Circular Liner in a Rigid Cavity Versus Thickness to Radius Ratio

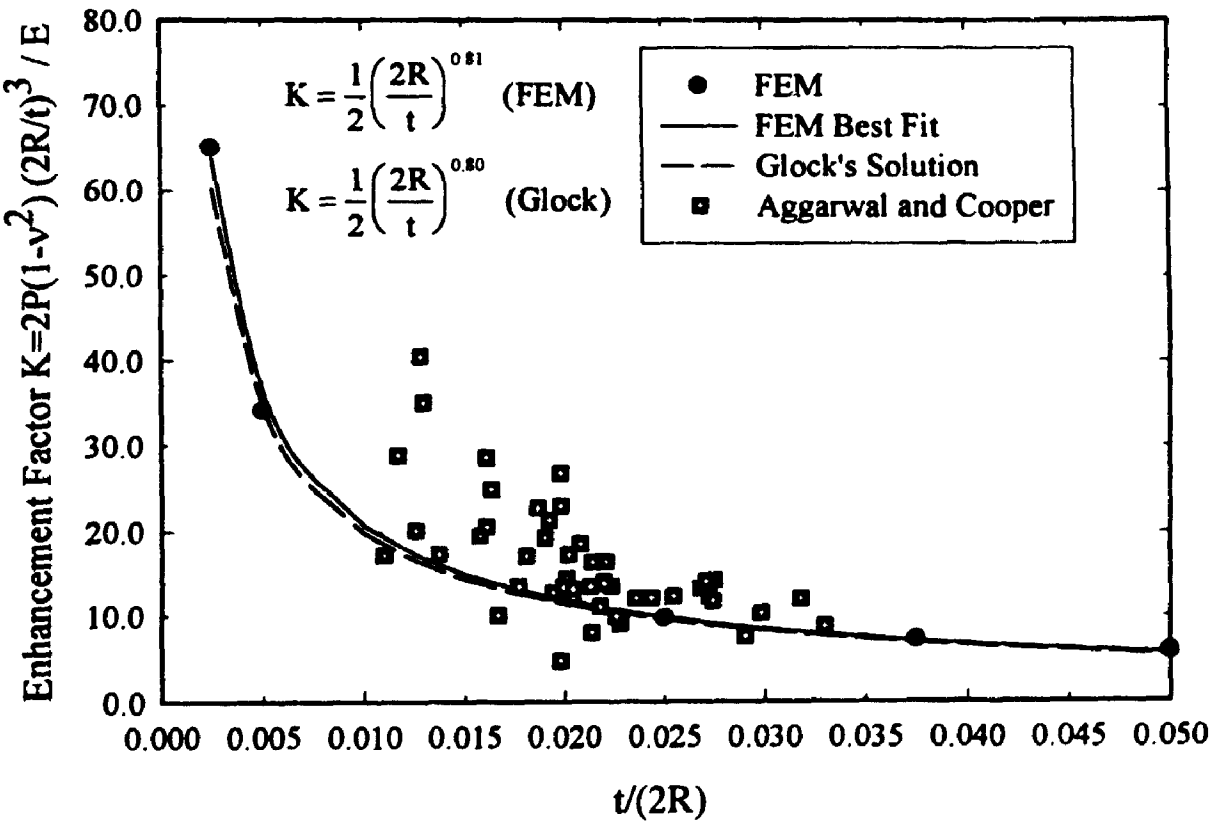

Figure 5.6. The Enhancement Factor for the Critical Pressure of a Circular Liner in a Rigid Cavity

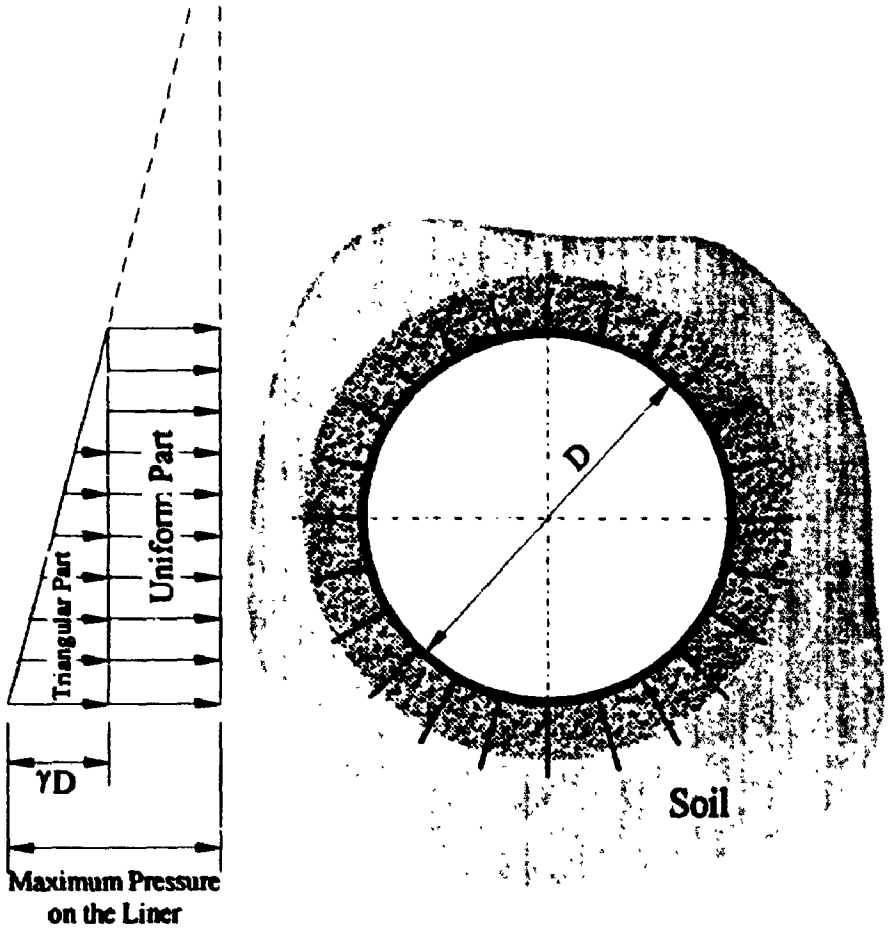

Figure 5.7a. Liner Under Hydrostatic Pressure

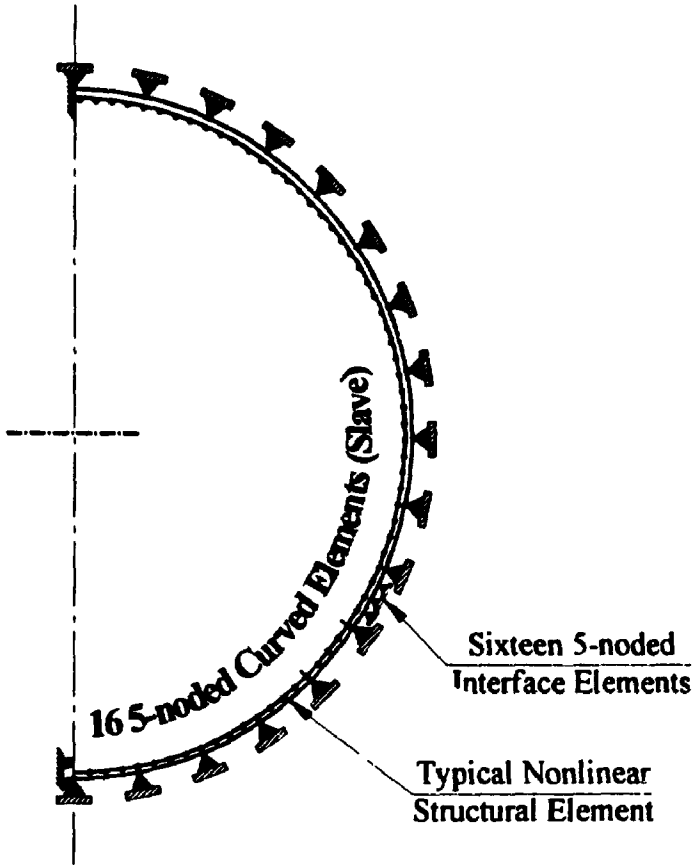

Figure 5.7b. FEM Model

Figure 5.7. Circular Liner Encased in a Rigid Pipe Under Hydrostatic Pressure Load

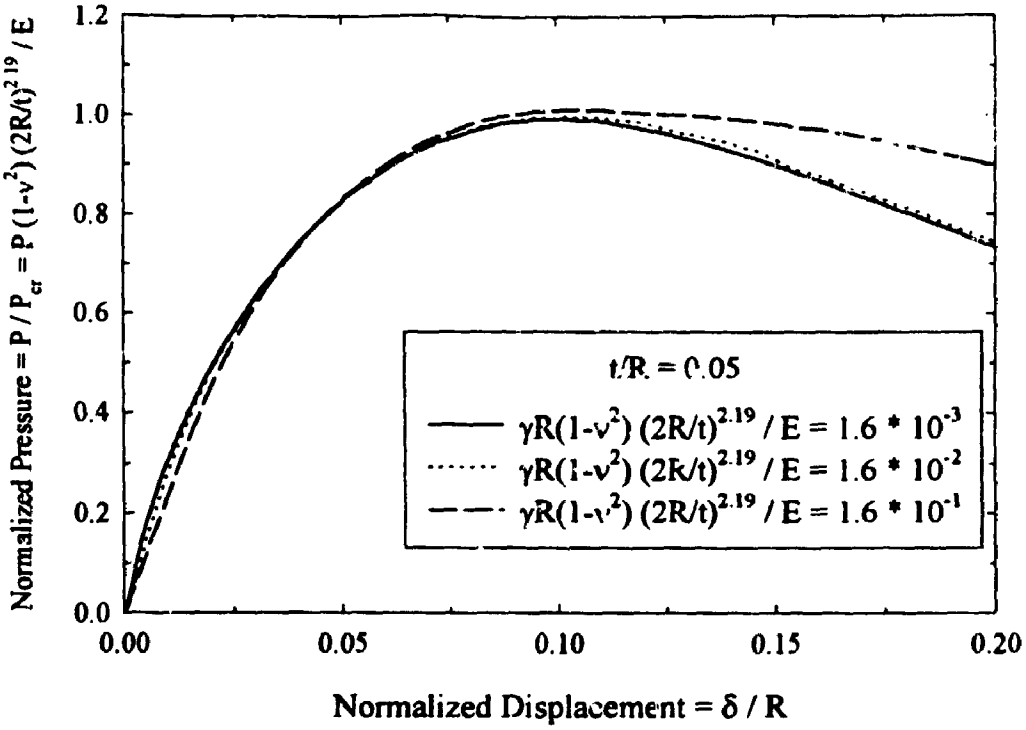

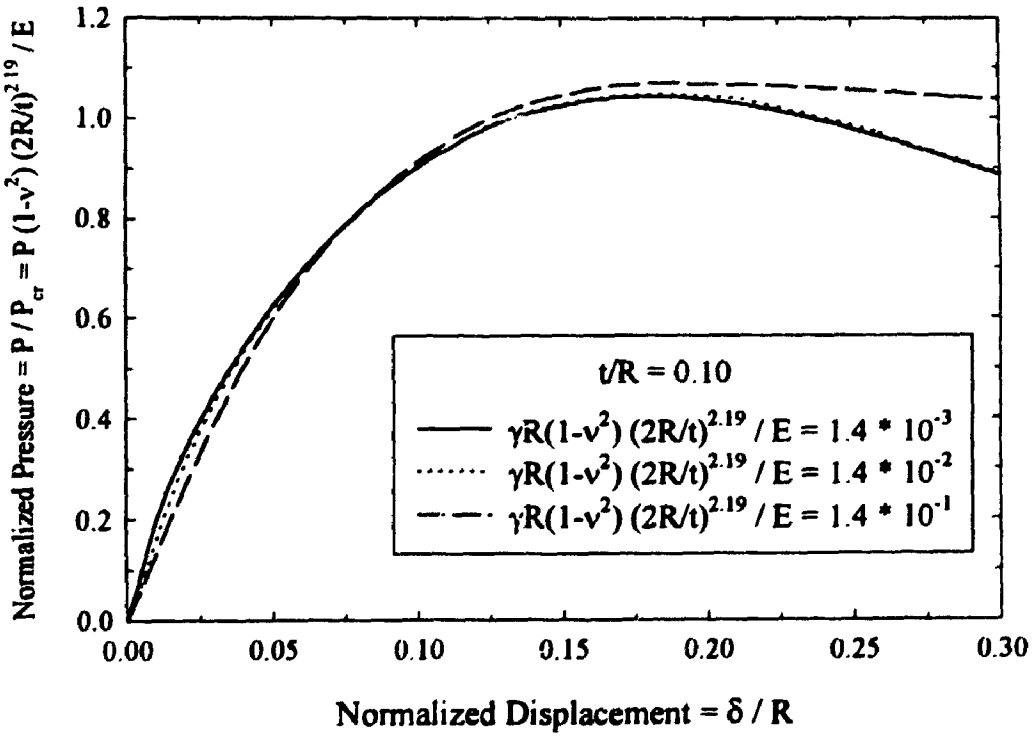

Figure 5.8. Load-Deflection of the Liner Under Hydrostatic Pressure for Different (t/R) Ratios

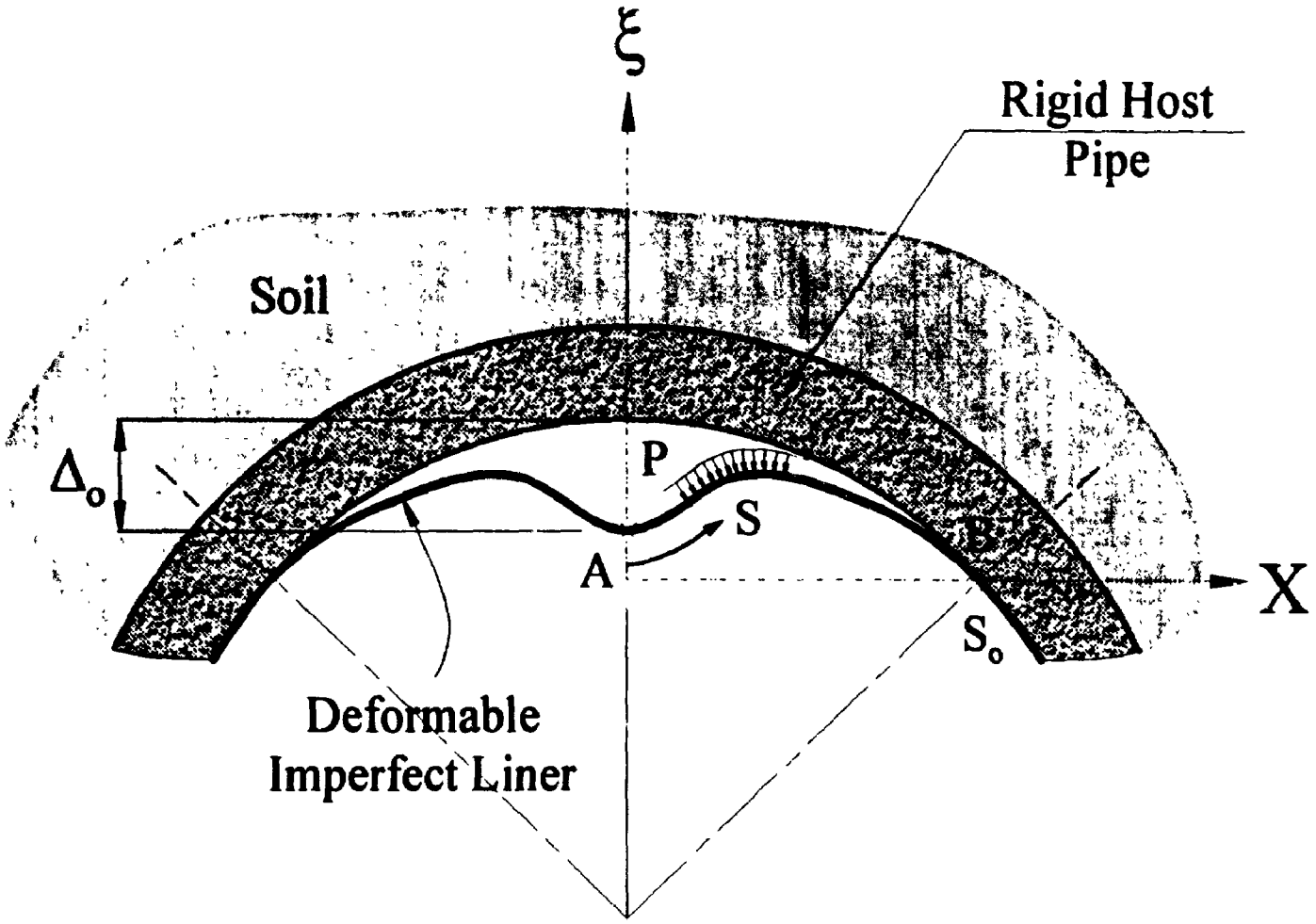

Figure 5.9. Definition of The Imperfection Geometry

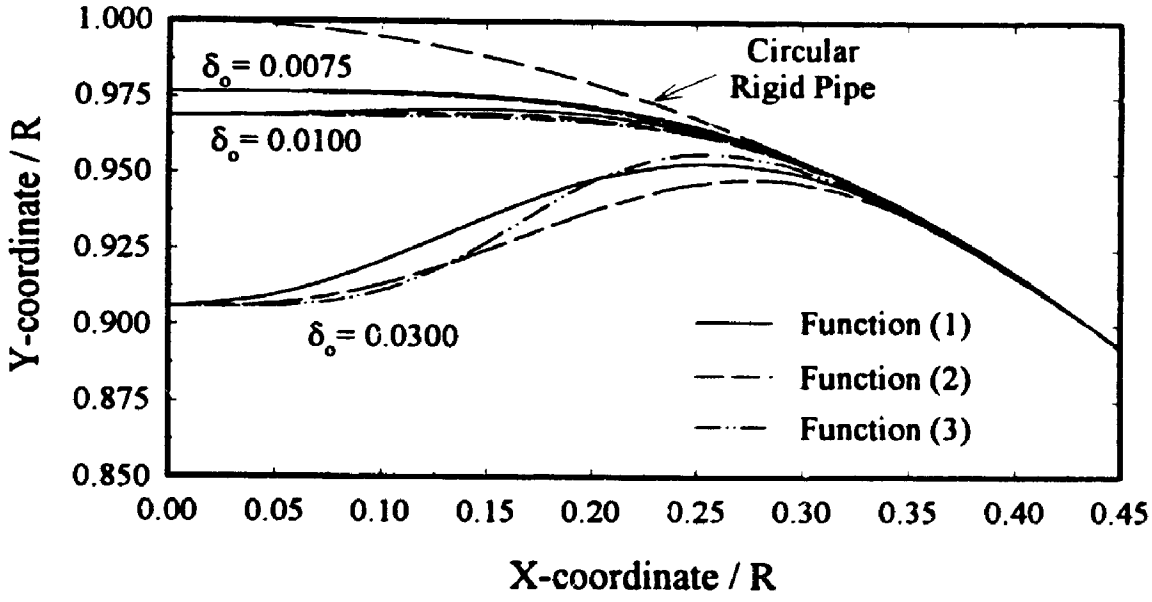

Figure 5.10. Graph for Comparison between Different Imperfection Functions

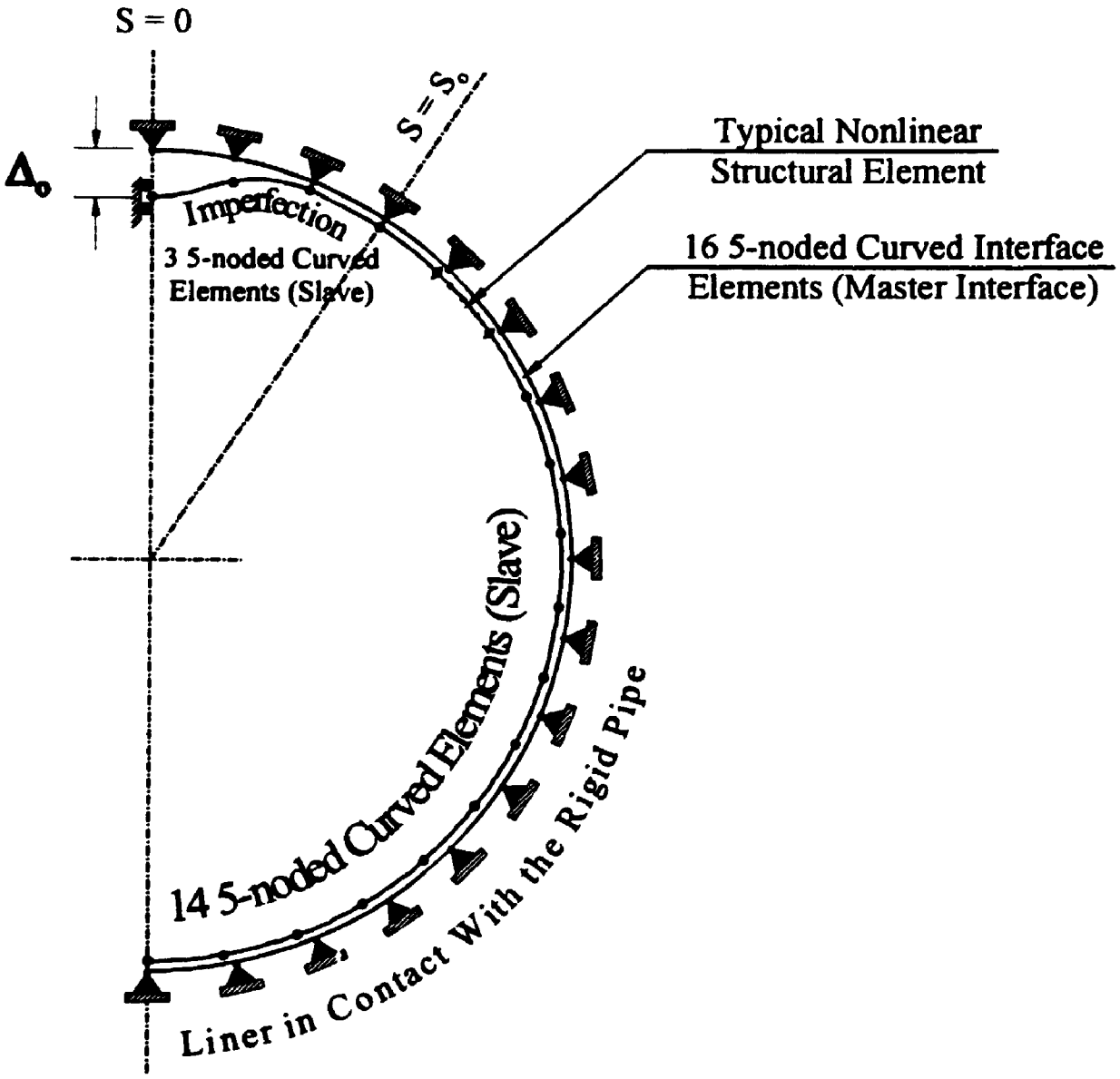

Figure 5.11. Finite Element Finite Model for Imperfect Liner

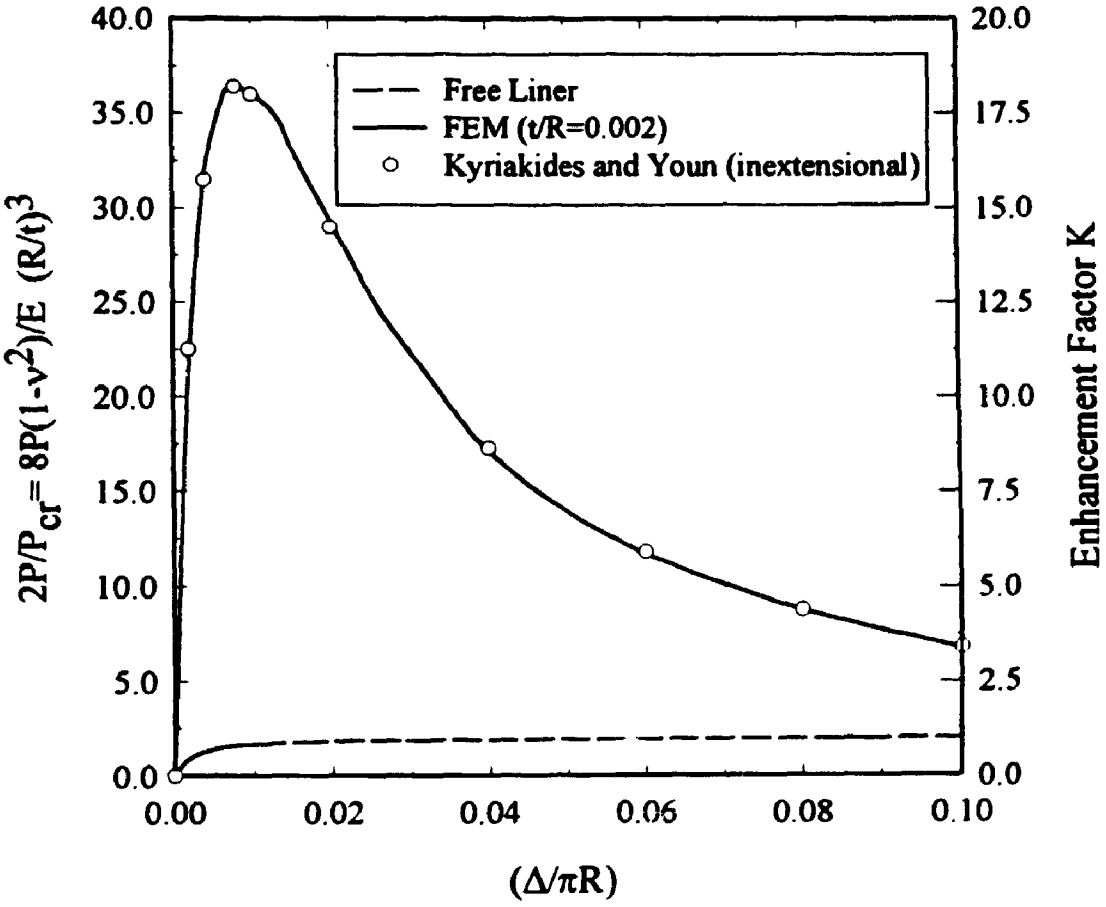

Figure 5.12. Comparison Between FEM and Kyriakides Semi-Analytical Solution

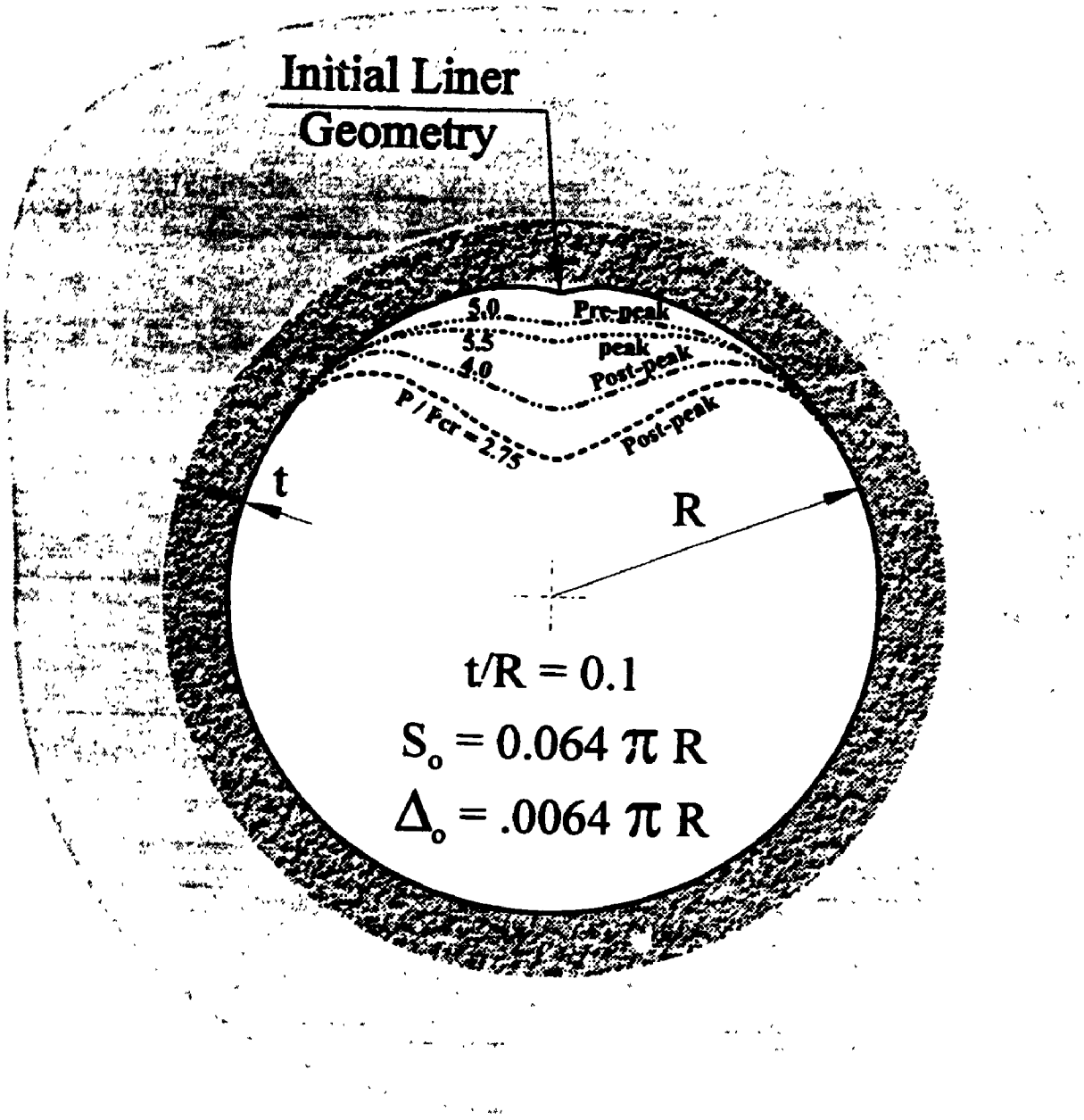

Figure 5.13. Deformed Liner at Different Load Levels

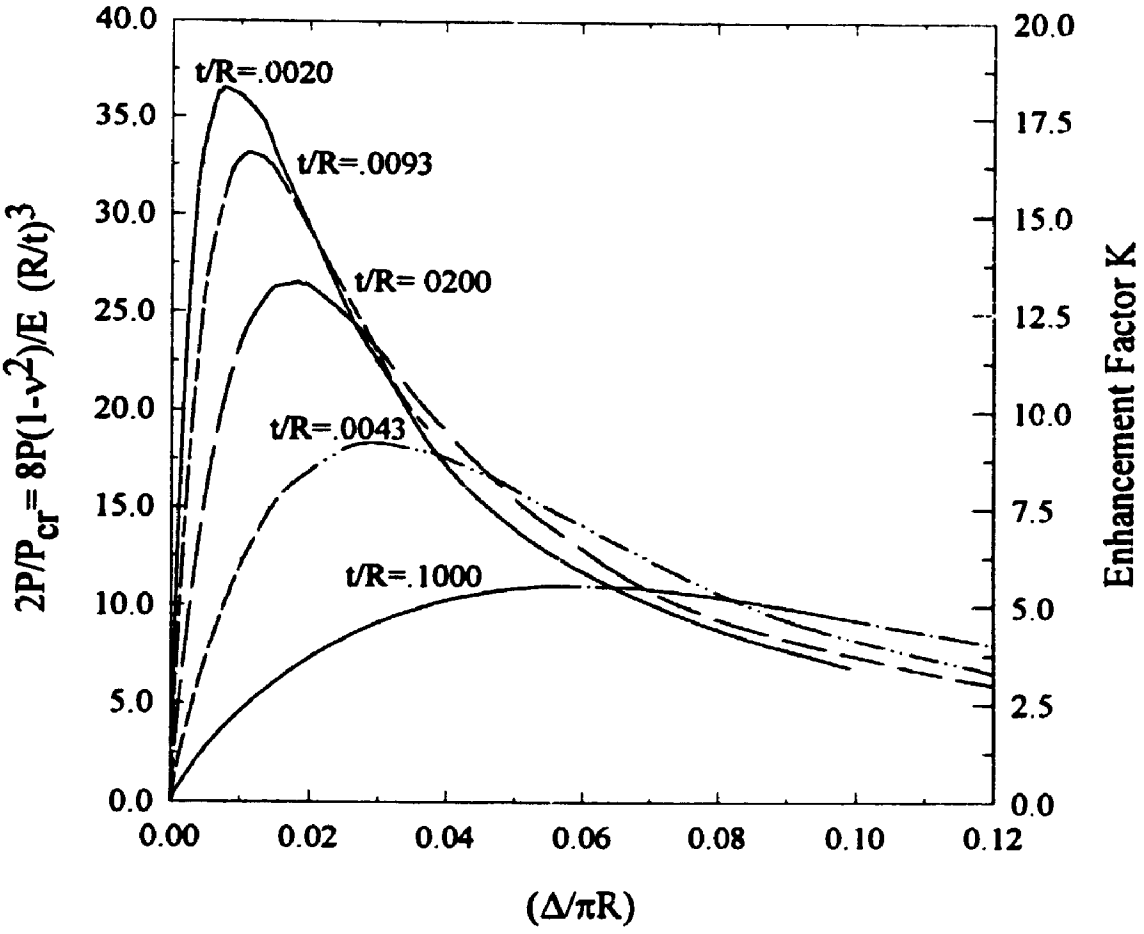

Figure 5.14. Effect of (t/R) Ratio on the Response of an Imperfect Circular Liner

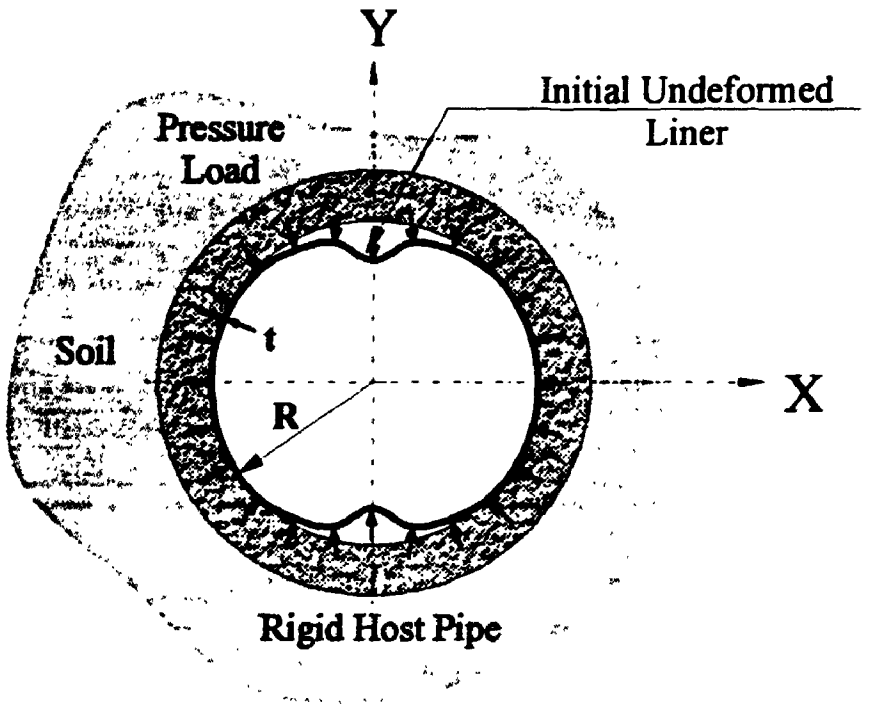

Figure 5.15. Geometry of a Liner with Two Local Imperfections

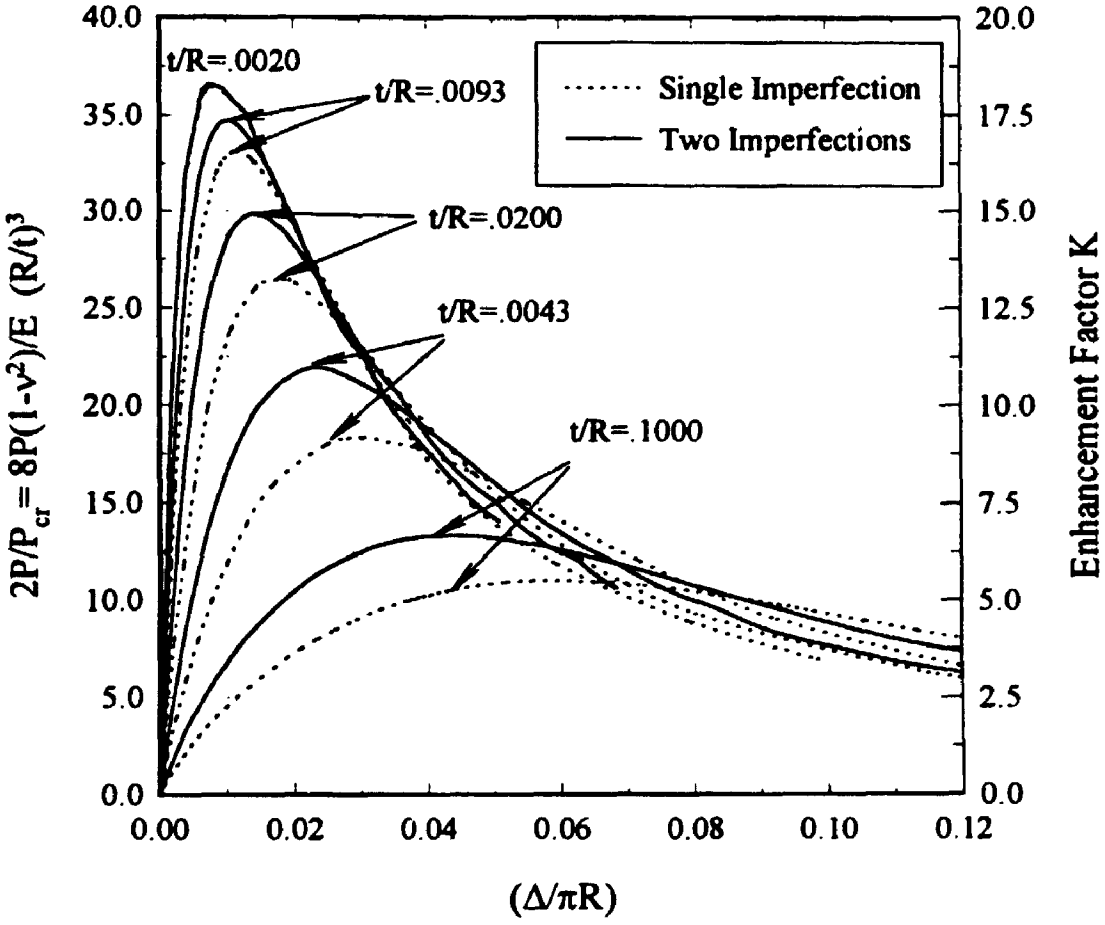

Figure 5.16. Comparison Between Responses of Single and Two Imperfections for Different t/R Ratios

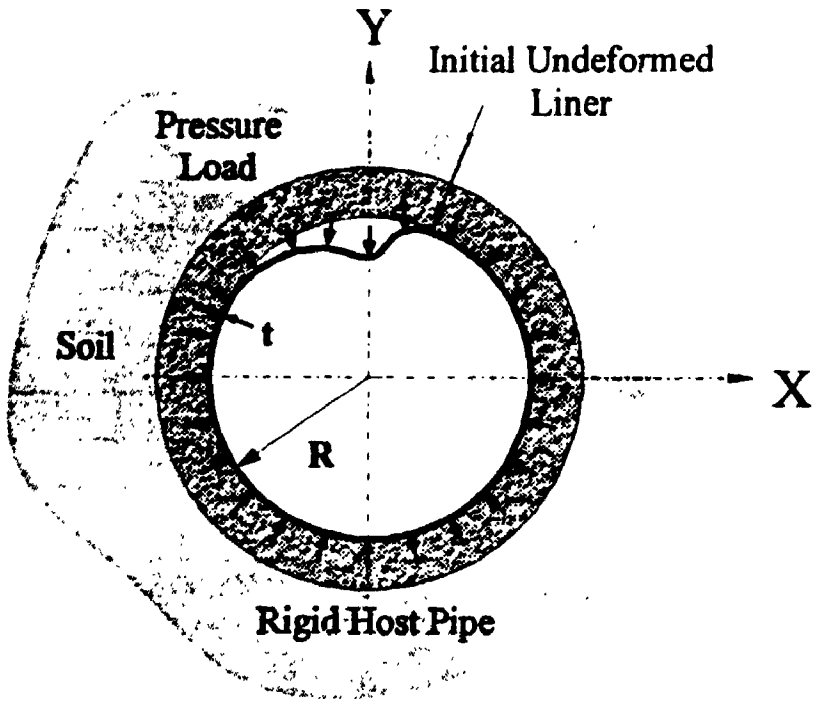

Figure 5.17a Liner with a Local Skew Imperfection

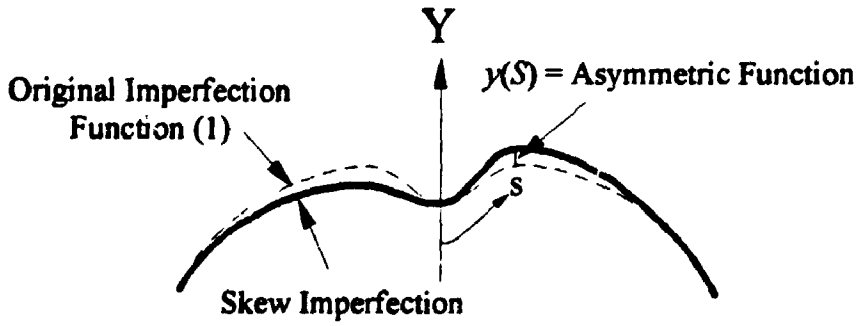

Figure 5.17b Geometry of the Local Skew Imperfection

Figure 5.17. Geometry of a Liner with a Local Skew Imperfection

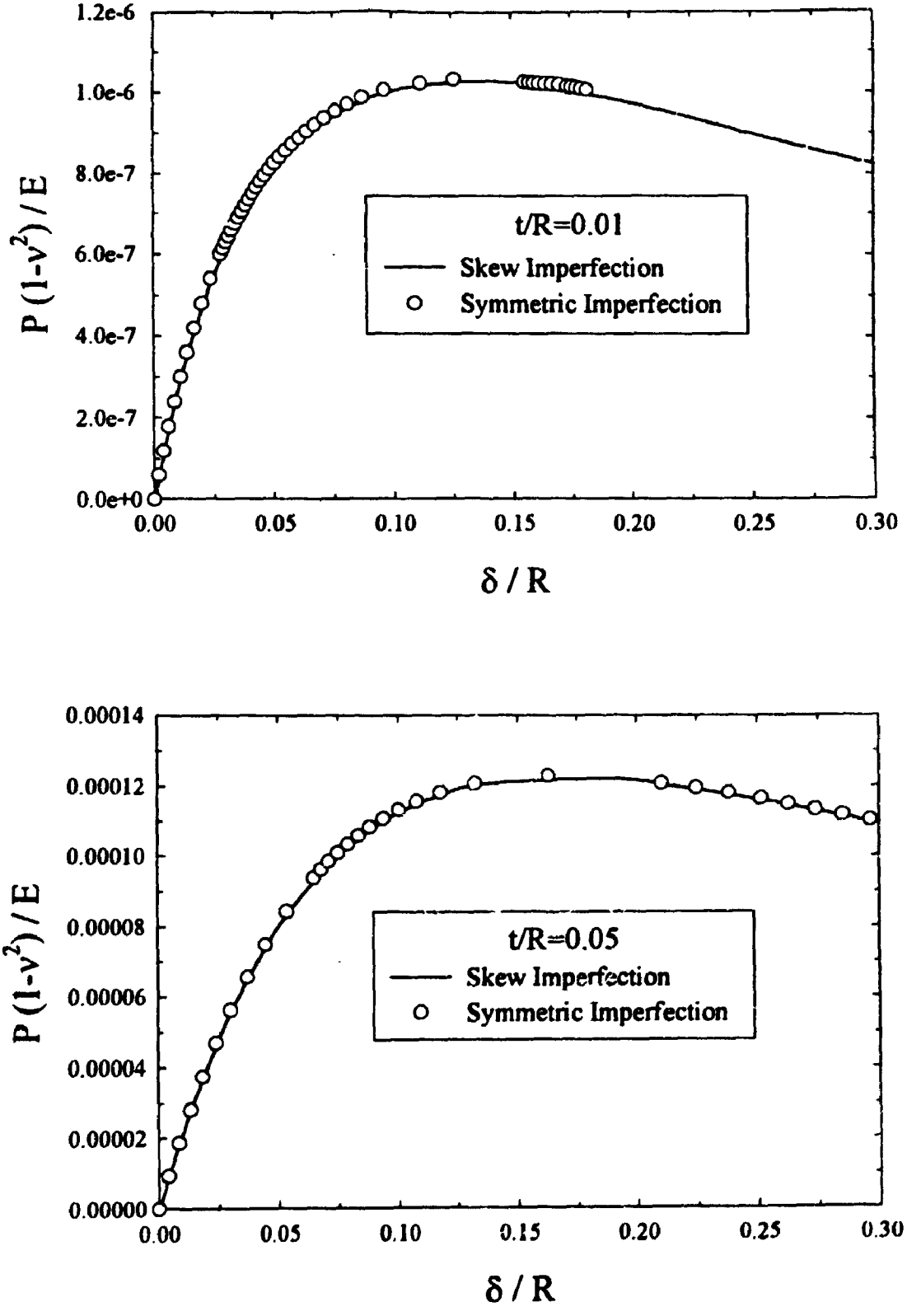

Figure 5.18. Effect of Imperfection Skewness on the Load-Deflection of the Liner Crown for Different (t/R) Ratios

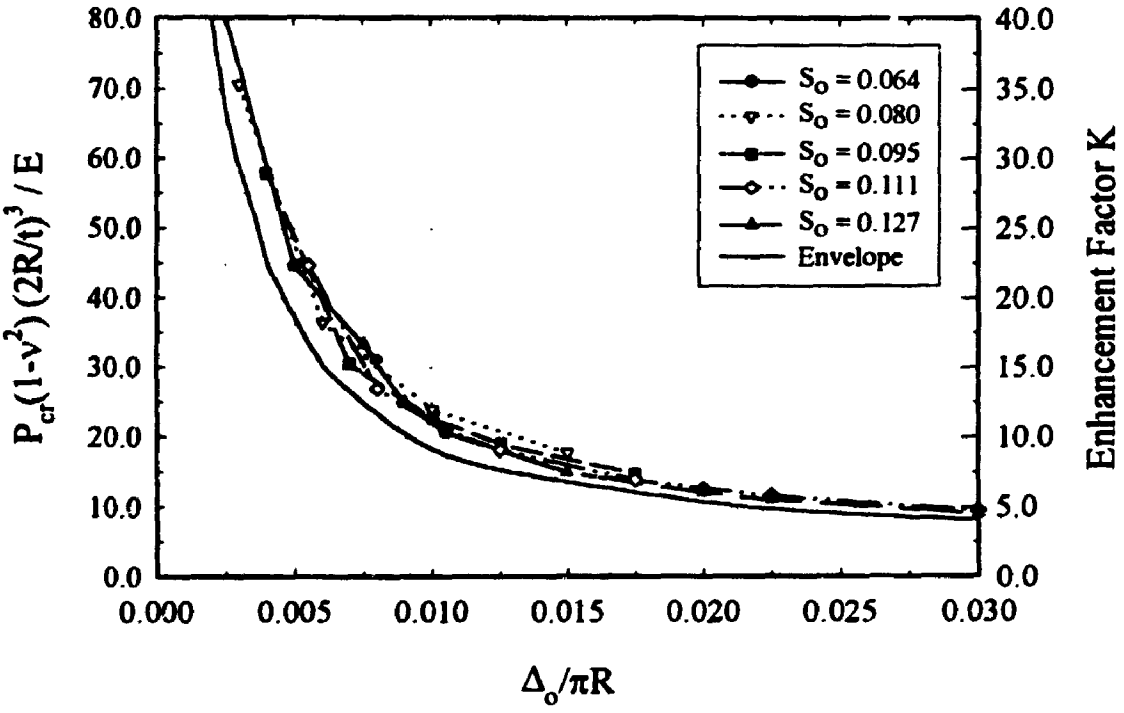

Figure 5.19. Enhancement Factor of The Critical Pressure for t/R=0.002

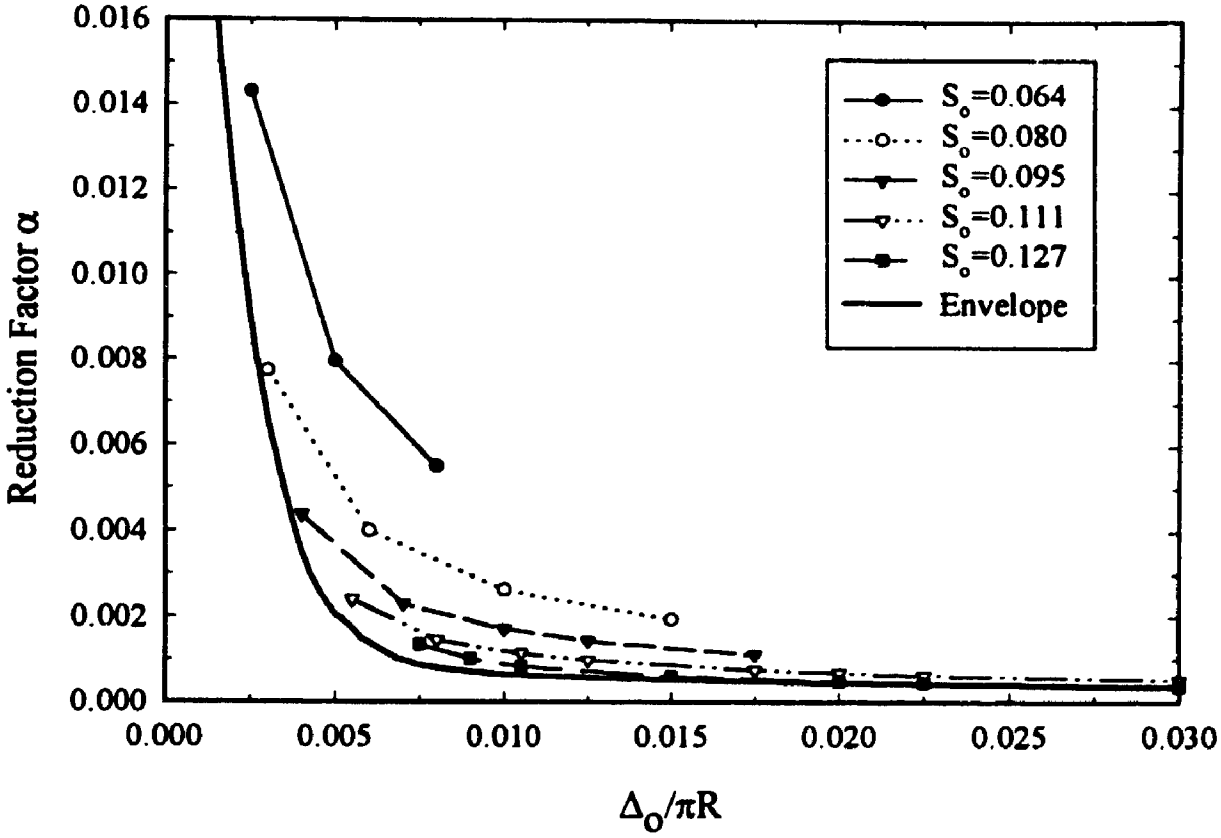

Figure 5.20. Reduction Factor for The Critical Pressure of Imperfect Liners (t/R=0.002)

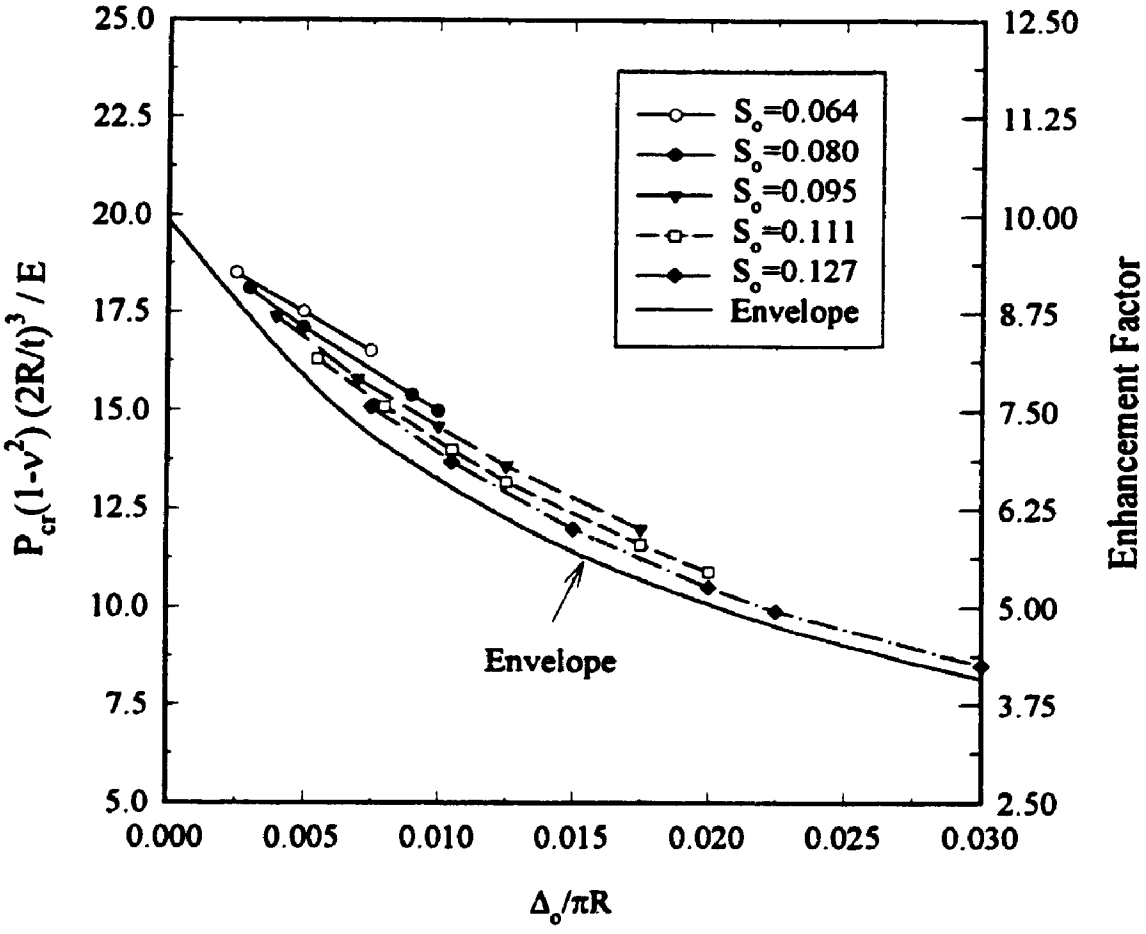

Figure 5.21. Enhancement Factor of The Critical Pressure for t/R=0.050

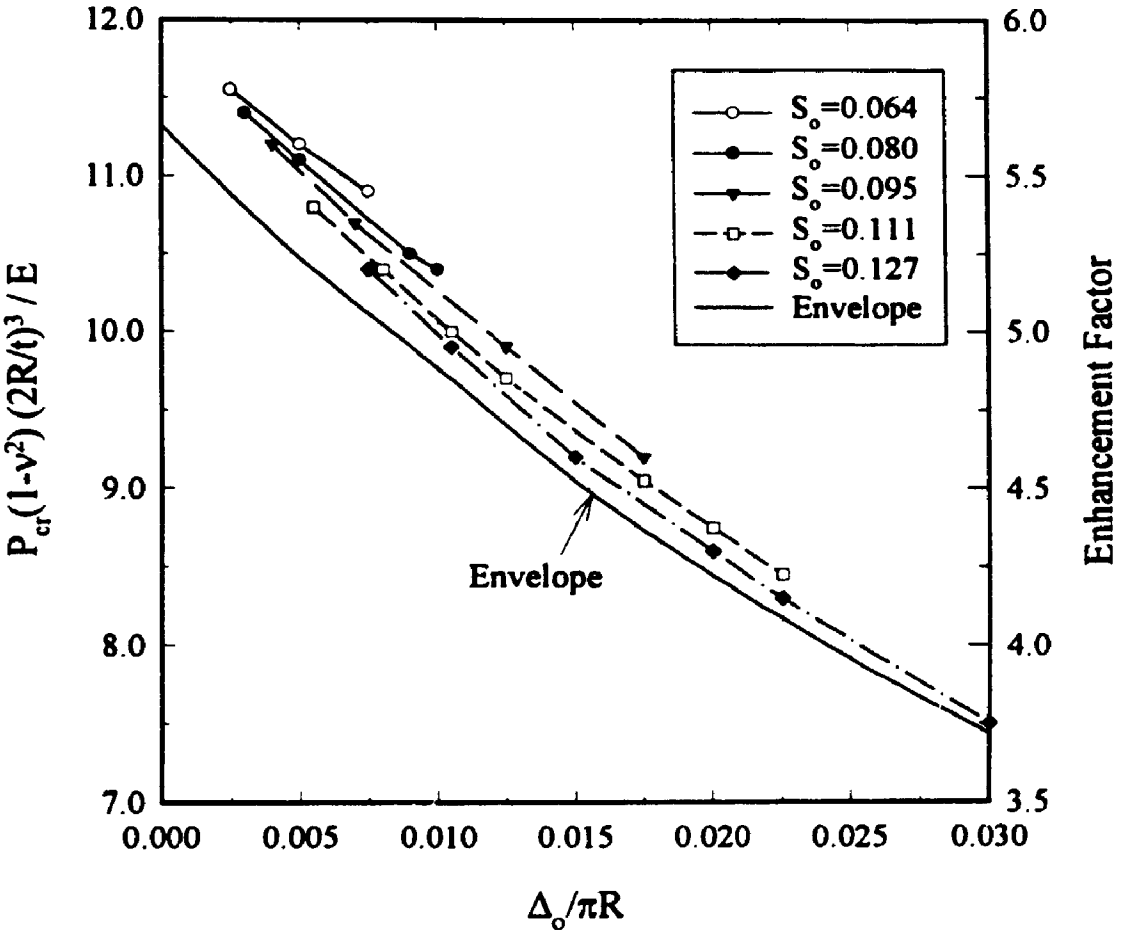

Figure 5.22. Enhancement Factor of The Critical Pressure for t/R=0.10

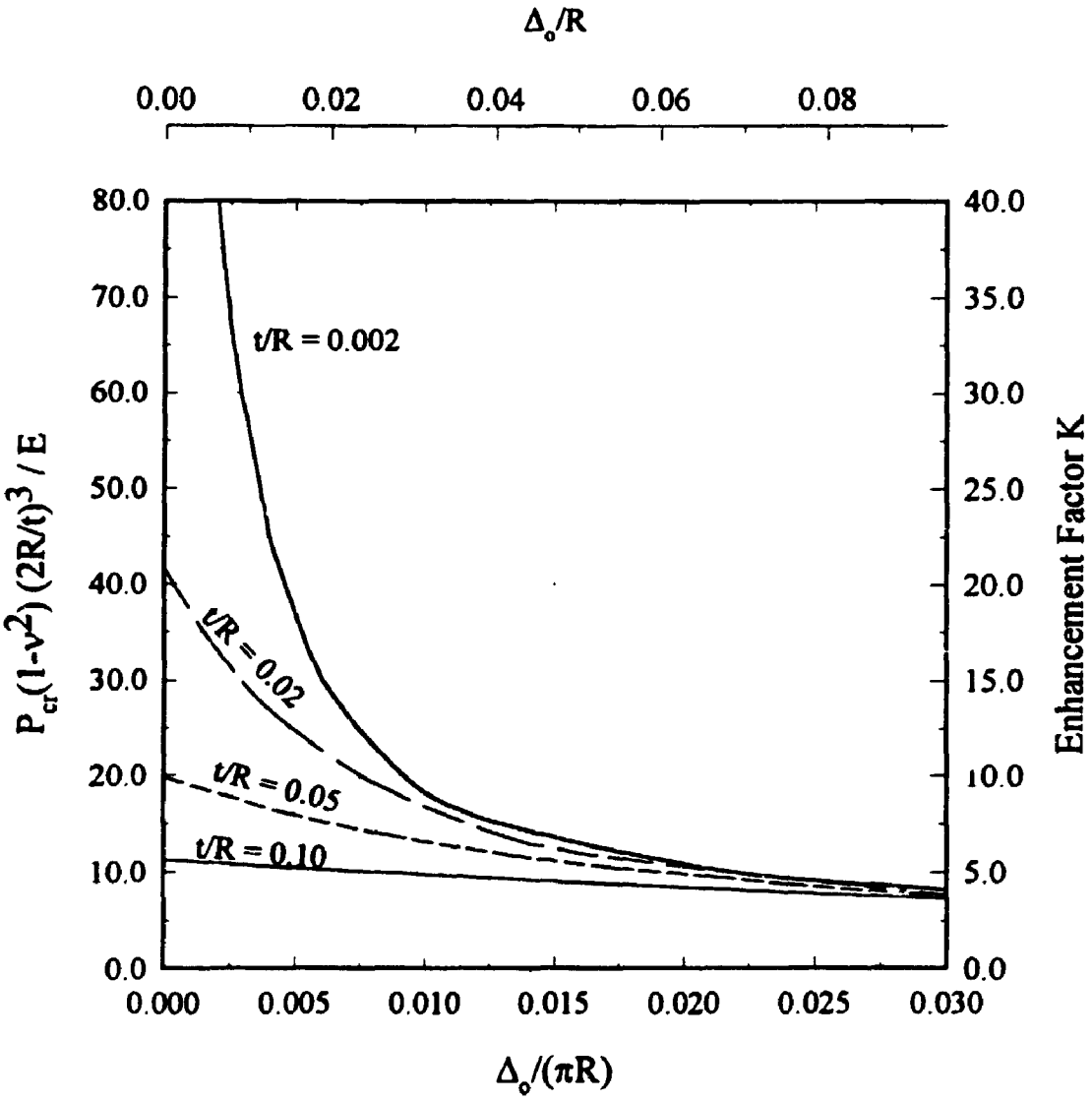

Figure 5.23. Enhancement Factor of The Critical Pressure for Different t/R Ratios

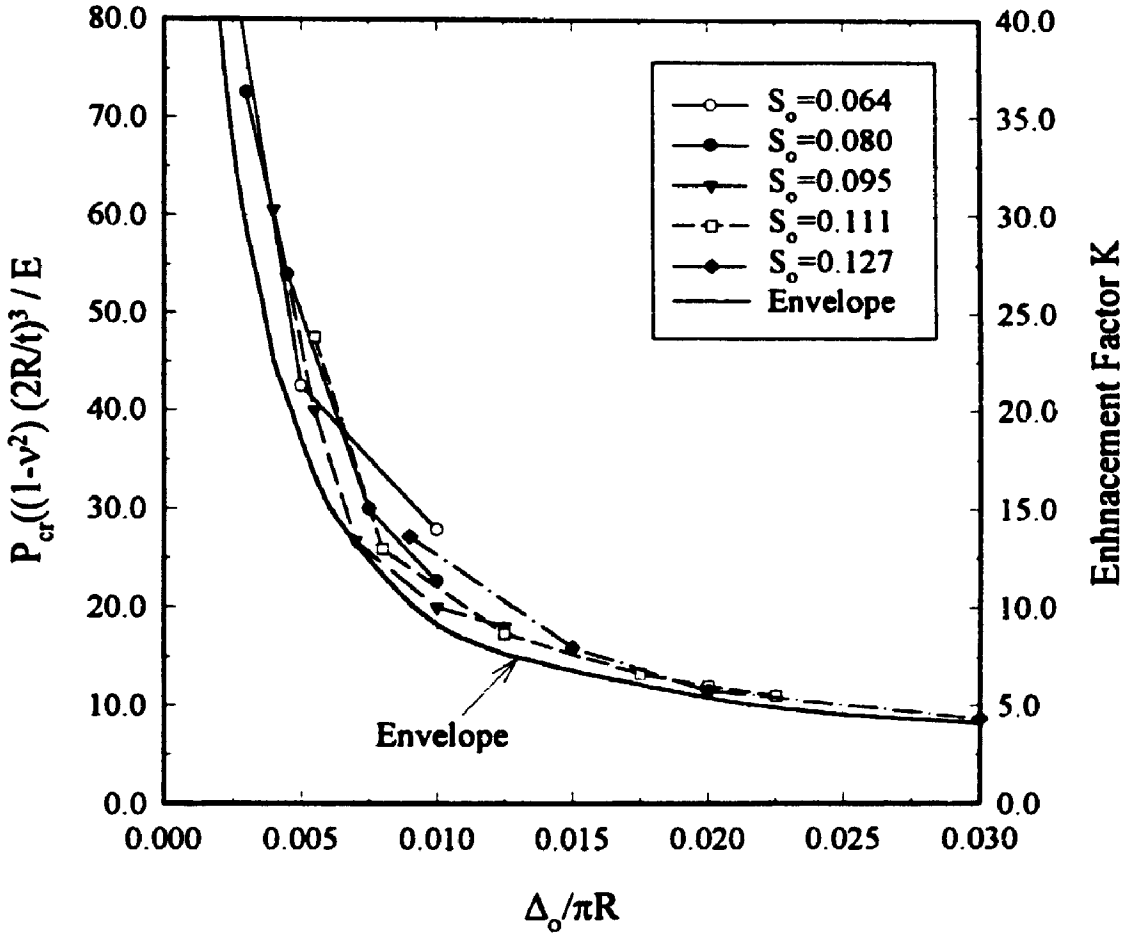

Figure 5.24. Enhancement Factor of The Critical Pressure for t/R=0.002 and Function (2)

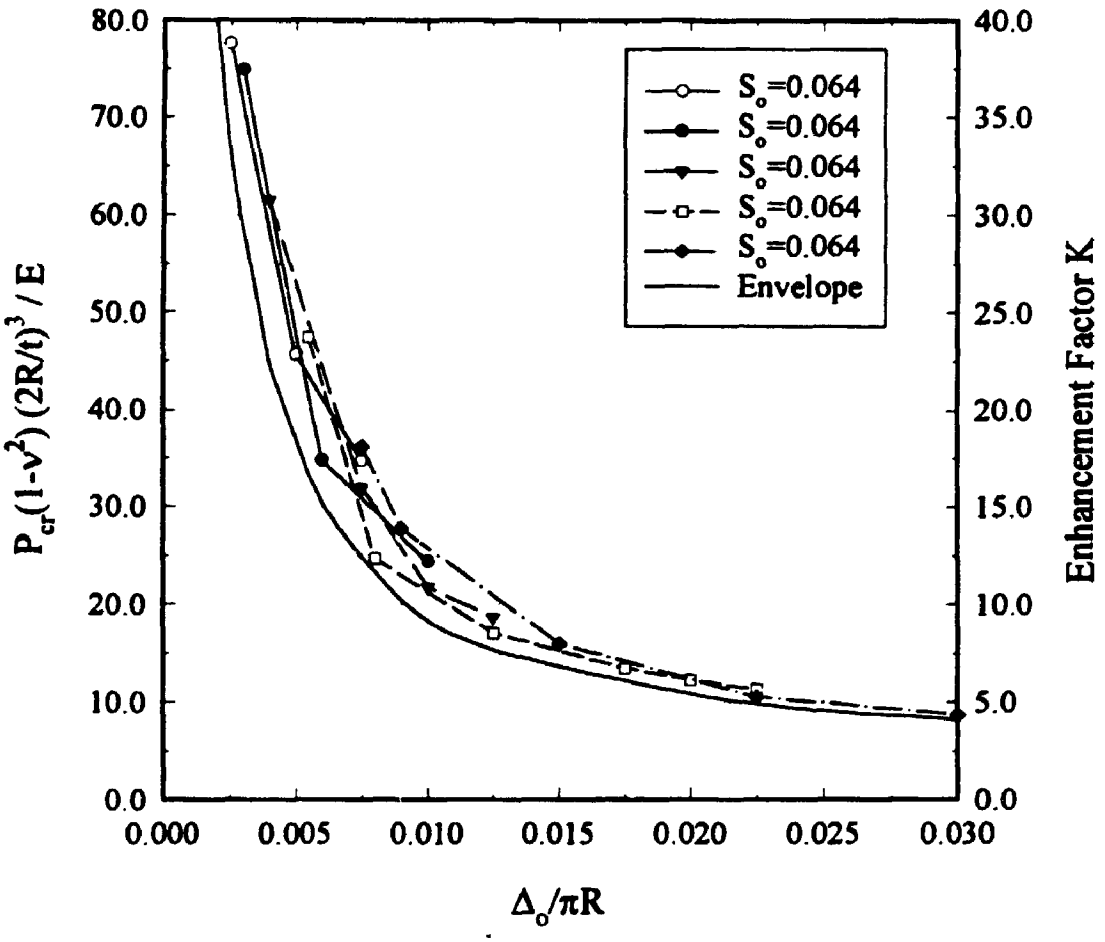

Figure 5.25. Enhancement Factor of The Critical Pressure for t/R=0.002 and Function (3)

CHAPTER SIX

Stability Analysis of Oval Shaped and Loosely Fitted Liners Under the Effect of External Pressure

6.1. Introduction

A summary of the available installation techniques is provided in chapter two. It is noted that any existing obstacles or imperfections in the host damaged pipeline are consequently reflected in the initial geometry of the installed liner. This generally decreases the critical pressure of the liner significantly.

The stability of a *perfect* liner or a liner with a *local* imperfection is discussed in the previous chapter. In this chapter, two other types of imperfections are considered. The first is due to the possible ovality (global imperfection) of the damaged pipelines. This will be referred to as *ovality imperfection*. The second type is due to loose fitting of a smaller diameter liner within the host pipeline. This will be referred to as *loose fitting imperfection*. The second imperfection is mainly due to an installation process that results in a liner which does not fit exactly into the host pipeline. Both imperfections reduce the buckling pressure of the liner seriously and will be discussed in detail later in the chapter.

The ovality imperfection is considered first and a literature review, a review of the ASTM [41] design formulas and a numerical study for the effect of ovality on the critical pressure (based on the results of the finite element analysis) are reported. A comparison between the FEM results and the proposed design tools in the ASTM standards is given to assess the appropriateness of the available ASTM design tools. The same local imperfection used in the previous chapter is introduced into the oval liner and its effect is assessed.

Finally, the loose fitting imperfection is considered. A literature review of the previous work is summarized. A numerical study undertaken using the FEM analysis, is reported for the problem.

6.2. Literature Review for The Ovality Imperfection

The effect of ovality on the critical pressure on liners is an issue which is known and is considered in the standard specifications (e.g., ASTM F1216-93 [41]). The following section summarizes the available literature dealing with the effect of ovality on liner behaviour.

6.2.1. Thermal Expansion of an Elliptical Ring Encased in a Smooth Rigid Cavity

Soong and Choi [40], have studied the effect of the ovality of a ring encased in a rigid cavity (Fig. 6.1a) on the stability of that ring when subjected to a thermal expansion (the same problem type reviewed before in section 5.3.1 for the circular ring case). Three buckling cases are considered; the no-friction one buckle case (buckle is symmetric about the short axis), the no-friction two buckle case, and the no-slip buckle case. In all the cases, the buckling is assumed to occur at the flatter part of the ring. Soong and Choi have solved the large deformation equilibrium equations of the ring. The solution was semi-analytical and a set of differential equations were solved numerically. The problem was more difficult than the case of a circular ring due to the changing radius of curvature for the part of the ring sliding on the walls of the rigid cavity. A parametric study was conducted and the results were presented showing that the critical thrust in the ring decreased with the increase of the ellipticity. Their results are a series of curves defining the thrust at the crown (point of

maximum radius of curvature) versus the critical thrust for different thickness to radius ratios, where the radius used is the radius of a circle whose circumference is equal to the ellipse circumference. They found that for the elliptical rings, the ellipticity reduced the critical thrust, because buckling occurred at the flatter part of the ring. Another finding is that neglecting the change in the radius of curvature due to the slippage of the attached part of the ring on the rigid cavity walls has an insignificant effect on the buckling thrust.

Li and Guice [32], studied the reduction factor of the hoop thrust at buckling of an elliptical ring compared to the circular ring of a radius R_o equal to the average of both the ellipse radii a and b (i.e., $R_o=(a+b)/2$) where a is the long radius (Fig. 6.2). The ring is assumed to be subjected to a thermal expansion. They approximated the buckled portion of the ellipse to be an axially compressed beam with a given initial shape (the shape is defined by Chicurel [12]). They obtained an approximate closed form solution for the ovality reduction factor α given by

$$\alpha = \frac{1}{\left(1 + \frac{q}{100}\right)^{\frac{8}{5}} \left(1 - \frac{q}{100}\right)^{\frac{1}{5}}} \qquad (6.1)$$

where q is percentage ovality defined by $100*(R_o-b)/R_o$ or $100*(a-R_o)/R_o$.

Li and Guice assumed that the influence of ellipticity on the thermal expansion solution was identical to ovality effects for the case of ring under pressure (Fig. 6.1b). However, the pressure problem is a different case with different boundary conditions. In the pressure case, after a portion of the ring separates from the confining rigid cavity, the contact pressure is released but not the external pressure. For the thermal buckling case, there is no external pressure and the contact pressure is released following the ring separation leaving the detached portion unloaded.

A comparison between their reduction factor and the one proposed by the ASTM standards [41] for the case of pressure was reported showing that the ASTM is very conservative. This comparison may not be valid; however, since the two loading conditions differ. This issue is examined in more detail later in this chapter.

6.2.2. ASTM Reduction Factor, Thrust and Moment for the Oval Liner

Various ASTM standards involves the calculation of the critical pressure of the elliptical (oval) pipe through application of a reduction factor α to the value of the critical pressure for the perfect circular pipe of radius R_o equal to $(a+b)/2$, where $2a$ nd $2b$ are the length of the ellipse axes (Fig. 6.2). The following equations is shown in ASTM specifications F1216-93

$$\alpha = \left[\frac{1 - \frac{q}{100}}{\left(1 + \frac{q}{100}\right)^2} \right]^3 \tag{6.2}$$

The equations for the maximum thrust, N, and bending moment, M, in an encased oval liner are also given as

$$N = \left(1 + \frac{q}{100} \right) P R_o \tag{6.3}$$

$$M = \frac{q}{100} \left(1 + \frac{q}{100} \right) P R_o^2 \tag{6.4}$$

Equations 6.3 And 6 4 are defined for the free oval liner and are assumed to be applicable for the encased oval liner where ovality is defined by q.

No previous rigorous study of the effect of ovality on the critical pressure, thrusts and moments appears to be available. In this chapter, a comprehensive parametric study for that effect and other parameters on the buckling pressure, thrust and bending moments is reported.

6.3. Finite Element Analysis of Oval Shaped Liners

The Finite Element Method is used to solve for the critical pressure, thrusts and bending moments for the elliptical liner encased in a rigid elliptical host pipe,. The geometrical non-linearity, the follower pressure and the non-linear interface behaviour (discussed before in chapter five) are considered in the finite element model. Figure 6.1b shows the geometry of the problem considered where $2a$ and $2b$ are the length of the two axes of the elliptical liner, and t is the liner thickness. Using the rigorous interaction analysis technique developed in chapter four, the liner is defined as the slave body using sixteen 5-noded structural elements. The rigid cavity interface is modelled using sixteen 5-noded non-linear interface elements. The asymmetric buckling mode (the case of one buckle) is developed by fixing the node at the liner invert. Figure 6.3 shows the model used in the analysis. The liner properties are defined as follows:

t is the liner thickness,

R_o is the average liner radius (i.e. $(a+b)/2$),

q is the % ovality and is defined by $q = 100 \times \left(\frac{R_o - b}{R_o} \right) = 100 \times \left(\frac{a - R_o}{R_o} \right)$

E is Young's modulus for the liner material, and

ν is Poisson's ratio for the liner material.

Figures 6.4a and 6.4b show the normalized pressure versus the normalized vertical deflection at the crown of the elliptical liner for different a/b and t/b ratios. The pressure is normalized by the critical load (calculated using the FEM) for the encased circular liner of radius R_o (which is equal to the average radius of a and b for the oval liner). The point corresponding to the maximum normalized pressure (critical pressure) defines the reduction factor α; the same definition is used in the ASTM specifications. This factor defines the amount of reduction in the critical pressure of the circular liner due to ovality.

The general behaviour of the elliptical liner is similar to the case of a circular liner where a peak pressure is reached after which any further increase in pressure produces liner collapse. In Fig. 6.4a, the cases of a/b=1.25 (i.e. q=11.11%) and different t/b ratios (t/b=0.005, 0.010, 0.050, 0.100) are shown. Figure 6.4b shows the cases of a constant ratio of t/b=0.050 and different a/b ratios (a/b=1.005, 1.05, 1.10, 1.15, and 1.25). The following conclusions may be extracted from these two figures:

- The effect of t/b on the reduction factor for critical buckling pressure, for ovality q=11.11% and other ovalities, is not significant. The change in the reduction factor is about 5% for a t/b ratio varying from 0.005 to 0.10 where a/b=1.25.
- The thicker the liner the more the crown vertical displacement at the critical pressure. This is attributed to the increasing circumferential deformations as t/b increases.
- The increase in ovality q (or a/b ratio) reduces the critical pressure. This behaviour is due to varying radius of curvature of the oval liner as the buckling occurs in the flatter part of the liner.

Figure 6.5a shows the deformed shape at different pressure levels (P=0, $0.5P_{cr}$, P_{cr} and post-peak $0.9P_{cr}$) for the case of a/b=1.25 and t/b=0.100. It is obvious that as the liner deforms, the first contact point between the liner and the rigid host pipe changes position and moves along the walls of the rigid oval host pipe. The large deformations shown for this case are due to the fact that the liner is deforming significantly in the circumferential direction.

Figure 6.6 shows diagrams for the bending moments M and thrust forces N generated in the liner at the critical pressure for different a/b and t/b ratios. The thrusts are normalized by PR_o while the bending moments are normalized by PR_o^2. Some conclusions may be drawn from this figure:

- The points on the liner where moments decay to zero, can be considered as hinges and the detached part of the liner as an arch (Fig. 6.5b). This mechanism controls the magnitude of the thrusts and moments.
- The thrust is mainly uniform on the liner with a slight increase at the liner shoulders (points of support for the detached part) relative to other locations.
- The bending moments generated in the liner for very small liner thicknesses (t/b=0.001) are practically insignificant in contrast to the case of large liner thicknesses (t/b=0.10). This is partially associated with the smaller deformations for lower t/b ratios.
- The bending moments are only present in the detached part of the liner, and rapidly decay in the part in contact with the rigid host pipe.
- It is also important to notice that both the bending moments and thrusts are functions of the thickness to radius ratio; the larger the t/b ratio, the less the thrusts and the larger the bending moments. This is due to tendency of the thick liner to deform more in the

circumferential direction than the thin one, allowing the release of some thrusts, which may be generated if such circumferential deformations are not allowed. Consequently, the more the generated deformations, the greater the bending moments.

- The values for the encased liner thrusts are bigger than the thrusts for the case of an unsupported liner under pressure. The deviation is significant for the case of thin liners, but decreases for thick liners. This is due to the hinged arch mechanism which controls the value of the thrusts. The value of the thrusts are dependent on the shape of the arch and the location of its hinged ends.

Figure 6.7 shows the change in the normalized thrusts N/PR_o and bending moments M/PR_o^2 at the liner crown versus the normalized pressure $P(1-\nu^2)/E$ for different a/b and t/b ratios. This figure shows that:

- For the small ovalities (e.g. a/b=1.005) and small pressures (significantly less than the critical pressure), the normalized thrusts and moments match the unsupported liner solution (e.g $N=PR_o$ and M=0.0). This is because when the deformations are small, the deformed arch takes almost a circular shape.
- As the pressure increases and the deformations become significant, the geometry of the hinged arch which develops takes a non-circular shape, and the thrusts deviate from $N=PR_o$.
- It is very clear that the ratio t/b has a significant effect on the thrusts even for small ovalities (a/b=1.005). This contradicts the equation used by the ASTM specifications, Eqns. 2.14, 6.2, which do not consider the t/b effect and only considers ovality ratio q.

- Generally, the larger the t/b ratio, the lower the normalized thrusts and the larger the normalized bending moments developed.
- The larger the ovality ratio q, the larger the liner bending moments and thrusts at the critical pressure.

Figure 6.8 shows the effect of ovality q on the thrusts and bending moments at the liner crown, at the critical pressure, for different t/b ratios. The least squares method with linear regression is used to define the dashed lines shown on the figure. This figure is suitable for design purposes. The ratios a/b or q and t/b are used as input values to calculate the thrust and moment at the liner crown at the critical pressure. These figures show that the critical thrusts and critical bending moments are functions of both ovality and liner thickness. The bending moments show less variation with ovality q than the thrusts. For thin liners, the variation is negligible. For thicker liners there is a small increase with ovality. The figure supports the same conclusions reported before when Figs. 6.6 and 6.7 were discussed.

Some minor scatter in the results is noticed in Fig. 6.8., which may be due to the fact that the actual point of contact does not match a nodal point in the finite element mesh (even with a fine mesh), and the analysis picked the nearest node instead. But it is clear that the scatter is very small and can be neglected. It is also noted that the effect of ovality on the critical bending moment can be neglected for practical purposes.

A comprehensive parametric study for the effect of the ovality q on the buckling pressure for different t/b ratios has also been undertaken. The results for the critical pressure are interpreted in the form used before by ASTM. A reduction factor α is defined relating critical pressure for encased elliptical liners to the critical pressure of the encased circular

liner of radius R_o. Figure 6.9 shows the variation of the reduction factor α versus the ovality q for different t/b ratios. It is clear that as ovality in the liner increases, the buckling pressure decreases significantly. The effect of t/b on the reduction factor is minor and can be neglected for practical purposes.

A comparison between the available reduction factors proposed by other researchers is also shown. The reduction factor proposed by Li and Guice [32] is not conservative and differs by more than 55% from the FEM solutions. This may be attributed to the fact that their solution was derived from a solution to the thermal buckling problem (although it was used for the pressure case). The FEM solution is more liberal than the ASTM reduction factor and differs by up to 40%. This is because of the inappropriate mathematical model used by ASTM to develop this reduction factor (the model used to obtain a solution for an unsupported liner). The ASTM guideline is conservative and should be modified to achieve more economical liner designs. An equation for the reduction factor, based on an envelope developed from the FEM results, for a practical range of t/b, is given by

$$\alpha = e^{\left(-\frac{q}{18}\right)} \tag{6.5}$$

This equation is a lower bound for all the practical t/b ratios considered. Using Eqn. 6.5 and the equation discussed and checked in the previous chapter for the critical pressure for an encased circular liner, the following equation predicts the critical pressure for elliptical liners

$$P_{cr} = e^{\left(-\frac{q}{18}\right)} \frac{E}{1-\nu^2} \left(\frac{t}{D_o}\right)^{2.19} \tag{6.6}$$

The following conclusions may be drawn from this study of oval liners:

- The effect of the t/b ratio on the critical pressure is negligible for practical purposes. However, the effect of t/b should be considered when evaluating the thrusts and bending moments at the critical pressure.
- The reduction factor α due to ovality is significant. It reduces the critical pressure for a 10% ovality (q=10%) by about 42%.
- The reduction factor proposed by Li and Guice is not conservative and may lead to unsafe designs due to the inappropriate assumption that the reduction for the case of thermal buckling is equal to that for the case of buckling under pressure.
- The current ASTM reduction factor is based on an inappropriate mathematical model and is conservative and needs to be modified.
- The equations (Eqns. 6.3 and 6.4) proposed by ASTM for the liner design based on thrusts and bending moments are unsuitable because they neglect the influence of the host pipe support. New design curves have been proposed which take into consideration the t/R_o ratio (or t/b ratio) and ovality effects on critical thrusts and moments.
- A new equation for the calculation of the critical pressure for elliptical liners, accounting for the effect of t/R_o and ovality has been proposed (Eqn. 6.6).

6.4. FEM Analysis of Oval Shaped Liners with Local Imperfection

Usually local imperfections exist in the liner due to the uneven shape of the rehabilitated pipe. The problem of local imperfections in elliptical liners has not been considered before although it is common in engineering practice in the rehabilitation industry. A single initial imperfection is considered and assumed to be at the flatter part of the liner. The same imperfection geometry and finite element model used in chapter five for the circular liners,

are used herein. The only modification to the imperfection is that the X-coordinate of each nodal point describing the imperfect liner is scaled using the ratio *a/b*. Therefore, the geometry of any problem starts with the imperfect circular liner with a radius equal to the *b* of the elliptical liner; then the whole geometry is distorted in the X direction by scaling all the X-coordinates of the nodal points by the ratio *a/b*.

A parametric study for the effect of the imperfection size on the critical pressure is conducted. The results are presented in Figs. 6.10, 6.11 and 6.12. The figures show the reduction factor versus the normalized imperfection amplitude at the crown ($\delta_o = \frac{\Delta_o}{\pi b}$) for different *t/b* ratios. Each dashed curve defines a normalized imperfection length S_o. The reduction factor is defined by the critical pressure for the imperfect oval liner divided by the critical pressure for the oval liner (both pressures are calculated using the FEM). Three different normalized imperfection lengths are considered (S_o=0.065, 0.111 and 0.175). Envelopes to the FEM results are chosen and shown in dashed-dotted lines. Figures 6.10, 6.11 and 6.12 show that the reduction factor starts at unity in the case of zero imperfection amplitude and decreases as the imperfection amplitude increases. Similar to the imperfect circular liners, the lower the *t/b* ratio, the lower the reduction factor. Furthermore, the influence of the imperfection amplitude on the reduction factor is very strong; the greater the Imperfection amplitude the lower the reduction factor. The envelopes for the cases considered can be used for design purposes and this is discussed in details in chapter eight.

6.5. Buckling of a Loosely Fitted Circular Pipe in a Rigid Cavity under Pressure

Another type of geometrical imperfections used for the liner problem is discussed in the following sections. The imperfection (Fig. 6.13) can be defined by a radial gap *d* between

the liner of outer radius R_i and the rigid pipe of inner radius R_o (i.e. loose fitting of a smaller diameter liner into the rigid pipe). These imperfections result from the common construction technique used in the installation of the cured-in-place liners (CIPP) into a rigid deteriorated concrete pipe. The liner resin is subjected to thermal treatment to be cured and fitted into the host pipe (concrete pipe) and then is allowed to cool down gradually. Thermal contraction leads to the gap between the liner and the host pipe.

6.5.1. Literature Review

The experimental work of Aggarwal and Cooper [1] is reviewed and discussed in chapter five. In that discussion, the effect of the gap between the liner and the host pipe was ignored. Because of the end restraints of the liner, it is expected that the experimental critical pressures will be higher than the theoretical ones. In the comparison accomplished in chapter five, it is found that some of the experimental results are well below the theoretical values. This may be due to the gap effect which is discussed in more detail in the following sections.

Lo and Zhang [34] studied the effect of the loose fitting imperfection on the critical liner pressure. In that study, an approximate solution for the critical buckling pressure was obtained based on the analogy between the buckling of the detached part of the liner and the buckling of shallow arches. No consideration is given to the circumferential deformations occurring in the liner. The symmetrical one buckle case and asymmetrical two buckle case were both studied and a range for the expected critical pressures was calculated. A comparison had been made between the expected range of the critical pressures and the experimental results. The comparison showed that this simple solution may be an

appropriate one. In the following section a FEM solution is obtained and is compared to both the Lo and Zhang solution and their experimental results.

6.5.2. Finite Element Analysis for a Loosely Fitted Pipe in a Rigid Cavity

The solution reported by Lo and Zhang [34] used the arch buckling assumption and consider neither geometrical non-linearity (large deformations) nor the circumferential strains in the liner. As shown before, for the cases of circular and oval liners, neglecting the circumferential strains may significantly affect the critical pressure.

The Finite Element Method is used to analyse the problem of a loosely fitted circular liner (or pipe) in a rigid circular cavity. Figure 6.14 shows the model used in the analysis. Twelve 5-noded elements are used to model the liner of inner radius R_i and twelve 5-noded interface elements to define the rigid cavity interface with outer radius R_o. A very small ovality (a/b=1.0005) is introduced in both the liner and the rigid cavity (as in chapter five), where $2a$ and $2b$ are the total width and total height of the oval. As discussed in the convergence study accomplished in chapter five, the solution converges to a single value corresponding to the circular liner case as a/b ratio decreases to 1.0. The analysis undertaken is similar to the previous analyses for the circular and oval liners.

Figure 6.15 shows the normalized deflection Δ/R_o of the liner crown versus the normalized load $P(1-\nu^2)/E$ for the case of t/R_o=0.05, d/R_o=0.05. A sudden change in the behaviour is noticed when the liner first touches the wall of the rigid pipe. The behaviour before that first contact corresponds to the unsupported liner.

The critical pressure for different t/R_o and d/R_o ratios is obtained. Figure 6.16 shows the critical pressure normalized by $\frac{E}{1-\nu^2}$ versus t/R_o. It is clear that the gap size d has a great

influence on the critical pressure. The critical pressure drops significantly as the gap size increases. An increase for the gap size from d/R_o=0.0005 to 0.0500 leads to a drop in the critical pressure by more than 80% for t/R_o=0.01 and a drop of about 40% for t/R_o=0.10. As before, the critical pressure is significantly influenced by the thickness to radius ratio t/R_o. Figure 6.17 shows the normalized critical pressure versus the change in d/R_o ratios for different t/R_o ratios. The pressure is normalized by the critical pressure of the free liner. This defines the enhancement factor for the critical pressure. The figure shows that the larger the t/R_o ratio the less the enhancement factor. This is similar to the previous cases of the circular and oval liners. The figure also demonstrates the fact that the critical pressure decreases as the gap increases. For tiny gap sizes, the drop in the enhancement factor is significant, particularly for small t/R_o ratios.

A comparison between the numerical results and the experimental work of Aggarwal and Cooper is shown in Fig. 6.18. As expected, the experimental results are higher than the theoretical values for the critical pressure. The finite element results represent a lower bound for all the experimental results which establishes confidence in the proposed numerical solution.

A comparison between the finite element results and both the approximate analytical solution and the experimental results of Lo and Zhang is shown in Fig. 6.19. The test data was obtained from encased pipe samples made with three different epoxy resin systems. The liners were fabricated by direct inversion into a steel host pipe of 152 mm (12 inches) inside diameter. The imperfection size was *calculated* based on the thermal contraction that occurred after the thermal treatment of the liner. The details for that experimental work can be found in Lo and Zhang [34].

In Fig. 6.19, the FEM solution for the cases of t/R_o=0.001 and 0.010, lies between Lo and Zhang's analytical solution for the symmetrical and asymmetrical buckling cases. For higher values of d/R_o where geometrical non-linearity becomes important, the two solutions deviate and the FEM result is more conservative.

A comparison between the FEM solution and test results shows that the FEM solution represents a lower bound for all the experimental results (for the case of t/R_o=0.036, 0.037). The deviation from the FEM solution may result from use of estimates of the gap size instead of accurate measurements. The scatter shown on the experimental results may be accounted for by the sensitivity of the behaviour for these relatively small d/R_o ratios, material non-linearity and the friction angle between the liner and the steel host pipe.

The two figures 6.16 and 6.17 may be good design tools for end-users, but they have to be checked and calibrated against more experimental results. The experimental results available, so far, are few and more research is needed to fully assess the appropriateness of the proposed solution.

Another form of presenting the results is shown in Fig. 6.20. The reduction factor measures the reduction in the critical pressure due to the gap compared to the critical pressure of a liner perfectly fitted in the rigid cavity. The figure illustrates that increases in the d/R_o ratio lead to reductions in stability (i.e. greater values of the reduction factor). This is because the large gap size allows the liner to deform significantly before coming into contact with the rigid cavity walls, with more loss of the stable circular shape. This reduces the critical pressure significantly. This reduction is more significant in the small t/R_o ratios because the lower flexural stiffness of the liner (compared to the hoop stiffness) allows more deformations to occur and consequently a greater reduction in the critical pressure.

6.6. Conclusions

The stability of oval liners, imperfect oval liners and loosely fitted liners has been studied in this chapter and proposed design tools are given. The following conclusions can be drawn from this study:

- A comparison between the FEM results and the proposed design equations in ASTM F1218-93 indicates that the ASTM reduction factors used to reduce the critical pressure due to ovality are conservative and a proposed reduction factor based on FE analysis seems to be a better alternative.
- Based on the FE results for the oval liner, the ovality reduction factor suggested by Li and Guice [32] is not conservative and may lead to unsafe liner designs
- The ASTM equations for the calculation of the critical design thrust and bending moment in the encased oval liners are based on the unsupported liner case and do not take into account the significant effect due to thickness to radius ratio. The new design curves proposed may be a good alternative to the ASTM design equations.
- A local imperfection in an oval liner can reduce the critical pressure significantly. The effect has been assessed using the finite element method, but has yet to be verified against experimental results.
- While the numerical solution for the circular liner fails to be a lower bound for all the experimental results by Aggarwal and Cooper [1], considering the gap effect gives a good agreement with the experimental results. The solution considering the gap is a lower bound of all the experimental results since the restraints applied to the liner ends increases significantly the stability of the liner.

- The loosely fitted liner stability solution has been checked against the approximate solution of Lo and Zhang and their experimental results. The new FEM solution is a lower bound for all the experimental results.

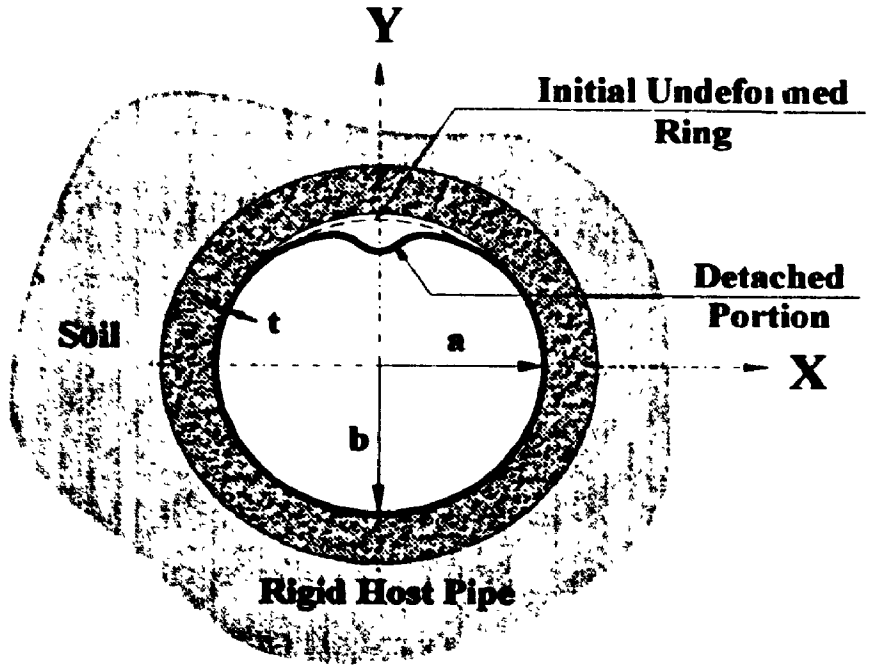

Figure 6.1a. Buckling Due to Thermal Expansion

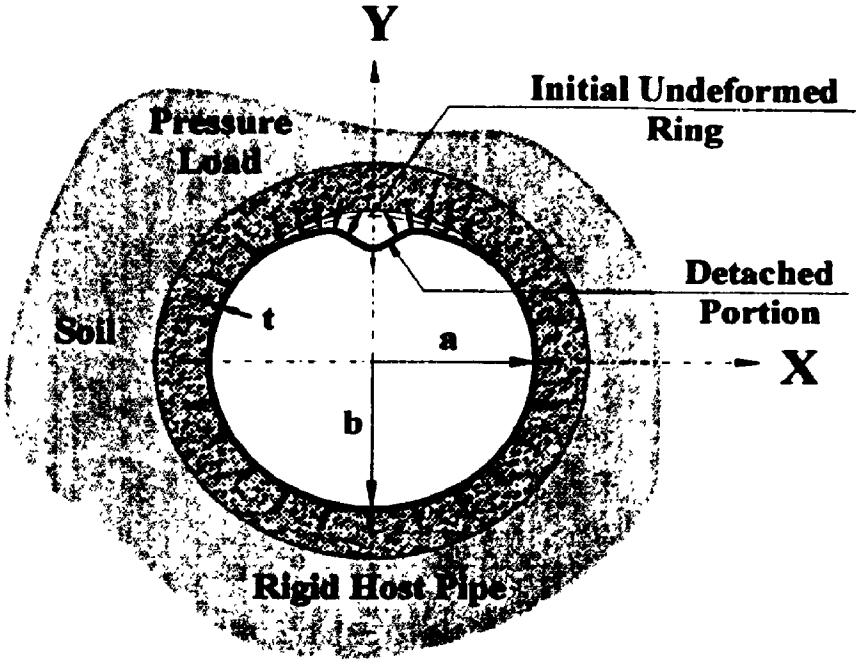

Figure 6.1b. Buckling Due to Pressure Load

Figure 6.1. Definition of Two Different Buckling Problems

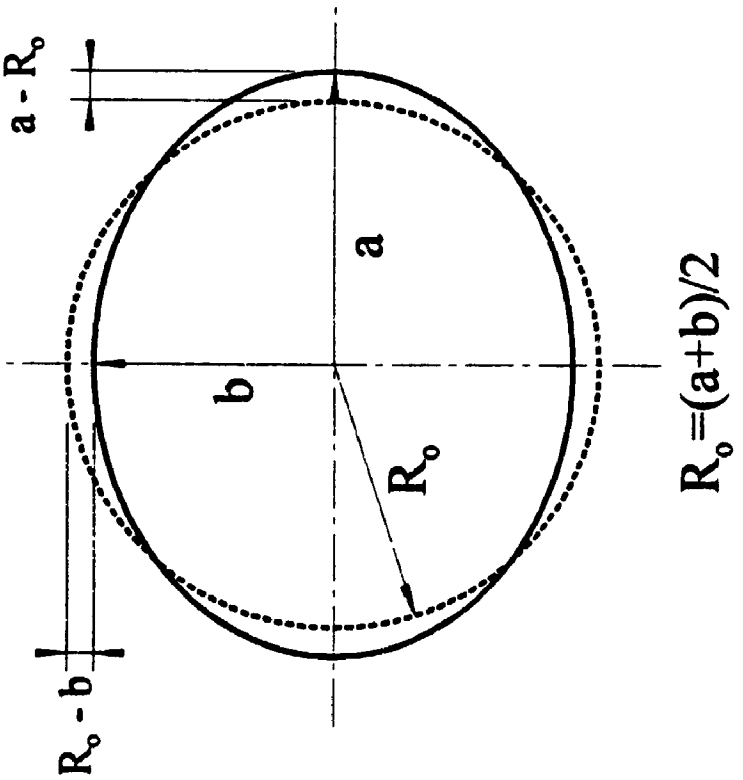

Figure 6.2. Definition of Ovality Geometrical Parameters

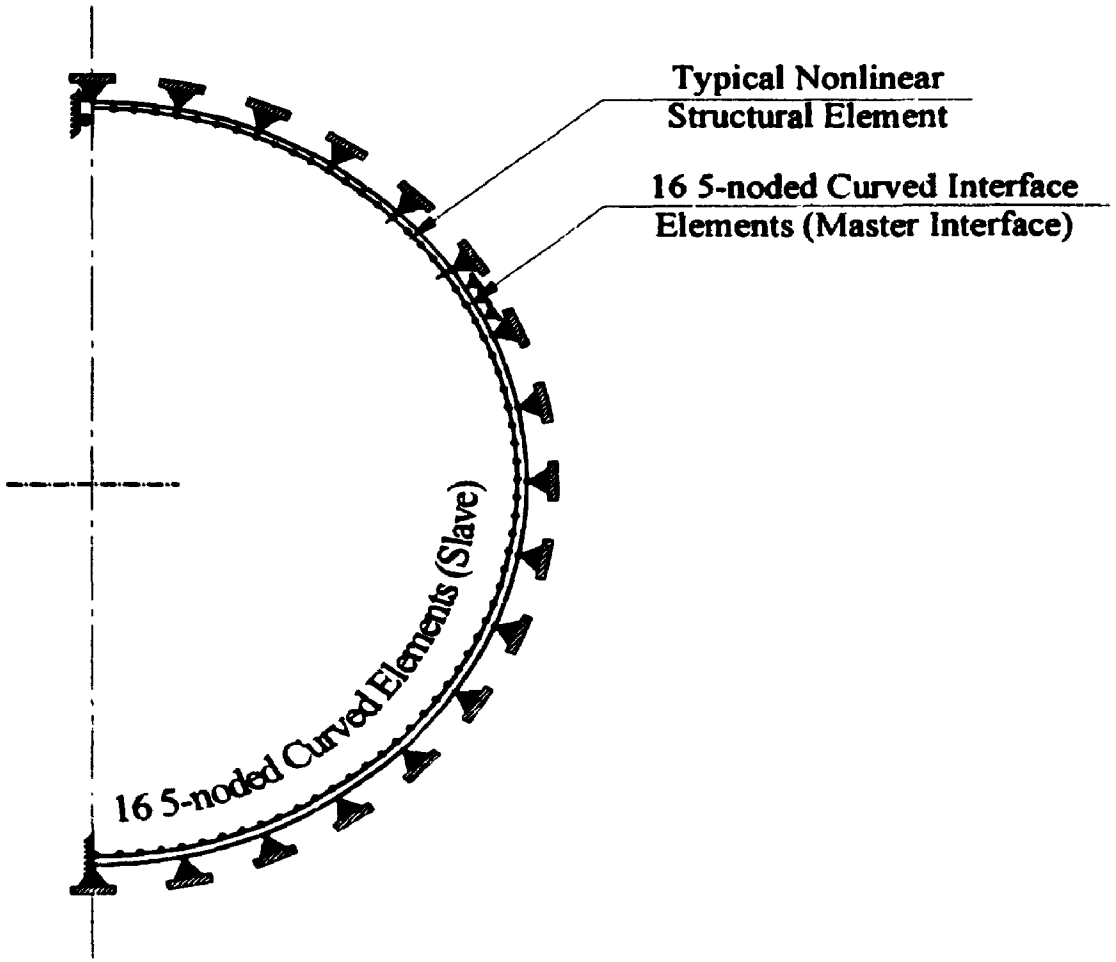

Figure 6.3. Finite Element Model for the Oval Liner Problem

Figure (6.4a)

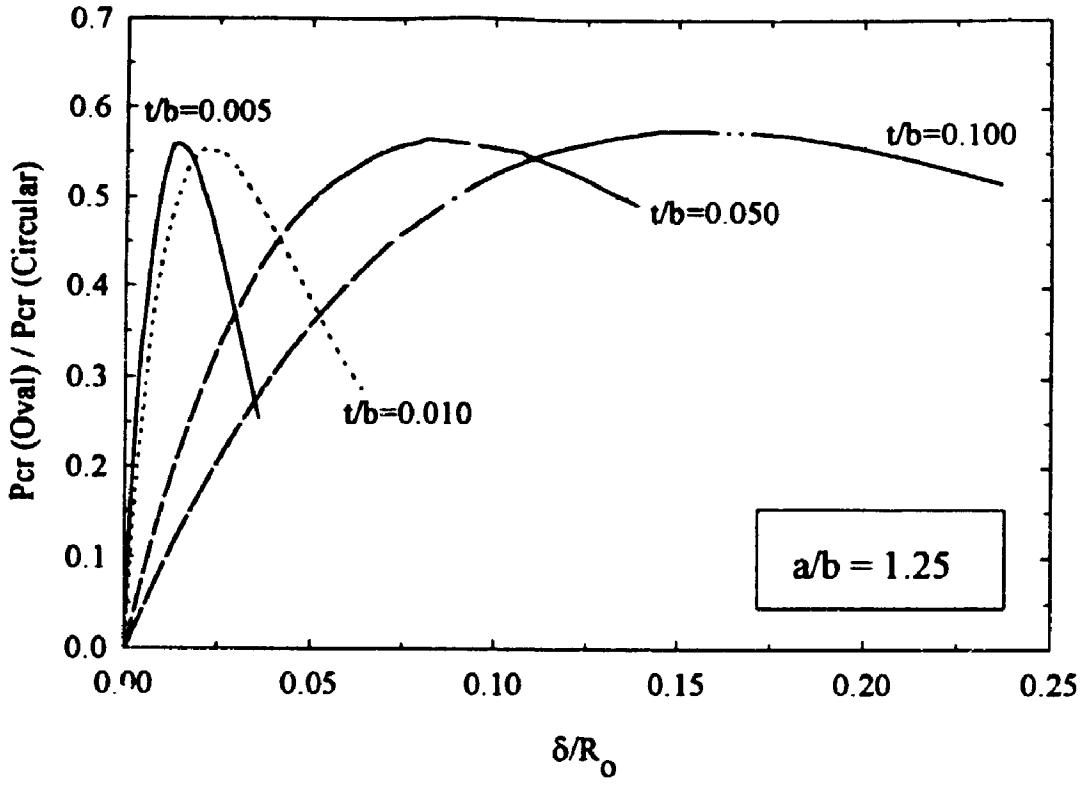

Figure (6.4b)

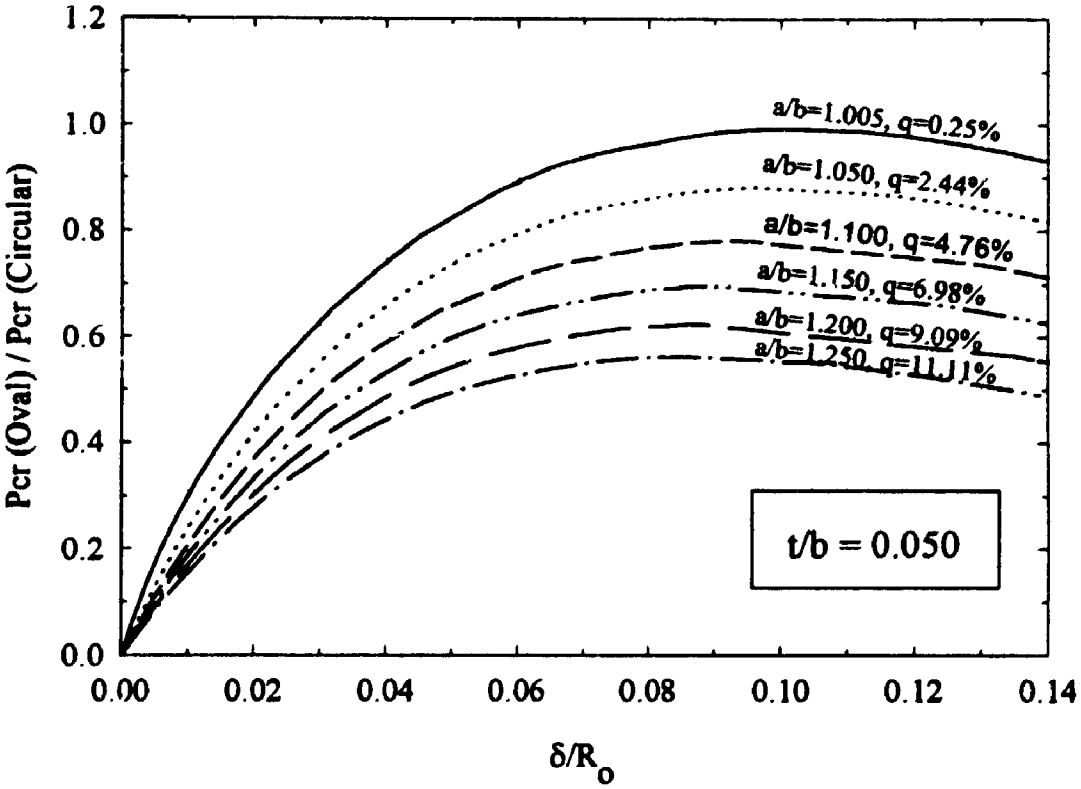

Figure 6.4. Load-Deflection at the Crown of the Oval Liner

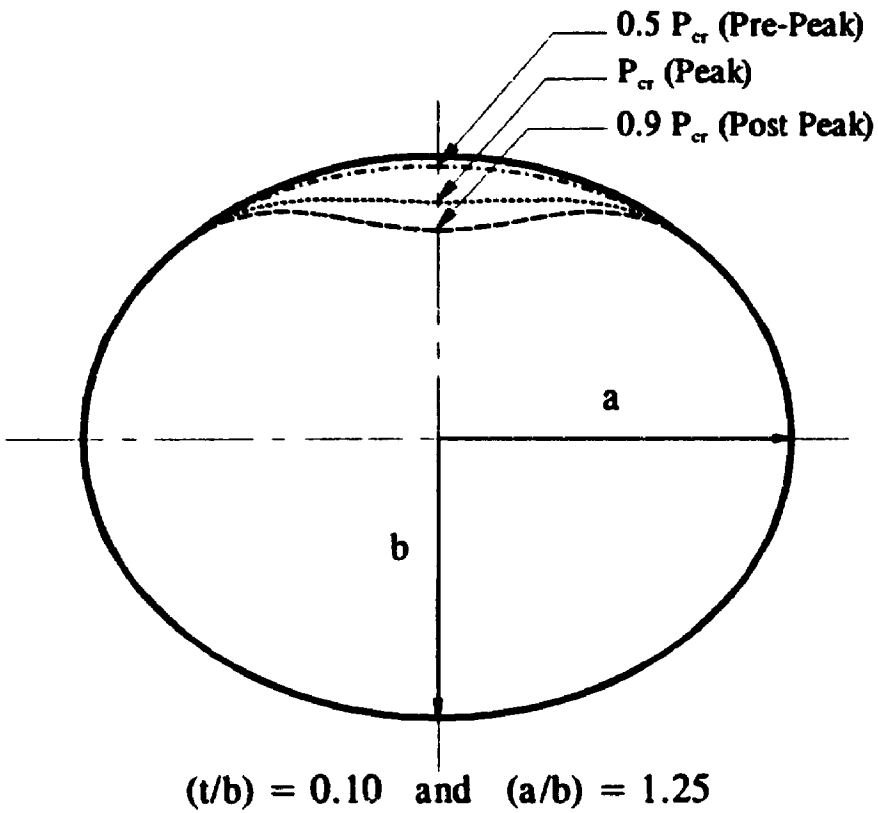

Figurer 6.5a. Deformed Shape

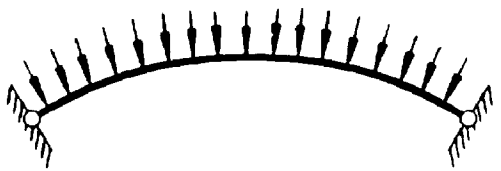

Figure 6.5b. Arch Mechanism

Figurer 6.5. The Oval Liner Deformed Shape at Different Load Levels and The Arch Mechanism

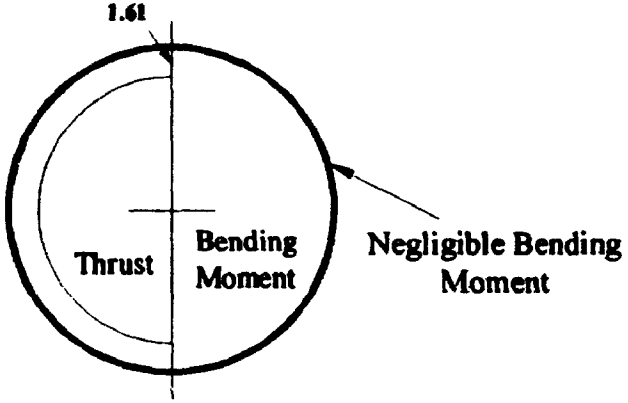

Figure 6.6a. Thrust N and Bending Moment M
(a/b=1.005, q=0.25, t/b=0.001)

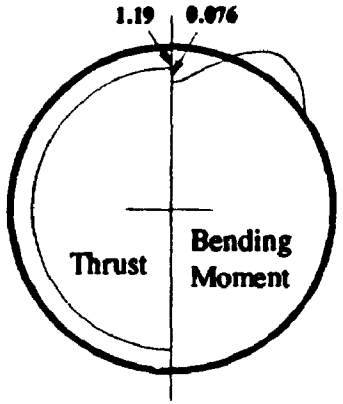

Figure 6.6b. Thrust N and Bending Moment M
(a/b=1.005, q=0.25, t/b=0.100)

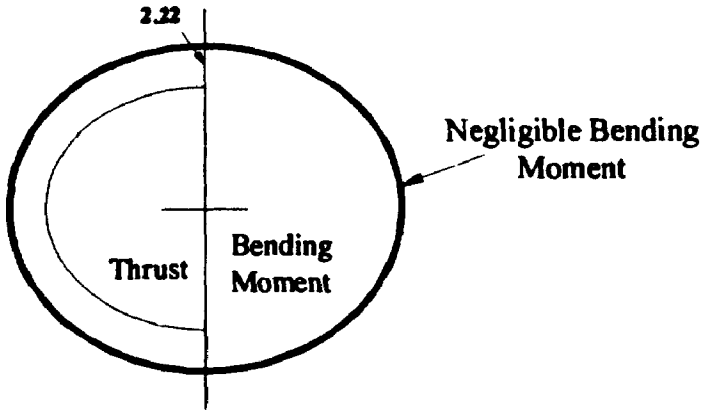

Figure 6.6c. Thrust N and Bending Moment M
(a/b=1.250, q=11.11, t/b=0.001)

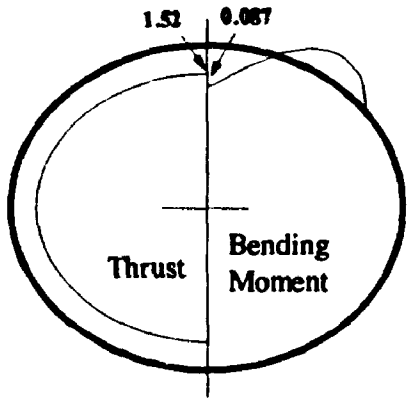

Figure 6.6d. Thrust N and Bending Moment M
(a/b=1.250, q=11.11, t/b=0.100)

Figure 6.6. Thrusts and Bending Moments at Buckling Pressure
for Different Ovalities (a/b) and Thickness to Radius Ratios (t/b)

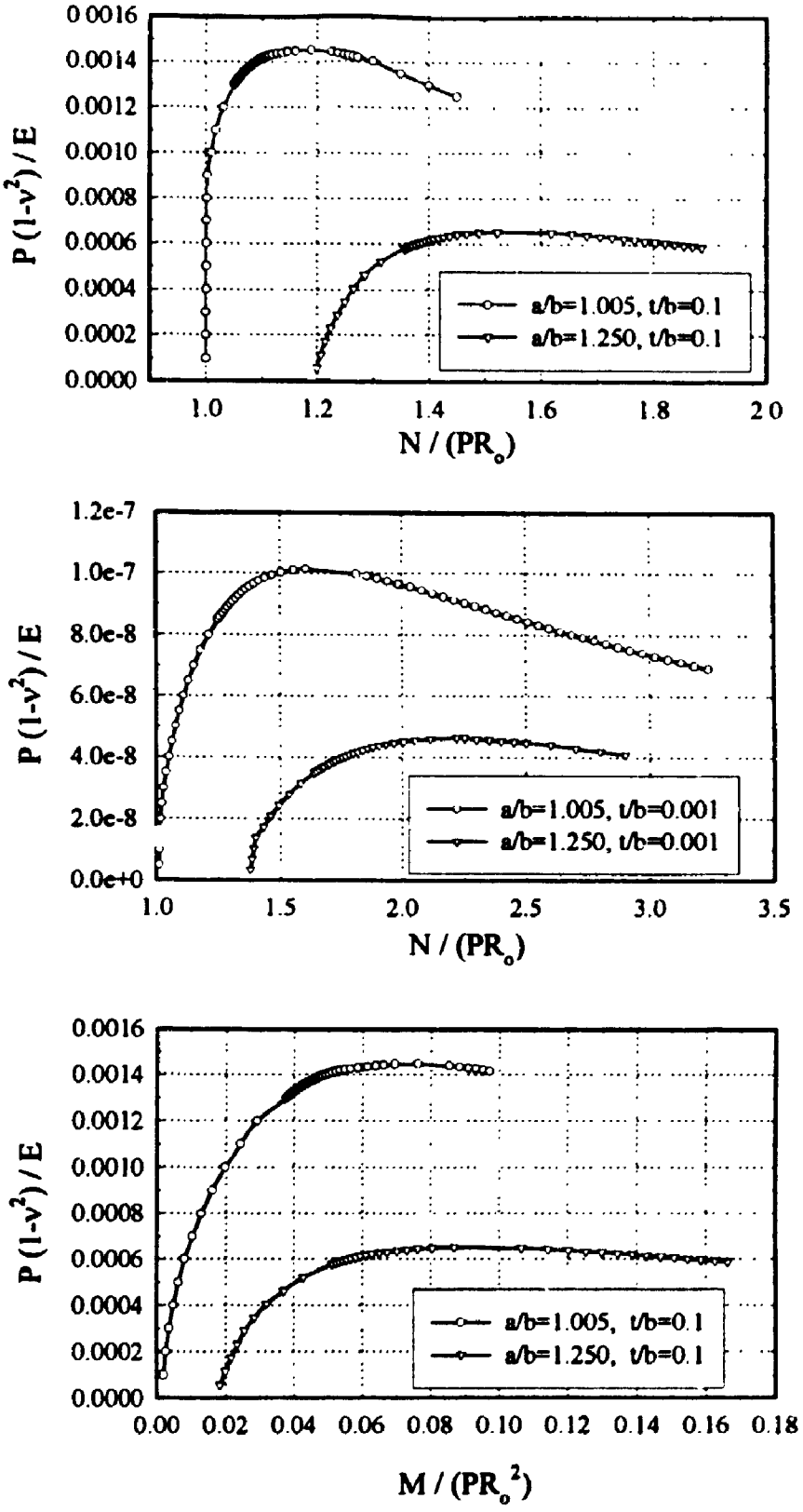

Figure 6.7. Thrusts and Moments for different Ovalities (a/b) and Thickness to Radius Ratios (t/b)

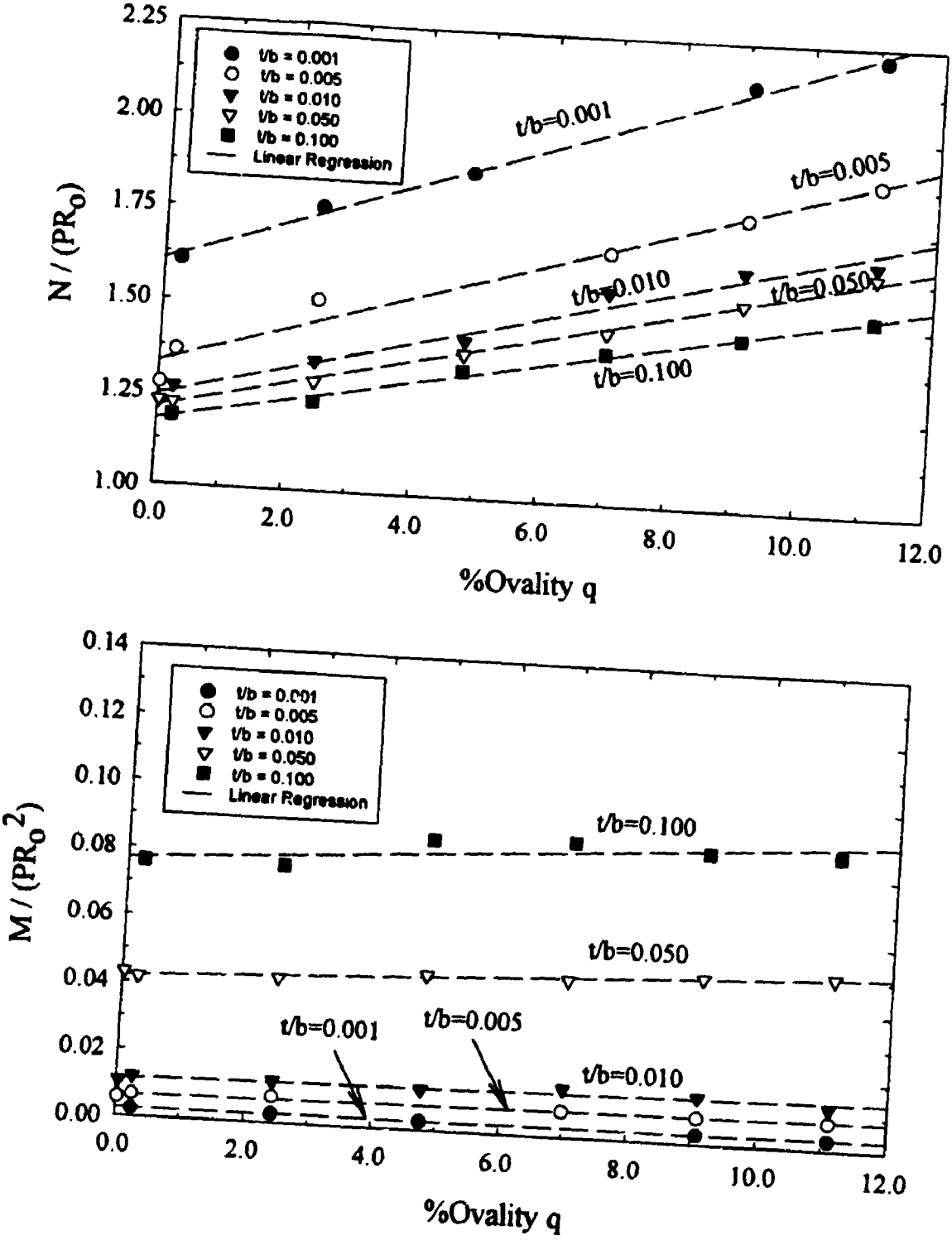

Figure 6.8. Effect of Ovality q and Thickness to Radius ratio (t/b) on the Thrusts and Moments

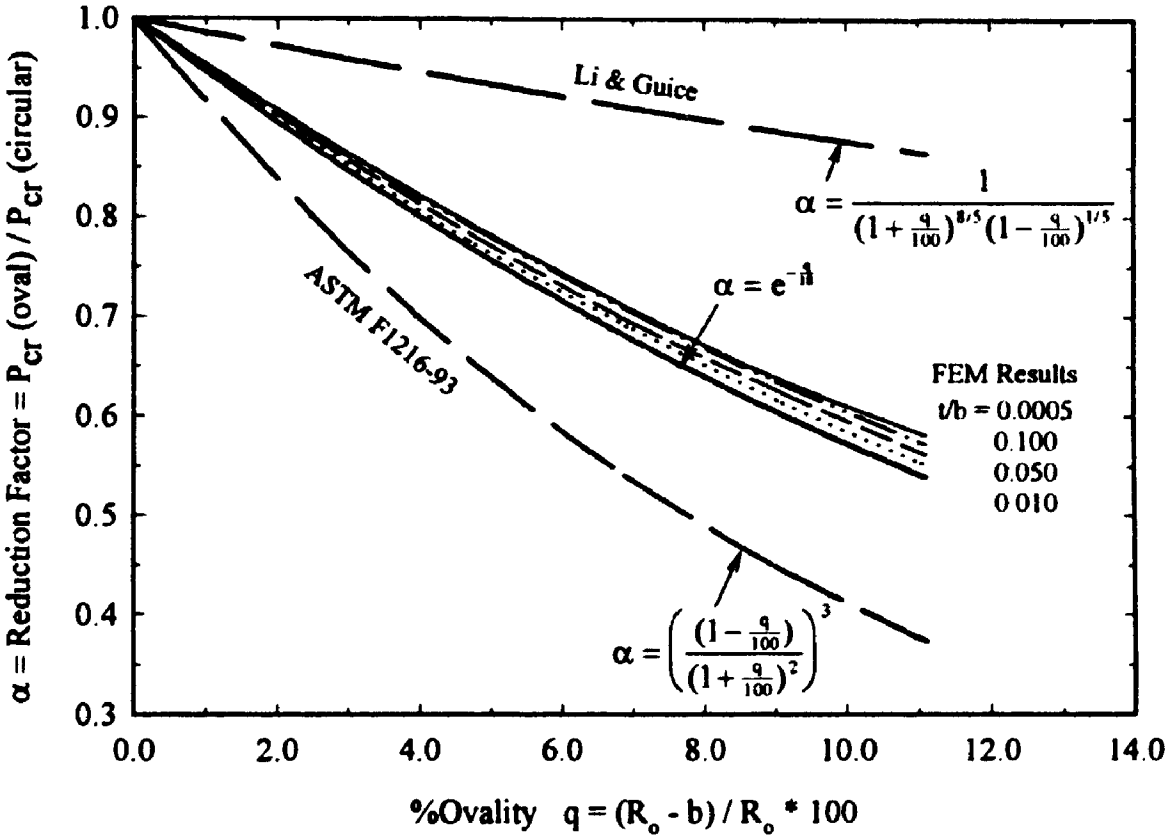

Figure 6.9. Critical Pressure Reduction Factor α Due to Ovality

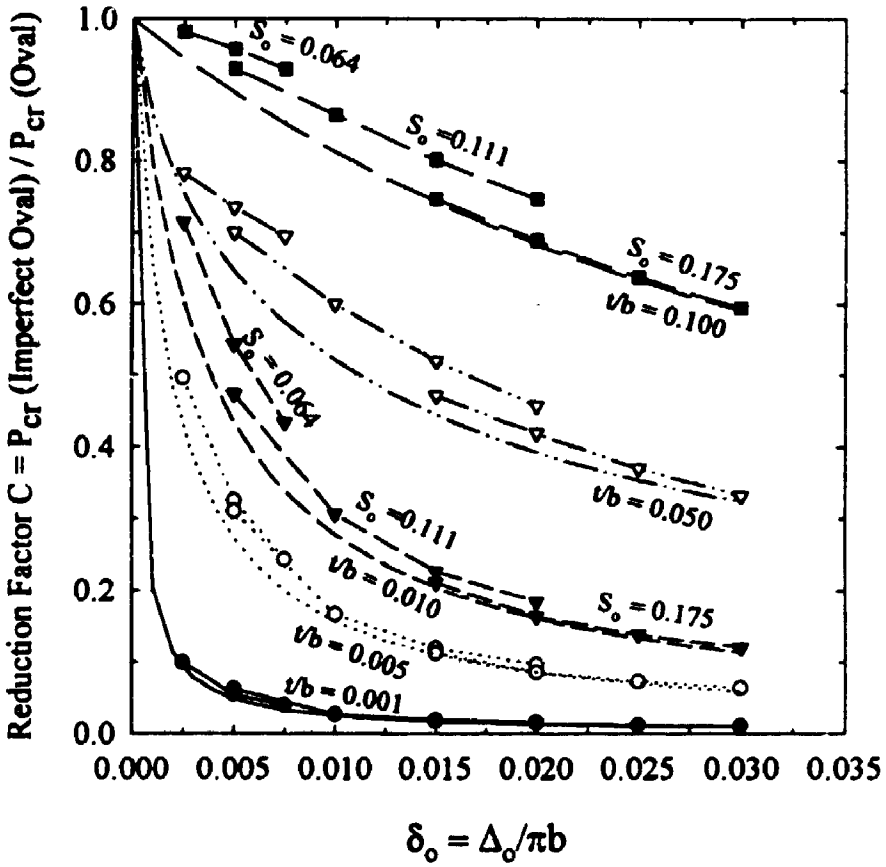

Figure 6.10. Reduction Factor due to Local Imperfection for Ovality a/b=1.005, q=0.25%

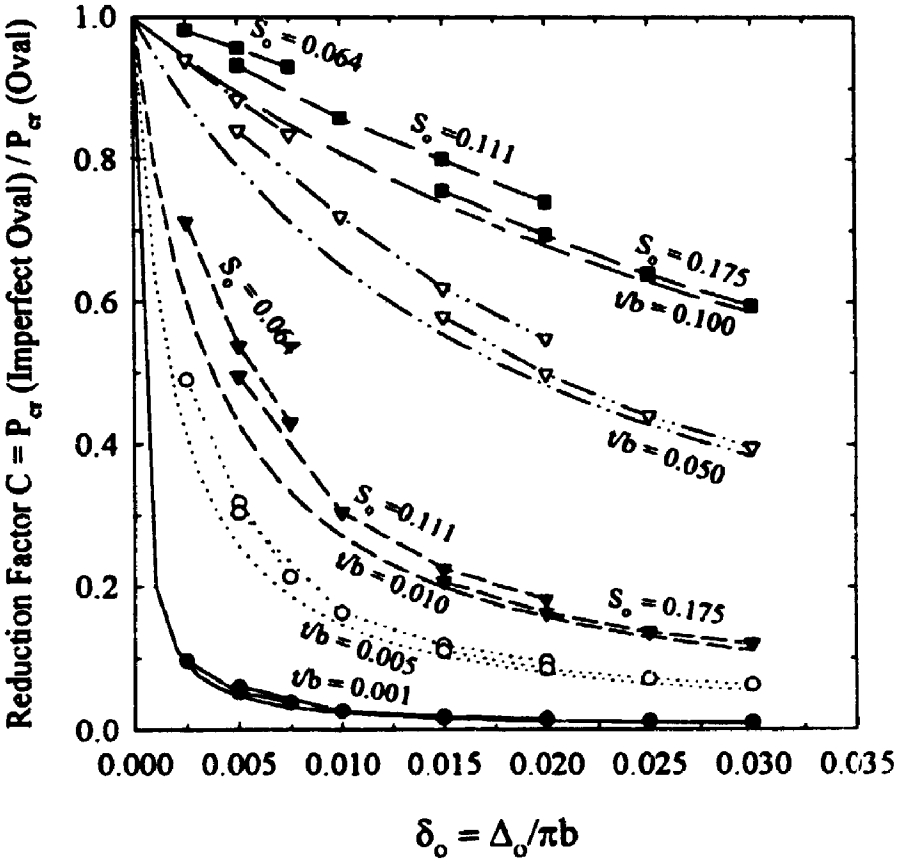

Figure 6.11. Reduction Factor due to Local Imperfection for Ovality a/b=1.10, q=4.76%

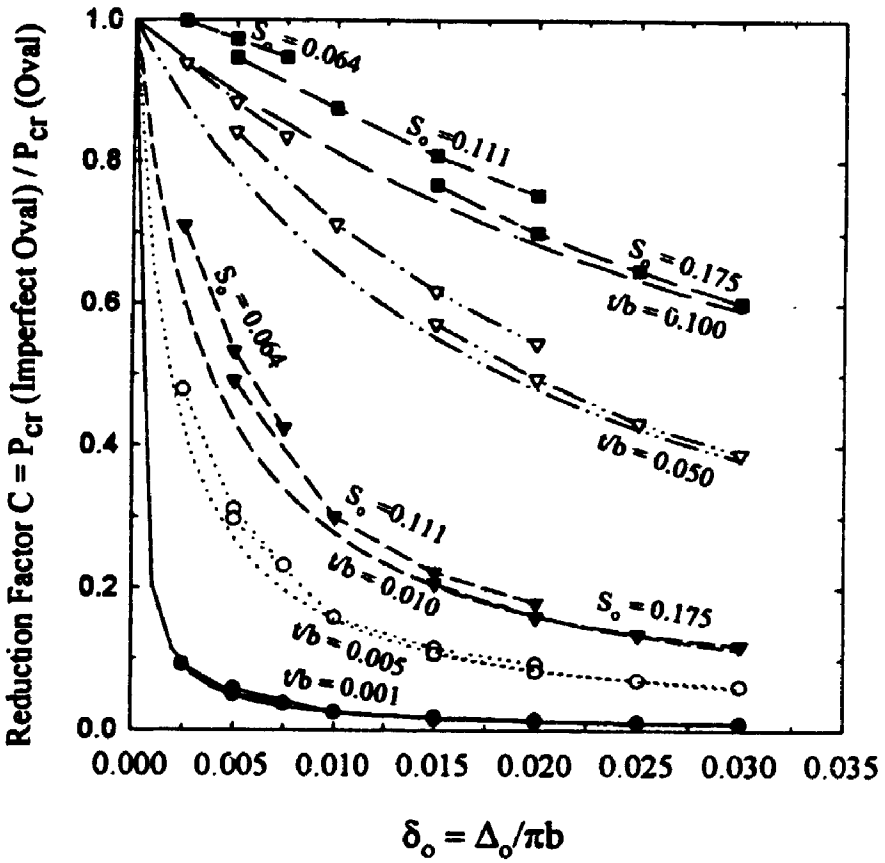

Figure 6.12. Reduction Factor due to Local Imperfection for Ovality a/b=1.25, q=11.11%

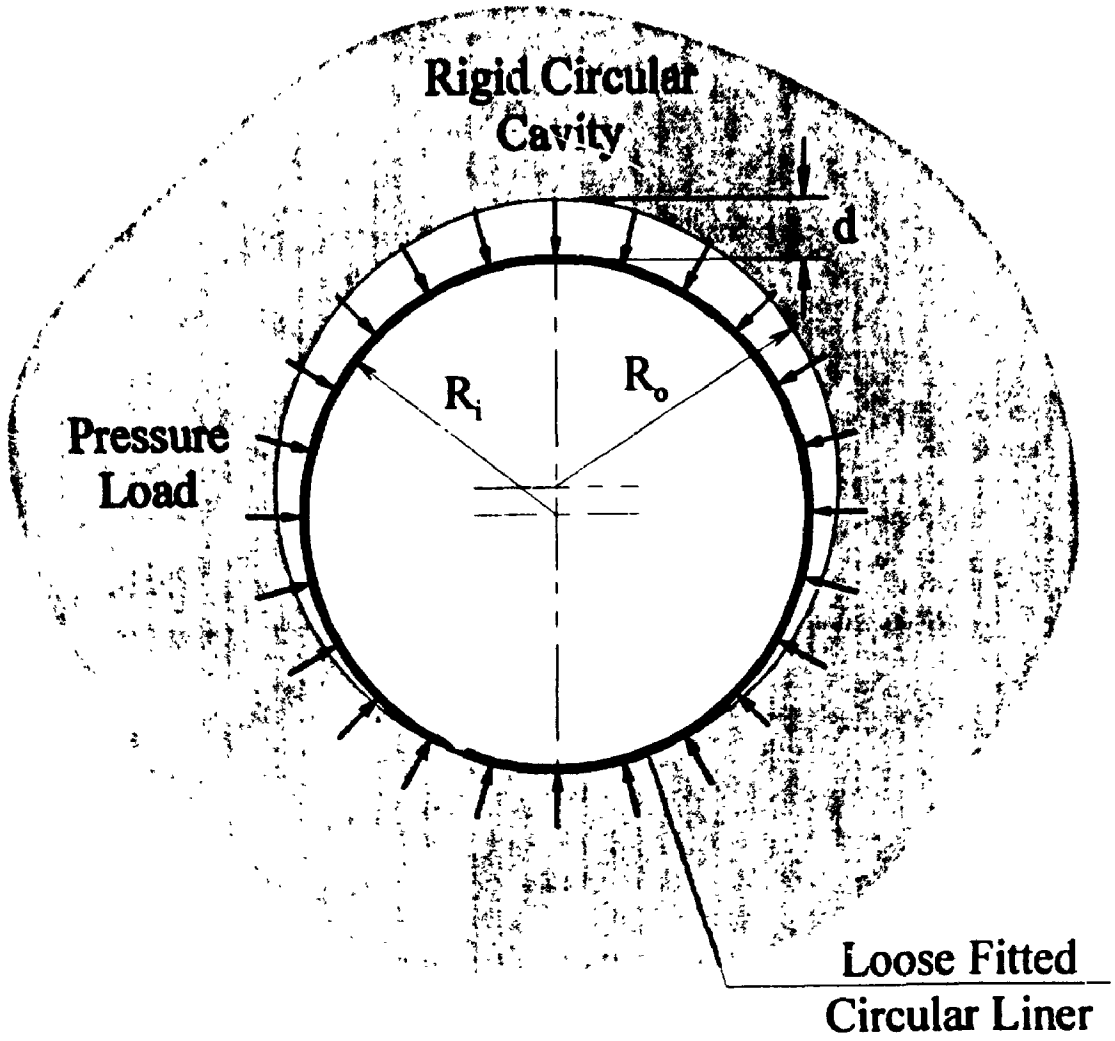

Figure 6.13. Problem Definition of a Loosely Fitted Circular Liner

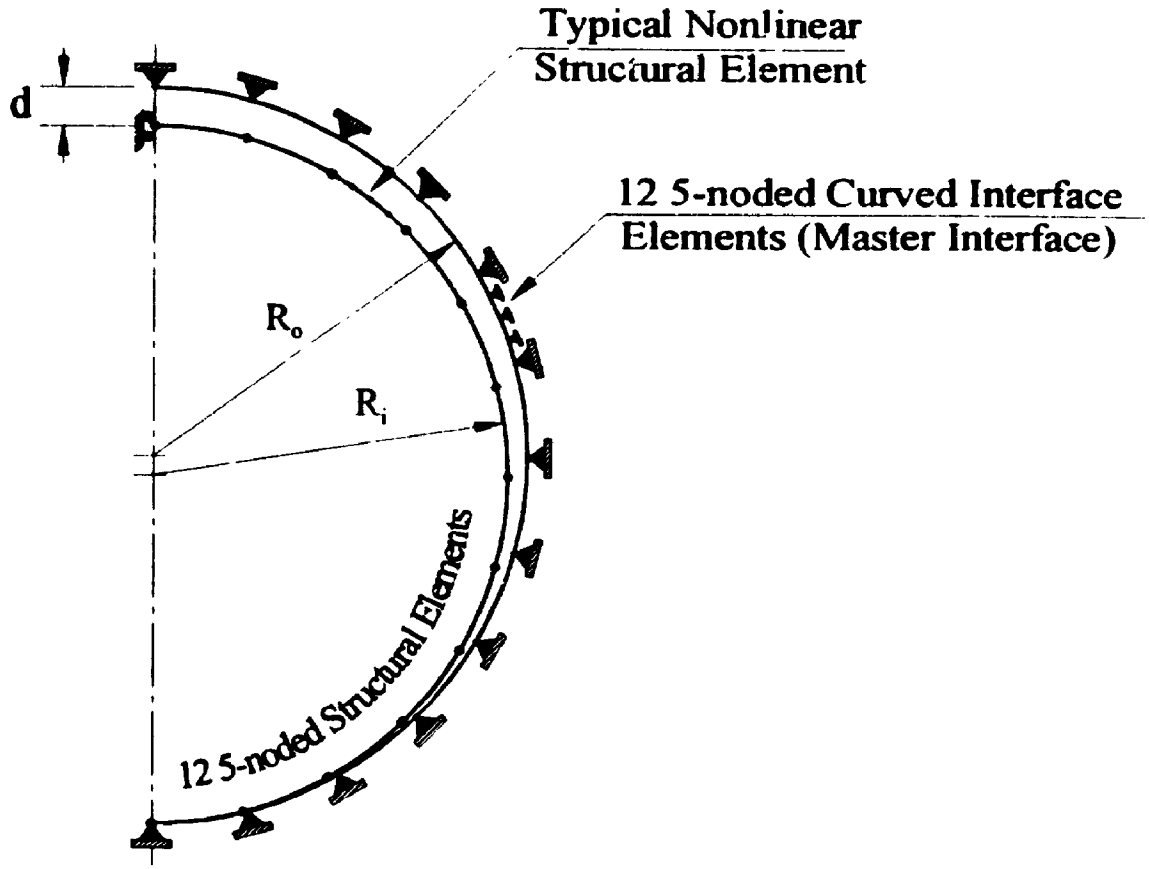

Figure 6.14. FEM Model used for the Analysis of a Loosely Fitted Liner

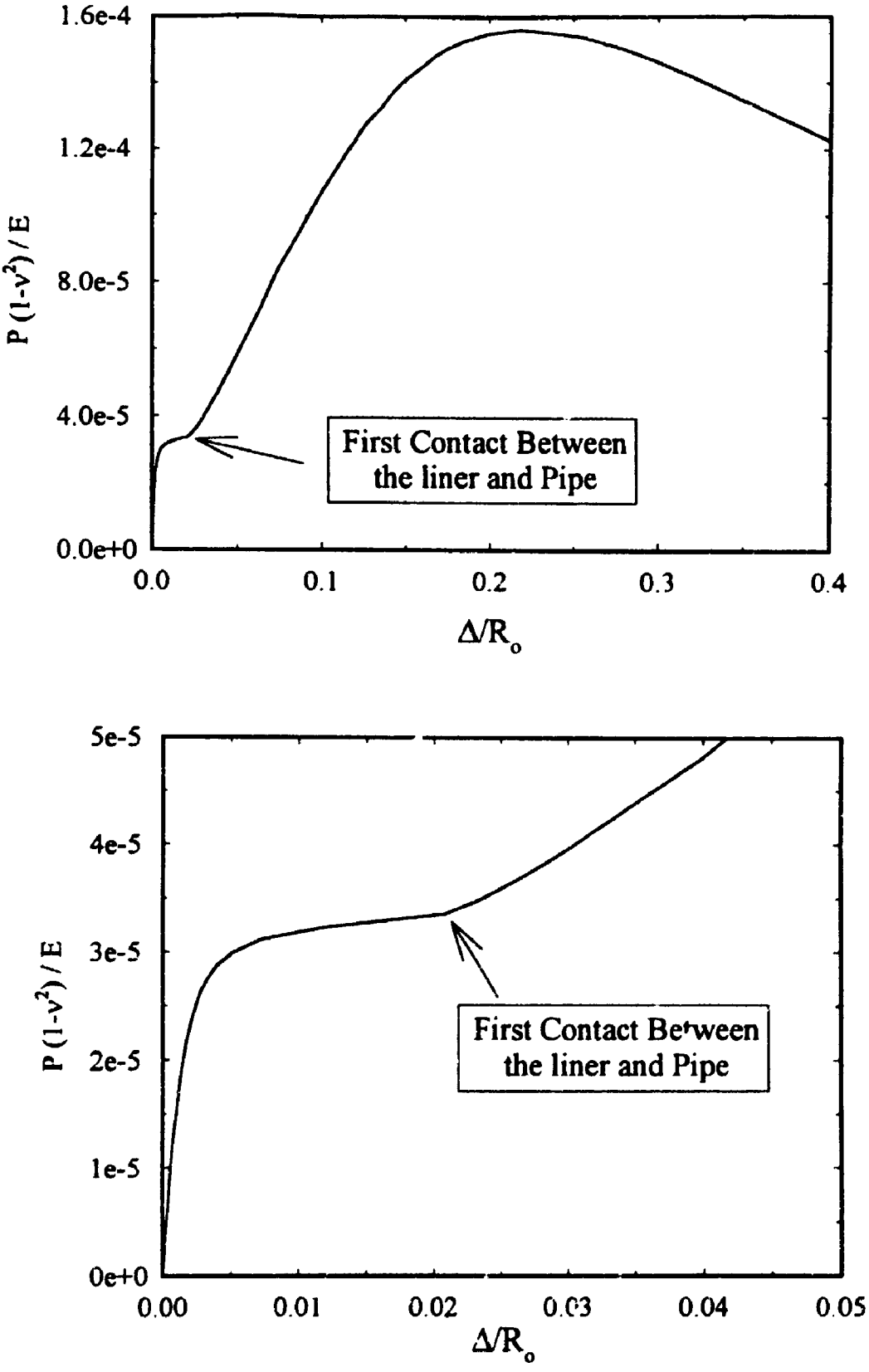

Figure 6.15. Load-Deflection of the Crown of a Loosely Fitted Liner (t/R_o=0.05, d/R_o=0.05)

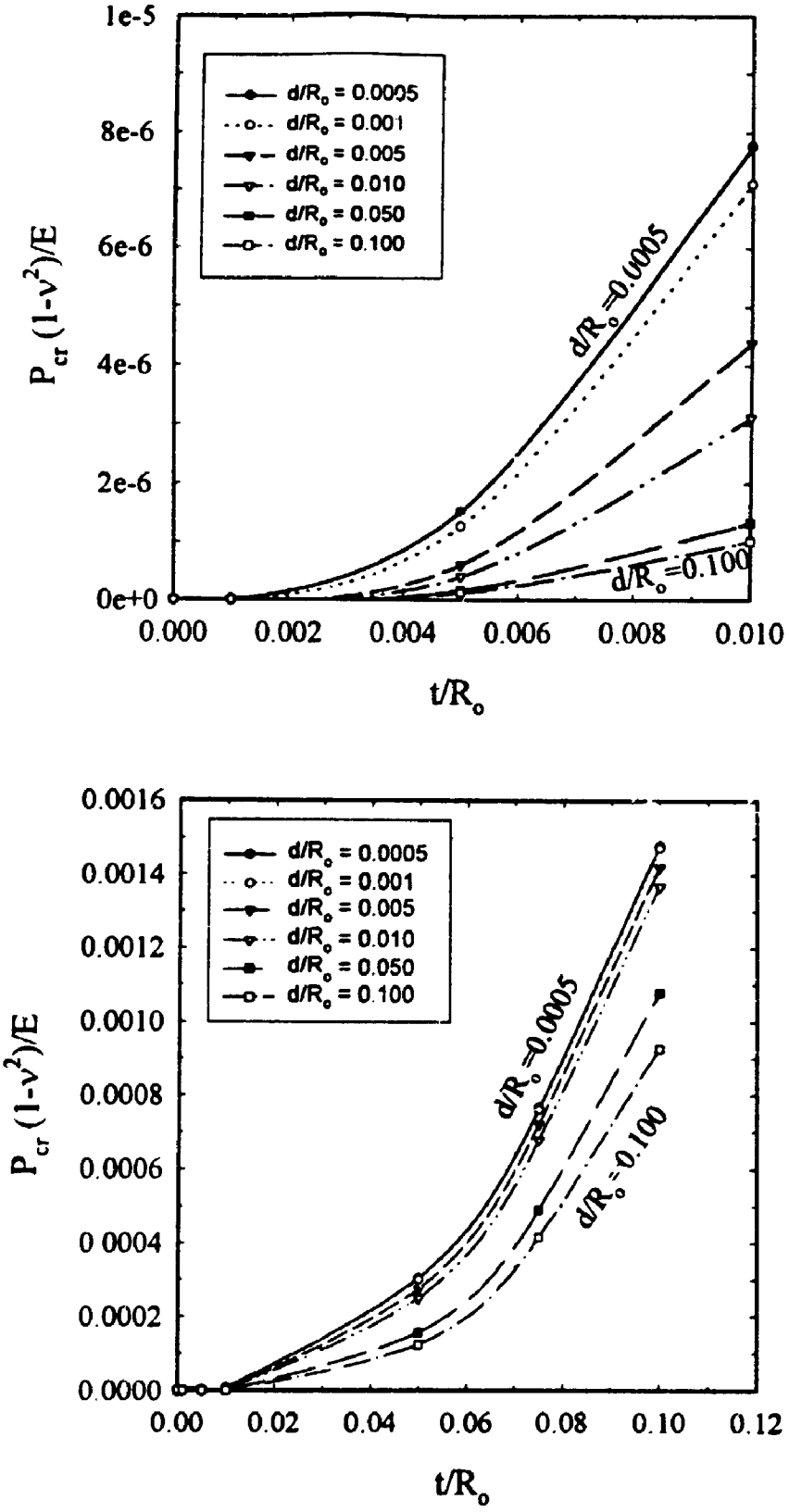

Figure 6.16. Critical Pressure for The Loosely Fitted Liner In a Rigid Cavity

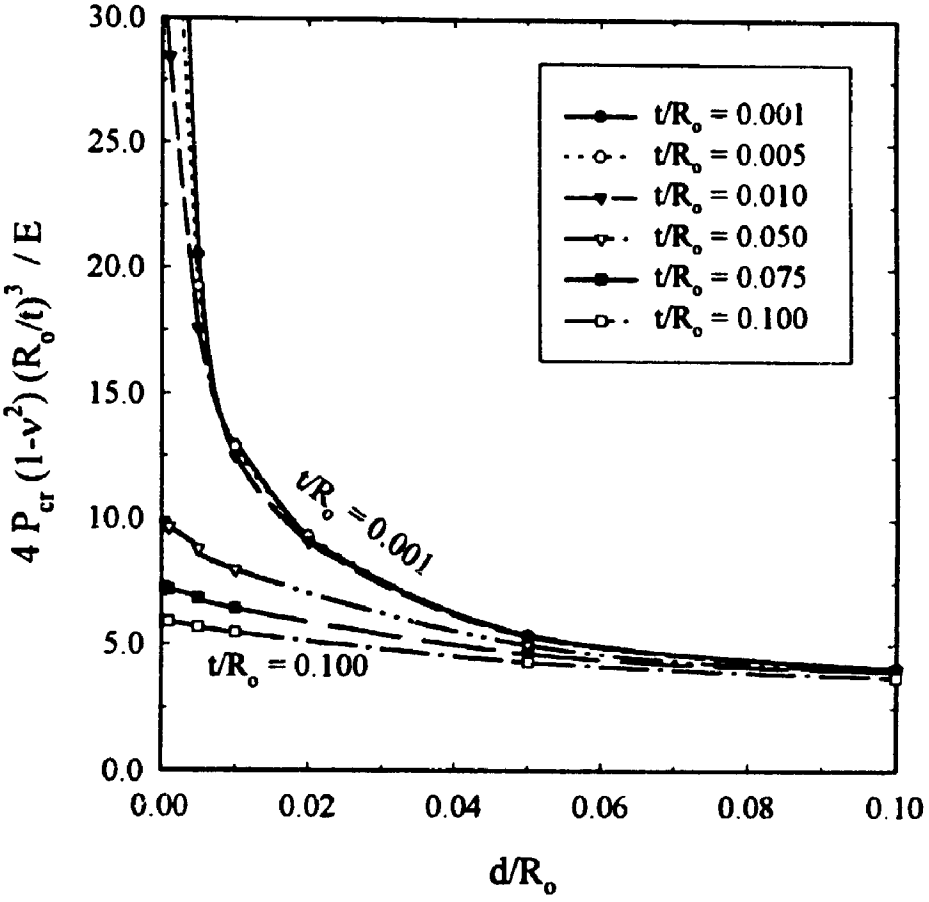

Figure 6.17. Effect of (d/R_o) Ratio on the Critical Pressure for The Loosely Fitted Liner in a Rigid Cavity

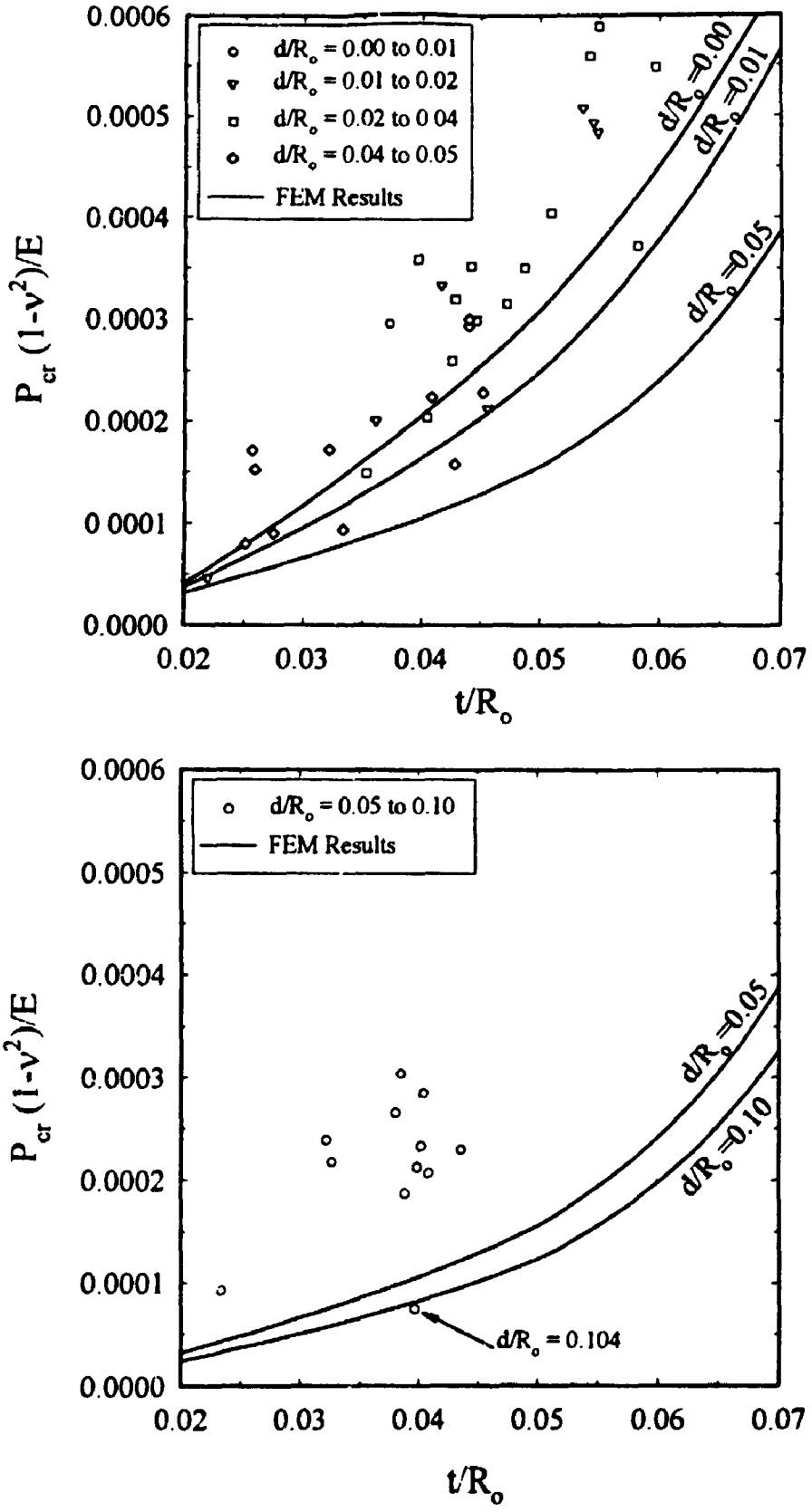

Figure 6.18. Comparison Between Aggarwal and Cooper Experimental Results and the Theoretical Critical Pressure for the Loosely Fitted Liner in a Rigid Cavity

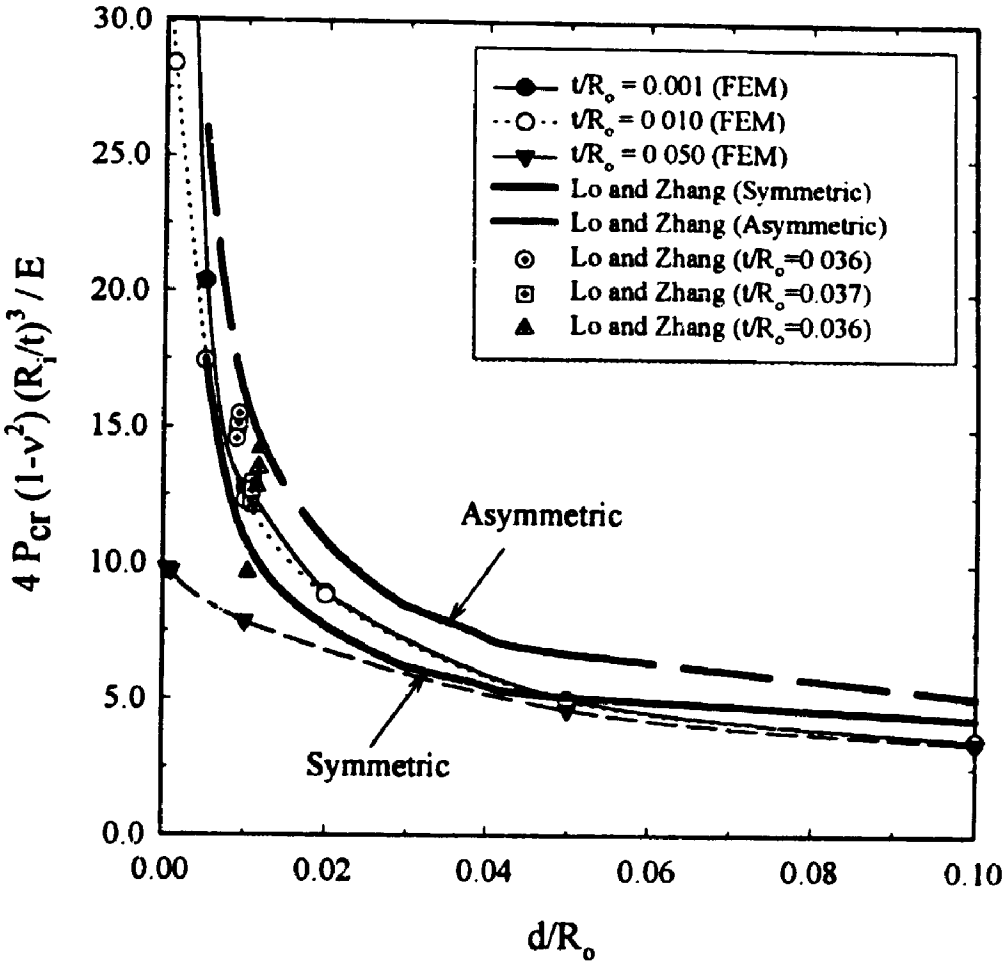

Figure 6.19. Comparison between FEM, Lo and Zhang solution, and Experimental Results

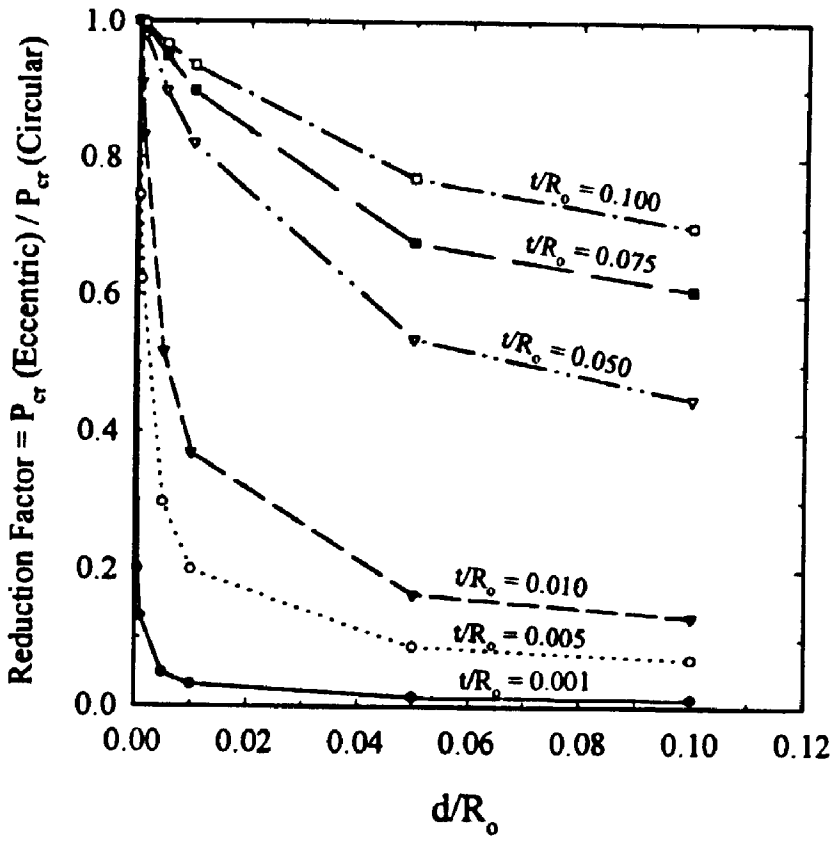

Figure 6.20. Reduction Factor to the Critical Pressure Due to The Loose Fitting Imperfection

CHAPTER SEVEN

Effect of Material Non-Linearity on the Liner Behaviour

7.1. Introduction

Liners for damaged pipelines are designed to satisfy various requirements. The yielding of the liner material is one of the principle design criteria. After discussing the elastic behaviour of the liner under external pressure, it is valuable to study the effect of material non-linearity on the liner stability.

The work presented in this chapter is not intended to be an extensive parametric study of the effect of the material non-linearity on the polymer liner behaviour as this would need the accurate modelling of the time-dependent behaviour of the polymer liner material which is beyond the scope of this thesis. However, the objective of this chapter is to examine whether yielding of the liner material controls the critical pressure. To investigate this issue it will be assumed that the liner material has a distinguishable yield stress. Although this is not true for most polymers (the polymer behaviour is significantly time-dependent with an indistinct transition from linear to non-linear response), this chapter gives some preliminary insight into the problem of material non-linearity. A bi-linear elasto-plastic material response with Young's modulus defined for long term material behaviour is used More sophisticated modelling of the material will be the subject of future research.

The Finite Element Method is used to analyse the materially non-linear problem The same rigorous interation and Arc-Length Control methods, discussed before, are used in the investigation.

7.2. Long Term Polymer Behaviour

For fluid pressure sustained over a long period, the "long term" material response controls the pipe deformations (and therefore the non-linear buckling process). The Young's modulus for the polymer material is time-dependent $E(t)$, where t is time. It can be defined at any time t in terms of the time-dependent stress $\sigma(t)$ and strain $\varepsilon(t)$ under uniaxial loading by

$$E(t) = \frac{\sigma(t)}{\varepsilon(t)} \tag{7.1}$$

Values of $E(t)$ can be estimated for various load paths at different times, including the creep condition (constant stress $\sigma(t)$ and increasing strain $\varepsilon(t)$ with time). It is clear that for problems involving sustained stress, $E(t)$ as defined in Eqns. 2.19 or 7.1 decreases as time increases Therefore, the time-dependent Young's modulus used in the critical pressure calculations, is estimated based on a reasonable design life for the liner assuming constant load is applied over the liner lifetime (say, 50 years). If a shorter design life is used, the liner would be stable as long as Young's modulus is greater than its assumed design value. Once Young's modulus becomes less than the design value the liner may be unstable.

7.3. Finite Element Model and Results

The same model used for the analysis of circular liners (Fig. 5.7) is used, but with a bi-linear work hardening elasto-plastic model (discussed in chapter three) for the liner material. The liner is represented by sixteen 5-noded structural elements and the smooth interface of the rigid cavity is modelled using sixteen 5-noded non-linear interface elements. The element cross section is modelled using two layers (which show almost identical results for

the case of three layers). The two parameters describing the material non-linearity are σ_y, E and E/E_t, where σ_y is the yield stress of the liner material. The ratio σ_y, E is chosen to ensure that the liner pressure corresponding to the yield stress is less than the elastic critical liner pressure. Two liner thicknesses are considered which correspond to thickness to radius ratios t/R=0.05 and 0.10. Different σ_y/E and E/E_t ratios are considered to study the effect of each parameter on the liner behaviour.

7.4. Effect of Strain Hardening of the Liner Material

Figures 7.1 and 7.2 show normalized vertical displacement δ/R at the circular liner crown versus the normalized pressure for different E/E_t ratios for the cases of t/R=0.05 and 0.10. The pressure is normalized by the critical pressure $\frac{E}{(1-\nu^2)}\left(\frac{t}{D}\right)^{2.19}$ developed from elastic finite element results in chapter five. Figure 7.3 shows the response for the case of an oval liner with ovality a/b=1.15, σ_y/E=0.01 and t/R=0.10. Many useful observations are extracted from these figures.

- For circular liners with t/R=0.05 and 0.10, and $E/E_t \leq 4$, the critical pressure decreases as the liner material strain hardening decreases (i.e. E/E_t decreases) until a limiting value (E/E_t>4) after which the critical pressure corresponds (approximately) to the pressure at the point of first material yield. This would suggest that for circular liners the peak pressure corresponds to first yield if strain hardening of the material is not significant
- For the case E/E_t=50.0 (Fig. 7.1), the resistance drops significantly after the initiation of the yielding process. Even for the other cases with smaller E/E_t ratios, the Arc- Length Control Method resulted in the use of very small pressure increments which indicates that the spread of plasticity is rapid.

- Figure 7.1 shows the two typical solutions for liner unloading from point X on the load path for E/E_i=2.0. The first solution (unloading path 1) is obtained using the Arc-Length Control method while the second (unloading path 2) is obtained using the Newton-Raphson method beyond point X. Both solutions are physically possible.

  The first path corresponds to unloading while steadily pumping fluid in to fill the growing gap between the rigid cavity and the liner. This represents the real physical outcome as the test continues to proceed following the peak or critical pressure.

  The second unloading path corresponds to unloading that occurs while allowing fluid to escape from the gap. Loading, by forcing the water into the gap, is reversed at point X as fluid is removed from the system.

  The Arc-Length Control Method is forced to pick the first unloading path because of the algorithm used for choosing the root of the second order equation generated in the analysis. The root chosen in that analysis has tangent to the load-deflection curve (in multi-dimensional space) that is almost the same or closest to that tangent of the previous solution step.

- The oval liner is more prone to yield than the circular liner. This is because bending moments generated in the oval liner are higher than those generated in a circular liner having the same average radius of the oval liner (as shown in chapter six).

- For practical cases, the yield may only be important for thick liners, where the yielding pressure is less than the elastic buckling pressure. For example, an encased "perfect" circular thick liner of thickness to radius ratio t/R=0.1, Young's modulus E=350MPa, Poisson's ratio ν=0.3, and yield stress σ_y=5MPa, has a critical pressure

$$P_{cr} = \frac{E}{(1-\nu^2)}\left(\frac{t}{2R}\right)^{2.19} = 0.554 \text{ MPa} \qquad (7.2)$$

and if we neglect any bending moments in the liner, then the stress becomes

$$\sigma = \frac{N}{A} = \frac{P_{cr} R}{t} = \frac{0.544}{0.10} = 5.44 \text{ MPa} > 5.0 \text{ MPa} \qquad (7.3)$$

So the thick liner yields before it buckles.

- For thin liners, the elastic buckling usually controls the calculation of the critical pressure and the yielding effect can be neglected. If the previous example is used again, but for a thin liner with t/R=0.01, then

$$P_{cr} = \frac{E}{(1-\nu^2)}\left(\frac{t}{2R}\right)^{2.19} = 0.0035 \qquad (7.4)$$

and

$$\sigma = \frac{N}{A} = \frac{P_{cr} R}{t} = \frac{0.0035}{0.01} = 0.35 \text{ MPa} < 5.0 \text{ MPa} \qquad (7.5)$$

So the thin liner does not yield before it buckles.

7.5. Deformed Shape of the Liner and Spread of Plasticity

The different deformed shapes for the case of E/E_t=3.0, t/R=0.05, and σ_y/E=0.005, are shown in Fig. 7.4. The plasticity zones are also interpreted from the value of the angle θ which defines the regions along the liner where plasticity has started in any part of the cross section. It is clear that, after buckling, the plasticity spreads (i.e. angle θ increases) along the liner significantly even after the reduction of the pressure (i.e. after post-peak pressure).

7.6. Effect of Yield Stress on the Liner Behaviour

Different σ_y/E ratios are considered to study the effect of various yield stresses on the liner behaviour. Figure 7.5 shows the normalized deflection of the liner crown versus the normalized pressure for different σ_y/E ratios; σ_y/E=0.005, 0.0045, 0.004, and 0.0035. The liner considered has t/R=0.05 and E/E_t=2.0. The figure shows that the behaviour is following the same trend except the point of yield differs depending on the yield stress.

7.7. Conclusions

The brief parametric study of materially non-linear response has clearly revealed that yield in the liner can significantly affect the liner stability under the influence of external fluid pressure. The plasticity of the liner material reduces the critical pressure when enough strain hardening is present. For cases involving small amounts of strain hardening or softening, the critical pressure corresponds to the yield pressure.

For practical cases, the previous behaviour may only be valid for thick liners, where the pressure causing yielding is less than the pressure at which elastic buckling occurs. For thin liners, the critical pressure is governed by elastic buckling and not yielding.

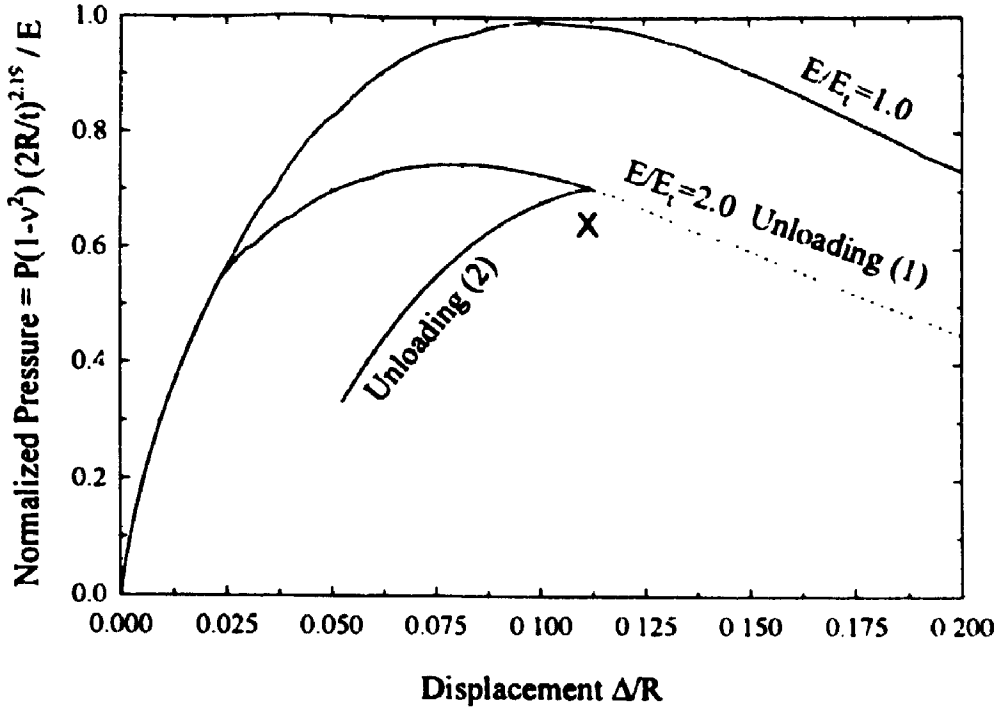

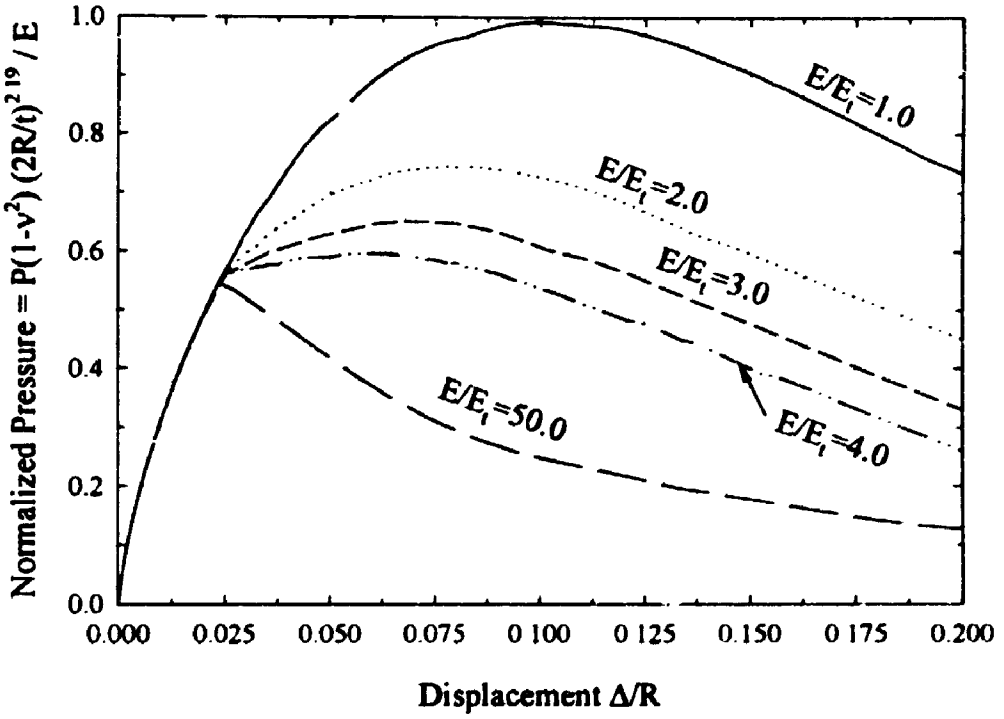

Figure 7.1. Liner Load-Deflection at the Liner Crown for Loading and Unloading Cases and Different E/E_t ratios (t/R=0.05, σ_y/E=0.005, ν=0.3)

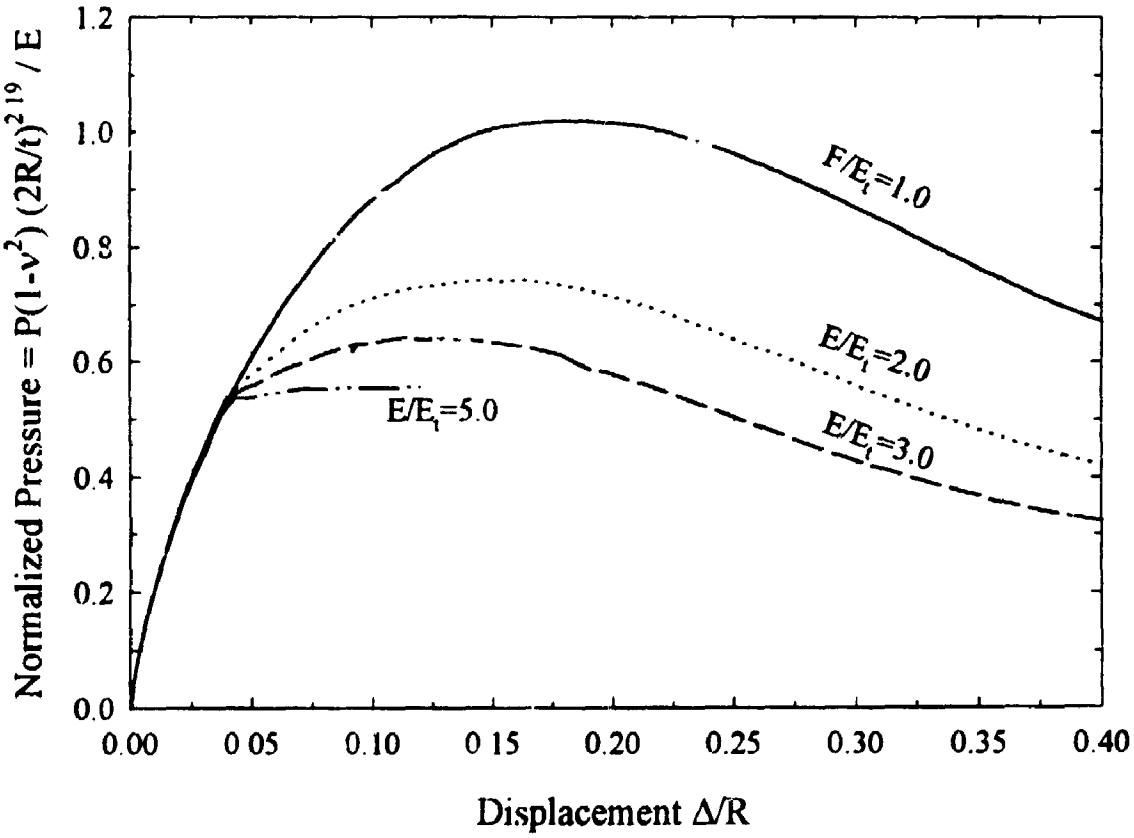

Figure 7.2. Liner Load-Deflection at the Liner Crown for Different E/E_t ratios (t/R=0.10, σ_y/E=0.01, ν=0.3)

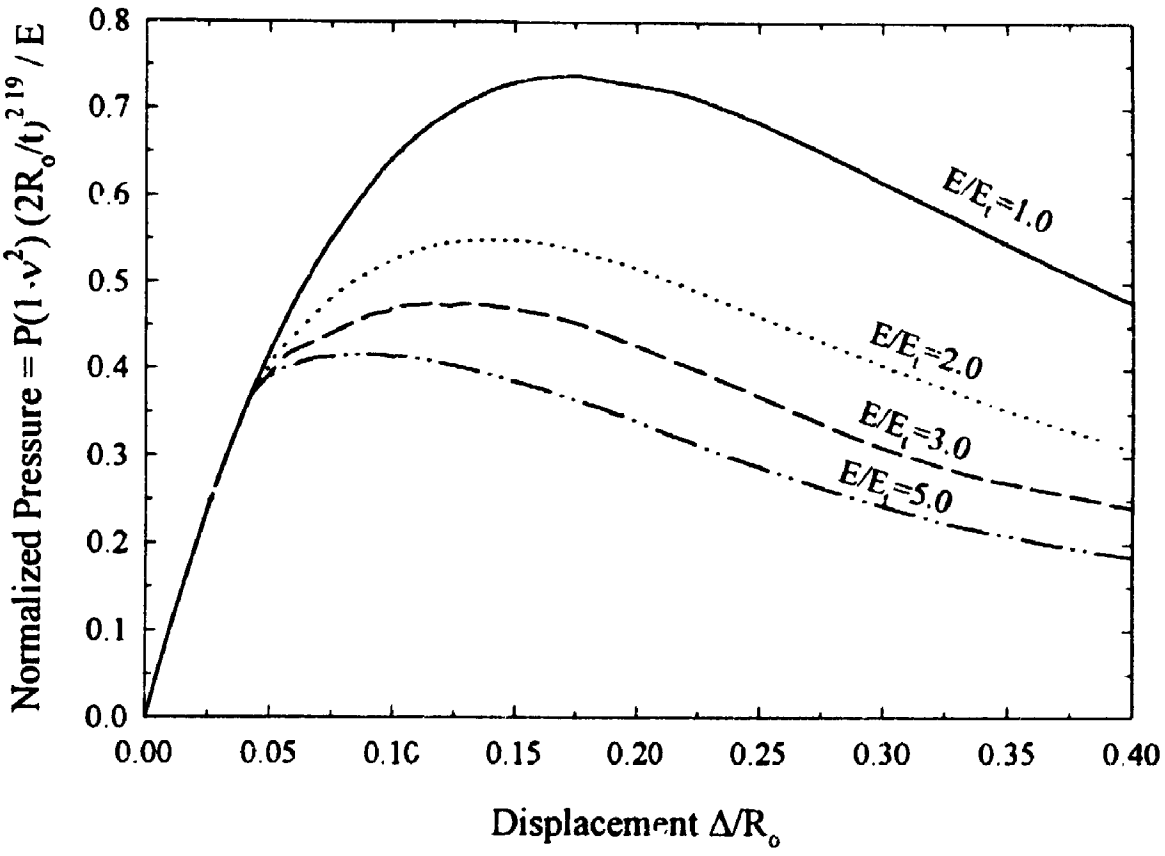

Figure 7.3. Liner Load-Deflection at the Oval Liner Crown for Different E/E_t ratios (t/R=0.10, a/b=1.15, σ_y/E=0.01, ν=0.3)

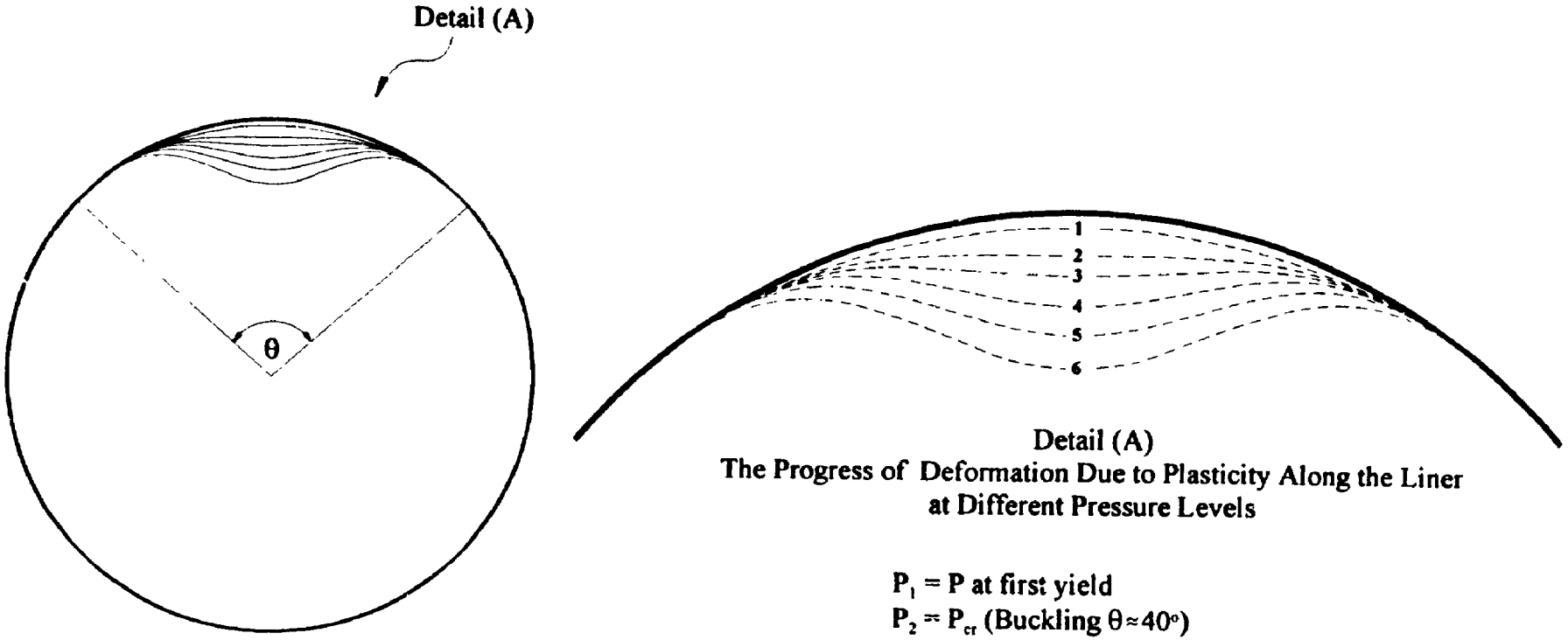

Liner Deformed Shape at Different Pressure Levels

Detail (A)
The Progress of Deformation Due to Plasticity Along the Liner
at Different Pressure Levels

P_1 = P at first yield
$P_2 = P_{cr}$ (Buckling $\theta \approx 40^o$)
$P_3 = 0.925\ P_{cr}$ (Post-Buckling $\theta=45^o$)
$P_4 = 0.620\ P_{cr}$ (Post-Buckling $\theta=67^o$)
$P_5 = 0.560\ P_{cr}$ (Post-Buckling $\theta=85^o$)
$P_6 = 0.444\ P_{cr}$ (Post-Buckling $\theta=90^o$)

Figure 7.4. Deformed Shape of an Elasto-Plastic Liner Under Pressure Load
($t/R=0.05$, $E/E_t=3.0$, $\sigma_y/E=0.005$, $\nu=0.3$)

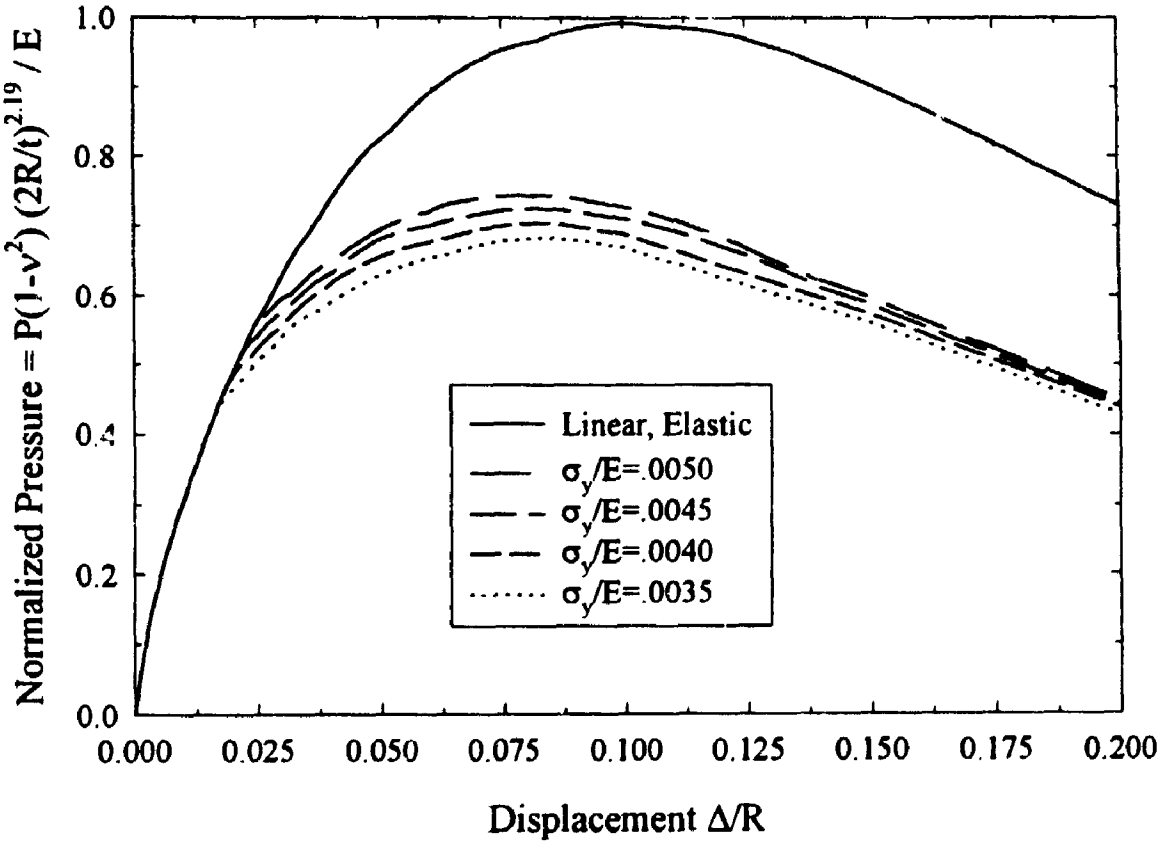

Figure 7.5. Liner Load-Deflection at the Liner Crown for Different σ_y/E ratios (t/R=0.05, E/E_t=2.0, ν=0.3)

CHAPTER EIGHT

Design of Polymer Liners Subjected to External Pressure

8.1. Introduction

The most conservative choice of buckling load for liners is that for the case of no external support. Besides being uneconomic with respect to material quantities, it also adds more cost and difficulty to the installation of the thick liner into the pipeline. In the previous three chapters, studies have been undertaken to evaluate the critical pressure on polymer liners. New design tools, useful for design engineers, may be extracted from this work. The design tools, discussed in this chapter, are a summary of the previous work and are proposed as an alternative to the available design equations and empirical correction factors recommended in ASTM specifications [41] The aim of this chapter is to evaluate the parameters required for the design of liners subjected to pressure (i.e. critical pressure, thrusts and bending moments). However, any other possible loading cases and design issues not covered in this study, should also be considered in the design.

8.2. Evaluation of the Liner Geometry and Material Properties

The idealization of the installed liner geometry is the most important step in liner design. In practice, the basic geometry of the pipeline is assessed after the pipeline to be rehabilitated is cleaned of any debris This information should be compared with the available construction drawings of the pipeline. The pipeline is then inspected for any protruding obstacles using a video camera supported on a device which moves inside the damaged pipeline. If the size of obstacles exceeds a certain limiting value a point repair

excavation is performed (e.g. ASTM [41] requires that obstacles which exceed the lesser of 16% of the pipeline inner diameter or 25mm to be removed). An experienced person, equipped with a robot carrying a video camera which is inserted inside the pipe, should perform the inspection to identify the different types of pipeline imperfections which will be mirrored later in the installed liner. Other types of imperfections due to the thermal contraction of the liner (if a heat treatment process is used) should also be estimated. A reasonable assessment of the expected liner geometry, both radius R, ovality q, and the imperfection shape (e.g. amplitude Δ_o) should be possible.

Beside the estimation of the liner geometry, the material properties of the liner are also required. In the absence of any time-dependent study of the liner material, the conventional method of designing the liners may be used. The elastic material modulus E (Young's modulus) and Poisson's ratio ν are defined based on the long term performance over the design life of the liner. Modulus is selected considering the time dependent behaviour of the polymer material under sustained load.

8.3. Critical Pressure, Thrusts, and Bending Moments in the Liner

The evaluation of the critical pressure, thrusts and bending moments, is the first step in the liner design. In this section, a proposed method for that purpose is reported. Other available tools or equations are also reported for comparison purposes

Two types of liners are considered; the first is an oval liner with a local imperfection and the second is a loosely fitted liner. Each case is considered in turn in the following sections.

8.3.1. Design Equations and Charts for Oval Liners

An oval liner with an ovality defined by the ratio between the lengths of the oval axes (i.e. *a/b*, *2b* being the length of the small axis) and a local imperfection of normalized amplitude $\delta_o=\Delta_o/b$ is considered. The case of the circular liner with a local imperfection is the special case when *a/b* approaches unity.

The elastic buckling pressure is given by the equation

$$P_{cr} = \frac{2E}{1-\nu^2}\left(\frac{t}{2R_o}\right)^3 K C \alpha \qquad (8.1)$$

where

E is the reduced Young's modulus based on the long term material response,

ν is Poisson's ratio based on the long term material response,

t is the liner thickness,

R_o is average radius of the oval liner (i.e. $R_o=(a+b)/2$),

K is an enhancement factor due to the encasement,

C is a reduction factor due to the local imperfection, and

α is a reduction factor due to ovality.

The first part in the expression for the critical pressure (i.e. $\frac{2E}{1-\nu^2}\left(\frac{t}{2R_o}\right)^3$), represents the critical pressure for the unsupported circular liner of radius R_o. This solution corresponds to a long liner responding under plane strain conditions.

The factor K increases the critical pressure for the circular liner due to encasement and is defined by

$$K = \frac{1}{2}\left(\frac{2R_o}{t}\right)^{0.8} \qquad (8.2)$$

where the exponent 0.80 is used instead of 0.81 (the value calculated form the least square curve fitting of the FE results) for simplicity. The error involved in this is practically negligible (about 4% for t/R_o=0.01).

In the ASTM design code, the recommended value for K is 7, which also corresponds to the value recommended by Aggarwal and Cooper [1] based on their experimental results for circular specimens of maximum t/R_o ratio equal to 0.07. According to Eqn. 8.2, this K value is not conservative for liners with t/R_o ratios higher than 0.07. For values of t/R_o ratios less than 0.07, K=7 is conservative and uneconomic.

The factor α, is a reduction factor due to ovality, and is dependent on the ratio a/b or the non-dimensional ovality parameter q. The reduction factor α, is defined by the exponential form

$$\alpha = e^{-\frac{q}{18}} \tag{8.3}$$

As shown in chapter six, the definition of the reduction factor α using Eqn. 8.3, is more appropriate and economical than the definition used in various ASTM specifications. Moreover, it was demonstrated that the ASTM approach is based on a reduction factor assuming equal ovality reductions for both unsupported and encased liner cases.

The factor C accounts for the reduction in the critical pressure due to a local imperfection. The imperfection is assumed to occur at the flattest part of the oval liner which is a conservative assumption suitable for design purposes. Imperfections in host pipe will frequently occur at the invert, given damage due to abrasion, misalignment associated with pipe settlement or the presence of solid material in the host pipe. Ovality resulting from earth loading on the host pipe will most often feature horizontal diameter increase and

vertical diameter decrease, so that imperfections may often be at the flattest part of the oval host pipe.

The reduction factor C is obtained from the chart in Fig. 8.1, which shows conservative "lower bound" design envelopes for a/b ratios of 1.0005, 1.10, and 1.25. The chart is suitable for circular liners ($b=R_o$) as well as oval liners. It is clear that even for small local imperfections, the reduction is significant, particularly for small t/b ratios. This would suggest that a minimum value for δ_o should be recommended by the design codes even for perfect circular liners In the author's opinion, δ_o=0.0025 ($\frac{\Delta_o}{b} = 0.008$) should be considered as that minimum value.

The thrusts and bending moments given for design are the values at the critical pressure in contrast to the values at the working stress level which may be used by some specifications. Figure 8.2 shows the variation of the thrust and bending moments at the point of maximum radius of curvature (i.e. at the centre of the buckle location) versus the ovality factor q for different values of t/b ratios. The design thrust and bending moment defined by ASTM are discussed before in chapter six and are shown to be based on the unsupported liner case. The thrust value may look greater than the usual design values $N=PR_o$, but this is due to of the formation of the hinged arch mechanism (discussed in chapter six) once liner separation starts.

8.3.2. Design Equations and Charts for Loosely Fitted Liners

The second type of liner considered is a loosely fitted liner with an outer radius R_i. The rigid host pipeline has an inside radius R_o. The gap between the liner and the circular rigid cavity is defined by d, where $d=2(R_o-R_i)$. The elastic buckling pressure is defined by

$$P_{cr} = \frac{2E}{1-\nu^2}\left(\frac{t}{2R_o}\right)^3 K \qquad \textbf{(8.4)}$$

where

E is the reduced Young's modulus based on a long term material response,

ν is Poisson's ratio based on a long term material response,

t is the liner thickness,

R_o is the average radius of the oval liner(i.e. $R_o=(a+b)/2$), and

K is an enhancement factor due to the encasement, and can be obtained from Fig. 8.3.

Conservative values for thrust and moments may be taken from Fig. 8.2 for the case of no ovality (i.e. q=0).

The design approach presented above have the liner thickness as an input which is used to calculate the elastic buckling pressure, and thrust and bending moment in the liner. Then the thrust and bending moment are used to calculate the stress in the liner and check it against the yield stress of the liner material to fully define the peak pressure of the liner. A factor of safety FS is then applied to the peak pressure to define the allowable pressure on the liner.

Another approach is to define the liner thickness as a function of the liner geometry, material properties, factor of safety, and the given applied pressure. Unfortunately, this definition of the liner thickness is very difficult to obtain due to the non-linear nature of the liner behaviour.

8.4. Recommendations

Due to the sensitivity of the problem for cases of small thickness to radius ratios, extra precautions should be taken during design by increasing the factor of safety or limiting the enhancement factors to a certain value. Extra evaluation of the proposed method based on experimental results is required, but it seems a better alternative to the ASTM design tools. The time-dependent effect of the polymer material is not considered, but is accounted for by simply using the material properties based on long term behaviour. The study of the liner stability over time may be considered in a future study.

8.5. Example Calculations

To illustrate the procedure for the calculation of critical liner pressure, thrusts and bending moments, an example calculation is now presented. The liner considered has the following properties:

- thickness t = 0.035 m,
- average outer radius R = 0.375 m,
- Young's modulus E = 200 MPa,
- Poisson's ratio ν = 0.3, and
- local imperfection amplitude δ_o = 0.01.

Different ovality ratios, a/b=0.00, 1.05 and 1.10, are considered (corresponding to q=0.00, 2.44, and 4.76). The calculations for the case of a/b=1.05 is shown herein, and the results of the other cases are shown in Table 8.1.

8.5.1. Calculation Using the Proposed Method

- **Calculation of P_{cr} According to the Proposed Method**

The proposed equation to calculate the critical pressure for the liner is given by

$$P_{cr} = \frac{2E}{1-\nu^2}\left(\frac{t}{2R_o}\right)^3 K\ \alpha\ C,$$

where

α reduction factor due to ovality, $\alpha = e^{-\frac{q}{16}}$

K enhancement factor due to encasement, $K = \frac{1}{2}\left(\frac{2R_o}{t}\right)^{0.8}$

C reduction factor due to local imperfections, and is obtained from Fig. 8.1 depending on δ_o and t/b ratio.

for a/b=1.05, the average radius R_o is given by

R_o = 0.375 - (0.035/2) = 0.3575 m = (a+b)/2, so that b = 0.349 m

The ratio t/b can be defined as

t/b = 0.035 / 0.349 = 0.10,

Ovality factor q is then written as

$q = (R_o - b) / R_o \times 100 = 2.38\ \%$

From Fig. 8.1, for t/b=0.10 and δ_o=0.01, the reduction factor C is 0.81. The critical pressure is then

$$P_{cr} = \frac{2\times 200}{(1-0.3^2)}\left(\frac{0.035}{2\times 0.3575}\right)^3 \times \frac{1}{2}\left(\frac{2\times 0.3575}{0\ 035}\right)^{0.8} \times e^{-\frac{2.38}{18}} \times 0.81$$

$$P_{cr} = 0.0516 \times 5.59 \times 0.876 \times 0.81 = 0.21\ \text{MPa}$$

- **Calculation of N_{cr} and M_{cr} According to the Proposed Method**

From Fig. 8.2, for ovality q=2.38% and t/b=0.10,

$$\frac{N_{cr}}{P_{cr} R_o} = 1.25, \text{ and } \frac{M_{cr}}{P_{cr} R_o^2} = 0.079$$

The thrust N_{cr} and moment M_{cr} at the liner crown calculated at the critical pressure are given by

N_{cr} = 0.094 MN/m

M_{cr} = 2.120 kN.m/m

- **Calculation of Stresses at Buckling**

For N_{cr}=0.094 MN/m and M_{cr}=2.120 kN.m/m, the stress σ_e in the liner cross section is given by

$$\sigma_e = \frac{N_{cr}}{t} + \frac{6M_{cr}}{t^2} = \frac{0.094}{0.035} + \frac{6 \times 0.00212}{0.035^2} = 2.69 + 10.38 = 13.07 \text{ MPa}$$

If the polymer has a long term yield stress of 9 MPa, and a safety factor FS=2 is used, then

$$P_{allowable} = 0.21 \times \frac{\sigma_y}{\sigma_e} \times \frac{1}{FS} = 0.21 \times \frac{9.0}{13.07} \times \frac{1}{2} = 0.072 \text{ MPa}$$

A reduction factor of σ_y/σ_e is applied to the elastic buckling pressure because the stress at buckling exceeds the polymer yield stress. This linear scaling of the buckling pressure is conservative and reasonable.

8.5.2. Calculation Using the ASTM Recommendations

- **Calculation of P_{cr} According to the ASTM Recommendations**

The ASTM recommended equation to calculate the critical pressure for the liner is given by

$$P_{cr} = \frac{2E}{(1-\nu^2)} \left(\frac{t}{2R_s} \right)^3 K \alpha$$

where

α reduction factor due to ovality, $\alpha = \left[\left(1 - \frac{q}{100}\right) / \left(1 + \frac{q}{100}\right)^2 \right]^3$

K enhancement factor due to encasement (recommended value is 7)

$R_o = 0.3575$ m

$$\alpha = \left[\frac{1 - 0.024}{(1 + 0.024)^2} \right]^3 = 0.808$$

$$P_{cr} = \frac{2 \times 200}{(1-0.3^2)} \left(\frac{0.035}{2 \times 0.3575} \right)^3 \times 7 \times 0.808$$

$$P_{cr} = 0.0516 \times 7.0 \times 0.804 = 0.29 \text{ MPa}$$

- **Calculation of N_{cr} and M_{cr} According to the ASTM Recommendations**

The critical thrust N_{cr} and moment M_{cr} at the liner crown are given by

$$N_{cr} = P_{cr} R_o \left(1 + \frac{q}{100}\right) = 0.29 \times 0.3575 \times 1.024 = 0.106 \text{ MN/m}$$

$$M_{cr} = P_{cr} R_o^2 \left(1 + \frac{q}{100}\right) \frac{q}{100} = 0.29 \times 0.3575^2 \times 1.024 \times 0.024 = 0.91 \text{ kN.m/m}$$

- **Calculation of Stress at the Buckling According to ASTM Recommendations**

For N_{cr}=0.106 MN/m and M_{cr}=0.926 kN.m/m, the stress in the liner cross section is given by

$$\sigma_e = \frac{N_{cr}}{t} + \frac{6 M_{cr}}{t^2} = \frac{0.106}{0.035} + \frac{6 \times 0.00091}{0.035^2} = 3.03 + 4.46 = 7.49 \text{ MPa}$$

which is 57% of stress at buckling using the proposed solution If the polymer has a long term yield stress of 9 MPa, and a safety factor FS=2 is used, then

$$\text{allowable } P_{cr} = 0.29 \times \frac{1}{FS} = 0.29 \times \frac{1}{2} = 0.145 \text{ MPa}$$

No reduction due to yield is applied to the critical pressure because the stress at buckling does not exceed yield stress. The ASTM method gives a value of the allowable critical pressure that is two times the value determined using the proposed method. In this case, a designer who uses the ASTM design method achieves a true factor of safety, FS, defined by

$$FS = \frac{0.21 \times \frac{9.0}{13.07}}{0.145} = 0.995 < 1.0 \qquad \text{(i.e. unsafe)}$$

8.6. Comparison Between the Proposed and the ASTM Calculation Methods

A comparison between the proposed and the ASTM calculation methods is shown in Table 8.1. The comparison shows the following:

- The ASTM specifications do not include the effect of local imperfections in the calculations.
- The bending moments calculated according to ASTM due to ovality are much less than the proposed design method. This is due to the assumed equality between the moments for the cases of unsupported and encased liners.
- For the example shown featuring a thick liner, the stresses at buckling calculated using the proposed method are greater than the stresses due to ASTM. The ASTM is relatively not conservative. This results because ASTM recommend an enhancement factor K=7.0 for all liners with no regard to thickness to radius ratio.

- For the example shown, the effect of bending moments on the stresses is more pronounced that the effect of thrust. This demonstrates the importance of providing an accurate assessment of these bending moments.

8.7. Example Calculation for Loosely Fitted Liner

To demonstrate the calculations involved for a loosely fitted liner an example calculation is given. A liner with R_o=0.365 m, t=0.035 m, E=200 MPa, and ν=0.3 is loosely fitted within a host pipe of radius 0.375 m leaving a gap of 0.02 m between the liner and the host pipe. The ASTM calculations are almost as in the previous example, as the ASTM does not consider any kind of imperfections at all. The critical pressure according to the ASTM is 0.313 MPa. For the proposed method, the critical pressure is defined by

$$P_{cr} = \frac{2E}{1-\nu^2}\left(\frac{t}{2R_o}\right)^3 K = \frac{2\times 200}{1-0.09}\left(\frac{0.035}{2\times 0.375}\right)^3 \times 4 = 0.179 \text{ MPa}$$

where K is obtained from Fig. 8.3 for d/R_o=5.33. This value is 57% of the value proposed by the ASTM procedure.

8.8. Conclusions

A proposed method for the design of the liners for rigid pipelines, is given. It is a simple and more accurate alternative to the ASTM specifications. Usage of the method should be subject to its evaluation against experimental data.

Liner Type		Perfect Liner		Oval Liner a/b=1.05		Oval Liner a/b=1.10	
		δ_o=0.0	δ_o=0.01	δ_o=0.0	δ_o=0.01	δ_o=0.0	δ_o=0.01
ASTM	(1) P_{cr} (MPa)	0.360		0.290		0.238	
	(2) N_{cr} (MN/m)	0.129		0.106		0 089	
	(3) M_{cr} (MN.m/m)	0.000		0.00091		0.0015	
	(7) σ_{cr} (MPa)	3.69		7.49		9.82	
Proposed Method	(4) P_{cr} (MPa)	0.300	0.240	0.259	0.210	0.228	0.185
	(5) N_{cr} (MN/m)	0.125	0.101	0.116	0.094	0.108	0.087
	(6) M_{cr} (MN.m/m)	0.0029	0.0024	0.0026	0.0021	0.0024	0.0020
	(7) σ_{cr} (MPa)	17.88	14.49	16.13	13.07	14.91	12.08

Table 8.1. Comparison Between the ASTM and the Proposed Design Method

1- $$P_{cr} = \frac{2E}{(1-\nu^2)} \frac{1}{(DR-1)^3} K \alpha, \quad K=7, \quad \alpha = \left[\frac{1 - \frac{q}{100}}{\left(1 + \frac{q}{100}\right)^2} \right]^3$$

2- $$N_{cr} = P_{cr} R_o \left(1 + \frac{q}{100}\right)$$

3- $$M_{cr} = P_{cr} R_o^2 \frac{q}{100} \left(1 + \frac{q}{100}\right)$$

4- $$P_{cr} = \frac{2E}{(1-\nu^2)} \left(\frac{t}{2R_o} \right)^3 K \alpha C, \quad \alpha = e^{-\frac{q}{18}}, \quad K = \frac{1}{2} \left(\frac{2R_o}{t} \right)^{0.8}, \text{ and}$$

C is obtained from Fig. 8.1 depending on δ_o and t/b ratio.

5- $$N_{cr} = \left(\frac{N_{cr}}{PR_o} \right) P_{cr} R_o, \quad \left(\frac{N_{cr}}{PR_o} \right)$$ is obtained from Fig. 8.2 depending on q and t/b ratio

6- $$M_{cr} = \left(\frac{M_{cr}}{PR_o^2} \right) P_{cr} R_o^2, \quad \left(\frac{M_{cr}}{PR_o^2} \right)$$ is obtained from Fig. 8.2 depending on q and t/b ratio

7- $$\sigma_{cr} = \frac{N_{cr}}{t} + \frac{6M_{cr}}{t^2}$$

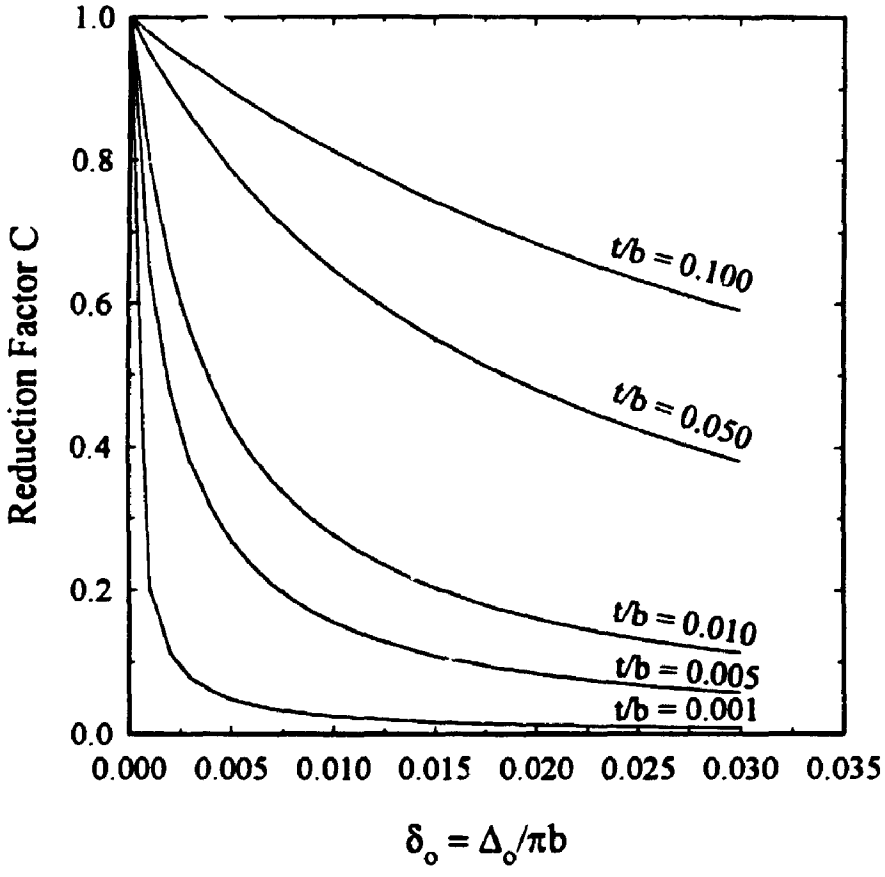

Figure 8.1. Reduction Factor due to Local Imperfection

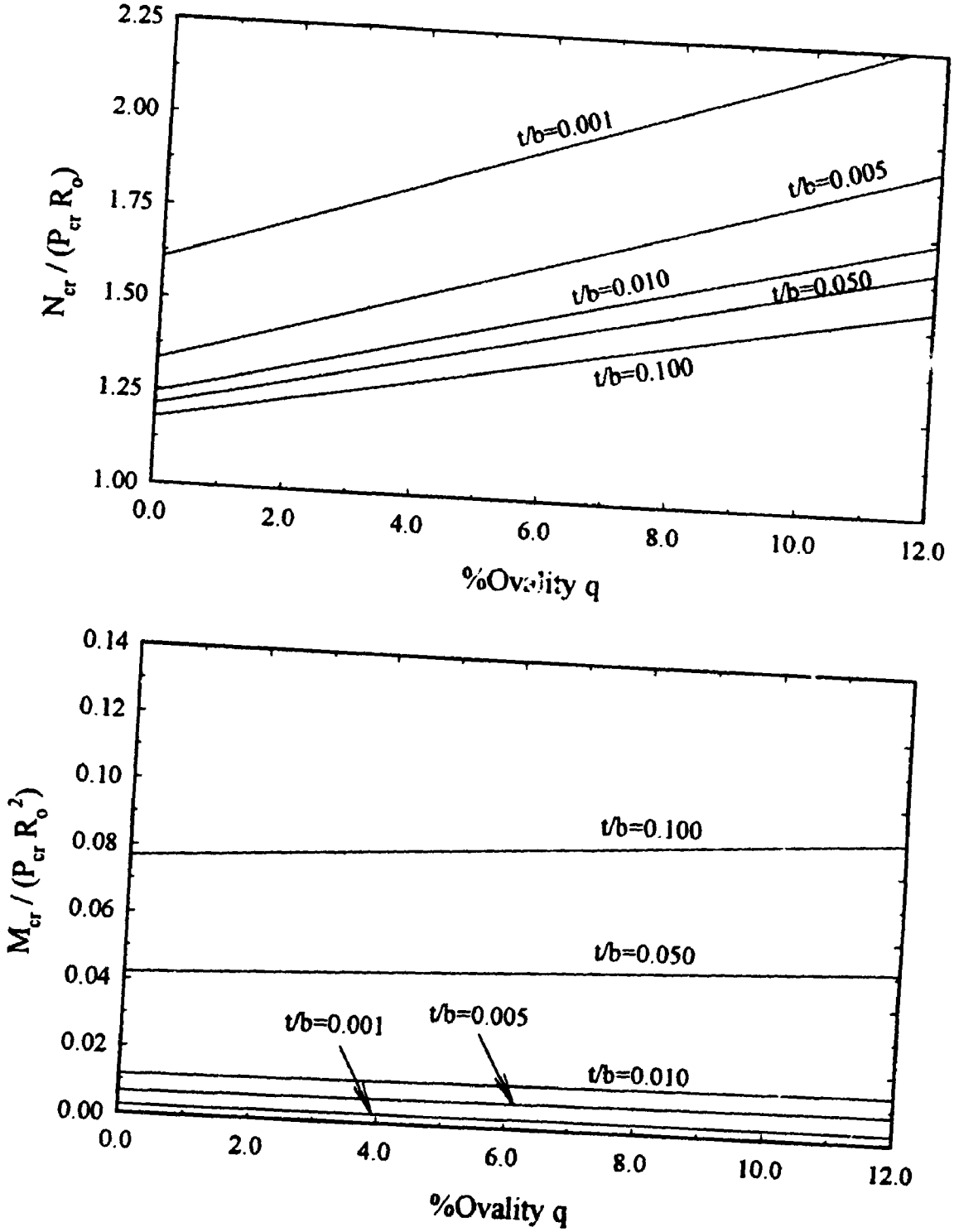

Figure 8.2. Effect of Ovality q and Thickness to Radius ratio (t/b) on the Thrusts and Moments

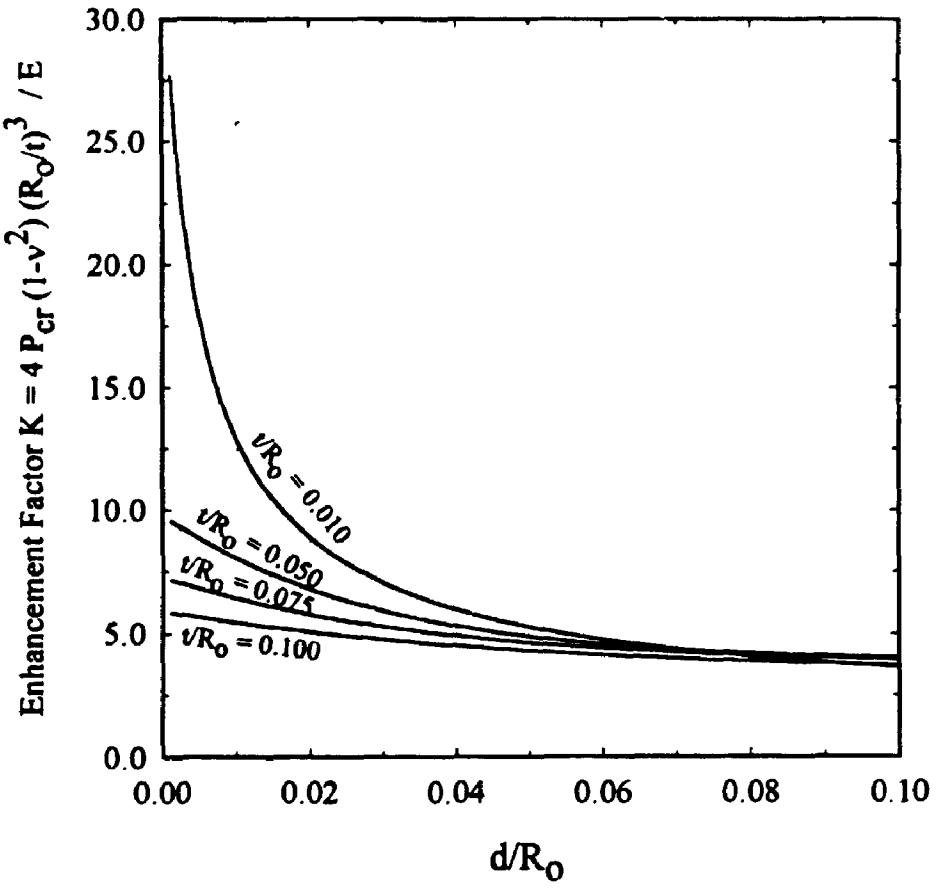

Figure 8.3. Enhancement Factor for Eccentric Liner in a Rigid Cavity

CHAPTER NINE

Summary and Conclusions

9.1. Introduction

The trenchless rehabilitation of damaged pipelines is developing as a competitive alternative to conventional methods of pipeline replacement. Its advantage stems from cost saving due to the reduced disturbance to the surroundings.

Most of the damaged pipelines are structurally safe, but due to hydraulic requirements (e.g., leakage) renovations are required. One solution is to apply an internal polymer liner to the pipeline. For this case, the liner needs to support loads from any transient pressure from grout pumped into the gap between the liner and the host pipe, the pressure of ground water that permeates into that gap, and internal fluid pressure. The critical pressure at which the liner may buckle has been the focus of much of the recent research. Different simplified assumptions have been used by these researchers, leading to a number of different solutions for the same problem.

In this thesis, a rigorous solution is developed for the problem. A non-linear Finite Element Analysis is used where material non-linearity and non-linear interaction are accounted for. The critical pressure, thrusts and bending moments in the encased liner are calculated. Liners are assumed to be either perfectly circular, elliptical, or circular with some initial geometrical imperfection. The imperfections varied from localized imperfections to global ones. Different parametric studies have been reported in the thesis, each targeting a different aspect of the problem. Based on those parametric studies, a method for calculating the critical pressure, thrusts and bending moments in the liner has

been proposed. The thesis includes new methods of analysis to replace the available methods reported in various ASTM specifications.

9.2. Solution Method

A new rigorous non-linear interaction technique is developed and coupled with the Arc Length Control Method to solve the liner buckling problem. Arc Length Control permits the solution of problems exhibiting a peak or snap-through load-defection behaviour. The interaction technique developed is of the Lagrange multiplier type. It is straightforward and does not sacrifice the simplicity or the accuracy of the FEM approach. The deformations are assumed to be large enough to change the geometry of the problem and the interface is assumed to be a frictional adhesive one with a *Coulomb* failure criterion. The technique examines the interaction of two bodies, namely the *Slave* and *Master* bodies. It simulates frictional slip, separation, bonding and re-bonding of the slave body with respect to the master body allowing for large deformations and non-matching nodes at the interface. The proposed solution is iterative where two levels of iterations are used. The first iteration level is used to satisfy equilibrium and to deal with the geometrical non-linearity, while the second is used to satisfy the interaction conditions at the interface. The interaction technique is illustrated with a number of test problems of varying complexity. These demonstrate that the approach performs well for problems involving interaction of two bodies under large deformations and that it is applicable to a very wide range of applications. Moreover, the method is applicable when one or both interacting bodies are prone to rigid body movements which was a serious drawback in other interaction techniques.

9.3. Parametric Study for the Circular Liners

Two distinct cases for circular liners are considered; perfect and imperfect liners. A comprehensive parametric study is accomplished for each case. For perfect liners, the finite element results are compared with available analytical and experimental data. The results of the Finite Element Analysis compare well with Glock's analytical solution [18] and represents a lower bound for almost 90% of the available experimental results by Aggarwal and Cooper [1]. If the effect of the gap between the liner and the host pipe is considered, FE solution represents a lower bound to all the test results.

It has also been demonstrated that while the assumption of inextensional liner (t/R=0) is acceptable for some applications, it is not for the case of a thick polymer liner subjected to pressure. The (t/R) ratio should be considered in the assessment of the critical liner pressure.

For liners with wavy local imperfection, the influence of both t/R and imperfection size on the critical pressure are discussed. Local imperfections, even with small amplitudes, reduce the critical pressure significantly, particularly for small t/R ratios. The effect of the shape of the imperfection on the critical pressure is also considered. The difference in the critical pressure for a sample of three different imperfection shapes is in the order of 15%. It is also shown that the case of a single imperfection is more critical than the case of a liner having more than one imperfection.

The effect of the pressure distribution is also studied. Two pressure distributions are considered; uniform and hydrostatic. It is shown that there is no significant difference in the critical pressure for the uniform pressure case and the maximum hydrostatic pressure which is critical for the non-uniformly loaded liner. The only difference is the post-buckling behaviour.

9.4. Parametric Study for the Oval Liners

Another type of imperfection is associated with the possible ovality (global imperfection) of the damaged pipelines. A comparison between the FEM results and the recommended design equations in ASTM F1218-93 indicates that the ASTM reduction factors used to reduce the critical pressure due to ovality are conservative. A proposed reduction factor based on FE analysis seems to be a better alternative.

Another comparison was reported between the reduction factor of Guice and Li [19] and the newly developed reduction factor. It showed that reduction factor recommended by Guice and Li may lead to unsafe design. This is attributed to the inappropriate application of a solution developed for the liner expansion problem to the case of a liner under pressure.

Based on FE results, thrusts and bending moments in oval liners have also been obtained. The FE results provide a more comprehensive solution than the corresponding ASTM equations. The ASTM equations are based on the assumption that the thrusts and bending moments of the unsupported liner case are the same for the encased liner. These do not take into account the significant effect of the liner thickness to radius ratio on the thrusts and bending moments.

The same local imperfection, used for the circular liner, was introduced into the oval liner and its effect has been assessed. Similar to the circular liner, the imperfection reduces the critical pressure significantly, particularly for small t/R ratios.

9.5. Parametric Study for the Loosely Fitted Liners

When heating is used in the liner installation process, the liner may end up loose relative to the host pipe. As fluid pressure develops between the liner and the host pipe, the liner

behaves as a free liner until it first touches the wall of the rigid host pipe. After that first contact, there is a sudden change in the liner behaviour, since the liner becomes supported on the rigid walls of the host pipe.

The critical pressure is strongly dependent on the size of the initial gap between the liner and the host pipe. The bigger the gap size, the lower the critical pressure. The loosely fitted liner stability has been checked against the approximate solution of Lo and Zhang [34] and their experimental results. Lo and Zhang used the arch buckling theory of Timoshenko and Gere [44] to study the buckling of the loosely fitted liner. They assumed that the liner is inextensional and that the deformations are small. The FEM solution for the cases of small gap size and t/R_o ratios, lies between Lo and Zhang's analytical solution for the symmetrical and asymmetrical buckling cases. When the gap size increases the geometrical non-linearity becomes important, the two solutions deviate and the finite element numerical results are more conservative. The finite element solution represents a lower bound for all the test results and the deviation from the numerical solution may result from using estimates of the gap size instead of accurate measurements.

A comparison between numerical solution and test results of Aggarwal and Cooper [1] shows that the finite element solution represents a lower bound for all the experimental results. The experimental critical pressures are higher than the numerical values due to the end restraints applied to the liner. This implies the importance of the choice of the liner length to radius ratio in any experimental work to minimize the effects of the liner end restraints.

The scatter shown in all the experimental results may be accounted for by the sensitivity of the behaviour for these relatively small gap size to radius ratios, material non-linearity and the friction angle between the liner and the host pipe.

9.6. Inelastic Response of the Liner

A brief parametric study of materially non-linear response has clearly revealed that yield in the liner can significantly affect the liner stability under the influence of external fluid pressure. For cases involving small amounts of strain hardening or softening, the critical pressure corresponds to the yield pressure. The plasticity of the liner material reduces the critical pressure when enough strain hardening is present.

For practical cases, the previous behaviour may only be valid for thick liners, where the yielding pressure is less than the elastic buckling pressure. For thin liners, the critical pressure is governed by e' - -tic buckling and not yielding.

9.7. Proposed Calculation Method

A proposed method for the design of the liners for rigid pipelines, is given. It is a simple and more accurate alternative to the ASTM specifications. A detailed example calculation is given to clearly demonstrate the proposed method. A comparison is made between the proposed and the ASTM calculation methods. The comparison shows that the ASTM specifications do not include the effect of local imperfections in the calculations, and this is a significant disadvantage. Moreover, the bending moments resulting from ovalities calculated according to ASTM, are much less than the proposed design method. This is due to the assumed equality between the moments for the cases of unsupported and encased

liners. For the example problem featuring a thick liner, the stresses at buckling calculated using the proposed design method are greater than the stresses estimated using the current ASTM procedure. The existing ASTM procedure does not produce a conservative solution since it employs an enhancement factor 7.0 for all liners with no regard to thickness to radius ratio.

9.8. General Conclusions

Although each chapter has its own conclusions, some general conclusions may be drawn from this study:

- The problem of buckling of an encased liner under pressure is very sensitive to the size (amplitude) of any local imperfections, but not the shape. Imperfection sensitivity is greatest for thin liners and is relatively small for thick liners.
- The current specifications (e.g. ASTM) need to be revised according to the findings of this study (discussed in chapter eight).
- The effect of the liner ovality is a reduction in the critical pressure but this reduction is less significant than the reduction due to local imperfections.
- The values for the thrust and bending moments in an encased oval liner are dependent on the liner ovality and thickness to average radius ratio. The bending moment values are greater than the values for the unsupported liner case which are proposed by ASTM.
- A tiny local imperfection, a nonuniform pressure distribution and a small ovality produces the same value of the critical pressure which corresponds to the circular liner case.

- The hydrostatic distribution of the pressure may be one factor which initiates buckling in liners even if the liner is perfectly circular.
- The case of a loosely fitted liner may be common due to the installation techniques used nowadays which produce a gap between the liner and the rigid host pipe. The ratio between the gap size and the liner radius controls the critical pressure. A small gap may reduce the critical pressure significantly below that for a tight liner, particularly for liner with small thickness to radius ratios.
- The material non-linearity affects the critical liner pressure. If the material strain hardening after yield is not significant, the critical pressure is equal to the pressure at the point of first yield. Liner design would then be based on the pressure leading to bending moments and thrusts which induce first yield.

9.10. Recommendations for Future Research

To end this dissertation, some recommendations for future research are made:

- An experimental study is essential to check the relevance of finite element calculations for the critical pressure. This study should feature testing with careful control on both local and global imperfections.
- A study to identify the different types of material imperfections which may exist in a liner is required. Numerical analysis of liners with material imperfections should follow.
- A study is required to statistically assess the imperfection sizes associated with different installation techniques.
- The study presented herein is limited to elastic and elasto-plastic material models with no time effects. The same simplification used in practice is employed assuming a time

dependent Young's modulus for the polymer material. Modulus is chosen to model response after a long period of time An appropriate non-linear visco-elastic or visco-plastic material model is required to analyse the time effect on the polymer liner behaviour. A study is needed to investigate a liner which is initially stable but which becomes unstable after a certain time. Models recently developed by Zhang and Moore [49, 50] for high density polyethylene may, for example, be used to investigate the impact of that polymer's rheology.

REFERENCES

1. Aggarwal, S. C., and Cooper, M. J., *External Pressure Testing of Insituform Lining*, Internal Report, Coventry (Lanchester) Polytechnic, 1984.

2. Argyris, J. H., Symeonidis, S., *Non-linear Finite Element Analysis of Elastic Systems Under Nonconservative Loading - Natural Formulation - I. Quasistatic Problems*, Comput. Meth. Appl. Mech. Engng, Vol. 26, pp. 75-123, 1981.

3. Bathe, K. J., *Finite Element Procedures in Engineering Analysis*, Prentice-Hall, Englewood Cliffs, N. J., 1982.

4. Bathe, K. J., Bolourchi, S., *A Geometric and Material Non-Linear Plates and Shell Element*, Comput. Struct., Vol. 11, pp. 23-48, 1980.

5. Bathe, K. J., and Chaudhary, A., *On Finite Element Analysis of Large Deformation Contact Problems*, Unification of Finite Element Methods, H. Kardesuncer Editor, Elsevier Science Publishers B. V. (North-Holland), Chapter 5, pp. 123-147, 1984.

6. Bathe, K. J., Ramm E., and Wilson E. L., *Finite Element Formulations for Large Deformation Dynamic Analysis*, International Journal for Numerical Methods in Engineering, Vol. 9, 353-386, 1975.

7. Bottega, W. T., *On the Constrained Ring*, J. Engng. Math., Vol. 22, pp. 43-51, 1988.

8. Bucciarelli, L. L. Jr., and Pian, T. H. H., *Effect of Initial Imperfection on the Instability of a Ring Confined in an Imperfect Rigid Boundary*, J. Appl. Mech, Trans. ASME, 979-984 (1964).

9. Bushnell, D., *A Strategy for the Solution of Problems Involving Large Deflections, Plasticity and Creep*, Int. J. Numer. Meth. Engng., Vol. 11, pp. 683-708, 1977.

10. Carrera, E., *A Study on Arc-Length-Type Methods and Their Operation Failures Illustrated by a Simple Model*, Computers & Structures, Vol. 50, No. 2, pp. 217-229, 1994.

11. Cheney, J. A., *Pressure Buckling of Ring Encased in Cavity*, Journal of Applied Mechanics, ASME, pp. 608-610, 1968.

12. Chicurel, R., *Shrink Buckling of Thin Circular Rings*, ASME J. Appl. Mech., Vol 35, No. 3, pp. 608-610, 1968.

13. Crisfield, M. A., *A Fast Incremental-Iterative Solution Procedure That Handles Snap-Through*, Comput. Struct., Vol. 13, pp. 55-62, 1981.

14. Da Deppo, D. A., Schmidt, R., *Instability of Clamped-Hinged Circular Arches Subjected to a Point Load*, Trans. Am. Soc. Mech. Eng., pp. 894-896, 1975.

15. El-Sawy, K., and Moore, I. D., *A Two-Level Iterative FEM Technique for Rigours Solution of Non-Linear Interaction Problems Under Large Deformations*, to appear in Computers & Structures.

16. El-Bayoumy, L., *Buckling of a Circular Elastic Ring Confined to a Uniformly Contracting Circular Boundary*, ASME J. Appl. Mech., Vol. 94, pp. 758-766, 1972.

17. Frieze, P. A., Hobbs, R. E. and Dowling, P. J., *Application of Dynamic Relaxation to the Large Deflection Elasto-Plastic Analysis of Plates*, Comput. Struct., Vol. 8, pp. 301-310, 1978.

18. Glock, D., *Überkritisches Verhalten eines starr ummautelten Kreisrohres bei Wasserdruck von außen und Temperaturdehnung*, Der Stahlbau, 7, 212-217, 1977, English Translation is "Critical Behaviour of Liners of Rigid Pipeline Under External Water Pressure and Thermal Expansion".

19. Guice, L. K., and Li, J. Y., *Buckling Models and Influencing Factors for Pipe Rehabilitation Design*, Proc., North Am. NO-DIG'94, Dallas, Texas, 1994.

20. Hannan, P. M., *Cured-In-Place Pipe: An End User Assessment*, Buried Plastic Pipe Technology, ASTM STP 1093, George S. Buczala and Michael J. Cassady, Eds., American Society for Testing and Materials, Philadelphia 1990.

21. Harding, J. E., Hobbs, R. E., and Neal B. G., *The Elasto-Plastic Analysis of Imperfect Square Plates Under in-Plane Loading*, Proc. Inst. Civ. Engrs. Part 2, 63, pp. 137-158, 1977.

22. Hsu, P. T.,Elkon, J., and Pian, T. H. H., *Note on the Instability of Circular Rings Confined to a Rigid Cavity*, ASME J. Appl. Mech. , Vol. 31, pp. 559-562, 1964.

23. Huffington, N. G., Numerical Analysis of Elastoplastic Stresses. Memorandum Report N. 2006, Ballastic Research Labratories, Aberdeen Proving Ground, Maryland, 1969.

24. Katona, M. G., *A Simple Contact-Friction Interface Element with Applications to Buried Culverts*, International Journal for Numerical and Analytical Methods in Geomechanics, Vol. 7, 371-384 (1983).

25. Kerja, I. and Cywiński Z., *Degenerated Isoparametric Finite Elements in Non-linear Analysis of 2D-Problems*, Computers & Structures, Vol. 41, No. 5, pp. 1029-1040, 1991.

26. Kodikara, J. K., Moore, I. D., *A General Interaction Analysis for Large Deformations*, International Journal for Numerical Methods in Engineering, Vol. 36, 2863-2876 (1993).

27. Kyriakides, S., and Babcock, C. D., *Large Deflection Collapse Analysis of an Inelastic Inextensional Ring Under External Pressure*, Int. J. Solids Structures, Vol. 17, No. 10, pp. 981-993, 1981.

28. Kyriakides, S., and Babcock, C. D., *Buckle Propagation Phenomena in Pipelines. Collapse: The buckling of Structures in Theory and Practice*, Proc. IUTAM Symp. on Collapse, London, Aug. 1982 (edited by J. M. T. Thomson and G. W. Hunt), pp.75-91, Cambridge University Press (1983).

29. Kyriakides, S., and Youn, S.-K., *On the Collapse of Circular Confined Rings Under External Pressure*, Int. J. Solids Structures Vol. 20, No. 7, pp. 699-713, 1984.

30. Levy, M., Me'memoire sur un nouveau cas inte'grable du proble'm de l'elastique et l'une de ses applications, [Memoir on a New Integrable Case of the Problem of Elasticity and One of its Applications], J. Math. Pure et Appl., (Lioville), Series 3, Vol. 10, pp. 5-42, 1884.

31. Li, F.-S., and Kyriakides, S., *On the Response and Stability of Two Concentric Contacting Rings Under External Pressure*, Int. J. Solids Structures Vol. 27, No. 1, pp. 1-14, 1991.

32. Li, J.Y., and Guice, L. K., *Buckling of Encased Elliptic Thin Ring*, ASCE, J. Engng. Mech., Vol. 121, No. 12, pp. 1325-1329, 1995.

33. Lo, H., Bogdanoff, J. L., Goldberg, J. E., and Crawford R. F., *A Buckling Problem of a Circular Ring*, Proceedings of the 4th U.S. National Congress of Applied Mechanics, ASME, pp. 691-695, 1962.

34. Lo, K. H. and Zhang, J. Q., *Collapse Resistance Modelling of Encased Pipes*, Buried Plastic Pipe Technology: 2nd volume, ASTM STP1222, Dave Eckstein, Ed., American Society for Testing and Materials, Philadelphia, 1994.

35. McAlpine, G., *Ovality Limitations in Pipe Rehabilitation Design*, NASTT NO-DIG'94, Dallas, Texas, 1994.

36. Nayak, G. C., Zienkiewicz, O. C., *Elastic-Plastic Stress Analysis. A Generalization for Various Constitutive Relations Including Strain Softening*, Int. J. Numer. Meth. Engng., Vol. 5, pp. 113-135, 1972.

37. Nyssen, C., *An Efficient and Accurate Iterative Method, Allowing Large Increment Steps, to Solve Elasto-Plastic Problems*, Comp. Struct., Vol. 13, pp. 63-71, 1981.

38. Pian, T. H. H., and Bucciarelli, L. L. Jr., *Buckling of Radially Constrained Circular Ring Under Distributed Loading*, Int. J. Solids and Structure, Vol. 3, pp. 715-730, 1967.

39. Riks, E., The Application of Newton's Method to the Problem of Elastic Stability, J. Appl. Mech., Vol. 39, pp. 1060-1066, 1972.

40. Soong, T. C., and Choi, I., *Buckling of an Elastic Elliptical Ring Inside a Rigid Boundary*, J. Appl. Mech., Vol. 52, No. 3, pp. 523-528, 1985.

41. *Standard Practice for Rehabilitation of Existing Pipelines and Conduits by the Inversion and Curing of a Resin-Impregnated Tube*, F1219-93, ASTM, Philadelphia, Pa, 1993.

42. Surana,K. S., *Geometrically Non-Linear Formulation for Two Dimensional Curved Beam Element*, Computers & Structures, Vol. 17, No. 1, pp. 105-114, 1983.

43. Svetlik, H. E., *Reduction, Renovation, Reversion :R^3*, Buried Plastic Pipe Technology, ASTM STP 1093, George S. Buczala and Michael J. Cassady, Eds., American Society for Testing and Materials, Philadelphia 1990.

44. Timoshenko, S. P., and Gere, J. M., *Theory of Elastic Stability*. McGraw-Hill, New York, 1961.

45. Wempner, G. A., *Discrete Approximation Related to Non-linear Theories of Solids*, Int. J. Solids Struct., Vol. 7, pp. 1581-1589, 1971.

46. Yamamoto, Y., and Matsubara, N., *Buckling Strength of Steel Cylindrical Liners for Waterway Tunnels*, Theor. Appl. Mech. (Japan) Vol. 30, pp. 225-235, 1981.

47. Yamamoto, Y. and Matsubara, N., *Buckling of a Cylindrical Shell under External Pressure Restrained by an Outer Rigid Wall*, Proc. Collapse and Buckling, Struct. Theory and Practice Symp., Cambridge University Press. London, England, pp. 493-504, 1983.

48. Zagustin, E. A., and Herrmann, G., *Stability of an Elastic Ring in a Rigid Cavity*, J. Appl. Mech., pp 263-270, 1967.

49. Zhang, C., and Moore, I. D., *Non-linear Mechanical Response of High Density Polyethylene: Part I - Experimental Investigation and Model Evaluation*, Journal of Polymer Engineering and Science (under review) (published as GEOT-5-96, University of Western Ontario)

50. Zhang, C., and Moore, I. D., *Non-linear Mechanical Response of High Density Polyethylene: Part II - Uniaxial Constitutive Modelling*, Journal of Polymer Engineering and Science (under review) (published as GEOT-6-96, University of Western Ontario)